

Arash Ajoudani

Transferring Human Impedance Regulation Skills to Robots



Springer

Editors

Prof. Bruno Siciliano
Dipartimento di Ingegneria Elettrica
e Tecnologie dell'Informazione
Università degli Studi di Napoli
Federico II
Via Claudio 21, 80125 Napoli
Italy
E-mail: siciliano@unina.it

Prof. Oussama Khatib
Artificial Intelligence Laboratory
Department of Computer Science
Stanford University
Stanford, CA 94305-9010
USA
E-mail: khatib@cs.stanford.edu

Editorial Advisory Board

Oliver Brock, TU Berlin, Germany
Herman Bruyninckx, KU Leuven, Belgium
Raja Chatila, ISIR—UPMC & CNRS, France
Henrik Christensen, Georgia Tech, USA
Peter Corke, Queensland Univ. Technology, Australia
Paolo Dario, Scuola S. Anna Pisa, Italy
Rüdiger Dillmann, University of Karlsruhe, Germany
Ken Goldberg, UC Berkeley, USA
John Hollerbach, University of Utah, USA
Makoto Kaneko, Osaka University, Japan
Lydia Kavraki, Rice University, USA
Vijay Kumar, University of Pennsylvania, USA
Sukhan Lee, Sungkyunkwan University, Korea
Frank Park, Seoul National University, Korea
Tim Salcudean, University of British Columbia, Canada
Roland Siegwart, ETH Zurich, Switzerland
Gaurav Sukhatme, University of Southern California, USA
Sebastian Thrun, Stanford University, USA
Yangsheng Xu, The Chinese University of Hong Kong, PRC
Shin'ichi Yuta, Tsukuba University, Japan

More information about this series at <http://www.springer.com/series/5208>

STAR (Springer Tracts in Advanced Robotics) has been promoted under the auspices of EURON (European Robotics Research Network)



Arash Ajoudani

Transferring Human Impedance Regulation Skills to Robots



Springer

Arash Ajoudani
Department of Advanced Robotics
Italian Institute of Technology (IIT)
Genova
Italy

ISSN 1610-7438 ISSN 1610-742X (electronic)
Springer Tracts in Advanced Robotics
ISBN 978-3-319-24203-3 ISBN 978-3-319-24205-7 (eBook)
DOI 10.1007/978-3-319-24205-7

Library of Congress Control Number: 2015950046

Springer Cham Heidelberg New York Dordrecht London
© Springer International Publishing Switzerland 2016

This work is subject to copyright. All rights are reserved by the Publisher, whether the whole or part of the material is concerned, specifically the rights of translation, reprinting, reuse of illustrations, recitation, broadcasting, reproduction on microfilms or in any other physical way, and transmission or information storage and retrieval, electronic adaptation, computer software, or by similar or dissimilar methodology now known or hereafter developed.

The use of general descriptive names, registered names, trademarks, service marks, etc. in this publication does not imply, even in the absence of a specific statement, that such names are exempt from the relevant protective laws and regulations and therefore free for general use.

The publisher, the authors and the editors are safe to assume that the advice and information in this book are believed to be true and accurate at the date of publication. Neither the publisher nor the authors or the editors give a warranty, express or implied, with respect to the material contained herein or for any errors or omissions that may have been made.

Printed on acid-free paper

Springer International Publishing AG Switzerland is part of Springer Science+Business Media
(www.springer.com)

Foreword

Robotics is undergoing a major transformation in scope and dimension. From a largely dominant industrial focus, robotics is rapidly expanding into human environments and vigorously engaged in its new challenges. Interacting with, assisting, serving, and exploring with humans, the emerging robots will increasingly touch people and their lives.

Beyond its impact on physical robots, the body of knowledge robotics has produced is revealing a much wider range of applications reaching across diverse research areas and scientific disciplines, such as: biomechanics, haptics, neurosciences, virtual simulation, animation, surgery, and sensor networks among others. In return, the challenges of the new emerging areas are proving an abundant source of stimulation and insights for the field of robotics. It is indeed at the intersection of disciplines that the most striking advances happen.

The *Springer Tracts in Advanced Robotics (STAR)* is devoted to bringing to the research community the latest advances in the robotics field on the basis of their significance and quality. Through a wide and timely dissemination of critical research developments in robotics, our objective with this series is to promote more exchanges and collaborations among the researchers in the community and contribute to further advancements in this rapidly growing field.

The monograph by Arash Ajoudani is a contribution aimed at developing teleimpedance control techniques for robotic systems, namely a manipulator arm, a dual-arm setup, a synergy-driven robotic hand, and a compliant exoskeleton. The concepts of common mode stiffness and configuration dependent stiffness control are introduced and experimentally evaluated in an assembly task. A novel real-time motion control strategy is proposed to regulate the desired Cartesian stiffness profile during the execution of observed bimanual tasks. Tactile feedback is used to develop intuitive control schemes for grasping tasks, while EMG signals are used for estimating knee joint torques, trajectory, and stiffness in real time. The results described in the volume suggest that the incorporation of human motor control principles into the design of robot controllers is expected to lead to versatile and stable behaviors when interacting with environments with dynamic uncertainties.

Remarkably, the monograph is based on the author's doctoral thesis, which was a finalist for the 2015 Georges Giralt Ph.D. Award. A very fine addition to STAR!

Naples, Italy
July 2015

Bruno Siciliano
STAR Editor

Acknowledgments

First of all, I would like to thank Prof. Antonio Bicchi, Dr. Nikos Tsagarakis and Prof. Darwin Caldwell for their outstanding support and valuable guidelines throughout my doctoral studies. Without their encouragement, constructive criticism, and constant feedback, my Ph.D. would not have been achievable. I would also like to thank Prof. Marco Gabiccini whose advice and insights were invaluable to me.

Robotics is a particular research domain which demands for collaborative interactions and keen enthusiasm. Thus, it is extremely important to work within a team of innovative and enthusiastic people. Advanced Robotics Department of Italian Institute of Technology, together with Centro E. Piaggio Department of University of Pisa, as international and dynamic working environments, provided me with the possibility of meeting and working with many brilliant researchers whose collaboration was extremely productive and led to a number of studies and several publications. Among the many colleagues those whose support and encouragement have been rewarding to me are: Dr. Jinoh Lee, Dr. Sasha Blue Godfrey, Dr. Matteo Bianchi, Dr. Manuel Catalano, and Dr. Giorgio Grioli.

I am thankful to my mother, Fereshteh, for her love and support throughout the years, through good times and bad. I am grateful to my father, Javad, who always gave me wise and insightful counsel, and I will always keep his memories in my heart. I would like to thank my bother, Nima, for being supportive and my dearest, Elena, for her love.

Finally, I would like to thank for the generous funding of my work, provided by the European projects: The Hand Embodied [31], Softhands [32], SAPHARI [33], WEARHAPS [34], and WALKMAN [35].

Genova
July 2015

Arash Ajoudani

Contents

| | | |
|--|--|-----------|
| 1 | Introduction | 1 |
| 1.1 | Motivation | 1 |
| 1.2 | Contributions | 3 |
| 1.3 | Outline | 4 |
| 1.3.1 | Outline of Part I | 4 |
| 1.3.2 | Outline of Part II | 5 |
| 1.3.3 | Outline of Part III | 6 |
| 1.3.4 | Outline of Part IV | 7 |
| 2 | On the Role of Compliance and Geometry in Mechanical Stability of the Humans and Robots | 9 |
| 2.1 | Stability in Human-Environment Interactions | 9 |
| 2.2 | Compliant Behavior in Robots | 12 |
| 2.2.1 | Compliant Mechanisms | 12 |
| 2.2.2 | Compliance Control | 14 |
| 2.3 | Redundancy Resolution and Its Application to Impedance Control | 15 |
| Part I Teleimpedance Control of a Robotic Arm | | |
| 3 | Teleimpedance: Teleoperation with Impedance Regulation Using a Body-Machine Interface | 19 |
| 3.1 | Human Arm Impedance Modeling in 3D | 22 |
| 3.2 | Stiffness Model Calibration/Identification | 25 |
| 3.2.1 | Identification of the EMG-to-Force Map | 27 |
| 3.2.2 | Identification of the EMG-to-Stiffness Map | 27 |
| 3.2.3 | Identification Results | 30 |

| | |
|---|----|
| 4 Replicating Human Stiffness Profile with a Cartesian Impedance Controller in Realtime | 33 |
| 4.1 Cartesian Impedance Control | 33 |
| 4.2 Teleimpedance: Peg-in-Hole Task | 35 |
| 4.2.1 Experimental Results | 37 |
| 4.3 Teleimpedance: Ball-Catching Task | 40 |
| 4.3.1 Experimental Results | 41 |
| 4.4 Conclusions | 44 |
| 5 Exploring the Roles of Common Mode Stiffness (CMS) and Configuration Dependent Stiffness (CDS) Control | 47 |
| 5.1 Controller Design | 48 |
| 5.1.1 CMS-CDS Controller | 48 |
| 5.1.2 Minimum-Effort Controller | 52 |
| 5.1.3 Soft Switching Logic | 52 |
| 5.2 Experiments | 53 |
| 5.3 Conclusions | 58 |
| Part II Human-like Impedance Control of a Dual-Arm Manipulator | |
| 6 Natural Redundancy Resolution in Dual-Arm Manipulation Using CDS Control | 61 |
| 6.1 Controller Design | 63 |
| 6.1.1 Dual-Arm Kinematics | 63 |
| 6.1.2 Impedance Control of Dual-Arm | 64 |
| 6.1.3 Task Prioritization | 68 |
| 6.2 Experimental Setup | 69 |
| 6.3 Results | 69 |
| 6.4 Conclusions | 73 |
| Part III Teleimpedance Control of a Robotic Hand | |
| 7 A Synergy-Driven Approach to a Myoelectric Hand | 77 |
| 7.1 Materials and Methods | 78 |
| 7.1.1 Overall Study Design | 78 |
| 7.1.2 The Pisa/IIT SoftHand | 79 |
| 7.1.3 Testing | 82 |
| 7.1.4 EMG Processing | 82 |
| 7.1.5 Control Architecture | 83 |
| 7.1.6 Questionnaire | 84 |
| 7.1.7 Data Analysis | 85 |
| 7.2 Results | 85 |
| 7.3 Conclusions | 88 |

| | |
|--|-----------|
| 8 Exploring Teleimpedance and Tactile Feedback for Intuitive Control of the Pisa/IIT SoftHand | 91 |
| 8.1 Human-SoftHand Interface | 93 |
| 8.2 Interaction Torque Observer | 94 |
| 8.3 Tactile Interfaces | 97 |
| 8.3.1 Mechano-Tactile Feedback | 97 |
| 8.3.2 Vibro-Tactile Feedback | 98 |
| 8.3.3 Texture Rendering and Psychophysical Considerations | 100 |
| 8.4 Control Architecture | 102 |
| 8.5 Experimental Setup | 103 |
| 8.5.1 Grasping Experiments | 104 |
| 8.5.2 Haptic Experiments | 104 |
| 8.6 Results | 107 |
| 8.6.1 Interaction Torque Observer | 107 |
| 8.6.2 Grasping Experiments | 107 |
| 8.6.3 Haptic Experiments | 112 |
| 8.7 Discussion | 114 |

Part IV Teleimpedance Control of a Compliant Knee Exoskeleton

| | |
|---|------------|
| 9 Teleimpedance Based Assistive Control for a Compliant Knee Exoskeleton | 119 |
| 9.1 Musculoskeletal Model of the Knee Joint | 120 |
| 9.1.1 Activation Dynamics | 121 |
| 9.1.2 Contraction Dynamics | 122 |
| 9.1.3 Musculoskeletal Geometry | 123 |
| 9.2 Model Identification-Calibration | 124 |
| 9.2.1 Model Identification Experiments | 124 |
| 9.2.2 Model Validation | 125 |
| 9.3 Knee Exoskeleton Hardware | 126 |
| 9.3.1 Mechatronic System | 127 |
| 9.4 Teleimpedance Based Assistive Control | 129 |
| 9.5 The Human-Exoskeleton System Dynamics for the Standing-Up Motion | 131 |
| 9.5.1 System Modeling and Simulation | 131 |
| 9.5.2 Stability and Performance Analysis | 133 |
| 9.6 Experimental Results | 136 |
| 9.7 Conclusion | 138 |

| | |
|--|-----|
| 10 Human-Inspired Balancing Assistance: Application to a Knee Exoskeleton | 139 |
| 10.1 Model-Based Joint Stiffness Estimation | 140 |
| 10.1.1 EMG-Driven Musculoskeletal Model Description | 140 |
| 10.1.2 Adjusting the Musculoskeletal Model Parameters | 141 |
| 10.2 Human Balancing Experiment | 144 |
| 10.2.1 Description of the Experimental Setup | 144 |
| 10.2.2 Data Analysis | 145 |
| 10.3 Balancing Assistance Control | 147 |
| 10.4 Knee Exoskeleton Application | 148 |
| 10.5 Conclusions | 151 |
| 11 Conclusions | 153 |
| Bibliography | 155 |

List of Figures

| | | |
|------------|---|----|
| Figure 2.1 | Stiffness ellipses during posture maintenance of subjects A, B, and C | 11 |
| Figure 2.2 | Stiffness ellipses (<i>upper figures</i>) and joint stiffness values (<i>lower figures</i>) of shoulder (R_{ss} , <i>continuous</i> <i>curve</i>), elbow (R_{ee} , <i>dotted curve</i>), and double-joints (R_{se} , <i>dashed-dotted curve</i> ; R_{es} , <i>dashed curve</i>) during transverse multi-joint movements for subjects A, B, and C | 11 |
| Figure 2.3 | Examples of position controlled robots | 12 |
| Figure 2.4 | Recent developments in robotic systems to achieve a compliant behavior | 13 |
| Figure 3.1 | The overall block diagram of teleimpedance | 21 |
| Figure 3.2 | Experimental setup used for the first calibration experiments. Subject applies constant forces in six directions while holding the handle attached to an idle spherical joint | 26 |
| Figure 3.3 | Electrode positions in EMG measurements | 26 |
| Figure 3.4 | Typical applied endpoint displacements and restoring forces in x , y and z directions. Each trial was 40 s long which the last 35 s of the trials were used for the further processings | 28 |
| Figure 3.5 | Power spectrum of the applied disturbances | 28 |
| Figure 3.6 | Multiple and partial coherence values over frequency | 30 |
| Figure 3.7 | Non-parametric (<i>solid lines</i>) and parametric second order (<i>dotted lines</i>) transfer functions of SISO impedance subsystems obtained from stochastic perturbations | 31 |
| Figure 4.1 | Peg-in-hole experimental setup. KUKA light weight robotic arm, EMG electrodes, peg, hole, position tracking markers and F/T sensor are shown | 36 |

| | | |
|-------------|---|----|
| Figure 4.2 | Dynamic interaction forces between peg and the hole and position tracking error in x, y and z directions, with a fixed high values of end point stiffness ([1200, 1200, 1200] N/m), b fixed low values of end point stiffness ([120, 120, 120] N/m) and c fixed and high along z and low along x and y directions ($K = [250, 250, 1200]$ N/m) | 38 |
| Figure 4.3 | Fully rectified eight channel raw EMGs (<i>upper plot</i>) and estimated and mapped endpoint stiffness (<i>lower plot</i>) in real-time for peg-in-hole task | 39 |
| Figure 4.4 | Dynamic interaction forces between peg and the hole (<i>upper graph</i>) and position tracking error in x, y and z directions (<i>lower graph</i>) based on teleimpedance | 39 |
| Figure 4.5 | Experimental setup of the ball-catching experiments. The slave KUKA LWR arm, EMG electrodes, position tracking markers and F/T sensor are shown | 40 |
| Figure 4.6 | Typical master's hand path in x,y and z directions with respect to its initial position, and while performing the ball-reception task | 42 |
| Figure 4.7 | Measured force values in z direction during the task with the slave robotic arm under constantly high, constantly low, and teleimpedance stiffness control. | 41 |
| Figure 4.8 | Absolute tracking position error in z direction during the task with the slave robotic arm under constantly high, constantly low, and teleimpedance stiffness control | 42 |
| Figure 4.9 | Fully rectified eight channel raw EMGs (<i>upper plot</i>) and estimated and mapped endpoint stiffness (<i>lower plot</i>) in real-time for ball-reception task | 42 |
| Figure 4.10 | Performance index plots over different elastic endpoint profiles (S: Stiff, C: Compliant and T: Teleimpedance) | 44 |
| Figure 5.1 | KUKA robot in initial joint configuration (a), under minimum-effort (b) and CMS-CDS (c) null-space controllers | 54 |
| Figure 5.2 | Normalized minimum-effort and CMS-CDS cost functions (<i>upper plot</i>), controlled by priority based soft switching logic. Interaction forces and joint angles are shown in <i>middle</i> and <i>lower plot</i> , respectively. A, B and C phases correspond to initial, minimum-effort and CMS-CDS joint configurations in Fig. 5.1. <i>Dotted (red)</i> and <i>dashed (blue)</i> horizontal | |

| | | |
|------------|---|----|
| | <i>lines in upper plot</i> represent the min-effort and CMS-CDS cost functions without proposed control of kinematic redundancy | 55 |
| Figure 5.3 | Robot endpoint stiffness ellipsoids (translational) replicated by teleimpedance under Cartesian stiffness (<i>solid line</i>), CMS-CDS (<i>broken line</i>) and only CMS (<i>dotted line</i>) controllers in interaction phase. Cartesian stiffness ellipsoids coincide with the desired ones | 55 |
| Figure 5.4 | Comparative analysis of Cartesian (Cart), CMS-CDS and only CMS controllers. Interaction forces along x (<i>blue</i>), y (<i>green</i>) and z (<i>red</i>) for Cartesian (<i>solid line</i>) and CMS-CDS (<i>dashed-line</i>) are shown in <i>upper plot</i> . <i>Lower-left plot</i> displays the effect of min-effort controller in defined cost function (C_g) during movement in Cartesian and CMD-CDS experiments. <i>Lower-right plot</i> compares the SEI index for experiments under Cartesian, CMS-CDS and only CMS controller. | 56 |
| Figure 5.5 | Muscular activities (<i>upper plot</i>) and resulting common-mode-stiffness (CMS) in CMS-CDS experiment (<i>lower plot</i>). | 57 |
| Figure 6.1 | Examples of acquired natural postures in humans as a consequence to the redundancy resolution for a minimum effort and b impedance control | 62 |
| Figure 6.2 | Dual arm manipulation diagram | 64 |
| Figure 6.3 | Dual-arm assembly (peg-in-hole) setup | 66 |
| Figure 6.4 | a Human performing a bimanual peg-in-hole task. Initial configuration b , and realized configuration as a result of proposed controller c . Human and robots' ending configuration coincide which gives evidence to the similarity in control principles | 70 |
| Figure 6.5 | Desired (<i>red, dashed</i>) and realized (<i>black, solid</i>) translational stiffness ellipsoids, corresponding to configuration c in Fig. 6.4. In this experiment, the translational stiffness matrix $K_{c_{des}} = [300, 300, 1000] \text{ N/m}$, is defined in relative coordinates. All off diagonal elements are set to zero. The hole is mounted along the z axis of Σ_G | 71 |
| Figure 6.6 | Common mode stiffness parameters of the two robots (<i>left and middle plots</i>) are adapted in addition to the CDS to decrease the error between the desired and realized stiffness ellipsoids (most <i>right plot</i>), in real time | 71 |

| | | |
|------------|--|----|
| Figure 6.7 | a Human performing a bimanual peg-in-hole task. Initial configuration (b), and realized configuration as a result of proposed controller (c). The hole was kept in a fixed position (subtask one), while the orientation was allowed to change due to the CDS. Human and robots' ending configuration coincide which gives evidence to the similarity in control principles | 72 |
| Figure 6.8 | Desired (<i>red, dashed</i>) and realized (<i>black, solid</i>) translational stiffness ellipsoids, corresponding to configuration in Fig. 6.4c. In this experiment, the translational stiffness matrix $K_{c_{des}} = [300, 1000, 300] \text{ N/m}$, is defined in relative coordinates. All off diagonal elements are set to zero. The hole is mounted along the Y axis of Σ_G | 72 |
| Figure 6.9 | Desired (<i>red, dashed</i>) and realized (<i>black, solid</i>) translational stiffness ellipsoids with different elongation w.r.t. Fig. 6.5. In this experiment, the translational stiffness matrix $K_{c_{des}} = [1000, 300, 300] \text{ N/m}$, is defined in relative coordinates. All off diagonal elements are set to zero | 73 |
| Figure 7.1 | Pisa/IIT SoftHand | 79 |
| Figure 7.2 | A schematic of the hand, showing the revolute joints in <i>dark grey</i> and the rolling contact joints in <i>light grey</i> (a) and a side-view schematic of the rolling contact joint in (b). The sequence in (c) shows the hand before, during, and after impact with a stiff surface | 80 |
| Figure 7.3 | The Pisa/IIT SoftHand joints can withstand severe forces in all directions, automatically returning to the correct assembly configuration. a Finger side bend. b Finger Back bend. c Finger Twist. d Finger Skew bend. | 81 |
| Figure 7.4 | Block diagram of the control pattern used to drive the Pisa/IIT SoftHand with myoelectric signals | 83 |
| Figure 7.5 | Photographic sequence of a typical grasp. Five phases are noticeable: in order, a reach, b grasp, c lift, d release, and e withdraw | 84 |
| Figure 7.6 | Activation of FDS (<i>top</i>) and EDC (<i>bottom</i>) during a typical grasping sequence. Different colors indicate the five phases of the grasp extracted from video recordings | 85 |

| | | |
|-------------|---|-----|
| Figure 7.7 | Actual and reference position sent to the motor (<i>top</i>) and the stiffness level used (<i>bottom</i>), determined by cocontraction. Different colors indicate the five phases of the grasp extracted from video recordings | 86 |
| Figure 7.8 | Questionnaire results for physical (<i>top</i>) and mental (<i>bottom</i>) effort. <i>Darker bars</i> indicate lower perceived amount of effort a Physical Effort, b Mental Effort | 87 |
| Figure 7.9 | Time spent above threshold averaged across subjects (<i>top</i>). Average FDS EMG amplitude (<i>bottom, bars</i>) and cumulative EMG (<i>bottom, line</i>) a Duration of EMG Activity, b EMG Activity | 88 |
| Figure 8.1 | Interaction torque observer block diagram | 96 |
| Figure 8.2 | Upper arm cuff, actuated by a DC motor picture (<i>left</i>) and schematics (<i>right</i>). The motor generated torque (<i>blue</i>), generates a pulling force (<i>green</i>) on the black tendon, which in turn causes, by constriction, a distribution of internal pressure (<i>red</i>) around the arm | 97 |
| Figure 8.3 | Loading scheme of the upper arm cuff | 98 |
| Figure 8.4 | Block diagram of the acceleration feedback system | 99 |
| Figure 8.5 | SoftHand equipped with the able-bodied adapter (forearm support) and fingertip accelerometers | 100 |
| Figure 8.6 | The end-effector on the KUKA/DLR arm with the accelerometer. Reference coordinates are also indicated | 102 |
| Figure 8.7 | Block diagram of the synergy-driven hand teleimpedance controller | 103 |
| Figure 8.8 | Experimental setup for haptic experiments | 105 |
| Figure 8.9 | Plastic bars (a) and the filing tools (b) used in haptic experiments | 105 |
| Figure 8.10 | The SoftHand molds around the obstacle by two (c_1) and three (c_2) fingers, during grasping | 107 |
| Figure 8.11 | Results of a grasping experiment with fixed stiffness gain. A soft, deformable ball was used as an object to grasp during the second and third closures and removed on the first and the last. The top three plots demonstrate the position tracking, motor current and motor voltage profiles, from the top down. Observed interaction torques once the soft obstacle was squeezed by two (c_1) or three (c_2) fingers are provided in the bottom plot | 108 |

| | | |
|-------------|---|-----|
| Figure 8.12 | Experimental results of the SoftHand grasping a hard object (mug), with the controller under a high, fixed stiffness gain ($K = 40 \text{ Nm/rad}$), b low, fixed stiffness gain ($K = 10 \text{ Nm/rad}$) for this subject | 109 |
| Figure 8.13 | Experimental results of the SoftHand grasping a hard object (mug), with the controller under teleimpedance ($a_{q_{norm}} = 1$, $b_q = 5.03$, $a_k = 1.87$, and $b_k = 0.579$, for this subject) | 110 |
| Figure 8.14 | SoftHand making an espresso | 110 |
| Figure 8.15 | Grasping delicate objects. | 111 |
| Figure 8.16 | a Average interaction forces for five subjects grasping different objects with SoftHand controlled under Stiff, Compliant and Teleimpedance controllers. b Average processed EMG signals for five subjects, grasping different objects. The averaging was performed on all trials either with or without the effect of interaction force feedback in Teleimpedance experiments | 111 |
| Figure 9.1 | Representation of the muscle-tendon unit based on Hill's model | 121 |
| Figure 9.2 | Comparison of the estimated torque of the knee joint and the one derived from the musculoskeletal model in extension (a) and flexion (b) identification trials. <i>Red (dashed)</i> and <i>blue (solid)</i> lines in the <i>upper plots</i> demonstrate the actual and estimated knee torque profiles. Corresponding knee angle trajectories during extension (a) and flexion (b) are plotted in <i>green (dotted)</i> . <i>Lower plots</i> demonstrate fully rectified EMG activities of the three dominant extensor (a) and flexor (b) muscles. | 126 |
| Figure 9.3 | The intrinsically compliant knee exoskeleton device. | 127 |
| Figure 9.4 | Functional principle of CompAct-RS; Stiffness can be adjusted theoretically from zero to infinite by varying the position of the pivot | 128 |
| Figure 9.5 | a Section of the CAD assembly of CompAct-RS and its components. b View of the elastic module. c Overall view of CompAct-RS | 128 |
| Figure 9.6 | Schematic of the derivation of the position and the stiffness reference | 130 |
| Figure 9.7 | Block diagram of the implemented teleimpedance controller that provides stiffness augmentation based on human stiffness trend | 130 |

| | | |
|-------------|---|-----|
| Figure 9.8 | Representation of the simplified physical system of the human-knee exoskeleton and the concept of the teleimpedance control | 132 |
| Figure 9.9 | Conceptual schematic that illustrates the interaction mechanics between exoskeleton and human including the teleimpedance controller | 132 |
| Figure 9.10 | Simulation results corresponding to the standing-up motion | 133 |
| Figure 9.11 | Bode plots of the transfer function $\frac{X_h}{X_e}$ for different values of the active stiffness K_c (Nm/rad) | 135 |
| Figure 9.12 | Natural frequency (a) and damping ratio (b) for different values of K_c and K_S | 135 |
| Figure 9.13 | Standing-up motion task for experimental evaluation | 136 |
| Figure 9.14 | Active stiffness of the teleimpedance controller during standing up based on the trace of the user's joint stiffness and the processed EMGs of the six muscles. | 137 |
| Figure 9.15 | The torque and position reference and the torque and position of the knee exoskeleton device | 137 |
| Figure 10.1 | Applied stochastic perturbations and resulting torque response while the subject was applying constant flexion torque of 10 %MVC | 142 |
| Figure 10.2 | Coherence and non-parametric transfer function of the impedance obtained from stochastic perturbations | 143 |
| Figure 10.3 | Active stiffness of the knee joint identified during perturbations for eight different conditions and the corresponding model-based stiffness estimates | 143 |
| Figure 10.4 | The averaged correlation coefficient (r) that is the maximum of the computed cross-correlation functions | 145 |
| Figure 10.5 | Averaged cross-correlation functions of all trials for the interval from 6th to 28th second with maximum lag of 2 s | 146 |
| Figure 10.6 | Lags of the maximum or minimum of the corresponding cross-correlation functions | 147 |
| Figure 10.7 | The knee exoskeleton, used in experiments | 148 |
| Figure 10.8 | Human balancing experiment. The subject is wearing the knee exoskeleton while electrodes are attached to six muscles about the knee to derive the stiffness estimates | 149 |

| | | |
|--------------|--|-----|
| Figure 10.9 | Center of pressure trajectory in the anteroposterior axis and knee angle changes during balancing under external disturbances | 150 |
| Figure 10.10 | The CoP-guided active stiffness of the impedance controller and the torque applied by the exoskeleton during the experiment of the balancing assistance. | 150 |

List of Tables

| | | |
|------------|--|-----|
| Table 3.1 | Muscles used for EMG measurements | 26 |
| Table 3.2 | Estimated hand impedance parameters | 31 |
| Table 7.1 | Dimensions and weights of test objects | 82 |
| Table 8.1 | Mean vibrotactile detection thresholds (μm), discriminable increments (Δf) and Weber Fractions ($\Delta f/f$) for frequency discrimination, on the forearm at the standard frequencies of 20, 50, 100, and 200 Hz [198] | 101 |
| Table 8.2 | Results of the fit of $Fd + Ob$ model using <i>glmer</i> function | 113 |
| Table 8.3 | Results of the fit of $Fd + Ob$ model using <i>glmer</i> function | 113 |
| Table 8.4 | Results of the fit of $Fd + Ob$ model using <i>glmer</i> function | 113 |
| Table 8.5 | Results of the fit of $Fd + Ob$ model using <i>glmer</i> function | 114 |
| Table 9.1 | Specifications of CompAct-RS | 129 |
| Table 10.1 | Conditions during the perturbation experiment | 144 |

Abstract

This book, which is based on my Ph.D. thesis, written in the Advanced Robotics Department of the Italian Institute of Technology and E. Piaggio centre of the University of Pisa, introduces novel thinking and techniques to the control of robotic manipulation. In particular, the concept of teleimpedance control as an alternative method to bilateral force-reflecting teleoperation control for robotic manipulation is introduced. In teleimpedance control, a compound reference command is sent to the slave robot including both the desired motion trajectory and impedance profile, which are then realized by the remote controller. This concept forms a basis for the development of the controllers for a robotic arm, a dual-arm setup, a synergy-driven robotic hand, and a compliant exoskeleton for improved interaction performance.

First part of this book concerns the teleimpedance control of a robotic arm. Here, the reference commands are derived from a novel body-machine interface (BMI) applied to the master operator's arm, using only nonintrusive position and electromyography (EMG) measurements. The proposed BMI exploits a novel algorithm to decouple the estimates of force and stiffness of the human arm while performing the task. The endpoint (wrist) position of the human arm is monitored by an optical tracking system and used for the closed-loop position control of the robot's end effector. A Cartesian stiffness controller is adopted to realize the desired compliant profile, derived from the proposed BMI model. The concept is demonstrated in two experiments, namely a peg-in-the-hole and a ball-catching task, which illustrate complementary aspects of the method. In addition to the improved interaction performance achieved, results suggest that contribution of the human/robot configuration to realization of a desired endpoint stiffness ellipsoid directionality is major. To that end, the concept of common mode stiffness (CMS) and configuration dependent stiffness (CDS) control is proposed and experimentally evaluated in an assembly task.

In the second part, relying on the observations on human bimanual coordination, a novel real-time motion control strategy is proposed to regulate the desired Cartesian stiffness profile during the execution of bimanual tasks. The novelty of the proposed control scheme relies on the use of CMS and CDS to regulate the

size and directionality of the task space stiffness ellipsoid. Thanks to the CDS control, the proposed scheme is not only proved to be effective in regulating the desired stiffness ellipsoid but also permits to resolve the manipulator redundancy in a manner that results in motions exhibiting similarities with those performed by a human during the execution of bimanual tasks. The effectiveness of the controller is evaluated in an experimental setup in which two cooperating robotic arms are executing an assembly task. Experimental results demonstrate that the proposed dual-arm CDS-CMS controller is effective in tracking the desired stiffness ellipsoids as well as in producing human-like natural motions for the two robotic arms.

Third part proposes a teleimpedance controller with tactile feedback for more intuitive control of the Pisa/IIT SoftHand. With the aim to realize a robust, efficient, and low-cost hand prosthesis design, the SoftHand is developed based on the motor control principle of synergies, through which the immense complexity of the hand is simplified into distinct motor patterns. In addition, for intuitive control of the hand, two tactile interfaces are developed. The first interface (mechanotactile) exploits a disturbance observer which estimates the interaction forces in contact with the grasped object. Estimated interaction forces are then converted and applied to the upper arm of the user via a custom-made pressure cuff. The second interface employs vibrotactile feedback based on surface irregularities and acceleration signals and is used to provide the user with information about the surface properties of the object as well as detection of object slippage while grasping. Grasp robustness and intuitiveness of hand control were evaluated in two sets of experiments. Results suggest that incorporating the aforementioned haptic feedback strategies, together with user-driven compliance of the hand, facilitate execution of safe and stable grasps, while suggesting that a low-cost, robust hand employing hardware-based synergies might be a good alternative to the traditional myoelectric prostheses.

Finally, last part presents a teleimpedance-based assistive control scheme for a compliant knee exoskeleton. Proposed controller captures the user intent to generate task-related assistive torques by means of the exoskeleton. To do so, a detailed musculoskeletal model of the human knee is developed and experimentally calibrated to better match the user's kinematic and dynamic behavior. EMG signals are acquired, processed, and used for the estimation of the knee joint torque, trajectory, and the stiffness trend in real time. Estimated stiffness trend is then scaled and mapped to a task-related stiffness interval to agree with the desired degree of assistance. The desired stiffness and equilibrium trajectories are then tracked by the exoskeleton's impedance controller. As a consequence, while the minimum muscular activity corresponds to low stiffness, i.e., highly transparent motion and higher cocontractions result in stiffer joint and stronger level of assistance.

Overall results suggest that incorporation of the human motor control principles into the design of the robot controllers will eventually permit them to reach interaction performances close to those achieved by the humans, demonstrating a versatile and stable behavior even when interacting with environments with dynamic uncertainties.

Chapter 1

Introduction

1.1 Motivation

Over the past decades, applications of robots in unstructured and hostile for human environments have seen an intensive use of Master-Slave teleoperation systems often based on feedback sensory data. In these systems, a human operator executes a task by controlling a manipulator (Slave) located in the remote environment using a robotic interface (Master) located at the human site. The execution of the remotely performed task is usually assisted by feeding back to the master and human operator kinesthetic feedback conveying information about the force interaction between the slave robot and the remote environment. Although these bilaterally controlled tele-operated systems outperform the pure position controlled systems, latencies in the communication channel between the master and slave robot may generate serious issues related to the stability of the bilateral teleoperation system [36, 37].

To guarantee the stability of the bilateral teleoperation system in the presence of time delays several control schemes have been proposed [38, 39]. Although these techniques have demonstrated good results, especially in the case of small and fixed time delays, in many cases the stable contact and task execution is achieved through a compromise with the transparency of the system. In particular, the application of high damping actions at the master device [40, 41] can generate forces which are superimposed to the ones fed back from the remote slave robot that will eventually reduce the transparency of the teleoperation system.

Despite the results and continuous improvements in the control and the stability of bilateral controlled teleoperation systems, there are still many tasks in which stability and reduced transparency, if not mere cost of sensing and actuating reflected forces, prevent application of bidirectional teleoperation. Tasks which are normally performed by humans without difficulty such as drilling, reaming, chipping and many others with large uncertainty in the environment constraints, cannot be easily conducted under sensory feedback based teleoperation control. This is not only due to the stability and transparency issues mentioned above but also in many cases due to inadequate or low quality sensory information (such as position, force, velocity).

It is well known that humans present a stable mechanical interface to the uncertain environment. This allows a limb (such as arm) to make a reliable contact with variety of objects and to realize a stable posture in the presence of destabilizing loads. Such versatile and stable movement skills are demonstrated due to the ability of humans to adjust dynamic characteristics of their musculoskeletal system. As a consequence, an environmental displacement will be immediately resisted by elastic restoring forces produced by the muscles [42]. This elastic resistance is quantified in terms of the joint stiffness.

The joint stiffness has been demonstrated to increase in proportion to the joint torque. In the meantime, cocontraction of the muscles acting on the joint can modify the joint stiffness profile, independently of the joint torque variations [43]. Joint stiffness modifications (as the static component of the joint impedance) take part in the stabilization of the joint position. Concurrently, the projection of the joint stiffness into the task coordinates (Cartesian, task or endpoint stiffness) will stabilize the corresponding task position. This projection employs the involved joint stiffness profiles, as well as the geometry of the limb. Therefore, the elastic response in Cartesian coordinates does not simply and only depend on the joint stiffness. Indeed, some studies report on the major contribution of the geometry to the mechanical stability of the human posture [44, 45].

Understanding how the mechanical properties of the human limb are modified during the execution of the functional tasks, not only will elucidate the underlying neuromotor strategies, it will also motivate the decisions made regarding the software and hardware designs of the robot. Traditionally, identification of the mechanical properties of the human limb is achieved by applying position(force) perturbations and probing the force(position) response [46]. However, realtime application of such technique is very limited due to the imposed violations to the task constraints. To this end, the use of electromyography (EMG) signals was proposed as an alternative candidate to the aforementioned classical techniques, since they carry patterns of activations regulated by central nervous system (CNS). It has been demonstrated that surface electromyography signals are highly correlated with joint stiffness and muscle tensions [47].

Inspired by the superior interaction performance of the human limbs (such as arms, hands and legs) achieved through the regulation of its task impedance, this book addresses the use of teleimpedance control as an alternative method to unilateral position based control or bilateral force reflecting control during teleoperated tasks. The novelty of the proposed teleimpedance control method is that it provides the robot with additional information compared to pure position data traditionally sent to the slave robot during teleoperation. This enriched command profile considers not only the reference position data but also the impedance profile required by the particular task. The impedance profile is estimated in realtime from EMG measurements. This combined command reference (position and impedance) is finally tracked by the teleoperated robotic platform by means of proposed impedance controllers. If necessary, the effect of geometry in realization of the desired endpoint stiffness profile is taken into account in the design of the robot impedance controller.

I believe that incorporation of the human motor control principles into the design of the robot controllers will eventually permit them to reach interaction performances close to those achieved by the humans, demonstrating a versatile and stable behavior even when interacting with environments with dynamic uncertainties. This will also lead to the generation of natural movements, similar to the ones observed in humans, due to the task-oriented redundancy resolution of the robot. Meanwhile, proposed teleimpedance algorithm, as a special case of human-in-the-loop control of robots in uncertain environments establishes a good basis for building autonomous controllers for robots.

1.2 Contributions

This book contributes to the areas of human impedance measurement and modeling, physical human-robot interaction, impedance control, redundancy resolution and teleoperation. Specifically, it introduces novel thinking and techniques to the modeling and identification of the human arm, dual-arm, leg and hand impedance profiles and establishes novel control techniques to track resulting references and realize a desired compliant behavior in a robotic arm, a dual-arm setup, a robotic hand and a compliant exoskeleton, respectively. The primary objectives and novel contributions of this book are listed below:

Contributions of Part I

- Modeling and identification of the human arm endpoint stiffness using electromyography measurements, in realtime.
- Replication of the human stiffness and position profiles in a teleoperated robot by means of a Cartesian impedance controller in highly dynamic tasks and the ones executed in an uncertain environment.
- Development of a common mode and configuration dependent stiffness controller, inspired by the human motor control principles, to realized a desired Cartesian stiffness profile in a robotic arm.

Contributions of Part II

- Natural redundancy resolution in dual arm robotic manipulation using configuration dependent stiffness controller. The development of the controller is inspired by the human motor control principles in dual arm coordination.

Contributions of Part III

- Modeling and identification of the human hand postural and stiffness synergy references using electromyography measurements.
- Development of an active impedance controller for the Soft Hand, a synergy driven anthropomorphic robotic hand. The proposed impedance controller tracks the desired postural and stiffness synergy references in realtime.

- Development of an interaction torque observer and a mechanotactile haptic interface to provide the user with the information about the grasping forces, regulated by the human postural and stiffness synergy commands.
- Development of a vibrotactile haptic interface to provide the user with the information about the texture and object slippage.

Contributions of Part IV

- Modeling and identification of the human knee joint stiffness profile using electromyography measurements, in realtime.
- Development of a novel teleimpedance based assistive control scheme for a compliant knee exoskeleton.
- Development of a novel teleimpedance based standing stabilizer for a compliant knee exoskeleton.

Following subsection provides some more detail on the novel contributions and objectives of this book.

1.3 Outline

An overview on the contribution of impedance and geometry to the mechanical stability of the humans and robots is presented in Chap. 2. The rest of this book is composed of four main parts: Teleimpedance Control of a Robotic Arm, Human-like Impedance Control of a Dual-Arm Manipulator, Teleimpedance Control of a Robotic Hand, and Teleimpedance Control of a Compliant Knee Exoskeleton. Within each part, chapters present novel contributions to the estimation of the human impedance profile in realtime, while the realization of the impedance and position trajectories are performed by the proposed impedance controllers.

1.3.1 *Outline of Part I*

First part of the book elaborates on the realtime estimation of the human arm endpoint impedance profile in 3D and replicating it in a torque controlled robotic arm. As a basis for the evaluation, a classical Cartesian impedance controller is adopted and implemented. Consequently, results of the development of the proposed controllers are compared.

Chapter 3 presents the concept of teleimpedance as a method for remotely controlling a robotic arm in interaction with uncertain environments. As an alternative to bilateral force-reflecting teleoperation control, in teleimpedance a compound reference command is sent to the slave robot including both the desired motion trajectory and impedance profile, which are then realized by the remote controller without explicit feedback to the operator. We derive the reference command from a novel

Body-Machine Interface (BMI) applied to the master operator's arm, using only non-intrusive position and electromyography (EMG) measurements, and excluding any feedback from the remote site except for looking at the task. The proposed BMI exploits a novel algorithm to decouple the estimates of force and stiffness of the human arm while performing the task. Part of this material has been published as author's original work in [1, 2].

Chapter 4 evaluates the efficiency of the teleimpedance algorithm using Cartesian impedance controller in two experimental tasks, illustrating different and complementary aspects of the method. The first concerns a classic peg-in-hole task, and is used to illustrate the stability, transparency, and safety characteristics of the method. The second experiment, a ball-reception task, is chosen to assess how effective is the incorporation of human impedance regulation skills in performing tasks with significant dynamics. In both experiments, the slave robot performs the task by tracking both the reference position profile (which corresponds to the endpoint position of the arm of the human operator as measured from an optical position tracking system) and the end-point stiffness profile (estimated from the muscular activities of the operator's arm) in real-time, via a Cartesian impedance controller. Eventually, the performance of the proposed algorithm is compared to the behavior of the robot arm with different constant stiffness settings. The text of this chapter is adapted from the author's publications [1–3].

Chapter 5 proposes a novel teleimpedance algorithm that replicates the human's arm endpoint stiffness in robot by controlling the common-mode stiffness (CMS) and configuration-dependent stiffness (CDS). The CDS controller utilizes the redundancy to realize a desired Cartesian stiffness profile. Design of the controller and its stability is addressed and experimentally evaluated in robotic peg-in-hole task. Results of the proposed method are compared to the ones derived from teleimpedance implemented using classical Cartesian stiffness control. The interaction performance achieved highlights the possibility of adopting common mode stiffness in robots with adequate degrees of redundancy, in order to realize the desired task space impedance. The text of this chapter is adapted from the author's publications [4, 5].

1.3.2 *Outline of Part II*

Second part of the book proposes a human-like impedance controller for a dual-arm robotic setup which consists of two torque controlled robots.

Chapter 6 proposes a novel realtime motion control strategy to regulate the desired Cartesian stiffness profile during the execution of bimanual tasks. The novelty of the proposed control scheme relies on the use of common mode stiffness (CMS) and configuration dependent stiffness (CDS) to regulate the size and directionality of the task space stiffness ellipsoid. Due to the CDS control, the proposed scheme is not only proved to be effective in regulating the desired stiffness ellipsoid but also permits to resolve the manipulator redundancy in a manner that results in motions exhibiting similarities with those performed by human during the execution of bimanual

tasks. The effectiveness of the controller is evaluated in an experimental setup in which two cooperating robotic arms are executing an assembly task. Experimental results demonstrate that the proposed dual-arm CDS-CMS controller is effective in tracking the desired stiffness ellipsoids as well as in producing human-like natural motions for the two robotic arms. The text of this chapter is adapted from the author's publication [6].

1.3.3 Outline of Part III

Third part of this book elaborates on the estimation and replication of the human hand impedance and position references along the first synergy of the hand movements. Here, Pisa/IIT SoftHand, a synergy driven anthropomorphic robotic hand, is adopted as a robotic platform.

Chapter 7 present the Pisa/IIT SoftHand with myoelectric control as a synergy-driven approach for a prosthetic hand. Commercially available myoelectric hands are more expensive, heavier, and less robust than their body-powered counterparts; however, they can offer greater freedom of motion and a more aesthetically pleasing appearance. The Pisa/IIT SoftHand is built on the motor control principle of synergies through which the immense complexity of the hand is simplified into distinct motor patterns. As the SoftHand grasps, it follows a synergistic path with built-in flexibility to allow grasping of a wide variety of objects with a single motor. Here we test, as a proof-of-concept, 4 myoelectric controllers: a standard controller in which the EMG signal is used only as a position reference, an impedance controller that determines both position and stiffness references from the EMG input, a standard controller with vibrotactile force feedback, and finally a combined vibrotactile-impedance (VI) controller. Four healthy subjects tested the control algorithms by grasping various objects. All controllers were sufficient for basic grasping, however the impedance and vibrotactile controllers reduced the physical and cognitive load on the user, while the combined VI mode was the easiest to use of the four. Results suggest a low-cost, robust hand employing hardware-based synergies is a viable alternative to traditional myoelectric prostheses. The text of this chapter is adapted from the author's publication [7].

Chapter 8 proposes a new teleimpedance controller with tactile feedback for more intuitive control of the Pisa/IIT SoftHand. The DC motor of the hand incorporates a novel teleimpedance control in which the user's postural and stiffness synergy references are tracked in real-time. In addition, for intuitive control of the hand, two tactile interfaces are developed. The first interface (mechanotactile) exploits a disturbance observer which estimates the interaction forces in contact with the grasped object. Estimated interaction forces are then converted and applied to the upper arm of the user via a custom made pressure cuff. The second interface employs vibrotactile feedback based on surface irregularities and acceleration signals and is used to provide the user with information about the surface properties of the object as well as detection of object slippage while grasping. Grasp robustness and

intuitiveness of hand control were evaluated in two sets of experiments. Results suggest that incorporating the aforementioned haptic feedback strategies, together with user-driven compliance of the hand, facilitate execution of safe and stable grasps. The text of this chapter is adapted from the author's publications [8, 9]. SoftHand teleimpedance results were also extensively addressed in the media [27–30].

1.3.4 Outline of Part IV

In the last part, a compliant knee exoskeleton tracks the human's knee joint equilibrium and stiffness profiles in realtime. Here, we elaborate on assistive aspects of the teleimpedance control in lower limb.

Chapter 9 presents a teleimpedance based assistive control scheme for a compliant knee exoskeleton. Proposed controller captures the user intent to generate task-related assistive torques by means of the exoskeleton. To do so, a detailed musculoskeletal model of the human knee is developed and experimentally calibrated to better match the user's kinematic and dynamic behavior. Three dominant antagonistic muscle pairs are used in our model, in which electromyography (EMG) signals are acquired, processed and used for the estimation of the knee joint torque, trajectory and the stiffness trend, in real time. Estimated stiffness trend is then scaled and mapped to a task-related stiffness interval to agree with the desired degree of assistance. The desired stiffness and equilibrium trajectories are then tracked by the exoskeleton's impedance controller. As a consequence, while the minimum muscular activity corresponds to low stiffness, i.e. highly transparent motion, higher cocontractions result in stiffer joint and stronger level of assistance. The novelty of the method therefore is the incorporation of the user intention into the control of the level of assistance provided by the compliant knee exoskeleton.

To evaluate the robustness of the proposed technique, a study of the dynamics of the human-exoskeleton system is conducted. In addition, experimental results of a standing-up task are demonstrated to further investigate the capabilities of the controller. Results indicate that the compliant knee exoskeleton incorporating proposed teleimpedance controller can effectively generate assistive actions that are volitionally and intuitively controlled by the user's muscle activity. The text of this chapter is adapted from the author's publication [10, 11].

Chapter 10 presents a generic technique to estimate active joint stiffness based on an EMG-driven musculoskeletal model whose parameters are adjusted using experimental data obtained from applied stochastic perturbations. To that end, a human balancing experiment was carried out to investigate correlations between the anteroposterior excursions of the center of pressure (CoP) with kinematic, kinetic, electromyographic measurements as well as the model stiffness of the knee joint. Motivated by the results of the cross-correlation analysis a human-inspired balancing

assistance control for lower limb exoskeletons is presented that permits volitional stiffness regulation. Preliminary experimental evaluation is conducted using an assistive knee exoskeleton. The results indicate that the proposed control technique can be generalized to command a whole lower limb exoskeleton in order to provide effective balancing assistance to the user. The text of this chapter is adapted from the author's publication [12].

Chapter 2

On the Role of Compliance and Geometry in Mechanical Stability of the Humans and Robots

2.1 Stability in Human-Environment Interactions

Humans demonstrate versatile and stable interactions with the uncertain environment. This is achieved through the modulation of the mechanical properties of the limb, and as a consequence, task-related restoring forces are applied in response to the environmental displacements [48–51].

Understanding the mechanisms behind the regulation of mechanical properties of the limbs in contact can provide insight into the motor control principles incorporated by the central nervous system (CNS). Such strategies thus can be potentially beneficial for the mechanical or software design of the robots, collaborating and interacting with humans.

One way to quantify the stability of the contact between the limb and the environment in postural tasks or during the movement is through the estimation of the endpoint stiffness [52]. Early studies conducted by Mussa-Ivaldi et al. [53] estimated the human arm endpoint stiffness profile by means of imposed displacements and resulting steady state force responses. Other studies analyzing the overall human arm impedance (inertia, damping and stiffness) have also been carried out [49, 54–56]. Perturbation based impedance estimation techniques are currently the most accurate and reliable, due to direct measurements of the applied force–displacement profiles. However, their application can be problematic when real-time estimation of the human arm impedance is required during the execution of the task. To that end, other studies propose more realtime techniques for the estimation of the human joint torque, or stiffness profiles [48, 57], relying on the strong correlation between task-oriented modifications of the joint torque and patterns of activations in the involved muscles [48, 58, 59]. For instance in [48], a relationship between the human arm joint stiffness and muscle activation during static force control in the horizontal plane by means of surface electromyographic (EMG) signals is established. In this study, the stiffness components of shoulder, elbow, and their cross-term and the EMG of six related muscles were measured during the tasks. Assuming that the EMG reflects the corresponding muscle stiffness, the joint stiffness was predicted from the EMG by

using a two-link six-muscle arm model and a constrained least-square error regression method. In another study [57] a mathematical muscle model based on anatomical and physiological data to estimate joint torque solely from EMG is developed. This model expresses muscle tension using a quadratic function of the muscle activation and parameters representing muscle properties. Using this model, authors were able to reconstruct joint torque from EMG signals with or without co-contraction, while the joint stiffness was directly obtained by differentiation of this model analytically.

In [60], the knee joint stiffness in isometric conditions is modeled and estimated using EMG combined with kinetic and kinematic measurements. This approach is claimed to be capable of including conditions with antagonistic muscle activation, a phenomenon commonly observed in physiological gait. Authors conclude that knee stiffness can be accurately estimated in isometric conditions using EMGs. This enables quantification of the knee stiffness during gait or similar movements of the lower body, without the need for applying perturbations.

Regardless of the technique used for the identification of the endpoint stiffness, it has been observed that its profile can be regulated in different ways. For instance, muscle activation can modify the stiffness via cocontraction of muscles involved in task execution [43], or through modifications in the sensitivity of reflex feedback [61, 62]. Former studies suggest that changes in muscle activation can appropriately change the joint stiffness (and the endpoint stiffness as a consequence), which results in increased stability and endpoint accuracy during postural tasks or movements [63–65]. Other studies report on the stiffness profile variations during more dynamic tasks. For instance in [65], it has been observed that cocontraction of the muscles increases with movement velocity and with magnitude of disturbance forces. In addition, it is proposed that higher levels of cocontraction, i.e. higher values of the endpoint stiffness profiles might be a strategy which is used by CNS early in learning a novel motor task to achieve a desired accuracy before fully learning of the dynamic models of the task.

The role of cocontraction in reduction of the kinematic variability is explored in [58]. In this study, impedance modulation is suggested as a means to suppress the effects of internal noise on movement kinematics. Simulation studies suggest that increasing the impedance through coactivation results in less kinematic variability, except for the lowest levels of co-activation, thus supporting the idea that muscular co-activation is in principle an effective strategy to meet accuracy demands.

Another way of changing the endpoint stiffness is through the change in the geometry of the limb. Due to this geometric dependence, endpoint stiffness is not uniform, but varies with the direction in which the endpoint is displaced [44]. For this reason, as an example, the arm can be less stable in certain directions than others. The postural stability can be quantitatively represented in the form of an ellipse, constructed from the eigenvalues of the endpoint stiffness matrix. The orientation of the ellipse (direction of maximum stiffness) is determined by the direction of the eigenvector associated with the maximum eigenvalue of the endpoint stiffness matrix [53]. The direction of minimum stiffness, i.e., the direction of least stability, is orthogonal to this direction. Figure 2.1 demonstrates the change in directionality

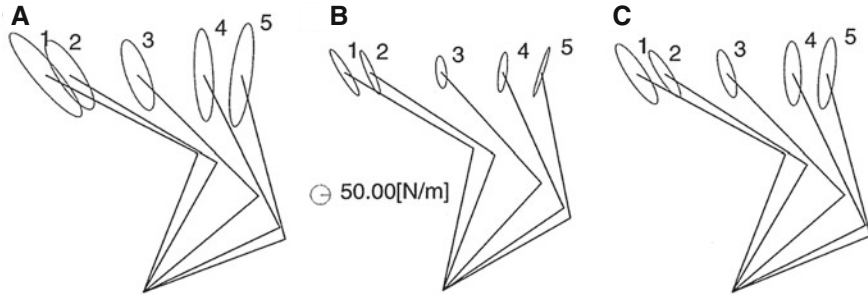


Fig. 2.1 Stiffness ellipses during posture maintenance of subjects A, B, and C

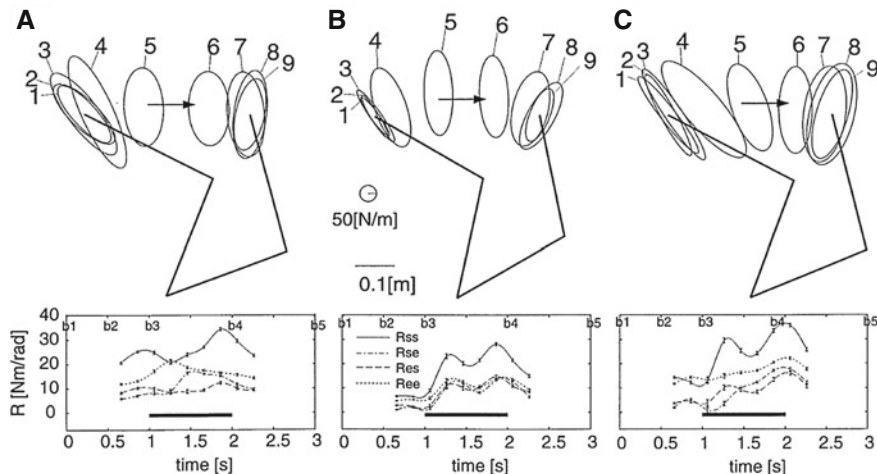


Fig. 2.2 Stiffness ellipses (upper figures) and joint stiffness values (lower figures) of shoulder (R_{ss} , continuous curve), elbow (R_{ee} , dotted curve), and double-joints (R_{se} , dashed-dotted curve; Res , dashed curve) during transverse multi-joint movements for subjects A, B, and C

of the endpoint stiffness ellipsoids in static postures, where such variation during dynamic movements are depicted in Fig. 2.2. Results are inserted from [63].

If no net endpoint force is exerted by the limb, the endpoint stiffness matrix, K_c , can be related to the joint stiffness matrix, K_J , by the following equation¹

$$K_e = J^{-T} K_J J^{-1}$$

where J symbolizes the Jacobian. Above equation highlights the effect of limb geometry in realization of the endpoint stiffness matrix.

The contribution of co-activation of involved muscles in the modulation of the stiffness ellipsoid size is shown to be more effective than adjustments in its direction-

¹More detailed discussions and formulations will be provided in later chapters.

ality [44, 45]. Furthermore, previous studies discuss on limited ability of humans in changing the orientation of the postural stiffness ellipsoid, even subsequent to learning stages [66]. Instead, limb postures are adaptively regulated by the CNS to realize the desired direction of the endpoint stiffness ellipsoid. Cost efficiency of the postural adjustments compared to cocontractions and the existence of cross-joint muscles in the limbs are deemed to be the two main factors illustrating such behavior.

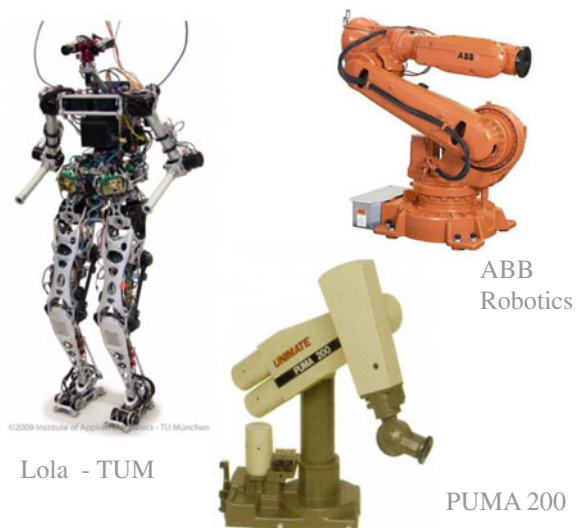
2.2 Compliant Behavior in Robots

2.2.1 Compliant Mechanisms

Replication of human-like impedance regulation mechanisms in robots can permit them to safely and efficiently operate in unstructured environments under unpredicted interaction scenarios. Previously, realization of the desired compliant behavior was extremely limited in position controlled robots (see examples in Fig. 2.3) due to the rigidity of the joints or the missing ability to command the joint torques directly. Rigidity of such robots potentially presents mechanical menaces to humans with whom robots are supposed to interact.

Over the last decades, the implementation of impedance regulation in robots is achieved by introduction of variable stiffness or torque controlled robots which can regulate actively their stiffness or full impedance properties by active/pассив control techniques [67, 68]. Most of the solutions proposed have a common objective which is the reduction of the impact forces during accidental collisions between the robot and its environment or humans [69].

Fig. 2.3 Examples of position controlled robots



In addition to the safety, the existence of elastic elements act as storage for energy which can be fed by the kinetic energy or the gravitational potential energy of the system. This energy then can be transferred back to the system within the next cycle.

As in these types of actuators two parameters, position and stiffness have to be independently controlled; two actuators per joint are needed. One approach for implementing these joint is the use of a bio-inspired antagonistic configuration of two actuators of equal size combined with elastic elements exhibiting a nonlinear force to deflection behavior. The biological inspired joint stiffness control is a rotational joint, actuated by two series elastic actuators with nonlinear springs [70].

More recently, developments of actuation systems which inherently integrate physical principles such as variable stiffness and damping [71–74] permitted the intrinsic regulation of the robot impedance (Fig. 2.4).



Fig. 2.4 Recent developments in robotic systems to achieve a compliant behavior

2.2.2 Compliance Control

With the advent of higher demands on robotic manipulation, interaction with the uncertain environment using compliance control [75] became the focus of many studies in robotic systems. The contrast between this approach and the traditional position or force control methods is rooted in the context of the desired disturbance response. To establish such behavior, several techniques have been proposed [76].

Impedance control is a well known technique that establishes such desired compliant behavior by modulating the mechanical properties of the robot, while interacting with the uncertain environment. This is done by establishing a mapping from the generalized velocities to forces and is described at the tip of the end effector, i.e. Cartesian coordinates [76, 77]. Consequently, the joint motor torques of the manipulator can be calculated and tracked (see Sect. 4.1 for details).

Admittance control is another approach to achieve aforementioned desired compliant behavior. This method is implemented by controlling the manipulator in position, while the outer loop controller is in charge of rendering the compliant behavior. This is performed by measuring the generalized interaction forces at the tip of the end effector and generating the reference Cartesian trajectories. Since the algorithm incorporates position control, it has been extensively used for the compliance control of the industrial manipulators [75], as well as exoskeletons or assistive devices [78]. The main drawback of this approach is the limited ability in realizing free movements or low-impedance profiles.

In addition to above methods, there exists another approach which establishes the mapping between the Cartesian impedance profile and joint impedance values. Here, joint impedance values are being tracked by joint-level impedance controllers to realize a desired Cartesian impedance profile. Such mapping is commonly called Conservative Congruence Transformation [79].

To realize a full Cartesian stiffness matrix $K_c \in \mathbb{R}^{6 \times 6}$, the controller must track 21 independent elements of the symmetric stiffness matrix, which includes the translational, rotational, and the coupling stiffness terms. This can be achieved through control of the joint torques, impedance values and configurations [80]. Various studies address the problem of tracking the desired stiffness profile by extending aforementioned general compliance control techniques. For instance, in [81] an overview of above approaches is presented and a new controller structure is proposed, which consists of an impedance controller enhanced by local stiffness control. This structure consistently takes into account the two time scale property of the joint and Cartesian control loops. Proposed approach is experimentally evaluated in on a light weight robot. In [82], the problem of impedance control for flexible joint robots is addressed and experimentally evaluated. Combination of active impedance controller with the passive joints to further increase the stiffness range has been addressed in [83]. In this study, an algorithm to optimize the passive and active Cartesian stiffness is proposed and tested on the VSA robot DLR Hand Arm System. In [84], an admittance control scheme for a dual robot upper-limb stroke rehabilitation system is proposed.

A model of the human arm is outlined and used to formulate an admittance controller operating in human upper-limb joint space.

Even though such well-established techniques have successfully demonstrated their effectiveness through reliable handling of the contact, few studies focus on the problem of planning the variable impedance [85–88]. For instance, a comparative study of approaches for controlling robots with variable impedance actuators, in ways that imitate the behaviour of humans is presented in [86]. While, in [88], a complimentary approach is proposed which utilizes the human sensorimotor learning ability to control the robot through a multi-modal interface.

2.3 Redundancy Resolution and Its Application to Impedance Control

Redundant robots possess more degrees of freedom than are required for the basic position control of the end effector. Presence of such redundant joints can provide high versatility and dexterity to execute a certain task.

The problem of redundancy resolution was first introduced in [89], where the Jacobian pseudoinverse was utilized to solve for the motion of the redundant joints. Soon after, this problem was extensively addressed in robotics [90–94], due to the higher demands on robotic manipulation. For instance in [95], minimization of instantaneous joint torques is taken into account to resolve for the motion of the manipulator in redundant manifold. In [77], an inertia-weighted Jacobian pseudoinverse is introduced and shown to result in joint torque reduction. Incorporation of additional subtasks such as optimal joint movements [96], collision avoidance [97] or manipulator joint/torque limit avoidance [98] have also been proposed.

More general techniques incorporate an objective function, $C(q)$, of the joint angles q , and project its gradient into the manipulator Jacobian nullspace, N_J , as follows

$$\dot{q} = J^+ \dot{x} + N_J \frac{\partial C(q)}{\partial q},$$

with x denoting the end effector position/orientation vector. $[.]^+$ is the pseudoinverse operator. It has been demonstrated that by using the above technique, while the desired end effector motion will be guaranteed, manipulator motions in redundant space will be regulated to stabilize a subtask variable. Such objective function can be chosen arbitrary; examples of that are gravity torque (or in general, minimum effort), manipulability, force manipulability, mechanical advantage, velocity ratio and end effector sensitivity [90].

More recent studies (e.g. see [91]), extended the above formulation for stabilization of the subtask variables in a prioritized order of occurrence. In this strategy, the desired end effector motions are usually the first priority, and others are executed in prioritized order using dynamic and kinematic redundant degrees of freedom.

Generally, redundancy resolution is performed using local or global optimum control techniques. Although the local approach is computationally inexpensive and instantaneously determines the present utilization of redundancy based on current sensory information, it lacks a guarantee of global optimality. On the other hand, the global approach is computationally costly. Thus, local approaches are the most appropriate for real time applications, where global techniques can be efficiently used for offline trajectory planning, etc.

To the author's knowledge, the problem of redundancy resolution for rendering a desired interaction performance has not been fully addressed; only few have highlighted the efficiency of the impedance control through redundancy resolution [99, 100]. For example in [99], an off line optimization technique has been utilized to realize a desired Cartesian stiffness profile in passively compliant, uncoupled joints. In [100], the issue of low stiffness in machining tasks is addressed with an integrated offline planner and real time replanner. The available manipulator stiffness is maximized during offline planning through a trajectory resolution method that exploits the nullspace of the robot machining system. In response to unmodeled disturbances, a real time trajectory replanner utilizes a time scaling method to reduce the tool speed, thereby reducing the demand on the actuator torques, increasing the robot's dynamic stiffness capabilities. During real time replanning, priorities are assigned to conflicting performance criteria such as stiffness, collision avoidance, and joint limits.

In this book, relying on the major contribution of the arm configuration to effective regulations of the endpoint stiffness ellipsoid direction, and its low-cost nature [44, 45, 66, 99, 100], we explore the role of *configuration dependent stiffness* (CDS) control, for single (Chap. 5) and dual-arm (Chap. 6) object manipulation. We propose a real time optimization technique for control of the joint variables in redundant space to realize a task-specific Cartesian stiffness matrix.

Part I

Teleimpedance Control of a Robotic Arm

Chapter 3

Teleimpedance: Teleoperation with Impedance Regulation Using a Body-Machine Interface

Master-Slave teleoperation systems for unstructured and hostile environments have been studied and applied for a long time, starting even before the emergence of robotics systems [101]. Earlier prototypes using position measurements from the human operator arm to be replicated by a rigid manipulator soon showed their limitations in dealing with interaction tasks in uncertain environments, due to high forces developing at contacts. The second generation of teleoperation systems therefore included means of feeding back to the operator information on the interaction forces between the slave robot and the remote environment. Although such bilateral teleoperation systems can outperform pure position-controlled ones, they require an active force display on the master side (e.g., an actuated exoskeleton), which imposes extra costs and discomfort for the operator. Furthermore, latencies in the communication channel between the master and slave robot may generate insufficient transparency or even stability issues in the bilateral teleoperation system (see e.g. [38, 102, 103]).

Despite the results and continuous improvements in the mechatronics and control of bilateral teleoperation systems [102, 104–106], there are still many tasks in which stability and reduced transparency, if not mere cost of sensing and actuating reflected forces, prevents application of bidirectional teleoperation. Tasks which are normally performed by humans without difficulty such as drilling, reaming, chipping and many others with large uncertainty in the environment constraints, cannot yet be easily conducted.

Part of these problems are certainly related to the slave side, where rigid manipulator arms are used to replace the sophisticated, adaptively compliant structure of the human arm. This aspect of problem has attracted much attention, and is at least partly solved, either by modern impedance control schemes on advanced arm hardware [82, 107], or by passively adaptive joints [72, 108, 109]. A second, perhaps harder, road-block is that we do not really know as yet just how to *choose* and program variable impedance in a flexible and effective enough way.

Indeed, humans have superior motor capabilities and skills which permit them to effectively modulate their motion/impedance in a smooth and efficient manner according to the task needs. The role of impedance regulation in increasing stability, accuracy and task readiness has been illustrated in many papers

[48, 49, 55, 59, 64, 65]. Such skills are deemed to be directed by learned goal-oriented internal models of the external world [110].

Behavioral studies of human motor skills give evidence of the existence of two independent mechanisms in Central Nervous System (CNS) [58, 59]. The former appears to be carried out by selective changes in patterns of activations in individual muscles to generate task-oriented force generation, while the latter is conducted by co-contraction of muscle groups, with no endpoint force changes. In addition to independency of these two subsystems, it has been observed that force and impedance variations observed while maintaining posture in response to mechanical disturbances show a linear relation with muscular activation levels [58].

Toward the twofold purpose of resolving some of the limitations of existing bilateral teleoperation systems, and of better understanding and exploiting the human skills in impedance regulation in interaction tasks, in this chapter we propose and investigate the concept of “teleimpedance”. In our approach, a compound reference command is obtained from the operator’s arm using a suitable Human–Machine Interface (HMI), which we use as a means of appointing the pathway between learned internal models and the external device to be controlled. Thus, results in this chapter may complement well work not only in classical teleoperation applications, but also in modern cooperative manipulation tasks involving e.g. a human and a humanoid [111, 112].

HMIs for teleoperation of robot arms have been the subject of much attention in recent years. Electroencephalography signals (EEG), which reflect correlated synaptic activities caused by post-synaptic potentials of cortical neurons, are most often used in Brain–Machine Interfaces as command sources for assisting, augmenting, or repairing human cognitive or sensory-motor functions [113, 114]. However, high level computational costs and complexity of present processing algorithms in EEG decoding have limited their application to few, very specific areas in the robotics field (e.g. [114]).

As an alternative for low-dimensional control spaces, Body–Machine Interfaces have been proposed [115], which allow for incorporation of relatively low-level and easier-to-handle biological signals in robotic applications. As far as the kinematic and dynamic requirements of tasks performed by the human arm are concerned, electromyography (EMG) signals, which are formed by superimposed patterns of activations of involved motor units, have been the choice input in many rehabilitative and human–robot functionality coordination [116–119]. Easy accessibility, fast adaptivity and stability of EMG signals are other advantages which motivated our choice of adopting EMGs in the real-time control of our teleimpedance system.

EMG can be used for different purposes. Using very simple filtering and averaging techniques, EMG can be effectively used to infer muscle activation levels rather accurately. Applying sophisticated processing techniques to whole segments of EMG recordings, time-frequency features can be accurately extracted (see e.g. [118]). More recently, the tendency of segmental processing to produce lag and jitter, which can be detrimental in real-time teleoperation, has been overcome by means of lag-free EMG processing techniques (see e.g. [120]).

EMGs can also be used to provide information on an arm or hand posture, which has been used e.g. for classification of hand gestures [116, 118] or arm movements [120]. Because EMGs directly relate to muscle forces and not positions, their use to infer arm positions has to be indirect. One way of extracting arm positions from muscle forces is to infer joint torques τ from EMGs, and integrate the forward dynamics of motion of the arm, using an estimated kinematic and dynamic model of the arm, e.g. in the general Lagrangian form $B(q)\ddot{q} + C(q, \dot{q})\dot{q} + G(q) + J^T F_{ext} = \tau$. A second possibility is to disregard dynamics. Under the hypothesis that the arm is only subject to the gravity torque term $G(q)$, the configuration q can be extracted inverting the map $G(q) = \tau$. This can be done (wherever $\frac{\partial G}{\partial q}$ is not singular) through a careful identification of the weight distribution, possibly learned through experiments [120]. However, neither method could be used in our applications, because a change in the weight distribution (as e.g. when the operator arm has to support an object's weight, as in a ball reception experiment discussed later), or external forces F_{ext} acting on the master's hand would completely alter the force-based position estimates.

Therefore, in the proposed teleimpedance control method we provide the robot with two separate references, i.e. a desired 3D endpoint position and a desired 3D endpoint stiffness, obtained in different ways. Corresponding to the high priority given in teleoperation systems to position referencing, our BMI uses accurate measurement of arm position references through an unobtrusive optical tracking system. On the other hand, we process EMGs so as to separate the effects of endpoint force generation and stiffness variation, and use the latter as a reference for the robot impedance controller. The proposed control algorithm consists in controlling the slave robot using the accurate estimate of the master's position as the positional reference for the robot end-effector, around which an impedance controller is superimposed, for which references along different directions are provided by the processed EMG signals. The overall block diagram of teleimpedance control scheme is shown in Fig. 3.1.

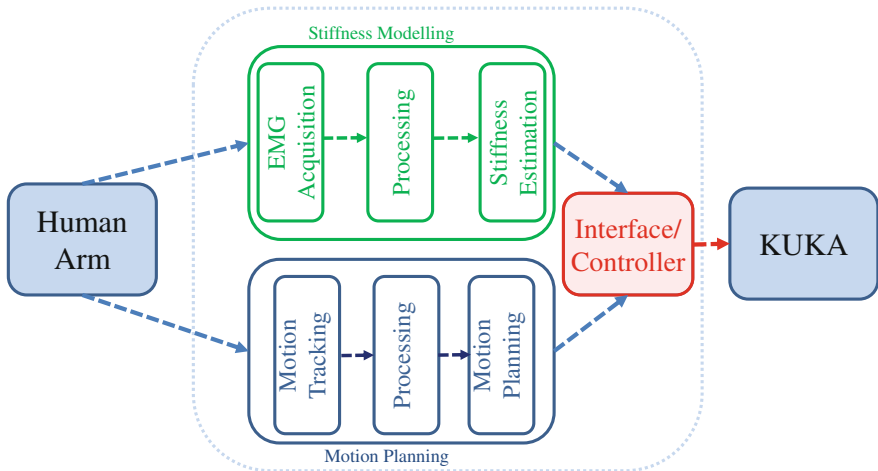


Fig. 3.1 The overall block diagram of teleimpedance

3.1 Human Arm Impedance Modeling in 3D

Contact reliability during tasks performed by humans in environments with stochastic uncertainties or while being exposed to mechanical disturbances can be ensured by a stable mechanical interface between human arm endpoint and the environment [48, 50, 51]. Quantification of this stability could be done by measurements of visco-elastic profile of human arm endpoint. Early studies conducted by Mussa–Ivaldi et al. [53] demonstrated spring like properties of human muscles. At around the same time, human arm endpoint stiffness profile was estimated by means of imposed displacements and resulting steady state force responses. Other studies analyzing the overall human arm impedance have also been carried out [49, 54–56].

Perturbation based impedance estimation techniques are currently the most accurate and reliable, due to direct measurements of the applied force–displacement profiles. However, their application can be problematic when real-time estimation of the human arm impedance is required during the execution of the task. As a consequence, this part of the work is devoted to application of continuous and adaptive biosignals (e.g. EMGs) which correlate with human impedance modifications [48]. This work proposes a new method for the estimation of human arm endpoint stiffness, based on extraction of stiffness-related EMG features in real-time.

Task-oriented modifications of the endpoint arm stiffness along with endpoint force variations in humans are shown to have strong correlation with the patterns of activations in the involved muscles [48, 58, 59]. Agonist–antagonist muscle co-contractions affect and modify selectively the overall stiffness and viscous profiles of the arm endpoint. Resulting modifications in force and impedance can be regarded as the effects of internal force regulation exerted by group of extensor and flexor muscles. It should also be noted that, when muscles act on multiple limb segments or about multiple axes of rotation (as is the case at the shoulder joint), the separation of muscles into agonist and antagonist can be oversimplifying, and a more general concept of muscle groupings or synergies should be considered [121].

Based on this and the observed approximate linear dependency of force/stiffness to muscular activation/coactivations [58, 59], the overall mapping between muscular activities and resulting arm endpoint force and stiffness in Cartesian coordination and around equilibrium position (close to isometric condition) can be compactly described by

$$\begin{bmatrix} F \\ \sigma \end{bmatrix} = \begin{bmatrix} T_F \\ T_\sigma \end{bmatrix} P + \begin{bmatrix} 0 \\ \sigma_0 \end{bmatrix}, \quad (3.1)$$

where $F, \sigma \in \mathbb{R}^3$ are the endpoint force and stiffness vectors, respectively, σ_0 is the intrinsic stiffness in relaxed conditions, and $P \in \mathbb{R}^n$ is the vector of muscular activities of the n considered muscles, as obtained from preprocessing EMG signals from electrodes applied on each muscle (details on the preprocessing are given in Sect. 3.2).

Ideally, a model for the estimation of endpoint force and stiffness values (in the vicinity of a specific arm configuration) from measured muscular activities could

be obtained by identification of the elements of T_F and T_σ . To obtain an accurate experimental identification, two ingredients are necessary. Firstly, precise measurements of 3D endpoint force F and stiffness σ are needed. Secondly, a rich and varied enough set of data samples should be generated by the subject. As a result of both these issues, while identification of the EMG-to-force map T_F is relatively easily done, to accurately identify the EMG-to-stiffness map T_σ is more difficult.

Because of such limitations in the estimation of T_σ , R. Osu and H. Gomi [48] proposed an algorithm for estimating the human arm stiffness which relies on identifying the map between muscular activities (as coded by EMGs) and joint torques (in formulas, $\tau = T_\tau P$, where T_τ is the EMG-to-joint torque map). In this work, authors estimate T_τ by combining shoulder and elbow torques in the horizontal plane with measured activities of six involved muscles. The identification of $T_\tau \in \mathbb{R}^{2 \times 6}$ is based on an assumed structure of the type

$$T_\tau = \begin{bmatrix} c_1 & -c_2 & 0 & 0 & c_5 & -c_6 \\ 0 & 0 & c_3 & -c_4 & c_7 & -c_8 \end{bmatrix}, \quad c_i > 0, \quad i = 1, \dots, 8 \quad (3.2)$$

which corresponds to the anatomical arrangement of the six considered muscles. Here, c_i are constant gains which correspond to the mapping from muscular activities to the joint torques, identified by experiments. Authors then propose an index of co-contraction around the joint (IMCJ, denoted here as L) that is evaluated as

$$L = |T_\tau| P,$$

where the absolute value of matrix T_τ is meant elementwise. Each element of $L \in \mathbb{R}^2$ is considered to be linearly related to the corresponding joint stiffness, i.e.

$$\sigma_i = m_i L_i + \sigma_{0,i}, \quad i = 1, 2$$

where the constants $m_i, \sigma_{0,i}$ are experimentally identified on the basis of stiffness measurements [48, 61].

It should be noted that the method relies upon the availability of an accurate estimate of joint torques, which can not be measured directly, and have to be computed from measured endpoint forces through the arm Jacobian as $\tau = J^T F$. Results based on the above method have demonstrated good performance for 2D joint stiffness estimation even during small movements in the vicinity of the posture.

However, application of this method to our problem poses some challenges. In our system, we want to estimate the 3D Cartesian endpoint stiffness using measurements of the activation of $n = 8$ involved muscles acting at the shoulder and elbow. Firstly, as observed in [122], anatomy does not warrant the separation in agonists and antagonists at a ball joint, as “any one of the muscles of the shoulder can be engaged in phase or antiphase with any other muscle” [121]. Furthermore, the use in [48] of an estimate of the arm Jacobian has the disadvantage of introducing errors due to imperfect adherence of the double shoulder and elbow joints to simple lower pair kinematic models [57], and a strong dependency on the subject’s limb proportions.

In conclusion, the assumption of a structure of the type (3.2) for the EMG-to-force map $T_F \in \mathbb{R}^{3 \times 8}$ is not justified in our case. By the same token, no simple relation between the EMG-to-stiffness map $T_S \in \mathbb{R}^{3 \times 8}$ and $|T_F|$ can be expected to hold.

To overcome the limitations of applicability of the method of [48] in our setting, we exploit the observation that in our experimental conditions the generation of forces can be considered to be decoupled from the regulation of stiffness. It is well known that in general end-point impedance has three components, depending on posture, force, and co-contraction, respectively. While the first two components may be large and even dominating [44] in a large enough range of variations, an ample literature reports the existence and independence of co-contraction contribution to stiffness [43, 62, 123]. Because in our experiments we only use small motions about a reference configuration for the arm and small end-point force variations, it can be safely assumed that the control of forces and stiffnesses are decoupled. Accordingly, for the first-order linearized model (3.1), we consider a decomposition of the space of muscular activations $\mathcal{P} \ni P$ as the direct sum of a force-generating subspace \mathcal{P}_F and the force-map null space $\mathcal{P}_k = \ker T_F$, i.e.

$$\mathcal{P} = \mathcal{P}_F \oplus \mathcal{P}_k.$$

By choosing a right-inverse T_F^R of T_F , i.e. any $n \times 3$ matrix¹ such that $T_F T_F^R = I$, we also affix a system of coordinates to these subspaces. In these coordinates, we can decompose the vector of muscular activations P in a force-generating component P_F and a null-space component P_k as

$$P = T_F^R T_F P + \left(I - T_F^R T_F \right) P \stackrel{\text{def}}{=} P_F + P_k.$$

The null-space component P_k contains information on the co-contraction component of stiffness generation. It is convenient to give an alternative description of P_k as follows. Let N_F denote a basis matrix for the kernel of T_F , and let $\lambda = N_F^+ P_k = Q P$ be the coordinates in that basis of P_k , where $Q \stackrel{\text{def}}{=} N_F^+ (I - T_F^R T_F)$. Hence the model of Cartesian stiffness regulation through co-contraction is written as

$$\sigma - \sigma_0 = M_\sigma Q P \quad (3.3)$$

where $M_\sigma \in \mathbb{R}^{3 \times 5}$ is a mapping from the kernel of T_F (the set of muscle activations that do not change endpoint force, in the selected coordinate frame) to stiffness variations. The map M_σ can then be identified and calibrated once, based on direct measurements of human arm end point stiffness, at different coactivation levels as described in the following section. It is worth to explicitly note that the choice of the right-inverse T_F^R and that of the kernel basis N_F are both arbitrary, and imply an

¹The existence of a right inverse is guaranteed by the fact that in nonsingular configurations T_F is full row-rank. Because $n > 3$, there exist infinite right-inverses: a particular choice is for instance $T_F^+ = T_F^T (T_F T_F^T)^{-1}$, i.e. the pseudoinverse of T_F .

arbitrary description of the co-contraction component, for which only the calibration matrix M_σ is relevant. In other terms, there is no “natural” choice of coordinates for \mathcal{P}_k , but, once one is given, this has to be used consistently for system calibration and operations.

Several caveats apply to the method for 3D stiffness estimation above, among which the fact that extrapolation of identified values of the maps to the whole workspace of the arm might not be valid, due to configuration dependency of human endpoint impedance and nonlinear dependency of the muscular activity and muscle tensions during movements. Also, large force variations would bring about stiffness changes of the same order or larger than co-contraction, thus violating the validity of the linearized model. However, as far as the tasks to be performed by the master arm remain in a vicinity of the static posture in which the parameters are estimated, and the human arm is not applying external forces, the approach provides a reasonable approximation of the endpoint stiffness profile in real time.

3.2 Stiffness Model Calibration/Identification

Materials and Methods One healthy subject (male; age 27) participated in the identification-calibration experiments. The subject stood upright with the feet side-by-side in front of a robotic arm. The robot arm was equipped at the endpoint with a handle connected to a 6-axis force and torque (F/T) sensor (ATI Mini-45). An idle spherical joint was used to connect the center of the handle to the F/T sensor, so as to avoid exertion of torques by the subject (see Fig. 3.2). Displacements of the human arm at its endpoint (considered as the wrist center) were tracked by an Optitrack system (Natural Point, Inc.), with nominal resolution is 0.02 mm. Optical markers were also placed at the shoulder and elbow of the subject’s arm. Both force and position measurements were acquired at a sampling frequency of 200 Hz, and filtered by a low-pass Butterworth filter with cutoff frequency 15 Hz to eliminate noise. In all experiments, surface electromyograms (EMGs) were used to trace muscular activities. Eight dominant muscles acting on elbow and shoulder joints (see Table 3.1 and Fig. 3.3) were chosen as the sources of EMG recordings. Analogue EMG signals were measured and amplified with a Delsys–Bagnoli 16 (Delsys Inc.) apparatus. Acquired signals were band-pass filtered in the frequency range (20, 450) Hz. Resulting EMG signals were sampled at 2 kHz (PCI-6220, National Instruments) and fully rectified for further processing. A digital non-causal FIR linear phase low-pass filter was used for the detection of the envelope of the signal, which approximately corresponds to muscle activity. The robotic arm is a 7 degrees-of-freedom KUKA LWR with DLR’s Fast Research (FR) Interface [124]. The data acquisition and synchronization interface between the KUKA controller, the EMG acquisition board, the Optitrack position streaming data, the six axes F/T sensor were developed in C++.

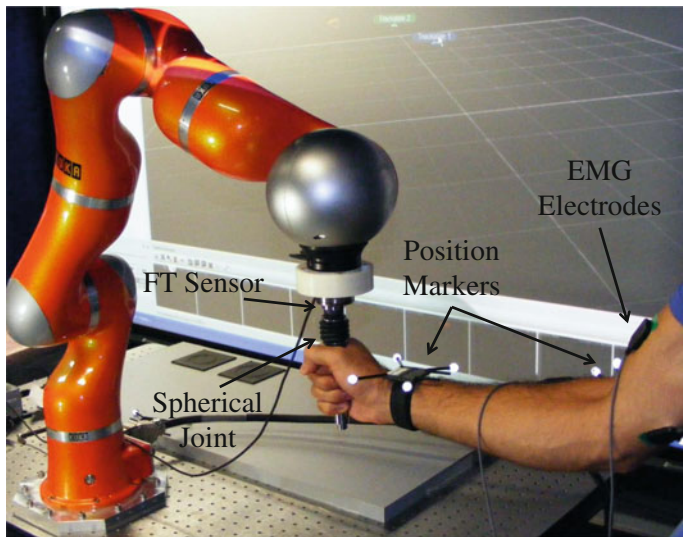
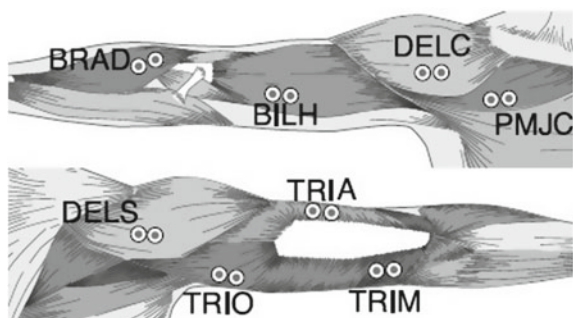


Fig. 3.2 Experimental setup used for the first calibration experiments. Subject applies constant forces in six directions while holding the handle attached to an idle spherical joint

Table 3.1 Muscles used for EMG measurements

| Flexors | | Extensors | |
|---|-------------------------|------------------------------|--------------------------|
| Monoarticular | Biarticular | Monoarticular | Biarticular |
| Deltoid clavicular part (DELC) | Biceps long head (BILH) | Deltoid scapular part (DELS) | Triceps long head (TRIO) |
| Pectoralis major clavicular part (PMJC) | | Triceps lateral head (TRIA) | |
| Brachioradialis (BRAD) | | Triceps medial head (TRIM) | |

Fig. 3.3 Electrode positions in EMG measurements



3.2.1 Identification of the EMG-to-Force Map

In a first set of experiments, aimed at estimating the force-generating map T_F , the robot was only used passively, with motors inactive and brakes turned on, serving only as a support structure for the F/T transducer mounted at endpoint of the arm. The subject was asked to apply constant forces of $\pm 5\text{ N}$, $\pm 10\text{ N}$ and $\pm 20\text{ N}$, respectively, along 6 directions ($\pm x$, $\pm y$ and $\pm z$) while holding the handle (isometric conditions). Force components applied by the subject were measured and shown in real time to the subject himself in the form of a graph with three colored bars on a screen. In each trial, the subject was instructed to apply forces so that bars reached and maintained given targets (corresponding in turns to the three different intensities in the 3 different directions). The subject was also instructed to use minimum muscular activity (minimum effort). Each trial was 60 s long. Data from the first 10 s were discarded to eliminate transient force fluctuations. For each direction and force level, four trials were executed and recorded (for an overall number of $4 \times 3 \times 2 \times 3$ trials) in EMG-to-force map identification experiments. In a subsequent postprocessing phase, all components of (T_F) were evaluated by means of a least-squared-error algorithm, and a basis of its nullspace and the projector matrix Q used in (3.3) were computed.

3.2.2 Identification of the EMG-to-Stiffness Map

In a second set of experiments, aimed at estimating the stiffness-regulating map M_σ , similar equipment and arrangements were used. In this case, however, the robot was actively controlled and its Cartesian stiffness was set to the highest value possible (3 kN/m in all directions). To minimize voluntary stiffening behavior of the subjects arm, following Perreault et al. [50] we applied continuous stochastic perturbations to the subject's hand through the handle in x , y and z directions. The amplitude of the applied perturbations had the peak-to-peak value of 20 mm in each direction. Figure 3.4 shows a typical applied endpoint displacements and restoring forces along x , y and z directions. Frequency spectrum of the perturbations were flat while decaying at the rate of 40 dB/Hz in frequencies higher than 4 Hz (Fig. 3.5). This perturbation profile and corresponding forces in response, ensure adequacy of data for the identification of endpoint dynamics [125]. The experiments for EMG-to-stiffness map identification were performed by measuring the subject's force response to these random perturbations while the subject was instructed to set his arm's stiffness at a given level. Restoring forces exerted by the subject's arm were monitored by means of the F/T sensor, positions of the subject's wrist center were measured via the optical tracking system, and EMGs were acquired simultaneously and synchronously.

A rough stiffness indicator was graphically shown consisting of a bar of length proportional to the norm $|P|$ of the vector of muscle activations. Four different stiffness reference levels were provided in different trials. The first set of random position

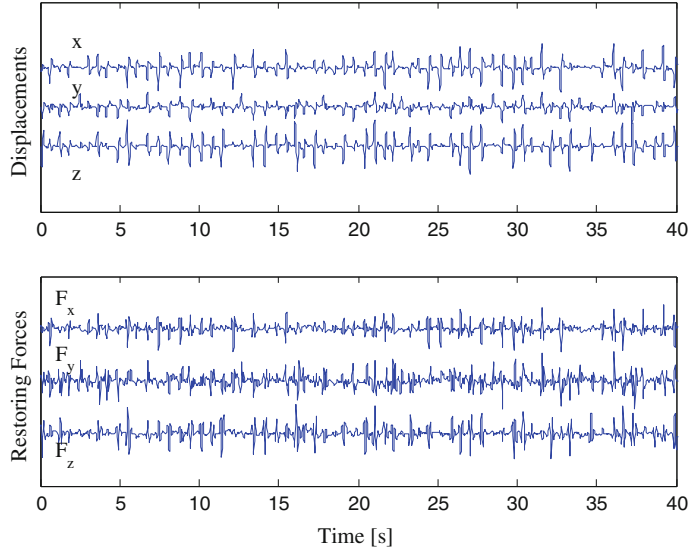


Fig. 3.4 Typical applied endpoint displacements and restoring forces in x , y and z directions. Each trial was 40 s long which the last 35 s of the trials were used for the further processings

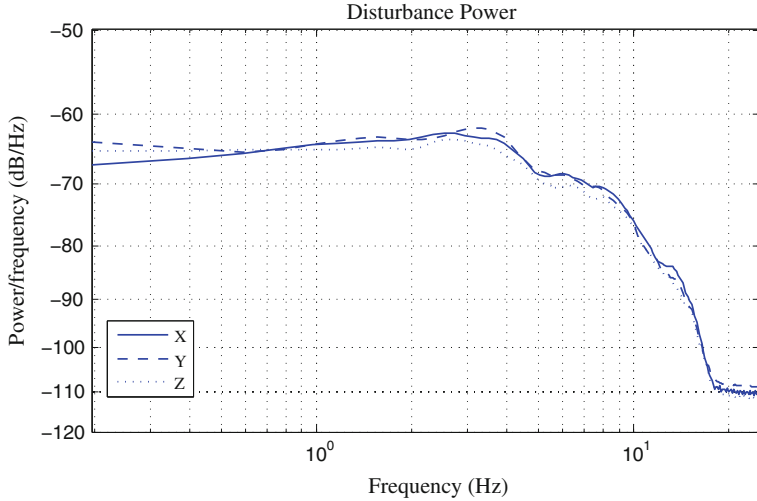


Fig. 3.5 Power spectrum of the applied disturbances

perturbations was applied to the subject's hand at minimum muscle activity level (relaxed arm). The corresponding data was used to estimate the intrinsic stiffness σ_0 based on the identification protocol described below. Also, the endpoint inertia parameters in the vicinity of the predefined posture were identified in relaxed conditions, to be used later as a constant (under the simplifying assumption of negligible

influence of muscle mass distribution on endpoint inertia) for the estimation of endpoint visco-elastic parameters in higher cocontraction trials. After such experiments in relaxed conditions, the subject was asked to stiffen his arm as hard as possible. The three reference levels of stiffness were hence defined by subdividing in four equal parts the measured interval of $|P|$ between its relaxed and maximum values.

Instructions given to the subject in the EMG-to-stiffness map identification phase included keeping the visualized index $|P|$ close to the set value during the experiment. Trials where the deviation from the preset level of $|P|$ were larger than 10 % were discarded. Five successful trials were recorded for each level of arm stiffness. Each perturbation trial lasted 40 s. The first 5 s were used for allowing the subject to adapt to required stiffness level. The force on the handle caused by arm weight was removed as bias, being constant for small deviations from the equilibrium configuration.

The estimate of endpoint stiffness in different trials was performed based on measurement of corresponding pairs of forces and positions at the subject's wrist, following standard methods (see e.g. [50]). For this reason, multiple-input, multiple-output (MIMO) dynamics of the endpoint impedance was decomposed into the linear subsystems associating each input to each output. Based on this assumption, and indicating with $F_x(f)$, $F_y(f)$ and $F_z(f)$ the Fourier transforms of the endpoint force along the axes of the Cartesian reference frame, with $x(f)$, $y(f)$ and $z(f)$ the transforms of the human endpoint displacements, the dynamic relation between the displacements and force variations can be described by

$$\begin{bmatrix} F_x(f) \\ F_y(f) \\ F_z(f) \end{bmatrix} = \begin{bmatrix} G_{xx}(f) & G_{xy}(f) & G_{xz}(f) \\ G_{yx}(f) & G_{yy}(f) & G_{yz}(f) \\ G_{zx}(f) & G_{zy}(f) & G_{zz}(f) \end{bmatrix} \begin{bmatrix} x(f) \\ y(f) \\ z(f) \end{bmatrix} \quad (3.4)$$

A non-parametric algorithm was adopted to identify the empirical transfer function of each of the SISO subsystems described above in frequency domain (MATLAB, The MathWorks Inc.). The smoothed spectral estimates of input and outputs (using windowing techniques) were fed to this algorithm in order to identify each SISO transfer function. Consequently, we adopted a parametric, second order, linear model of each impedance transfer function of the type

$$G_{ij}(s) = I_{ij}s^2 + B_{ij} s + K_{ij}, s = 2\pi f\sqrt{-1} \quad (3.5)$$

where I , B and K denote the endpoint inertia, viscosity and stiffness matrices, respectively. The parameters of the second order linear model were identified based on least squares algorithm in frequency range from 0 to 10 Hz. Although simple, this model has been shown to be adequate to the representation of the endpoint impedance of the human arm in a large class of tasks [50, 55].

Finally, in the postprocessing phase, experimental EMG vectors P were mapped in the EMG-to-force map nullspace through the previously computed projector matrix Q . The elements of the stiffness matrix K were used as estimates for the components of σ , and the map M_σ was estimated by applying a least-squared-error method to (3.3).

3.2.3 Identification Results

The strength of linear dependency between measured force signals and estimates via the least-squared-error identification of the components of T_F was evaluated by Pearson's product-moment correlation coefficient. The coefficient is defined as

$$R_k = \frac{\sum \hat{f}_k f_k - \frac{\sum \hat{f}_k \sum f_k}{N}}{\sqrt{\left(\sum f_k^2 - \frac{(\sum f_k)^2}{N}\right)\left(\sum \hat{f}_k^2 - \frac{(\sum \hat{f}_k)^2}{N}\right)}}, \quad k = x, y, z \quad (3.6)$$

where f_k and \hat{f}_k are measured and estimated values of force in the Cartesian directions, and N is the number of pairs of data. The fit was consistently good in the three directions, resulting in average $R^2 = 81\%$.

Multiple and partial coherence indexes which investigate the linear dependency of each output to all system inputs, and between single input and single output, respectively, are shown in Fig. 3.6. Figure 3.7 demonstrates the results of non-parametric and second order model identification of the hand impedance transfer functions in the frequency range from 0 to 10 Hz, according to methods described above. The second order parametric impedance models presented (69.7 %) of the data variance across all directions in minimum muscular activity trials in the frequency range of 0–10 Hz. Values of estimated endpoint inertia, damping and stiffness along the Cartesian directions are presented in (Table 3.2). Estimated values are in good accordance with the former results of impedance estimation in 2D [54, 56] and 3D [45].

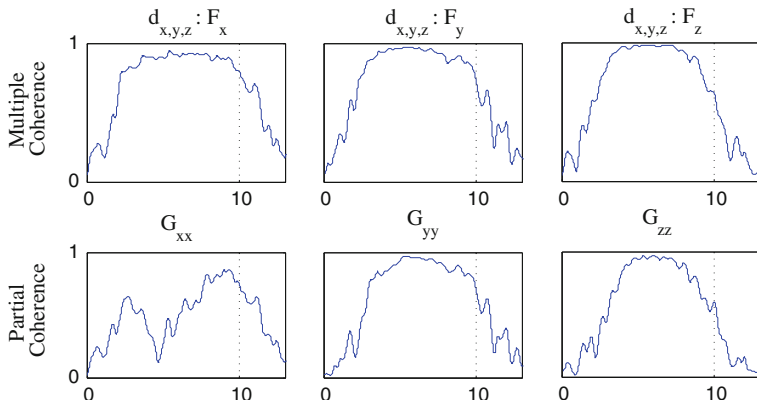


Fig. 3.6 Multiple and partial coherence values over frequency

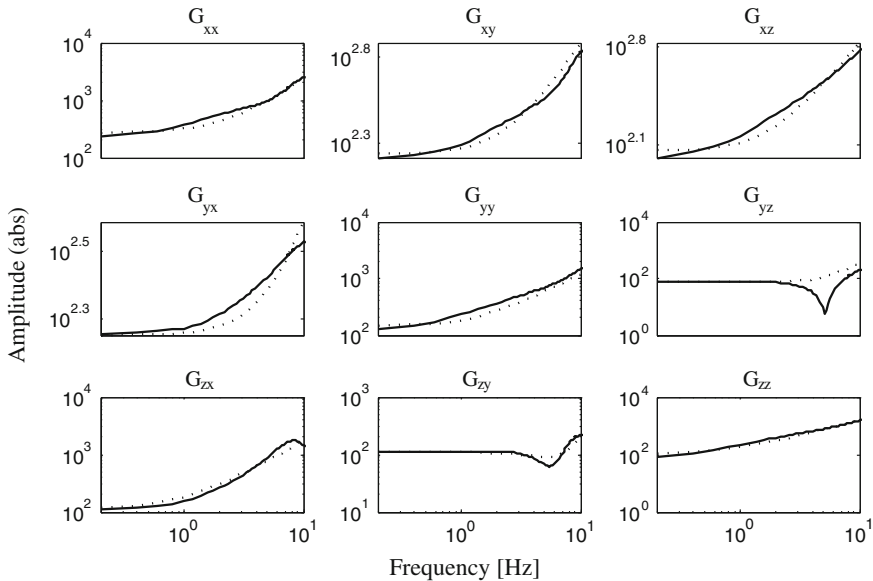


Fig. 3.7 Non-parametric (*solid lines*) and parametric second order (*dotted lines*) transfer functions of SISO impedance subsystems obtained from stochastic perturbations

Table 3.2 Estimated hand impedance parameters

| Stiffness (N/m) | | | Viscosity (N s/m) | | | Inertia (kg) | | |
|-----------------|--------|--------|-------------------|-------|-------|--------------|------|------|
| K | | | B | | | I | | |
| 240.58 | 163.99 | 102.35 | 21.33 | 7.09 | 6.96 | 1.02 | 0.32 | 0.15 |
| 181.81 | 128.97 | 78.78 | 3.77 | 17.72 | 3.29 | 0.17 | 0.78 | 0.09 |
| 113.36 | 107.18 | 81.01 | 23.12 | 1.90 | 26.06 | 0.19 | 0.12 | 0.87 |

Extracting the symmetric and antisymmetric parts ($K_s = (K + K^T)/2$ and $K_a = (K - K^T)/2$, respectively) of the estimated stiffness matrix, it can be observed that the estimate is rather strongly symmetric ($\|K_a\|/\|K_s\| \approx 0.04$).

Chapter 4

Replicating Human Stiffness Profile with a Cartesian Impedance Controller in Realtime

In this chapter, we evaluate the efficiency of the teleimpedance algorithm in two experimental tasks, illustrating different and complementary aspects of the method. The first concerns a classic peg-in-hole task, and is used to illustrate the stability, transparency, and safety characteristics of the method. The second experiment, a ball-reception task, is chosen to assess how effective is the incorporation of human impedance regulation skills in performing tasks with significant dynamics. In both experiments, the slave robot performs the task by tracking both the reference position profile (which corresponds to the endpoint position of the arm of the human operator as measured from an optical position tracking system) and the end-point stiffness profile (estimated from the muscular activities of the operator's arm) in real-time, via a Cartesian impedance controller. Eventually, the performance of the proposed algorithm is compared to the behavior of the robot arm with different constant stiffness settings.

4.1 Cartesian Impedance Control

The dynamical model of the robot with no joint elasticity can be written as follows

$$M(q)\ddot{q} + C(q, \dot{q})\dot{q} + g(q) = \tau + \tau_{ext}, \quad (4.1)$$

with $M(q)$ and $C(q, \dot{q})$ representing the mass and the Coriolis/centrifugal matrices, and $g(q)$ and τ_{ext} denoting the gravitational and external torque vectors. $q \in \mathbb{R}^n$ symbolizes the joint angles (n being the number of joints of the manipulator) and it's relation with the Cartesian coordinates, $x \in \mathbb{R}^m$, is established through the forward kinematics; i.e., $x = f(q)$. In addition, the relation between the joint and Cartesian velocities/accelerations is established by the manipulator Jacobian, $J(q)$, as follows¹

¹The redundant case will be discussed in next chapter.

$$\dot{x} = J(q)\dot{q}, \quad (4.2)$$

$$\ddot{x} = J(q)\ddot{q} + \dot{J}(q)\dot{q}. \quad (4.3)$$

As a consequence, the external torques, τ_{ext} , can be related to the generalized external forces, F_{ext} , by $\tau_{ext} = J(q)^T F_{ext}$.

To realize a desired compliant profile, we need to establish a mass-spring-damper relation in between the Cartesian displacements, $\Delta x = x - x_d$, and the external force as follows

$$F_{ext} = \Lambda_d \Delta \ddot{x} + D_d \Delta \dot{x} + K_d \Delta x, \quad (4.4)$$

with Λ_d , D_d and K_d denoting positive definite matrices and representing virtual mass, damping and stiffness of the system. Above equation highlights the main distinction between the classical force or position control techniques and the Cartesian impedance control (one way of rendering a compliance behavior), since it implements the dynamic relation (Eq. 4.4) between the task variables, rather than individual control of them [75].

Now, by inserting Eqs. 4.3, 4.2 and $\tau_{ext} = J^T(q) F_{ext}$ into Eq. 4.1 and rearranging it, we acquire [77]

$$\Lambda(x)\ddot{x} + \mu(x, \dot{x})\dot{x} + F_g(q) = F_\tau + F_{ext}, \quad (4.5)$$

with

$$\Lambda(x) = J(q)^{-T} M(q) J(q)^{-1}, \quad (4.6)$$

$$\mu(x, \dot{x}) = J(q)^{-T} (C(q, \dot{q}) - M(q) J(q)^{-1} \dot{J}(q)) J(q)^{-1}, \quad (4.7)$$

$$F_g(q) = J(q)^{-T} g(q), \quad (4.8)$$

$$F_\tau = J(q)^{-T} \tau. \quad (4.9)$$

Therefore, the control input, F_τ , can be calculated by

$$\begin{aligned} F_\tau &= \Lambda(x)\ddot{x}_d + \mu(x, \dot{x}_d)\dot{x}_d + F_g(q) \\ &\quad - \Lambda(x)\Lambda_d^{-1}(D_d \Delta \dot{x} + K_d \Delta x) + (\Lambda(x)\Lambda_d^{-1} - I)F_{ext}, \end{aligned} \quad (4.10)$$

and the required joint torques will be calculated $\tau = J(q)^T F_\tau$, as a consequence. In this equation, the feedback of external forces can be avoided by setting $\Lambda_d = \Lambda(x)$, which leads to the following dynamic relation

$$F_\tau = \Lambda(x)\ddot{x}_d + \mu(x, \dot{x}_d)\dot{x}_d + F_g(q) - D_d \Delta \dot{x} - K_d \Delta x. \quad (4.11)$$

In this chapter, proposed teleimpedance controller incorporates the Cartesian impedance control law (Eq. 4.11) to realize the desired stiffness matrix, K_d ,² which is derived from the realtime model, developed in Chap. 3.

4.2 Teleimpedance: Peg-in-Hole Task

Efficiency of teleimpedance approach to cope with contact stability issues is first evaluated in a Peg-in-hole task, a classical benchmark for spatial planning with uncertainties [13, 14].

The experiment was designed in order to explore the role of stiffness regulation during dynamic interaction between the peg and the hole, particularly its effect on the interaction forces. A reference configuration for the operator's arm was initially chosen so that he/she could perform the peg-in-hole task comfortably. Stiffness identification experiments were made in preparation for the experiment, in the same reference configuration for the human arm. Wrist, elbow and shoulder joint markers were used to gather arm postural data. In the actual experiment, the human operator was placed so that the slave endpoint frame was translated to the master's own wrist frame laterally along the direction of the master's shoulder-to-shoulder line (Y axis). A geometric calibration was used to make sure that the reference human arm configuration corresponded to a robot's pose matching the hole position. In the experiment, the operator was allowed to start motion from an arbitrary position, was asked to move his/her hand to reach the reference configuration, and finally to teleoperate the robot to insert the peg in the hole. The master could see the slave arm, including the peg and hole. No peg was held by the master, nor did he receive any feedback except from seeing the slave arm operations. It should be noted that in the reaching phase, where stiffness calibration is not accurate, there are no interactions with the environment.

The experiment consisted in four parts. In the first part, the Cartesian stiffness of the slave endpoint was set to a relatively high, constant level ($K = [1200, 1200, 1200]$ N/m) throughout the task. The second part was analogous, with low constant stiffness values ($K = [120, 120, 120]$ N/m). Third part concerns with the endpoint stiffness profile of the slave under constant and high along z and low along x and y directions ($K = [1200, 250, 250]$ N/m). Values of high and low endpoint stiffness profiles were chosen based on human arm endpoint stiffness interval. The forth part used variable impedance in the three directions, as derived from the proposed EMG processing method (teleimpedance control). Damping values in all experiments were set to a constant value of $D = [0.7, 0.7, 0.7]$ N.s/m. Further extensions of the method, providing the possibility of reproducing the off-diagonal stiffness terms and/or the endpoint damping behavior of the human with the slave robot arm [126], are possible but were not demonstrated yet.

²Here, only the diagonal elements of the desired stiffness matrix is taken into account.

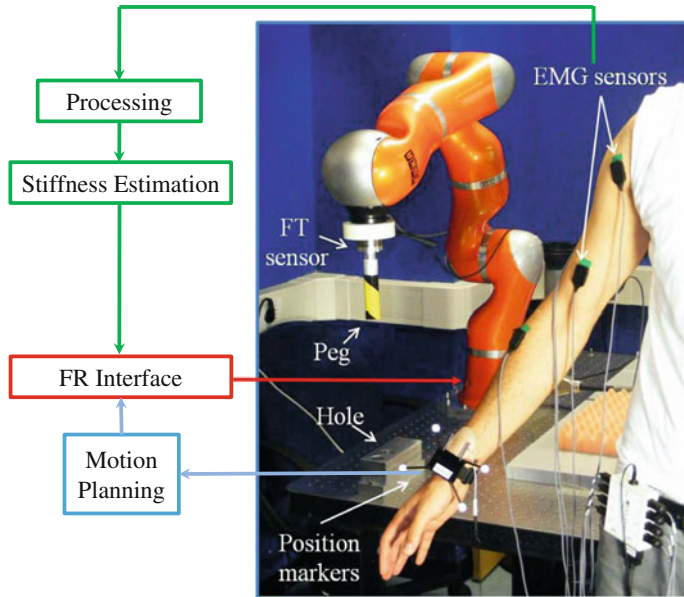


Fig. 4.1 Peg-in-hole experimental setup. KUKA light weight robotic arm, EMG electrodes, peg, hole, position tracking markers and F/T sensor are shown

The experimental setup and information flow are shown in Fig. 4.1. Body markers were attached to the wrist, elbow and shoulder of the human master's arm to track its motion. The reference trajectory calculation for robot motion was provided by the wrist marker, while shoulder and elbow were used to make the final configuration of the master's arm coincide with the reference position, removing possible differences in the redundancy manifold. The robot base frame was considered as the overall reference frame for other frames (Optitrack and FT sensor). The position path of the human wrist was measured, low-pass filtered (cutoff 15 Hz) and used for trajectory planning. At the same time, EMG signals were acquired from the master arm and used to evaluate its endpoint stiffness based on the model and calibration described in the previous section. All processing and control algorithms were performed in real-time. Software interfaces, sampling frequencies, and hardware specifications are identical to those reported in the previous section. The KUKA LWR's Fast Research Interface was used for commanding the position and Cartesian impedance controllers of the slave arm. Incremental position references were sent to the robot, calculated from the position tracking errors in three dimensions (4.12) as

$$e_x = X_{\text{human}} - X_{\text{slave}} \quad (4.12)$$

where e is three dimensional tracking error vector between the reference Cartesian position vector of human wrist X_{human} , and the current Cartesian position vector of

the robot end-effector, X_{slave} . This approach was used to cope with drift and tracking inaccuracy due to possible delays between reference commands and generated movement in the slave end-effector. The reconstructed values of the master arm stiffness were used as inputs for the robot endpoint impedance controller algorithm, described [82, 107] and implemented in the FRI. A video of the experiment is available at [22].

4.2.1 Experimental Results

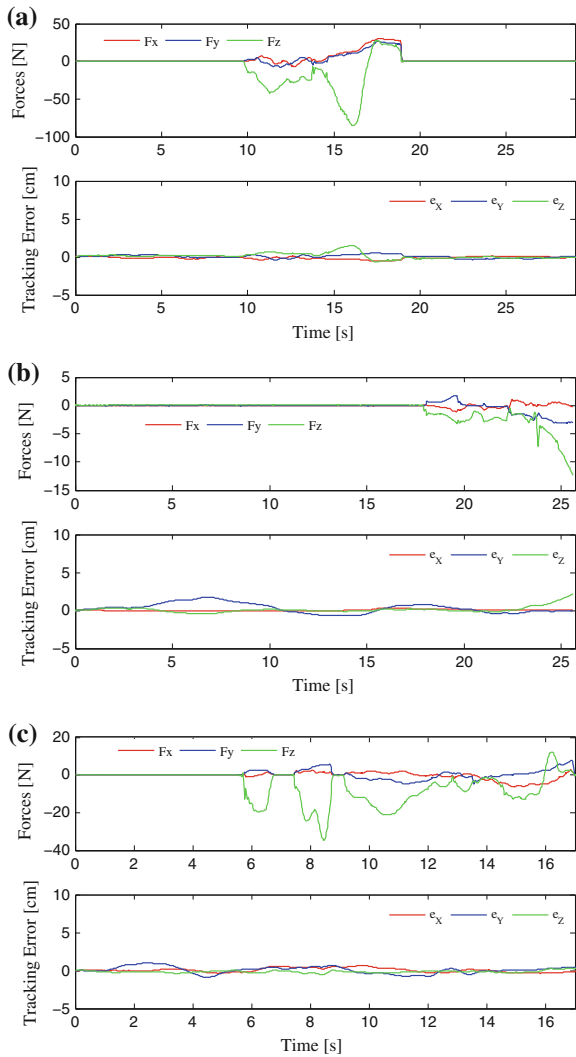
Figure 4.2 present experimental results for the interaction forces between the peg and the hole, and the position tracking errors in three dimensions. As shown Fig. 4.2a, when the slave arm is controlled to a constant high stiffness (equal to 1200 N/M in all principal directions), the task could be successfully accomplished. However, even small position errors generated relatively large forces (up to 80 N in the negative z direction) at time $t = 10$ s when the interaction starts. This phenomenon indicates possible damaging effects both for the robot and for equipments/objects manipulated during the execution of the task.

Figure 4.2b demonstrates results from the second experiment, in which the task was executed with the slave arm stiffness fixed to low values (120 N/m in all principal directions). Position errors (particularly in y direction) can be observed to be slightly increased in the reaching phase which is due to compliance of the robot leading to reduced dynamics and bandwidth. Once the peg is positioned close to the hole ($t \approx 18$ s), interaction forces raise to a value which is notably lower than in the former case. Small end-effector position adjustments, as a result of the master's hand movements, succeeded in aligning the peg with the hole ($t \approx 23$ s). After reaching the alignment, the master started the insertion phase by simply moving the hand down. An increase of the force in the vertical insertion direction can be consequently observed, which however is not sufficient to win friction forces between peg and hole and accomplish the task. As a consequence, the slave's end-effector could not track the subject's reference and position error increase, eventually reaching the slave arm controller's safety threshold and entering a fault condition ($t \approx 26$ s).

Figure 4.2c demonstrates typical results from third experiment. As depicted in the plots, even though the task is accomplished and interaction forces along x and y direction between peg and the hole surface are significantly reduced compared to first experiment, the algorithm still suffers from high interaction forces resulting from even very small position errors along z direction, specially when peg slides on the surface of the hole (from $t \approx 5.9$ s to $t \approx 8.6$ s).

Figures 4.3 and 4.4 demonstrate the experimental results obtained with application of teleimpedance control. In this experiment the operator guides the peg to the hole area keeping the arm in a natural, low stiffness profile. In this phase, the arm is rather far from the posture where stiffness values were estimated, and calibration data obtained are invalid: however, in this phase position control is sufficient to

Fig. 4.2 Dynamic interaction forces between peg and the hole and position tracking error in x, y and z directions, with **a** fixed high values of end point stiffness ($[1200, 1200, 1200]$ N/m), **b** fixed low values of end point stiffness ($[120, 120, 120]$ N/m) and **c** fixed and high along z and low along x and y directions ($K = [250, 250, 1200]$ N/m)



guarantee good overall guidance in free space. Once the peg reaches to the reference configuration ($t \approx 12.5$ s), the operator begins moving his hand down towards the hole and exerting moderate forces. After some time (at $t \approx 17.5$ s), the master increases further his muscular activation to increase and adjust the endpoint stiffness (Fig. 4.3) until a suitable level of stiffness is reached as to overcome friction. In this phase, the operator appears to be guided by a comparison of proprioception relative to his hand position, with visual feedback from the slave's endpoint. Finally, the operator moves his hand downwards till the peg is fully inserted into the hole. Similar stiffness levels were used to successfully pull the peg out from the hole.

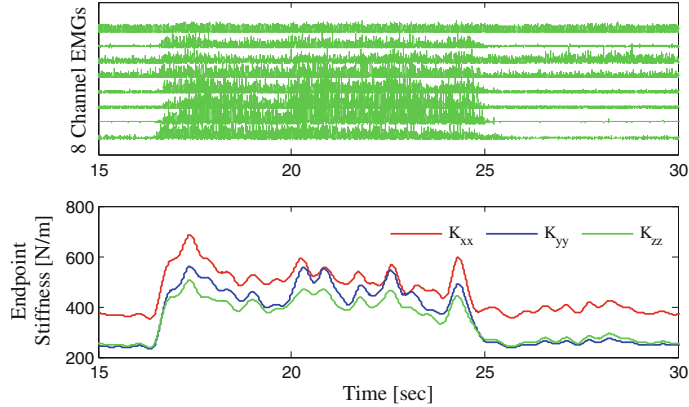


Fig. 4.3 Fully rectified eight channel raw EMGs (*upper plot*) and estimated and mapped endpoint stiffness (*lower plot*) in real-time for peg-in-hole task

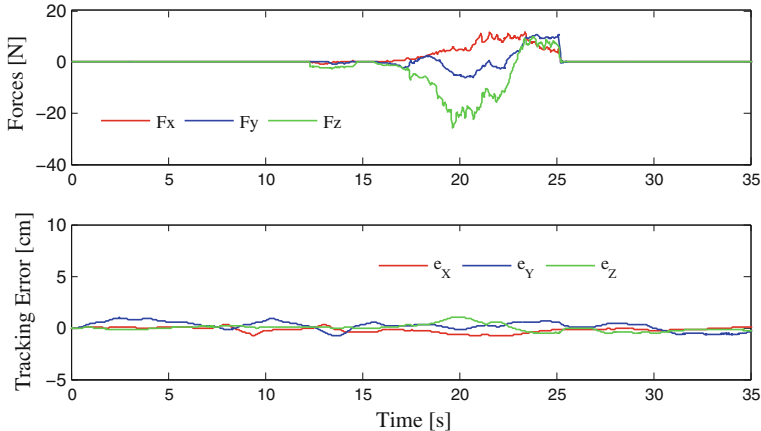


Fig. 4.4 Dynamic interaction forces between peg and the hole (*upper graph*) and position tracking error in x, y and z directions (*lower graph*) based on teleimpedance

($t \approx 23$ s to $t \approx 25$ s). As depicted in Fig. 4.4, both position tracking errors and interaction forces remain within acceptable levels, both in the search phase (between 13 and 17.5 s, where high stiffness caused high interaction forces), and in the insertion phase (roughly between 17.5 and 21 s, where low stiffness generated large tracking errors and ineffective forces). It should be noted again that the insertion and pull out phases were performed at a pose of the arm close to where the parameters of the end point stiffness model were estimated and calibrated.

4.3 Teleimpedance: Ball-Catching Task

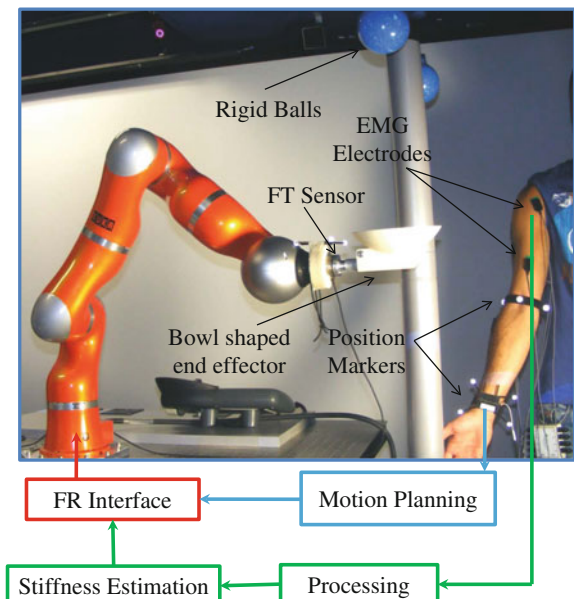
Further evaluation of the proposed teleimpedance technique in conditions involving more significant dynamics was done through the execution of ball-catching task. The task consisted of receiving a ball thrown at the arm's endpoint and bringing it to a stop in the reference position.

Two identical rigid balls ($m = 0.92\text{ kg}$, radius 52.5 mm) were suspended at the same distance above the human and robotic arm endpoints. The subject was prepared to receive the ball and instructed to hold his arm in a posture very close to that used during calibration experiments. The slave arm position, under gravity compensation, was corresponding. The balls were simultaneously dropped using a single manual release mechanism.

The subject was instructed to receive the ball and stabilize its position back to the original arm's posture as smoothly and expeditedly as possible. The position of the slave endpoint was controlled along the master's wrist trajectory before and during catching, whereas the Cartesian stiffness values were controlled to constantly high, low or regulated to the master's stiffness level in three different experimental phases, exactly as described in the previous section.

The experimental setup and information flow are shown in Fig. 4.5. Software interfaces, marker placements, sampling frequencies, hardware specifications and calibration data were identical to those reported in previous sections. A video of the experiment is available at [23].

Fig. 4.5 Experimental setup of the ball-catching experiments. The slave KUKA LWR arm, EMG electrodes, position tracking markers and F/T sensor are shown



4.3.1 Experimental Results

Typical master's hand path in x, y and z directions, and while performing the task are shown in Fig. 4.6. These trajectories demonstrate the small range of required motion to perform the task and assure the validity of the identified model in reference posture. The measured forces at the endpoint of the slave robotic arm during the task in the three stiffness control modes (constantly high, constantly low, and teleimpedance) are reported in Fig. 4.7, while the corresponding deviation errors from the reference equilibrium position are in Fig. 4.8. The regulation of the human arm muscle activations and resulting endpoint stiffness modifications during the catching experiment are shown in Fig. 4.9. At the beginning of the experiment, a small constant increase in muscular activity could be observed, which led to relatively small increase in endpoint Cartesian stiffness values, compared to fully relaxed trials, which may refer to task readiness impedance tuning [55]. Increased stiffness at the time of impact and its progressive decrease afterward are the results of explicit muscular activity regulation by the subject.

As it could be expected, the stiffer the arm, the smaller the deviation is, as it can be seen in the experimental results under constant high stiffness (Fig. 4.8, left). The price paid for the accuracy and reduced deviation from equilibrium position with high values of endpoint stiffness is the occurrence of bouncing: indeed, the second force peak (at $t \approx 5.26$ s) in the stiff case (Fig. 4.7, left) shows a second impact of the ball.

To obtain a more stable contact is to reduce the endpoint stiffness values; however, using a constantly low stiffness directly affects the position deviation, which may get to very large, possibly unacceptable values (Fig. 4.8, middle). Another drawback of such compliant control is the insufficiency of generated torques for repositioning the ball to its equilibrium even after transient end. The latter issue could be mended by the master controlling his arm in a posture such as to compensate for the F the slave, but this would cause a large discrepancy between the master and slave arm postures, affecting the naturalness of teleoperation.

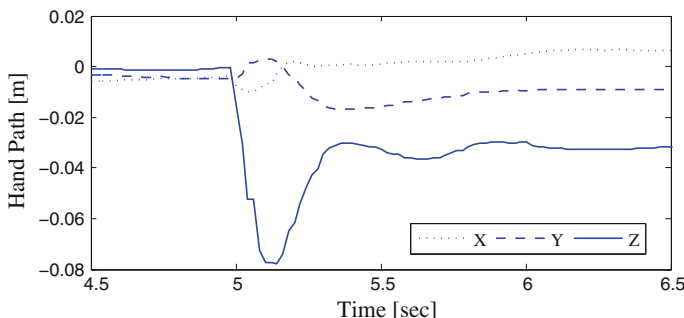


Fig. 4.6 Typical master's hand path in x,y and z directions with respect to its initial position, and while performing the ball-reception task

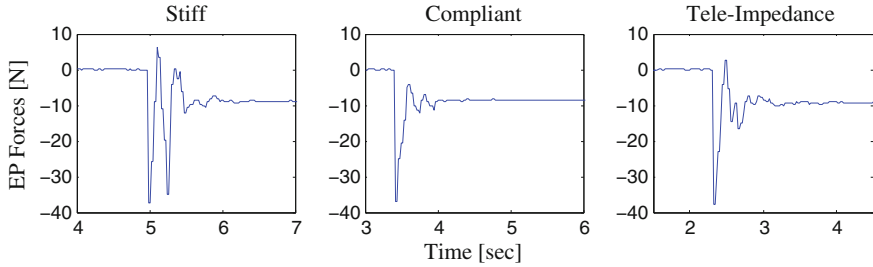


Fig. 4.7 Measured force values in z direction during the task with the slave robotic arm under constantly high, constantly low, and teleimpedance stiffness control

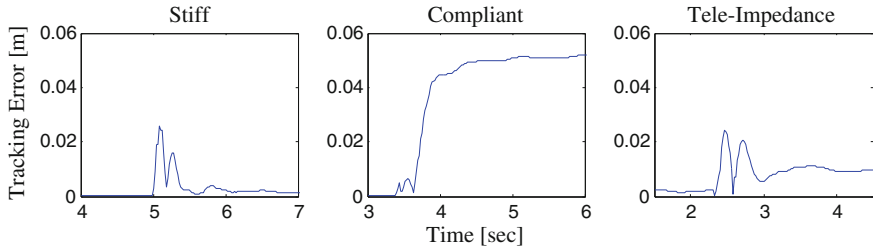


Fig. 4.8 Absolute tracking position error in z direction during the task with the slave robotic arm under constantly high, constantly low, and teleimpedance stiffness control

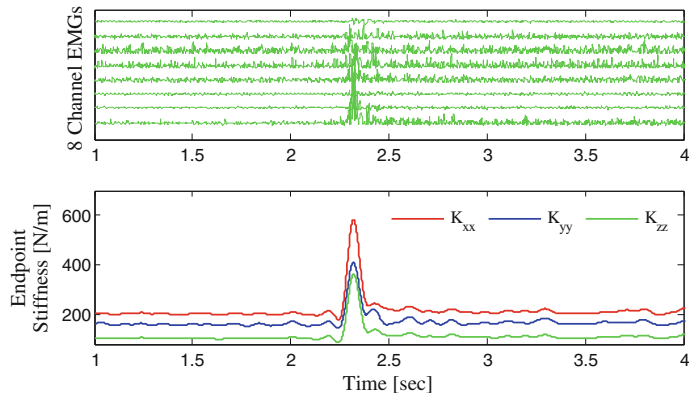


Fig. 4.9 Fully rectified eight channel raw EMGs (upper plot) and estimated and mapped endpoint stiffness (lower plot) in real-time for ball-reception task

The transient behavior of the system under teleimpedance appears to benefit from the active control of stiffness, increasing at the very first impact instants (from $t \approx 2.3$ s to $t \approx 2.4$ s), leading to a reduced deviation from reference equilibrium position. Also, the bouncing phenomenon appears to be avoided thanks to the subsequent phase of stiffness reduction (between $t \approx 2.4$ s to $t \approx 2.7$ s, see Fig. 4.9). This

behavior is in accordance with previous studies which have shown the capabilities of the human body to minimize soft-tissue vibrations and impact transitions by means of increased damping or decreased stiffness (modified resonance frequency) within involved tissues (see e.g. [127]). In addition, other behavioral studies demonstrated an increase of cocontraction levels in human arm while performing tasks which need quick torque generations and/or to cancel components of torques orthogonal to the desired direction [65].

To attempt a comparative analysis of performance in the ball reception task with the three control modes, we used three quantitative indices. The first index is computed as the integral of the difference between the vertical component of wrist force F_z and its steady-state value (i.e., the hand plus ball weight F_w) as

$$LOI = \int_{\Delta t} |f_z - f_w| dt, \quad (4.13)$$

where δt is the time interval duration between the first impact and steady stabilization. A high value of the “lift off index” LOI indicates a reception with multiple bouncing and/or long underdamped ball trajectories.

The second index is the maximum deviation from the equilibrium position in z direction at steady state, evaluated as

$$PEI = \max_{t \in \Delta t} |e_z|(t). \quad (4.14)$$

A high value of the “position error index” PEI indicates a reception where the slave arm is brought to postures too far from the master’s.

As a third index, we consider an estimate of the damping ratio of the bouncing phenomenon, experimentally estimated (see e.g. [128]) using the logarithmic decrement between the first and second force peaks

$$\delta = \log \left(\frac{f_{z,p,1}}{f_{z,p,2}} \right)$$

as

$$DRI = \frac{1}{\sqrt{1 + \left(\frac{2\pi}{\delta}\right)^2}},$$

High values of the “damping ratio index” DRI indicate the capability of the system to absorb energy and damp it quickly.

Fourth and last, the “bouncing time index” BTI was introduced as the duration of the interval during which contact between the ball and robot’s end effector is completely lost. The value is calculated by summing the intervals along which f_z is zero (complete disconnection) or positive (as result of acceleration of bowl) after the first impact.

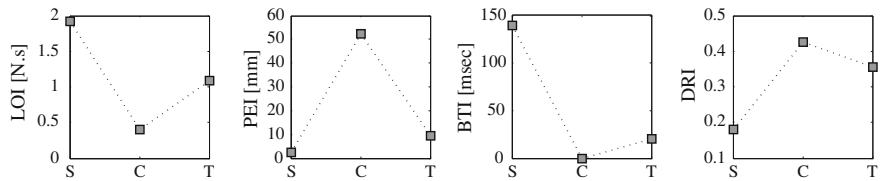


Fig. 4.10 Performance index plots over different elastic endpoint profiles (S: Stiff, C: Compliant and T: Teleimpedance)

Figure 4.10 shows the values obtained in experiments for the four indices in the three different stiffness regulation modes. Teleimpedance control apparently strikes a good compromise among the two extremes, consistently scoring close to the best performance obtained by either of the two constant settings, thus enabling the human ability to be effectively transferred to the slave arm.

4.4 Conclusions

In this chapter the concept of teleimpedance was introduced, as a method to effectively transfer task-oriented stiffness control from the human master to the robotic slave arm. As an alternative to position-based or closed-loop bilateral force-reflecting teleoperation, the proposed approach enriches the command sent to the slave robot by combining the position reference with a stiffness (or full impedance) reference estimated from the arm of the human operator. The stiffness command to the robot was derived in real time from the measurement of EMGs from eight muscles of the operator arm. A novel method was proposed for the estimation of stiffness in the human arm. This model was identified and calibrated through direct measurements of endpoint impedance. The procedures used for the calibration of the model were introduced and the teleimpedance control concept was illustrated through two complementary tasks. Although results obtained in this chapter are encouraging, they have to be considered preliminary. Among the limitations of the present technique is the local validity of calibration data, and the need for recalibration in different poses and for different subjects. In addition, utilization of electromyography signals in real environments suffers from some robustness issues. For instance, EMG signals are exposed to noise as results of cross talk and motion artifacts. Thermal and humidity variations might also give rise to EMG's variability, drift and inaccuracy. Need for recalibration as an outcome of subject-to-subject and day-to-day variations are other well-known disadvantages. Although in our experiments we found that the use of the same calibration data at relatively distant postures, and with other subjects than the person used for parameter estimation, was surprisingly effective, these were only anecdotal findings at this time, and the problem deserves much further work in the future.

Our approach to telemanipulation is unilateral in force, but requires visual feedback from the task scene. Although teleimpedance is intended to allow the user to control the robot forces indirectly through intuitively setting its stiffness, for particularly fragile environments (such as when the slave robot interacts with another human, or in surgery applications) this might not be enough, and it should be complemented with other means—e.g. simple augmented visual feedback giving indications about forces actually occurring at the interaction point.

The teleimpedance idea is to replicate in the robot whatever stiffness ellipsoid the human master uses. Our implementation and experiments show that indeed the method works, and tasks get better done than without teleimpedance control.

It is worth pointing out here that there is a classical literature in robot control that points out the advantages of using cartesian impedance control with different stiffness in different directions, e.g. for the peg-in-hole task [129, 130]. There are also many results in neurophysiology which suggest that humans voluntarily orient their end-effector impedance ellipsoid using muscle co-contraction, in directions according to the task and/or the expected disturbances [49, 51, 131]. However, there are also different views on the issue, such as [66], who contend that *individuals can voluntarily change stiffness orientation but the magnitude of these changes is small, and that end-point force direction determines direction and magnitude of the stiffness orientations that can be achieved.*

However, as it can be noticed from Fig. 4.3 and especially in Fig. 4.9, in our experiments the human subject's stiffness changes in the three directions were rather strongly correlated, suggesting that the subject might be controlling the size more than the shape of the stiffness ellipsoid in time during the different phases of the task. As a consequence, we do not have sufficient evidence to state that better performance is gained through replicating directional stiffness over a simpler, single-channel stiffness command.

Chapter 5

Exploring the Roles of Common Mode Stiffness (CMS) and Configuration Dependent Stiffness (CDS) Control

As mentioned in the introduction of this book, humans demonstrate versatile and stable interactions with uncertain environments. Such stability is guaranteed by generating efficient and task-related restoring forces in response to environmental displacements [51], and is accomplished by co-activation of the muscles acting on the joints.

Qualitative representation of the human endpoint stability in a certain posture is performed by the stiffness ellipsoid [48]. The contribution of the co-activation of involved muscles in the modulation of the stiffness ellipsoid size is shown to be more effective than adjustments in its directionality [44, 45]. Furthermore, previous studies discuss on limited ability of humans in changing the orientation of the postural stiffness ellipsoid, even subsequent to learning stages [66]. These observations give evidence to some coordinated stiffening trend of the arm joints in humans (this notion is consistent with the experimental results achieved in Figs. 4.3 and 4.9). As a result, in a static posture, human arm endpoint will be less stiff in certain directions than others. To compensate for that, adaptively selected postures further regulate the direction of the endpoint ellipsoid to realize a task-required elastic profile. Indeed, contribution of the predictive postural control to mechanical stability in humans is shown to be more effective than the role of co-contraction [44, 45]; however, postural adjustments are extremely limited by the task constraints and mainly rely on the kinematic redundancy.

Replication of human-like impedance regulation mechanisms in robots can permit them to safely and efficiently operate in unstructured environments under unpredicted interaction scenarios. In this direction, while classical impedance control techniques (see Sect. 2.2) have demonstrated their efficacy in rendering any desired compliant behavior, only few studies explored the dominant role of kinematic redundancy for that purpose. For instance, in the work of [99], based on a desired endpoint stiffness matrix, the joint stiffness levels were optimized and kept fixed. Consequently, a nullspace optimization algorithm (in a less realtime planning layer) was adopted to

additionally reduce the endpoint stiffness error. The minimum number of kinematic degrees of redundancy in order to replicate the desired full stiffness matrix was deeply discussed.

Incorporation of human motor control principles in realization of the desired Cartesian stiffness profile (referenced from human), not only will lead to effective task accomplishments, it will generate natural motions, similar to the ones observed in humans. To that end, relying on the growing body of evidence about coordinated stiffening behavior of the human arm joints in a constant posture [1, 66], we implement a *common mode stiffness* (CMS) across the joints and combine it with control of *configuration dependent stiffness* (CDS) to realize a desired endpoint stiffness. Thus, we propose an algorithm that simultaneously regulates the CMS and CDS based on the error between time-varying desired stiffness matrix and the realized one at the robot endpoint. In a phase that there is no interaction between the robot and the environment, we implement a minimum effort controller to drive the robot joints in redundant manifold to a configuration in which the effect of gravity loading on the robot joints are minimum. This will produce natural free arm movements [132, 133] and will provide a reasonable initial configuration for our realtime CDS optimization algorithm.

Therefore, the algorithm combines the human's free movement efficiency and interaction performance based on the minimization of the effect of gravity loading on the robotic joints and the error between time-varying desired stiffness matrix and the one realized at the robot endpoint, respectively. Task-oriented prioritization of the minimum-effort and CMS-CDS criteria while assuring smoothness of joint trajectories is performed by a decision rule obtained by a priority based soft switching logic. Results of the implementation of the multiple-criteria controller are experimentally evaluated in a peg in the hole task and compared to those derived from implementation based on the original teleimpedance control, during interaction phase.

5.1 Controller Design

5.1.1 CMS-CDS Controller

To realize the human's desired endpoint stiffness profile at the slave's end effector, different strategies might be exploited. Cartesian impedance control [81] as a well-grooved technique, establishes a mass-spring-damper relationship between the Cartesian position and force. Implementation of such control scenario requires joint torque sensing and control. Recently the development of robotic systems equipped with passive variable stiffness actuation introduced a new design paradigm towards robots with intrinsic variable joint compliance properties. In these systems, to realize the full endpoint stiffness matrix the implementation of cross-joint stiffness must be taken into account in the robot design. An alternative solution can be provided by designing a hybrid controller which exploits passive and active control [83]. In order

to further investigate this problem, in this chapter, a human inspired control strategy is proposed.

Previous studies give evidence to coordinated stiffness variations across human arm joints in a static posture [3, 66] and as a result, angular changes of the endpoint stiffness ellipsoid is severely limited. In such situation, secondary but dominant control strategy which exploits self-selected postures takes role and modifies the endpoint impedance profile to meet task needs [45]. Inspired by the superior interaction performance of the human arm achieved through the regulation of common mode stiffness and self-selected posture, we suggest and design a controller which regulates the common mode stiffness across the joints in addition to a nullspace controller which further minimizes the error between desired and realized endpoint stiffness.

Let K_c be the vector of common stiffness across the joints. Inspired by the correlation of stiffness changes in human arm joint as result of co-contractions, we consider a constant scaling factor across all joints as follows

$$K_s = J(q)^T K_h J(q) \quad (5.1)$$

where J denotes the manipulator Jacobian, q is the vector of joint angles and $K_h \in \mathbb{R}^{6 \times 6}$ is the human endpoint stiffness. The diagonal matrix $K_s \in \mathbb{R}^{n \times n}$, with n number of joints in robot, will be calculated and normalized once and used for the rest of controller design. As a result $K_c = k_{cms} K_s$ where k_{cms} is optimized common mode stiffness in each time step. One may also consider optimization of constant joint scales (K_s) based on application and task needs.

In order to realize the desired endpoint stiffness matrix (K_h) provided by teleimpedance algorithm, the following equation must be satisfied ideally

$$K_h \simeq (J^+)^T K_c J^+ \quad (5.2)$$

where J^+ denotes the pseudo-inverse, generally given by

$$J^+ = D^{-1} J^T (J D^{-1} J^T)^{-1}$$

with D being a positive definite matrix. For the given problem we set $D = K_c$ as a metric tensor in the pseudo-inverse [99]. In this case if we take the time derivative of the Eq. (5.2), we will get

$$\begin{aligned} \dot{K}_h &\simeq [(J^+)^T K_s \dot{J}^+ + (\dot{J}^+)^T K_s J^+] k_{cms} \\ &+ [(\dot{J}^+)^T K_s J^+] \dot{k}_{cms} \end{aligned} \quad (5.3)$$

where two terms in first bracket of Eq. (5.3) being each others transpose. Definition of derivative of the pseudo-inverse of jacobian in symbolic equation is problematic due to its complexity. However, based on a proven theorem [134], we can establish the derivative of pseudo-inverse of Jacobian matrix as follows

$$\begin{aligned}\frac{dJ^+}{dt} = & -J^+ \frac{dJ}{dt} J^+ + J^+(J^+)^T \frac{dJ^T}{dt} N_J^\perp \\ & + {}_J N^\perp \frac{dJ^T}{dt} (J^+)^T J^+\end{aligned}\quad (5.4)$$

where N_J^\perp and ${}_J N^\perp$ are the projectors on the orthogonal complement of the column and row space of J , respectively.

Equation (5.3) can be factorized with respect to \dot{q} . Therefore, by reshaping the equation in vector form through the operator $\text{vect}(\cdot)$ (the operator extracts the 21 independent elements of 6×6 symmetric matrix), we get

$$\begin{aligned}\text{vect}\{\dot{K}_h\} \simeq & \text{vect}\{k_{cms}[(J^+)^T K_s A_q + A_q^T K_s J^+]\} \dot{q} \\ & + \text{vect}\{[(J^+)^T K_s J^+]\} \dot{k}_{cms}\end{aligned}\quad (5.5)$$

where $A_q = \frac{dJ}{dq}$. To simplify the expressions we can introduce $J_q \stackrel{\text{def}}{=} \text{vect}\{k_{cms}[(J^+)^T K_s A_q + A_q^T K_s J^+]\}$ and $J_k \stackrel{\text{def}}{=} \text{vect}\{[(J^+)^T K_s J^+]\}$. Therefore we can write

$$\dot{K}_h = J_q \dot{q} + J_k \dot{k}_{cms}\quad (5.6)$$

Now, if we take into account that \dot{q} is allowed to vary in the nullspace of J , while complying with the prescribed motion of the end-effector, then we can write

$$\dot{q} = J^+ K_p e_p + N_J^\perp \dot{\lambda}\quad (5.7)$$

where K_p is the gain matrix for Cartesian position error e_p and $\dot{\lambda}$ a free parameter controlling the nullspace velocity component. Above expression is a classical inverse kinematics problem, based on the pseudo-inverse of the Jacobian. Now, combining Eqs. (5.7) and (5.6) we get

$$\dot{K}_h = J_q (J^+ K_p e_p + N_J^\perp \dot{\lambda}) + J_k \dot{k}_{cms}\quad (5.8)$$

Defining $\dot{\tilde{K}}_h \stackrel{\text{def}}{=} \dot{K}_h - J_q J^+ [K_p e_p]$ and $J_\lambda \stackrel{\text{def}}{=} J_q N_J^\perp$, we can write

$$\dot{\tilde{K}}_h = [J_\lambda \ J_k] \begin{bmatrix} \dot{\lambda} \\ \dot{k}_{cms} \end{bmatrix} =: J_y \dot{y}\quad (5.9)$$

Above equation resembles the structure of inverse kinematics problem of defective robots, since we are dealing with the tracking of $\dot{\tilde{K}}_h \in \mathbb{R}^{21}$ by using k_{cms} and degrees of kinematic redundancy. Now, by defining the vectorial stiffness error

$e_s = \text{vect}\{K_h - k_{cms}[(J^+)^T K_s J^+]\}$, we can set up classical update laws. Consequently, by exploiting the update law based on the pseudo-inverse of J_y we get

$$\dot{y} = J_y^+ [\tilde{K}_h + K_{ps} e_s], \quad (5.10)$$

where K_{ps} is the gain associated to the stiffness error e_s .

5.1.1.1 Stability Analysis

To evaluate the convergence of the above algorithms,¹ we can introduce a Lyapunov candidate

$$V = \frac{1}{2} e_s^T K_{ps} e_s. \quad (5.11)$$

With positive definite and symmetric K_{ps} , the function will be positive definite in e_s . Time derivative of the function is

$$\dot{V} = e_s^T K_{ps} \tilde{K}_h - e_s^T K_{ps} J_y \dot{y}. \quad (5.12)$$

By inserting the control law from Eq. (5.10), we obtain

$$\dot{V} = e_s^T K_{ps} (I - J_y J_y^+) \tilde{K}_h - e_s^T K_{ps} J_y J_y^+ K_{ps} e_s. \quad (5.13)$$

In Eq. (5.13), we can easily recognize some interesting properties of the two terms. Since $J_y J_y^+$ is a projector onto the range space $\mathcal{R}(J_y)$ of J_y , it has the same column space as J_y , that is $\mathcal{R}(J_y J_y^+) = \mathcal{R}(J_y)$. In fact, a simple SVD decomposition of J_y in the form $J_y = USV^T$, with $U = [u_1 \ u_2 \ U_n]$, where u_1 and u_2 are the unit orthogonal vectors that form a basis for $\mathcal{R}(J_y)$, results in $J_y J_y^+ = u_1 u_1^T + u_2 u_2^T$. This also makes clear that there are two positive and unitary eigenvalues, corresponding to the eigenvectors u_1 and u_2 , and the zero eigenvalue with multiplicity equal to $\dim(\mathcal{N}(J_y^T))$ along the orthogonal complement $\mathcal{N}(J_y^T) = \mathcal{R}(U_n)$.

This indicates that the second term is negative definite as long as $K_{ps} e_s \in \mathcal{R}(J_y)$, and it vanishes when $K_{ps} e_s \in \mathcal{N}(J_y^T)$. On the contrary, the projector $(I - J_y J_y^+)$ is such that the first term vanishes when $\tilde{K}_h \in \mathcal{R}(J_y)$ (it is worth observing that $\mathcal{N}(I - J_y J_y^+) = \mathcal{R}(J_y)$), while being different from zero with unspecified sign otherwise. Therefore, we can conjecture that if the time dependent term \tilde{K}_h is dominated by the second term (in the cases when $K_{ps} e_s \notin \mathcal{N}(J_y^T)$), then $\dot{V} < 0$ and the local asymptotic tracking is guaranteed.

¹Concerning our experimental setup, we simplify the analysis to two degrees of redundancy. However, the analysis can be performed in general case. Alternative solution can be proposed by using Jacobian transpose instead of pseudo-inverse in Eq. (5.10).

5.1.2 Minimum-Effort Controller

The proposed minimum effort null-space controller minimizes the effect of gravity loading on the robotic joints in reaching phase. Therefore, a cost function which incorporates joint torques as result of joint masses and the payload is defined as follows

$$C_g(q_e) = \tau_g^T W \tau_g, \quad (5.14)$$

where W , q_e and τ_g denote constant diagonal weighting matrix, vector of joint angles and configuration dependent gravity vector, respectively. Accordingly, concerning static conditions (relatively small endpoint velocity), the gravitational torque vector of the joint masses and the payload is obtained as follows

$$\tau_g = \sum_{i=1}^n J_{com_i}^T m_i g, \quad (5.15)$$

where m , n and g denote the joint mass (including payload), number of joints and vector of gravitational accelerations, respectively. J_{com} represents the modified manipulator Jacobian and provides the relationship between joint torques and the gravitational forces, acting on the center of mass of each joint. The modified manipulator jacobian was calculated for each center of mass of the robot joints and the payload.

Optimization of above cost function (Eq. (5.14)) subject to task constraints is performed by projecting the gradient of the cost function C_g onto the null space of the manipulator Jacobian (J) [91]. Therefore we obtain

$$\dot{q}_e = J^+(q_e)\dot{x} + [I - J^+(q_e)J(q_e)]\nabla_{q_e} C_g(q_e), \quad (5.16)$$

where J^+ and ∇ are the Jacobian pseudo-inverse and the gradient function, respectively. By satisfying above condition in iterative way, null-space configuration will be adapted in order to minimize the joint mass and payload gravity torque, which in the meanwhile asymptotic stability is guaranteed [91].

Similar technique can be applied for a reaching phase which will be followed by payload pickup phase, since the algorithm provides minimum-effort kinematic solution among all possible postures.

5.1.3 Soft Switching Logic

In order to choose the task-related policy among minimum-effort and CMS-CDS controllers, a priority based decision rule is implemented. In the first phase of the proposed teleimpedance control, in which the human guides the robot's end-effector in free space, the minimum-effort null-space controller will be held responsible for

control of degrees of kinematic redundancy, subject to dictated task constraints. Once the robot comes in a contact with the environment, if the interaction forces raise above a predefined value, the CMS-CDS controller takes role and q_c will be applied (q_e and q_c are estimated joint angles corresponding to the minimum-effort and CDS controllers which are calculated by Eqs. (5.16) and (5.7), respectively). In order to produce smooth angular trajectories, a priority based soft-switching technique is defined as follows

$$q = \begin{cases} q_e, & |F_I| \leq F_0 \\ \xi q_c + (1 - \xi)q_e, & F_0 < |F_I| \leq F_c + F_0 \\ q_c, & |F_I| > F_c + F_0 \end{cases} \quad (5.17)$$

where F_0 and F_c represent the predefined forces due to noise/acceleration and minimum contact force, respectively. F_I is formed by integration of the forces over all directions and ξ is a function of force defined by

$$\xi = \frac{F_I - F_0}{F_c}. \quad (5.18)$$

5.2 Experiments

In this section, we evaluate the effectiveness of the bimodal, bio inspired controller in a peg-in-hole task, as a classical benchmark for spatial planning with uncertainties. As mentioned previously, the performance of the proposed methodology relies on the number of degrees of kinematic redundancy. In our experimental setup, a KUKA robotic arm with 7 joints is employed. Therefore, by taking into account a fully constrained task, only 1 degree of kinematic redundancy will be utilized for the analysis. A payload (due to the peg, FT sensor and the flange masses) was considered at the end-effector of the robot. The experimental setup and information flow are shown previously in Fig. 4.1.

*In our first experimental setup,*² KUKA robot joint angles were commanded to an initial configuration (posture A in Fig. 5.1). Following that, the minimum-effort controller drives the robot's null-space configuration towards configuration B in which the effect of gravitational torque in robot joints is minimized. Then, the operator inserts the peg into the hole by pressing the hole along the direction of the peg. In this phase, the switching logic attributes the high priority to the CMS-CDS controller, as a response to the raise of the interaction forces. Consequently, the CMS-CDS con-

²Comparative analysis of the stiffness matrix is generally performed by stiffness ellipsoids. However, such graphical presentation is troublesome in time-varying case. For this reason, in this work, experiments are divided in two parts with constant and time-varying desired stiffness profiles. In later case, the analysis is performed by observing the interaction forces and defining related indexes. A video of the experiment is available at [24]. Original teleimpedance video links are also provided [2, 3].

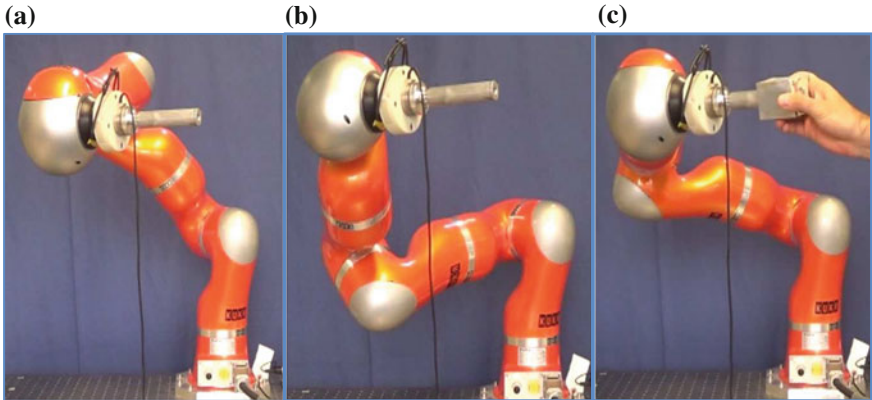


Fig. 5.1 KUKA robot in initial joint configuration (a), under minimum-effort (b) and CMS-CDS (c) null-space controllers

troller drives the robot in configuration C in which the error between the desired full stiffness matrix and the one realized at the KUKA's end effector is minimum. In this particular experiment, a fixed, symmetric and positive definite full stiffness matrix was chosen as desired one for the CMS-CDS controller. The stiffness matrix was chosen in such a way that the realized stiffness at the end effector of the robot, was high enough to overcome frictional forces between the peg and the hole.

Normalized min-effort and CMS-CDS cost functions (upper plot), interaction forces (mid plot) and joint angles (lower plot) from the experiment are depicted in Fig. 5.2. As it can be seen in the upper plots, once the priority based soft switching logic is turned on ($t \simeq 1$ s), the minimum-effort null-space controller takes over and reduces C_g by approximately 22 % (see phase B). Such behaviour is being altered by the raise of the interaction forces ($t \simeq 7.7$ s). In this phase (see phase C), the realized stiffness ellipsoids (translational part), by means of different stiffness control strategies (Cartesian (which also denotes desired stiffness profile), CMS-CDS and only CMS controllers) are demonstrated in Fig. 5.3. The 3D stiffness ellipsoids are projected in three planes. Effective changes in the orientation of the realized stiffness ellipsoid are seen once the CDS is combined with CMS (even by holding only 1 degree of kinematic redundancy in fully constrained task) which lead to 11.2 % reduction in the norm of the stiffness error. Obviously, by adopting adequate degrees of redundancy (e.g. reducing the position/orient constraints or exploiting sufficiently redundant robots), the error will decrease significantly. In addition, as shown in the lower plots of Fig. 5.2, the priority based soft-switching technique generates smooth angular changes in the transient phase. A video of the experiment is available at [24].

Second experimental setup concerns with the peg-in-hole task in a teleoperation scenario. The operator was asked to move his/her hand in the space to reach the reference configuration (where the stiffness model is calibrated), and finally to teleoperate the robot to insert the peg in the fixed hole. The master had visual feedback

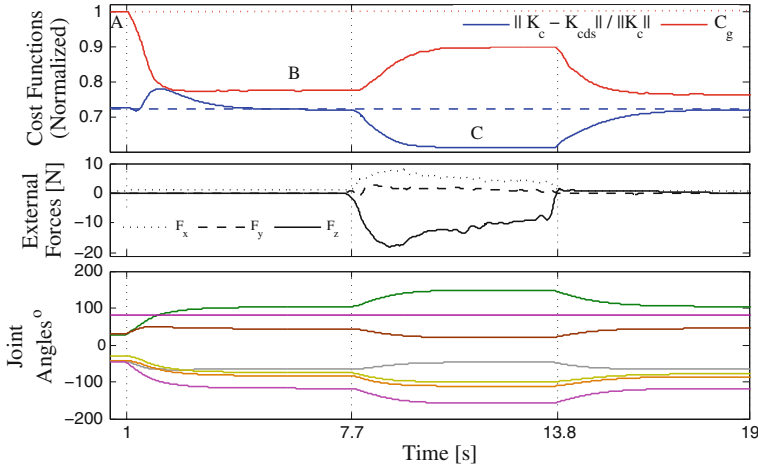


Fig. 5.2 Normalized minimum-effort and CMS-CDS cost functions (*upper plot*), controlled by priority based soft switching logic. Interaction forces and joint angles are shown in *middle* and *lower plot*, respectively. A, B and C phases correspond to initial, minimum-effort and CMS-CDS joint configurations in Fig. 5.1. Dotted (red) and dashed (blue) horizontal lines in *upper plot* represent the min-effort and CMS-CDS cost functions without proposed control of kinematic redundancy

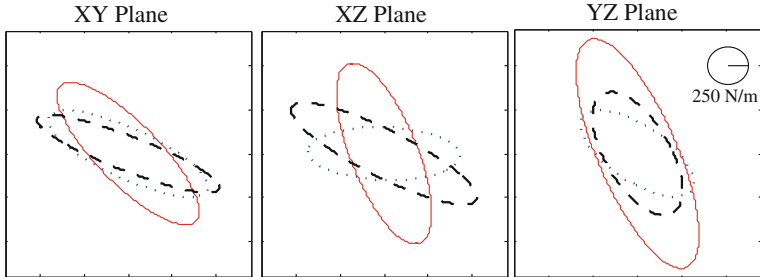


Fig. 5.3 Robot endpoint stiffness ellipsoids (translational) replicated by teleimpedance under Cartesian stiffness (*solid line*), CMS-CDS (*broken line*) and only CMS (*dotted line*) controllers in interaction phase. Cartesian stiffness ellipsoids coincide with the desired ones

from the slave arm, including the peg and hole. No peg was hold by the master, nor did he receive any feedback except visual. Body markers were attached to the wrist in order to provide the reference trajectory for robot motion. The robot base frame was considered as the overall reference frame for other frames (Optitrack and FT sensor). The position and orientation path of the human wrist was measured, low-pass filtered (cutoff 15 Hz) and used for trajectory planning. Incremental joint position references were sent to the robot, derived from the position tracking errors in six dimensions (e_p). This approach was used to cope with drift and tracking inaccuracy due to possible delays between reference commands and generated movement

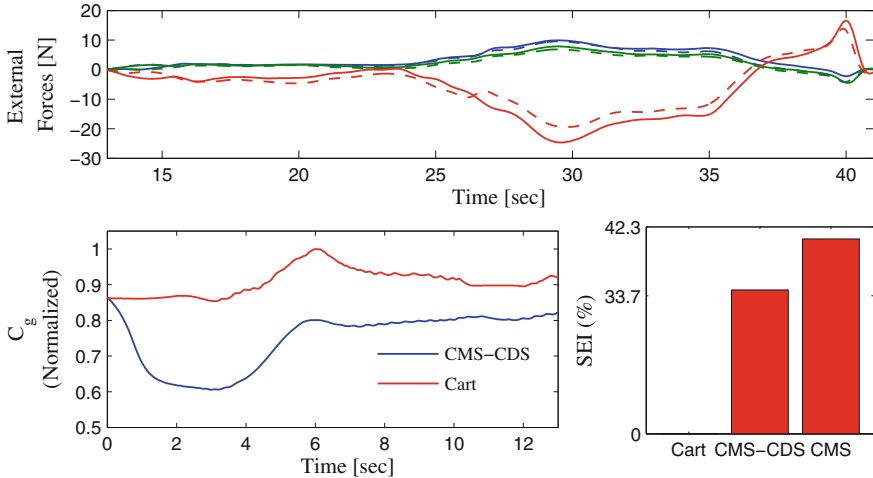


Fig. 5.4 Comparative analysis of Cartesian (Cart), CMS-CDS and only CMS controllers. Interaction forces along x (blue), y (green) and z (red) for Cartesian (solid line) and CMS-CDS (dashed line) are shown in upper plot. Lower-left plot displays the effect of min-effort controller in defined cost function (C_g) during movement in Cartesian and CMS-CDS experiments. Lower-right plot compares the SEI index for experiments under Cartesian, CMS-CDS and only CMS controller

in the slave end-effector. Software interfaces, sampling frequencies (processing and control), and hardware specifications are all identical to those reported in Chap. 4.

Throughout the first phase of the experiment, the master's arm endpoint stiffness profile (estimated translational and fixed rotational as discussed in Chap. 3) along with the equilibrium trajectories were replicated in KUKA, in real-time, by means of original teleimpedance algorithm (Cartesian impedance controller, Chap. 4). The diagonal elements of the rotational part of stiffness matrix were set to 20 N m/rad .

Recorded trajectories during the whole experiment were used as reference for the comparative analysis of the proposed controller. This approach was used in order to match the equilibrium path of both controllers (CMS-CDS and Cartesian) in interaction phase, while evaluating the effect of min-effort controller in reaching phase. Figure 5.4 demonstrates the comparative analysis of described experiments. Upper graph displays the interaction forces between the peg and the hole under Cartesian and proposed CMS-CDS control. As seen in the plots, the realized forces by two controllers are comparable. Since the equilibrium path are chosen to be the same, similarity between the interaction forces will give evidence to the approximate similarity between the realized stiffness profiles by means of both controllers. In addition, in order to numerically compare the realized stiffness error between the Cartesian and proposed controller, we define a stiffness error index as follows

$$SEI = \frac{1}{K_{cmax} - K_{cmin}} \frac{\sum |K_{realized} - K_c|}{n_p}, \quad (5.19)$$

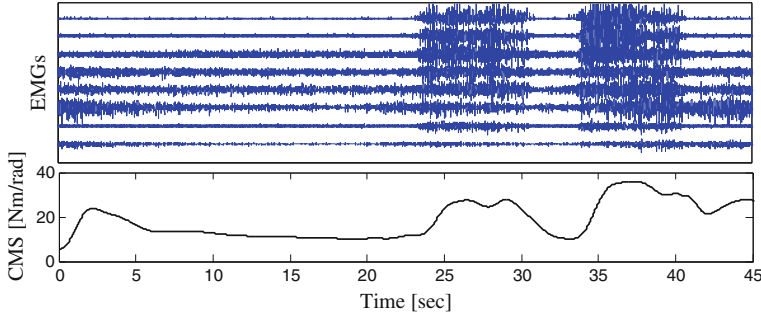


Fig. 5.5 Muscular activities (*upper plot*) and resulting common-mode-stiffness (CMS) in CMS-CDS experiment (*lower plot*)

with n_p being the number of data points. The above index was calculated for Cartesian, CMS-CDS and only CMS controllers for the same equilibrium path and desired stiffness profile. The average value of the calculated indexes along x , y and z directions are provided in Fig. 5.4, lower right plot. As seen in the graphs, while Cartesian controller flawlessly tracks the desired stiffness profile, application of CDS controller results in notable amount of reduction in tracking error compared to only CMS case, even by holding only 1 degree of kinematic redundancy. Results of effective reduction of gravitational torques in robot's joint due to min-effort controller in reaching phase are demonstrated in the same figure, lower left plot.

EMG variations of human arm muscles during the insertion and pull-off phase are brought in Fig. 5.5, upper plot. As noted above, during the interaction phase of the original teleimpedance algorithm, the stiffness profile of the human arm endpoint in reference posture is estimated and applied based on EMG signals. This time-varying stiffness profile and the equilibrium path are used as references for our proposed CMS-CDS controller. Lower plot in Fig. 5.5 demonstrates the estimated common-mode-stiffness profile in CMS-CDS experiment, with the reference stiffness profile extracted from the original teleimpedance experiment.

It is worth noting that inspired by observations in human arm impedance regulation mechanism, the purpose of this study was to explore the single stiffness synergy across the arm joints. However, one may consider increased number of controlled joint stiffness values (CMS) to possibly improve stiffness tracking performance. Eventually, our proposed CDS controller will be adopted to further reduce the error between the desired stiffness matrix and the one realized at the robot endpoint. Such scenario will provide the possibility of design and control of robotic arms with $n + m$ actuators, with n and m being number of joints and stiffness synergies, respectively (where in this work $m = 1$).

5.3 Conclusions

In this chapter, inspired by neuromotor strategies for movement and interaction efficiency, a bimodal controller, which consisted of minimum effort and CMS-CDS teleimpedance controllers, was developed. The initial teleimpedance algorithm [2, 3] provides the robot with the task-related human impedance combined with the position/orientation trajectories. This reference command is being executed under classic Cartesian impedance control. However, in the proposed multiple-criteria controller, the minimum-effort controller will minimize the effect of gravity loading on the robotic joints in reaching phase, while during the interaction with uncertain environment, the CMS and CDS are simultaneously adapting relying on the error between time-varying human's endpoint stiffness and the one, realized at robot's end-effector. The design of CMS-CDS controller was inspired by CNS policies in order to make up for imposed limitations by multi-joint impedance regulation mechanism. A priority based soft switching logic was developed to attribute the high priority to the task-suitable cost, while assuring the smoothness of the joint angles in switching phase. The energy-efficiency and interaction performance achieved highlights the possibility of adopting such sophisticated human-like strategies in humanoid robots or the ones with adequate degrees of redundancy, in order to accomplish tasks in a certain class of robotic manipulation.

Part II

Human-like Impedance Control

of a Dual-Arm Manipulator

Chapter 6

Natural Redundancy Resolution in Dual-Arm Manipulation Using CDS Control

In recent years the fast growing interest in versatility and flexibility of robotic systems working closely and interacting with humans in co-operative tasks or acting as assisting or prosthesis systems had led to the development of a wide range of systems: from full body humanoid robot co-workers to anthropomorphic manipulator prosthesis and exoskeleton systems aiming to aid and improve the life of humans with special needs. Apart from resembling the human body in terms of kinematics and physical appearance, and to increase their acceptability and compatibility, such systems should be also capable of generating motions that look natural and demonstrate similarities with those executed by humans. To achieve this, it is profitable therefore to incorporate in the motion control architecture of these systems human principles of motor control [132].

The goal is to obtain a good performance, while rendering a human-like natural motion, which is deemed to emerge as a consequence of the stabilization of some task-related criteria. To illustrate the underlying concept, examples of natural postures of the human while holding a cup or using a screwdriver are depicted in Fig. 6.1a and b, respectively. In these particular examples, subtask criteria are rooted in the concepts of minimum effort (6.1a) and impedance control (6.1b), which lead to the generation of corresponding configurations. Inspired by similar observations, the problem of redundancy resolution has been extensively addressed in the field of robotics by establishing task-related artificial potential fields [90, 91, 94], while, only few studies have drawn attention to the acquired human-like natural motion [132, 135, 136].

With the advent of higher demands on dual-arm manipulation [15–17], interaction with the environment using impedance control [76] became the focus of many studies in dual-arm systems. In this direction, object-level impedance control of cooperating robots has gained great attention due to the feasibility of controlling task forces/velocities while avoiding the occurrence of high internal forces [137]. In [138], an internal force based impedance controller has been proposed and its effectiveness was evaluated in an assembly task in a planar setup. Following that,

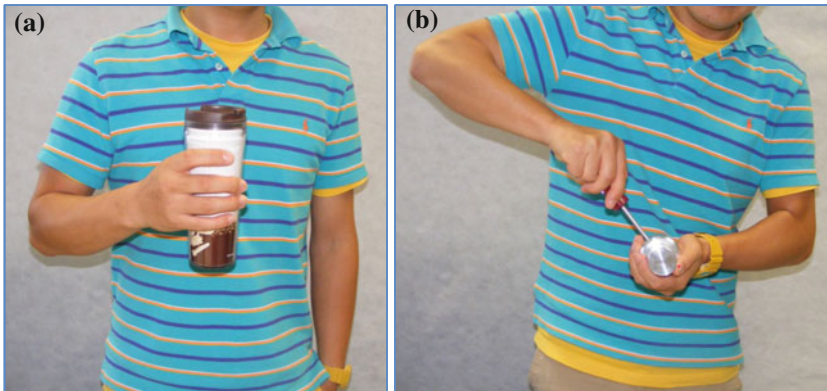


Fig. 6.1 Examples of acquired natural postures in humans as a consequence to the redundancy resolution for **a** minimum effort and **b** impedance control

Bonitz et al. [139] extended the aforementioned concept to a condition in which the dynamics of the object is not known. In [140], a decentralized impedance controller is proposed and its contact efficiency has been evaluated in an industrial setup, where two cooperating manipulators carry a common object. The authors in [137, 141] have presented object-level impedance controllers with coupling stiffness which is defined by a potential function. Even though such well-established techniques have successfully demonstrated their effectiveness through reliable handling of the contact, only few have highlighted the efficiency of the Cartesian impedance control through redundancy resolution [98, 99].

In this chapter, relying on the major contribution of the arm configuration to effectively regulate the directionality of the realized endpoint stiffness ellipsoid, and its low-cost nature [44, 45, 66], we explore the role of *configuration dependent stiffness* (CDS) control [4], for dual-arm object manipulation. Therefore, the joint variables are controlled in redundant space to realize a task-specific Cartesian stiffness profile. In addition, with the purpose of obtaining a good tracking performance while rendering natural movements, we incorporate the optimality principles in human motor control in the development of proposed impedance controller. In this direction, given the growing body of evidence in support of coordinated stiffening behavior of the arm joints in humans (e.g. see [2, 44, 45]), we utilize the concept of *common mode stiffness* (CMS) control. To establish this concept, we assume a correlated stiffening behavior among the joints of each robot. A real time optimization technique is then proposed to adjust the CMS and CDS variables and realize a desired Cartesian stiffness profile of the tool, w.r.t the object: While the CMS variations contribute to the modifications of the size of the realized stiffness ellipsoid (analogous to the role of co-contractions in human arm), CDS control will elongate the realized stiffness ellipsoid toward the desired Cartesian profile.

The effectiveness of the proposed controller is evaluated in a dual-arm assembly task. The acquired good tracking performance and similarities between the natural postures of the human operators and the ones realized by the robots illustrate the contact efficiency of the proposed algorithm, while highlighting the advantages of the integration of human motor principles in redundancy resolution of dual-arm manipulation. Therefore, utilization of similar motion control strategies in humanoids co-operating with humans or upper limb assistive exoskeleton or prosthesis devices can result in the generation of more natural motions improving the acceptability and compatibility of such devices.

6.1 Controller Design

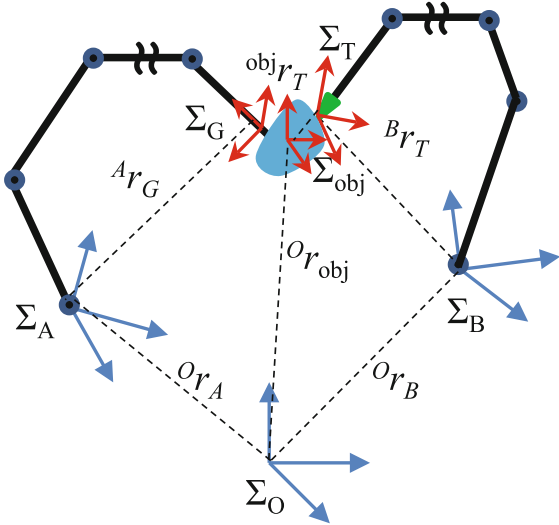
6.1.1 Dual-Arm Kinematics

Observations on human bimanual coordination suggest that the central nervous system (CNS) stabilizes the first synergy of the two cooperating arms to a larger degree (higher control levels) than if it did for control of each arm joints, separately. Indeed, as regards the human dual-arm activities in its most natural way, two hands cooperate in a way that they form a kinematic chain [142]: while the first synergy stabilizes the relative position/orientation of the two hands (as a dominant task requirement), lower hierarchical levels of control stabilize remaining task variables by controlling the redundant degrees of freedom [143, 144]. Above observations promote the idea of utilizing a similar kinematic representation in dual-arm robotic manipulation of the object to accommodate the stabilization of the task variables as well as rendering a natural redundancy resolution.

To that end, in our setup, a relative Jacobian is used which creates a unified, coordinated control between the two arms. Normally, the expression of the relative Jacobian combines the individual Jacobians of each arm, such that the resulting Jacobian maps the joint velocities of the two arms to the relative velocity between the end-effectors [145]. This allows users to directly specify the relative trajectory between the two end-effectors such that coordinating the trajectories of the two arms becomes an easy task. Such representation has been incorporated with force-guided control [146] and impedance control [147] as well.

The dual-arm manipulation setup is shown in Fig. 6.2. In our setup, $q_G \in \mathbb{R}^{n_A}$ and $q_T \in \mathbb{R}^{n_B}$ denote the joint variables of the manipulators A and B, respectively. Here, we assume that manipulator A is rigidly holding the object, while manipulator B is executing the defined task with the tool. The position vectors of the origins of gripper frame (Σ_G) and the tool frame (Σ_T) with respect to the base frames of the two manipulators (Σ_A and Σ_B) are denoted as ${}^A r_G$ and ${}^B r_T$, respectively. In addition, the position vectors of the origins of the tool and the object frame with respect to Σ_A and Σ_B are denoted as ${}^{\text{obj}} r_T$ and ${}^{\text{obj}} r_G$, respectively. According to [145], the transformation of the joint velocities $\dot{q} = [\dot{q}_G^T \ \dot{q}_T^T]^T \in \mathbb{R}^n$, onto the task

Fig. 6.2 Dual arm manipulation diagram



space linear and angular velocities $v = [{}^{\text{obj}}\dot{r}_T \ {}^{\text{obj}}\omega_T]^T \in \mathbb{R}^6$ is performed by the relative Jacobian, J_R , as follows

$$v = J_R(q)\dot{q}, \quad (6.1)$$

with $n = n_A + n_B$, where n_A and n_B denote the number of DoFs of the two manipulators.

6.1.2 Impedance Control of Dual-Arm

To establish the mapping between the forces acting on the tool, ${}^{\text{obj}}F_T$, referenced from the object frame, and the required joint torques, τ , we can exploit the principle of virtual work. Therefore, we can write

$$\begin{aligned} \Delta W_\tau &= \tau^T \Delta q, \\ \Delta W_F &= {}^{\text{obj}}F_T^T \Delta {}^{\text{obj}}x_T. \end{aligned} \quad (6.2)$$

with ΔW_τ and ΔW_F , denoting the work done by the joint torques and displacements, and forces acting on the object and relative displacement of the tool w.r.t. object frame of reference, $\Delta {}^{\text{obj}}x_T$, respectively. Now we can write

$$\tau = J_R^T(q) \ {}^{\text{obj}}F_T = J_R^T(q) \ K_c \Delta {}^{\text{obj}}\tilde{x}_T.$$

with $\Delta^{\text{obj}}\tilde{x}_T = {}^{\text{obj}}x_{Td} - {}^{\text{obj}}x_T$. On the other hand, to establish the stiffness mapping between the joint and Cartesian spaces, we employ the following expression [79],

$$K_J = \frac{\partial \tau}{\partial q} = \frac{\partial (J_R^T(q) K_c \Delta^{\text{obj}}\tilde{x}_T)}{\partial q},$$

The above equation can be written as follows, around the equilibrium position,

$$K_c = [J_R(q)(K_J - K_g)^{-1} J_R(q)^T]^{-1}, \quad (6.3)$$

where the diagonal elements of the joint stiffness matrix $K_J \in \mathbb{R}^{n \times n}$ are formed by the diagonal elements of the joint stiffness matrices of the two robots (K_{J_G} and K_{J_T}). Here, we assume that all joint stiffness matrices do not have coupling terms, i.e. they are always of diagonal shape. The stiffness matrix K_c specifies the Cartesian stiffness profile which is defined with respect to Σ_G , and $K_g = \frac{\partial J_R^T(q)}{\partial q} {}^{\text{obj}}F_T \in \mathbb{R}^{n \times n}$, captures the effect of geometry in presence of external forces.

A very interesting outcome of the above relation is the definition of the desired Cartesian stiffness (the Cartesian stiffness between Σ_T and Σ_{obj})¹ in relative coordinates. This means that the need for transferring the configuration-dependent, desired Cartesian stiffness matrices of the two robots with respect to the world frame to the task coordinates is simplified, thanks to the definition of the relative Jacobian. Such realization will be profitable for dual-arm asymmetric manipulation tasks using tools (e.g. carving, peeling, peg-in-hole, etc.) (Fig. 6.3) [142], since the specification of the task parameters in relative coordinates is more intuitive.

To realize the desired Cartesian stiffness matrix (by tracking 21 elements in the symmetric matrix K_{cd}), in absence of preload forces (i.e. $K_g = 0$), we differentiate the Eq. (6.3) w.r.t. time as follows²:

$$\begin{aligned} \dot{K}_c = & -K_c \left[\frac{dJ_R(q)}{dt} K_J^{-1} J_R(q)^T + J_R(q) \frac{d(K_J^{-1})}{dt} J_R(q)^T \right. \\ & \left. + J_R(q) K_J^{-1} \frac{dJ_R(q)^T}{dt} \right] K_c, \end{aligned} \quad (6.4)$$

with the first and the last terms of the above equation being the transpose of each other. To that end, if we take into account that \dot{q} is allowed to vary in the null-space of the relative Jacobian, while complying with the prescribed relative motion of the two end-effectors, we can write

$$\dot{q} = J_R^+ v + N_J \dot{\gamma}, \quad (6.5)$$

¹since Σ_G is considered rigidly attached to Σ_{obj} , the components of the stiffness matrix are expressed in Σ_{obj} .

²By taking into account that for a square and invertible matrix X , $\partial X^{-1} = -X^{-1}(\partial X)X^{-1}$.

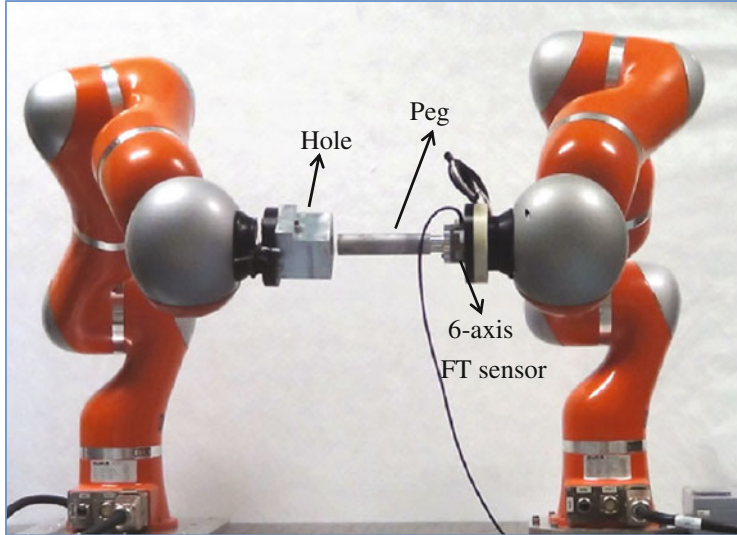


Fig. 6.3 Dual-arm assembly (peg-in-hole) setup

where J_R^+ denotes the pseudo-inverse of the relative Jacobian, $\frac{dJ_R}{dt} = \frac{dJ_R}{dq}\dot{q}$, and $N_J \in \mathbb{R}^{n \times n-6}$ is a basis of the nullspace projector $(I - J_R^+ J_R)$ of the relative Jacobian. $\dot{\gamma} \in \mathbb{R}^{n-6}$ is the vector of nullspace velocities, and $I \in \mathbb{R}^n$ is the identity matrix. Now, by combining Eqs. (6.5) and (6.4), and defining

$$\begin{aligned} P_1 &= \frac{dJ_R(q)}{dq} [J_R^+ v] K_J^{-1} J_R(q)^T \\ P_2 &= \frac{dJ_R(q)}{dq} [N_J \dot{\gamma}] K_J^{-1} J_R(q)^T \\ P_3 &= J_R(q) \frac{d(K_J^{-1})}{dt} J_R(q)^T \\ &= J_R(q) \dot{K}_J^{-1} J_R(q)^T, \end{aligned}$$

we can write

$$\dot{K}_c = -K_c [P_1 + P_2 + P_3 + P_1^T + P_2^T] K_c. \quad (6.6)$$

Now, if we decompose the nullspace velocity vector, we can write

$$\begin{aligned} \dot{\gamma} &= \begin{bmatrix} 1 \\ \bar{0}_{n-7} \end{bmatrix} \dot{\gamma}_1 + \cdots + \begin{bmatrix} \bar{0}_{n-7} \\ 1 \end{bmatrix} \dot{\gamma}_{n-6}, \\ &= I_{\gamma_1} \dot{\gamma}_1 + \cdots + I_{\gamma_{n-6}} \dot{\gamma}_{n-6}. \end{aligned} \quad (6.7)$$

Here, relying on the growing body of evidence in support of coordinated stiffening behavior of the arm joints in humans (e.g. see [2, 44, 45]), we explore the concept of common mode stiffness introduced in [4], in our dual-arm setup. Therefore, we assume that the joint stiffness values are controlled in a coordinated manner. To replicate similar behavior, we choose a constant diagonal scaling matrix, K_{scales} , (in descending order from base joint to the end-effector [63]) for each arm while introducing two independently controlled common mode stiffness values, k_{cms_1} and k_{cms_2} . Therefore we write:

$$\dot{K}_J = K_{\text{scales}_1} \dot{k}_{cms_1} + K_{\text{scales}_2} \dot{k}_{cms_2}. \quad (6.8)$$

By combining Eqs. (6.6), (6.7) and (6.8), while factoring w.r.t. the scalar nullspace velocities, $\dot{\gamma}_i$, and common mode stiffness changes, \dot{k}_{cms_i} , we define

$$\begin{aligned} J_{\gamma_i} &= \text{vec} \left\{ \frac{dJ_R(q)}{dq} [N_J I_{k_{J_i}}] J_R(q)^T + \sim^T \right\} \dot{\gamma}_i \\ J_{K_{cms_i}} &= \text{vec} \left\{ -J_R(q) K_J^{-1} K_{\text{scales}_i} K_J^{-1} J_R(q)^T + \sim^T \right\} \dot{k}_{cms_i} \end{aligned}$$

where the operator vec extracts the 21 independent elements of 6×6 symmetric matrix, and the symbol \sim denotes the same term, placed in the same set of brackets. Now, by defining $\dot{\tilde{K}}_c = \dot{K}_c + K_c [P_1 + P_1^T] K_c$, we can write

$$\text{vec}\{\dot{\tilde{K}}_c\} = [J_\gamma \ J_{K_{cms}}] \begin{bmatrix} \dot{\gamma} \\ \dot{k}_{cms} \end{bmatrix} =: J_y \dot{y}. \quad (6.9)$$

with $J_\gamma = [J_{\gamma_1} \ \dots \ J_{\gamma_{n-6}}]$, $J_{K_{cms}} = [J_{K_{cms_1}} \ J_{K_{cms_2}}]$, $\dot{\gamma} = [\dot{\gamma}_1 \ \dots \ \dot{\gamma}_{n-6}]^T$, and $\dot{k}_{cms} = [\dot{k}_{cms_1} \ \dot{k}_{cms_2}]^T$.

The above equation resembles the structure of inverse kinematics problem, in which we are dealing with the tracking of $\dot{\tilde{K}}_c \in \mathbb{R}^{21}$ by using common mode stiffness values, k_{cms} , and degrees of kinematic redundancy in a dual-arm setup. Now, by defining the vectorial stiffness error $e_s = \text{vec}\{K_{cd} - K_c\}$, we can set up classical update laws. Consequently, by exploiting the update law based on the pseudo-inverse of J_y we get

$$\dot{y} = J_y^+ [\text{vec}\{\dot{\tilde{K}}_c\} + K_{ps} e_s], \quad (6.10)$$

where K_{ps} is the gain associated to the stiffness error e_s . The proposed controller adapts the CMS (k_{cms}) and CDS (γ) related variables to realize a desired Cartesian stiffness profile, while complying with the desired motion of the tool w.r.t. the gripper frame of reference.

6.1.3 Task Prioritization

To execute a dual-arm manipulation task, the object must be held in a reasonable position, inside the workspace, w.r.t. the world frame of reference. This is accompanied by the desired relative motion of the tool w.r.t. the object frame, and cost-efficient motion of the remaining degrees of freedom in dual-arm kinematic chain. Therefore, the task can be decomposed into subtasks with prioritized order of occurrence.

An efficient solution for stabilization of the task variables in prioritized order is presented in [91]. Following that, to preserve a desired position of the object w.r.t. the world frame, the first priority subtask is established as follows

$$\dot{q}_G = J_1^+ \dot{r}_1, \quad (6.11)$$

where $J_1 \in \mathbb{R}^{3 \times n_A}$ is the first-priority task Jacobian and $\dot{r}_1 \in \mathbb{R}^3$ is the velocity vector of the origin of the gripper frame.³ Our secondary subtask establishes the relative movement of the two end effectors and its kinematic relationship is defined by the relative Jacobian of the two cooperative manipulators (Eq. 6.1). Now, given the two subtasks, we setup the task-priority based kinematic control [91], as follows⁴

$$\dot{q} = J_1^+ \dot{r}_1 + \hat{J}_2^+ (\dot{r}_2 - J_2 J_1^+ \dot{r}_1) + (I - J_1^+ J_1)(I - \hat{J}_2^+ \hat{J}_2) \dot{\gamma}, \quad (6.12)$$

where I is the identity matrix, $J_2 = J_R$, $\dot{r}_2 = v$, and $\hat{J}_2 = J_2(I - J_2^+ J_2)$. To ensure robustness against kinematic singularities, we use the damped least squares inverse solution which is defined by $B^+ = B^T(BB^T + \lambda I)^{-1}$, with $\lambda \in \mathbb{R}$ denoting the damping factor [92].

The third term in above equation projects the vector $\dot{\gamma}$ (Eq. 6.9), into a subspace ($C \in \mathbb{R}^{n-9}$, assuming $n > 9$) which is formed by remaining DoF that do not affect any of the subtask variables, while, in the meantime decreases the error between the desired and realized relative stiffness profiles. Due to the fact that the proposed algorithm incorporates human impedance regulation principles in realization of the desired Cartesian stiffness profile, we expect to obtain similar performance and natural redundancy resolution as compared with the humans.

The proposed CDS controller can also be utilized for humanoid robots or upper body assistive devices with joints with fixed-passive stiffness values to fairly realize a desired Cartesian stiffness profile w.r.t. the object frame. In addition, once the concept of common mode stiffness is integrated in the hardware,⁵ the CDS controller can be adopted to further reduce the error between the realized and desired Cartesian stiffness profiles.

³Here we do not consider any constraints on the orientation of the first subtask.

⁴Such representation accommodates the incorporation of additional subtasks such as joint and torque limit avoidance etc.

⁵By designing robotic arms with $n + 1$ actuators, with n being the number of joints and 1 corresponding the actuator for modifying the stiffness of all joints in a coordinated manner.

6.2 Experimental Setup

The efficiency of the proposed approach to cope with contact stability issues while generating natural motions in redundant space is evaluated in a Peg-in-Hole task, a classical benchmark for spatial planning with uncertainties.

The dual-arm setup incorporated two seven DoF KUKA LWR, with DLR's Fast Research (FR) Interface [124]. A peg and a hole were designed and mounted on the end effectors of the two robots. To illustrate the capabilities of the proposed controller in effective modulations of the size and directionality of the realized endpoint stiffness in task coordinates, the hole was mounted along different (x, y and z) directions of Σ_G . Then, three different desired Cartesian, $K_{c_{des}}$, stiffness profiles (stiff along the direction of the hole, while realizing a compliant profile along other directions to avoid high interaction forces) were defined and tracked by our proposed controller. A 6-axis force and torque (F/T) sensor (ATIMini-45) was mounted in between the peg and the robot end effector to monitor the interaction forces. Performance analysis of the proposed algorithm was carried out considering the realized stiffness matrix error and normalized to the norm of $K_{c_{des}}$ as follows

$$e_K = \frac{\|K_c - K_{c_{des}}\|}{\|K_{c_{des}}\|}.$$

In addition, to provide a graphical representation of the stiffness profiles, the translational part of the realized and desired stiffness matrices were projected into xy , xz and yz planes of the object frame of reference, Σ_{obj} , resulting in three stiffness matrices ($K_{ij} \in \mathbb{R}^2$, $[i, j] = \{x, y, z\}$). Following that, the major axis α_{\max} , and minor axis α_{\min} , of the ellipsoids along with the major axis direction, φ_{ij} , were determined using singular value decomposition:

$$\begin{aligned}\varphi_{ij} &= \arctan 2(U_{\max_j}, U_{\max_i}) \\ \alpha_{\max_{ij}} &= [\mathbf{E}_{\max}(K_{ij}^T K_{ij})]^{\frac{1}{2}} \\ \alpha_{\min_{ij}} &= [\mathbf{E}_{\min}(K_{ij}^T K_{ij})]^{\frac{1}{2}},\end{aligned}$$

with \mathbf{E} denoting the eigenvalue operator and $K_{ij} = (USV^T)_{ij}$.

The joint damping values were all considered fixed $D_i = 0.7$ N s/m. The control and synchronization interface between the KUKA controllers and the six axis F/T sensor were developed in C++.

6.3 Results

Figure 6.4a demonstrates the natural posture of the human operator executing an assembly task. As observed here, the redundant DoFs in both arms are adapted to elongate the stiffness profile in the direction of the hole, to overcome the frictional

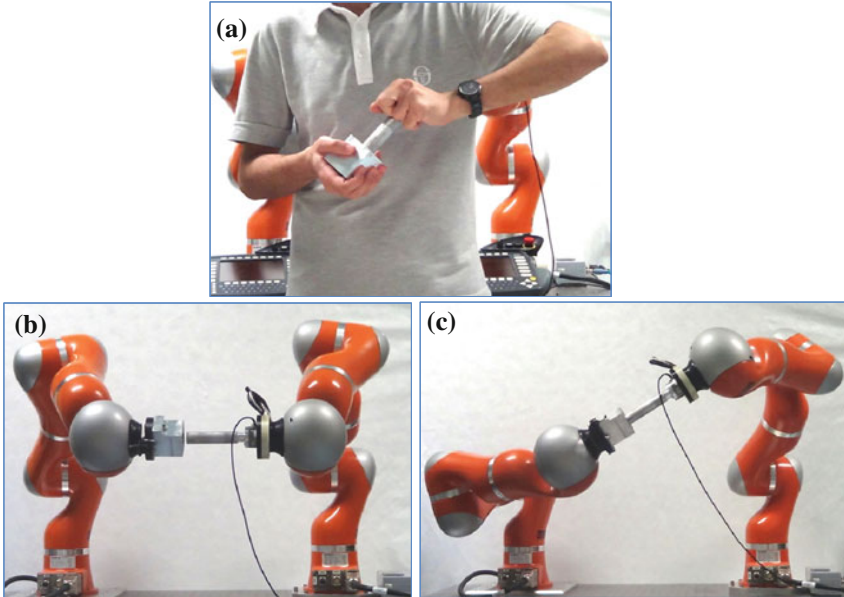


Fig. 6.4 **a** Human performing a bimanual peg-in-hole task. Initial configuration **b**, and realized configuration as a result of proposed controller **c**. Human and robots' ending configuration coincide which gives evidence to the similarity in control principles

forces, while rendering a compliant behavior in remaining directions to avoid high interaction forces.

The proposed algorithm establishes the real time tracking of the desired stiffness profile in relative coordinates through the optimization of the CMS and CDS. Starting from an initial configuration (Fig. 6.4b), the CDS control drives the redundant joints to a configuration (c) which is depicted in Fig. 6.4.

The desired (red, dashed) and realized (black, solid) ellipsoids are projected into the object's frame of reference and are depicted in Fig. 6.5. As seen in the plots, efficient elongation of the stiffness ellipsoid is perceived due to the CDS control. Figure 6.6 illustrates the adaptation of the CMS values of the two robots (most left and middle plots), synchronized with CDS control of the dual-arm setup. As a result, the error between the desired and realized stiffness ellipsoids is decreased in real time (Fig. 6.6, most right plot).

In another experiment, the hole was mounted along the y axis of Σ_G and the desired stiffness ellipsoid was defined to render a stiff behavior along the direction of the hole, while being compliant along other directions. Starting from an initial configuration depicted in Fig. 6.7b, the CDS control drives the redundant joints to a configuration which is depicted in Fig. 6.7c. Since the position of the hole is considered fixed, the CDS controller has maximally adjusted the configuration of the manipulator on the left, not to violate the constraints on the position of the hole. At the same

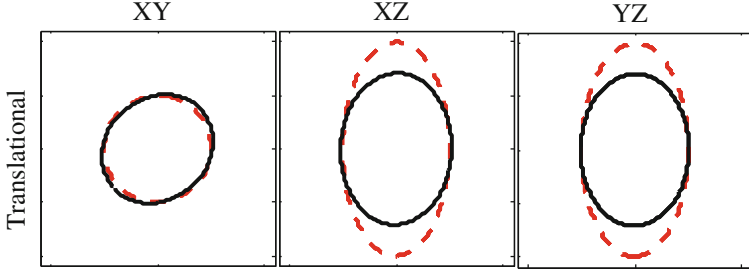


Fig. 6.5 Desired (red, dashed) and realized (black, solid) translational stiffness ellipsoids, corresponding to configuration c in Fig. 6.4. In this experiment, the translational stiffness matrix $K_{c_{des}} = [300, 300, 1000]$ N/m, is defined in relative coordinates. All off diagonal elements are set to zero. The hole is mounted along the z axis of Σ_G

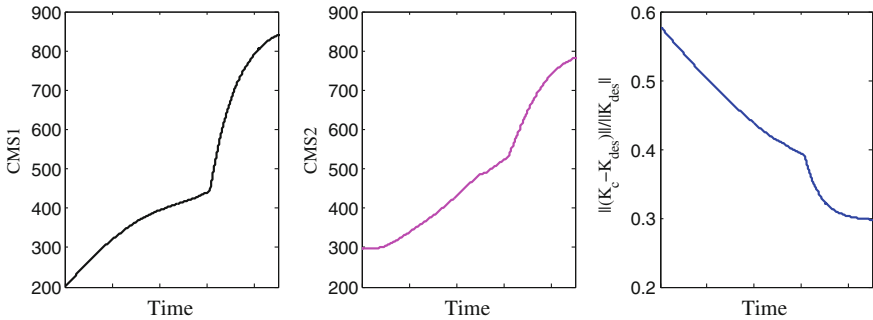


Fig. 6.6 Common mode stiffness parameters of the two robots (left and middle plots) are adapted in addition to the CDS to decrease the error between the desired and realized stiffness ellipsoids (most right plot), in real time

time, efficient control of the configuration of the manipulator on the right has been achieved. Similarities between the natural posture of the human operator (Fig. 6.7a), and the one realized by the proposed controller, once again, give evidence to the analogy between incorporated control principles. The normalize error between the realized and desired task stiffness profile was $e_K = 27\%$. This error includes all 21 elements of the stiffness matrices. Projected stiffness ellipsoids of this experiment are brought in Fig. 6.8.

Figure 6.9 illustrates the projected stiffness ellipsoids, as results of the tracking of different elongation of the desired stiffness ellipsoid in relative coordinates (the hole was mounted along x in this experiment). The CDS and CMS values are adapted to effectively align the realized stiffness ellipsoid with the desired one. This lead to the normalized error of $e_K = 30\%$.

Effective modulations of the size and the directionality of the realized stiffness ellipsoid in above examples illustrate the capabilities of the proposed controller in realization of the desired Cartesian stiffness profile. In addition, our proposed CDS

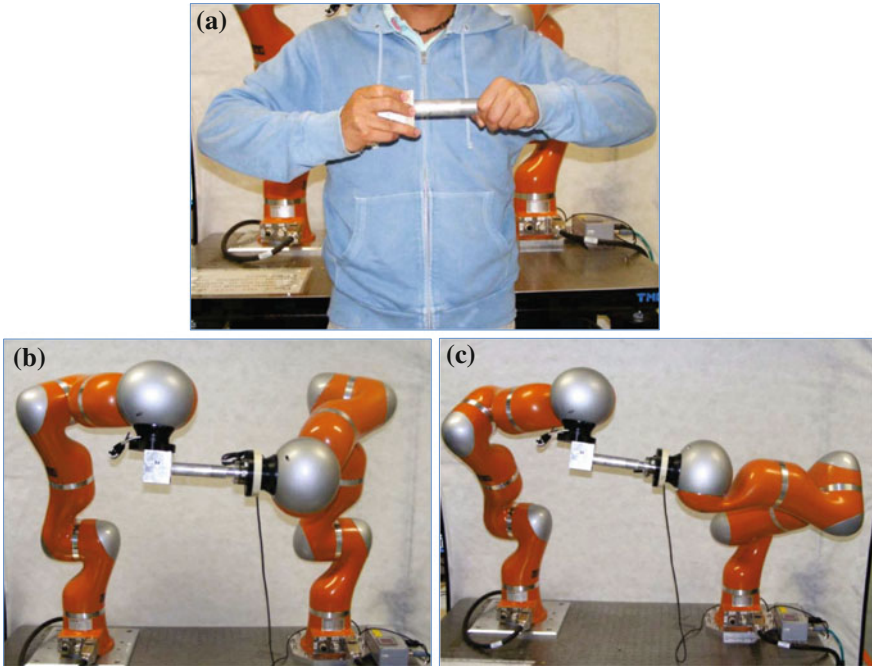


Fig. 6.7 **a** Human performing a bimanual peg-in-hole task. Initial configuration **(b)**, and realized configuration as a result of proposed controller **(c)**. The hole was kept in a fixed position (subtask one), while the orientation was allowed to change due to the CDS. Human and robots' ending configuration coincide which gives evidence to the similarity in control principles

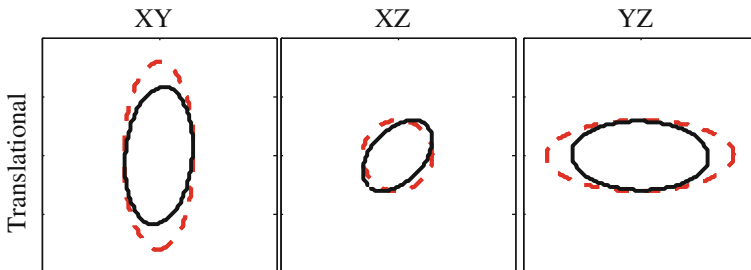


Fig. 6.8 Desired (red, dashed) and realized (black, solid) translational stiffness ellipsoids, corresponding to configuration in Fig. 6.4c. In this experiment, the translational stiffness matrix $K_{des} = [300, 1000, 300]$ N/m, is defined in relative coordinates. All off diagonal elements are set to zero. The hole is mounted along the Y axis of Σ_G

controller achieves a natural redundancy resolution of the dual-arm setup, which highlights its application in control of the humanoids or upper body assistive or prosthesis devices.

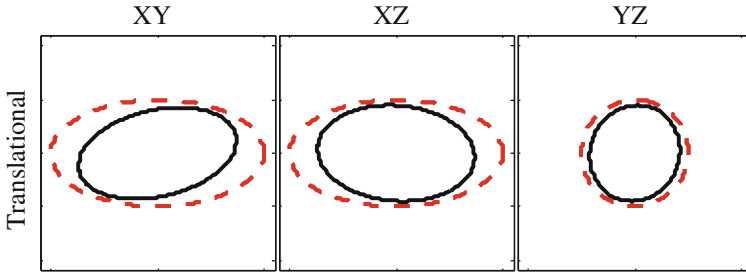


Fig. 6.9 Desired (red, dashed) and realized (black, solid) translational stiffness ellipsoids with different elongation w.r.t. Fig. 6.5. In this experiment, the translational stiffness matrix $K_{cdes} = [1000, 300, 300]$ N/m, is defined in relative coordinates. All off diagonal elements are set to zero

6.4 Conclusions

In this chapter we proposed a new on-line motion controller which regulates the Cartesian stiffness ellipsoid in a manner inspired by human motor control and impedance regulation principles. The presented scheme not only achieves effective task space stiffness control but also intrinsically performs redundancy resolution of the manipulator arm in a manner that results in the generation of natural motion resembling those executed by human in similar tasks. In particular, given the growing body of evidence on coordinated stiffening behavior of the human arm joints, two common mode stiffness (CMS) controllers were utilized. The CMS concept was introduced in our dual arm controller by changing the joint stiffness values of each robotic arm in a correlated manner. This allows to regulate the size of the realized Cartesian stiffness ellipsoid for each arm. Simultaneously, to align the realized stiffness ellipsoid with the desired one, we explored the concept of configuration dependent stiffness (CDS) in dual arm impedance control. Effectiveness of the proposed algorithm in efficient modifications of the realized size and directionality of the task stiffness ellipsoid, while generating natural movements, was evaluated in three assembly experiments. Implementation of the CMS-CDS controller resulted in good tracking performance, in addition to the generation of natural movements, similar to the ones realized by human operators.

Part III

Teleimpedance Control of a Robotic Hand

Chapter 7

A Synergy-Driven Approach to a Myoelectric Hand

The primary causes of amputation are trauma, disease, and war, the proportions of which are skewed towards the former two in developed countries and the latter in the developing world. It is estimated that one in 200 people in the United States have a missing limb [148], although global numbers are difficult to estimate [149]. Following amputation, an individual must overcome significant physical and functional loss as well as the psychological trauma of change in independence and appearance. Prostheses have emerged to help cope with these immense changes. Body-powered prostheses were created to restore function and have seen great advancements in the last century. These prostheses provide several benefits including functionality, robustness, and limited sensory feedback. The next generation of prostheses has seen the incorporation of electronic components controlled via electromyographic (EMG) signals from the muscles in the residual limb. These myoelectric prostheses can provide greater control of the hand and a more aesthetically pleasing appearance.

The most basic, and most common, myoelectric hands have a single degree of freedom (DOF) and incorporate various levels of control complexity. At a minimum, they offer on/off control and can be used by amputees with limited EMG signals. For users with more residual muscle and/or more control over those muscles, proportional controllers allow the user to vary grip force and/or grip speed relative to their EMG output, examples include the Hosmer myoelectric hand (Centri) or the DMC (Otto Bock). In a technological leap forward, new anthropomorphic hands have emerged. The i-limbTMultra (Touch Bionics, Inc) and the Bebionic 3 (RSL Steeper) are two of these that, while much more expensive than their basic counterparts, can adopt multiple realistic postures and grips. The trade-off of the increased DOFs and functionality is control complexity; the user must employ sequential contractions or co-contractions to select and operate the desired grip pattern.

Many different avenues of research are being pursued to improve on current commercial devices. One of these is employing complex machine learning algorithms to allow more natural control [18, 19, 150, 151]. This technique works well to classify a variety of postures in a lab setting, but depends on large training sets and few, if any,

have been rigorously tested outside of the lab. To accommodate a larger functional range, the control burden on both the controller and the user necessarily grows. In response to this burden, the Pisa/IIT SoftHand [152] was developed as a joint venture between the Centro Piaggio of the University of Pisa and the Advanced Robotics Department of the Italian Institute of Technology. The SoftHand borrows knowledge gained from neuroscience and motor learning to encode specific movement patterns, called synergies [153, 154], directly into the hand's hardware. The SoftHand actuates on the first synergy identified through Principal Component Analysis (PCA) of common hand movements, incorporating over 50 % of the natural variety of the hand, and providing flexibility in the grasp pattern to facilitate molding around grasped objects.

In this chapter, we introduce myoelectric control of the Pisa/IIT SoftHand. To do so, we harvest EMG signals from two electrodes placed on the proximal forearm, thus minimizing set up time and improving the likelihood the user will have sufficient muscle to control the device. From these two signals, we determine desired position as well as stiffness. As a result, the user can adjust the grasping motion as well as the compliance of the robotic hand in realtime. In order to improve control of the device and minimize the user's reliance on visual feedback, vibrotactile feedback proportional to grasping force was included. Here, the stiffness control and vibrotactile feedback features are evaluated against a simple position controller for ease of use and physical and cognitive load. Thus, the goal of this study is to provide proof-of-concept for a low cost, low cognitive load hand capable of grasping a variety of objects and withstanding harsher environments, while in Chap. 8, we elaborate on more sophisticated design of the controller, disturbance observer and feedback interfaces.

7.1 Materials and Methods

7.1.1 Overall Study Design

Four healthy, right-handed males participated in this study (mean age: 29.75 ± 2.01 years). Testing took place at the Istituto Italiano di Tecnologia and each testing session lasted roughly 45 min. Subjects lightly squeezed a ball to mimic grasping during which EMG signals from the finger flexors and extensors were used to control the grasping action of the SoftHand (Fig. 7.1). Subjects repeated a series of grasps four times: with and without impedance control and with and without vibrotactile force feedback. Our primary outcome measure was the number of successful grasps with each testing mode. Following completion of testing, subjects were asked to answer a short questionnaire to rate the ease of use of the device and control interface.

Fig. 7.1 Pisa/IIT SoftHand

7.1.2 The Pisa/IIT SoftHand

The Pisa/IIT SoftHand [152] (Fig. 7.1) was developed in a partnership between the Centro E. Piaggio of the University of Pisa and the Advanced Robotics department of the Istituto Italiano di Tecnologia in Genoa, Italy. The goal was to build a robust and safe hand at low cost, while simplifying some of the immense complexity of the hand through the use of synergies. Two design strategies were combined to achieve this result: soft synergies and underactuation. As previously mentioned, synergies are a motor control strategy that coordinates the articulation of the many joints of the hand into coherent movement patterns. By incorporating synergies into the hardware design, there is a risk of poorly approximating the object to be grasped and providing uneven force at the contact points. In soft synergies, introduced in [154], the synergy serves as a reference position for a virtual hand, thus enabling better control of the interaction forces between the hand and the grasped object through variation of the virtual hand position or the stiffness matrix connecting the virtual and real

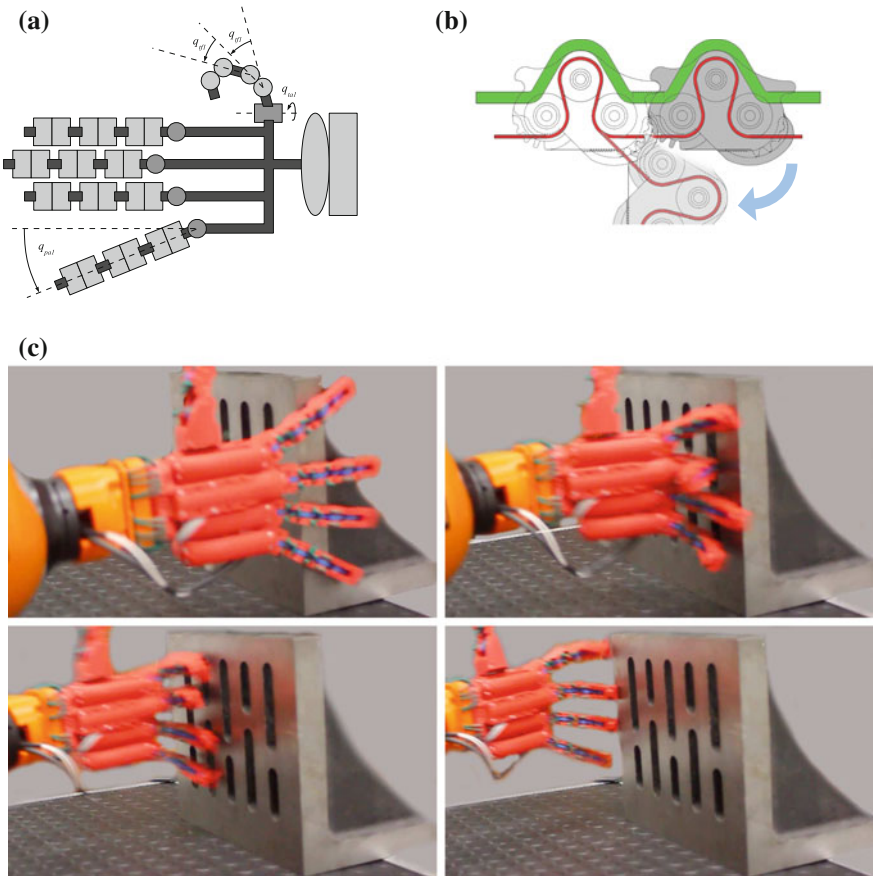


Fig. 7.2 A schematic of the hand, showing the revolute joints in *dark grey* and the rolling contact joints in *light grey* (a) and a side-view schematic of the rolling contact joint in (b). The sequence in (c) shows the hand before, during, and after impact with a stiff surface

hands. A fully actuated robotic hand introduces one actuator per degree of freedom (DOF), thus increasing weight, cost, and control complexity of the final device. Underactuation [155], however, reduces the number of actuators without reducing the number of DOFs and also imparting a quality of shape adaptability on the device. These two strategies were combined to produce an “adaptive synergy” design strategy incorporating the neuroscientific basis of soft synergies with the shape adaptability of underactuation.

Using the adaptive synergy approach, a humanoid hand was designed anthropomorphically with 19 DOFs, 4 on each of 4 fingers, and 3 on the thumb (Fig. 7.2a). At rest, the hand measures roughly 23 cm from tip of the thumb to the tip of the little finger, 23.5 cm from the wrist interface to the tip of the middle finger, and 4 cm thick at the palm. The fingers are capable of flexion/extension as well as ab/adduction. For

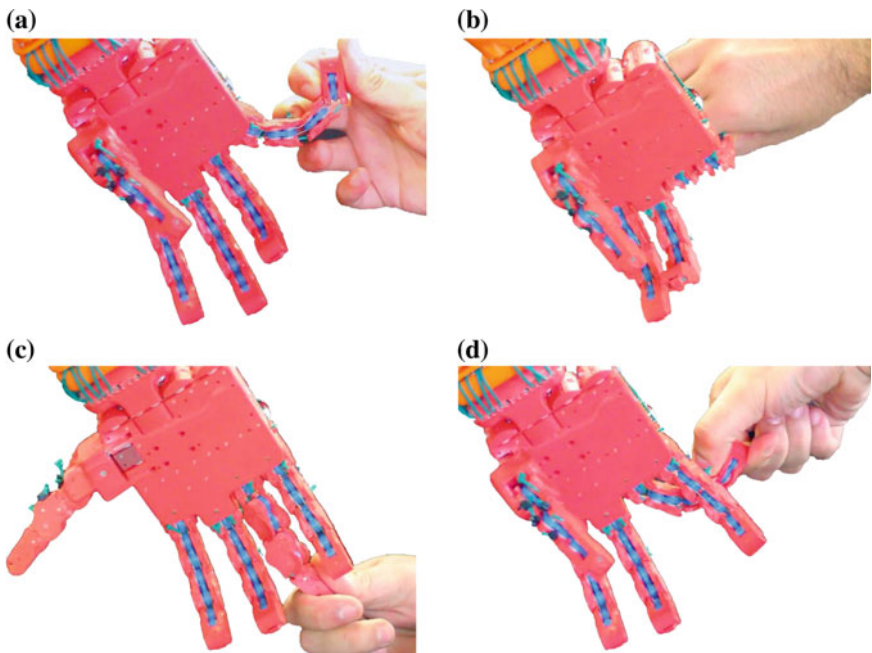


Fig. 7.3 The Pisa/IIT SoftHand joints can withstand severe forces in all directions, automatically returning to the correct assembly configuration. **a** Finger side bend. **b** Finger Back bend. **c** Finger Twist. **d** Finger Skew bend

ab/adduction of the fingers and at the equivalent of the carpometacarpal joint of the thumb (responsible for rotating the thumb from lateral pinch to C grasp, for example), traditional revolute joints were employed. One of the most important considerations in the design was safety: the hand must be robust enough to be of use to humans but also compliant enough to ensure safe interaction with humans. For this reason, a soft robotics approach was taken for the rest of the joints by incorporating rolling contact joints with elastic ligaments, as seen in Figs. 7.2b and 7.3. The rolling contact joints ensure anatomically correct motion when actuated but easily disengage on impact to allow safe interaction with humans while preserving the hand. The elastic ligaments also allow deformation while ensuring the hand returns to its original configuration (Fig. 7.2c). A single tendon runs though all joints to simultaneously flex and adduct the fingers upon actuation.

The hand is actuated by a single motor to move the fingers on the path of the first synergy [156] allowing the physical hand to mold around the desired object. The motor employed is a 6 Watt Maxon motor RE-max21 with an 84:1 gear reduction and a 12 bit magnetic encoder, resolution of 0.0875° (Austrian Microsystems AS 5045). The electronics board and battery pack are located in the back of the hand. In previous testing with a human interface [152], the hand was able to grasp a total of 107 objects spanning a wide variety of sizes, shapes, weights, and softness, including an

Table 7.1 Dimensions and weights of test objects

| Object | Water bottle | Screwdriver | Spray bottle | Ball |
|------------|---------------|---------------|---------------|--------------|
| Dims (mm) | 307 × 55 × 55 | 294 × 25 × 25 | 275 × 84 × 47 | 94 × 94 × 94 |
| Weight (g) | 250 | 50 | 500 | 500 |

AA battery, eyeglasses, drill, and phone. With the current motor, maximum holding torque is 2 N m and maximum holding force is roughly 20 N perpendicular to the palm.

7.1.3 Testing

Each participant attempted to grasp 4 objects: in order, a water bottle, a screwdriver, a spray bottle, and a ball. (See Table 7.1 for dimensions and weights of the tested objects.) These objects were selected to require various typical grasp shapes and represent various levels of softness and weight. Four modes of SoftHand operation were used: in order, Standard (no impedance control or vibrotactile feedback), Impedance mode, Vibrotactile mode, and combined Vibrotactile and Impedance mode (VI mode). Because this study involved healthy subjects, the SoftHand was attached to the arm by a platform strapped to the forearm. Subjects stood in front of a table and reached to an object. Successful grasp was achieved when the SoftHand held the object securely off the surface of the table. Each grasp was attempted 3 times, for a total of 12 grasps per mode over 4 modes, for an overall total of 48 grasps. Subjects were allowed a brief familiarization period with the device in each mode to minimize learning effects; mode and grasp order were fixed for all subjects as stated above.

7.1.4 EMG Processing

Double differential surface electromyography (EMG) electrodes were placed on the flexor digitorum superficialis (FDS) and the extensor digitorum communis (EDC) according to the methods outlined in [157] and were used in conjunction with the Delsys-Bagnoli 16 system (Delsys Inc.). A reference electrode was placed at the elbow. EMG signals were read into MATLAB Simulink (Mathworks, Inc.) using the Real-Time Windows Target feature of MATLAB. The incoming signal was filtered and rectified before being fed into the control scheme to determine user intent and required motor output and stiffness levels.

7.1.5 Control Architecture

The control algorithm (Fig. 7.4) was run in Simulink and communication with the hand as well as onboard sensing was achieved using QB Control (QB Robotics SRL), which provides embedded integrated control of dc motors and measurement of the rotary magnetic encoders and analog sensors. Prior to testing, subjects were asked to keep muscles at rest followed by repeated brief, forceful contractions. From these measures, we established minimum thresholds of activity and maximum contraction levels for scaling of the position reference and impedance signals. (Note: the goal was not to identify maximum voluntary contraction level but instead to set a comfortable maximum to allow control signal scaling for driving the SoftHand.) After filtering the EMG signals as described above, the amplitude was used to determine the position reference output to the motor. The gain used was set by the EMG amplitude maxima determined in the calibration process. Additionally, in impedance and VI modes, an index defined as a function of the sum of the FDS and EDC amplitudes was used to set the stiffness level. Therefore

$$\tau = K(FDS, EDC)[\theta_{ref}(FDS, EDC) - \theta_{msrd}], \quad (7.1)$$

with τ , θ_{ref} and θ_{msrd} denoting the torque synergy, EMG driven postural equilibrium reference and measured motor angular position, respectively. The stiffness gain, K , was set to a constant value in standard and vibrotactile modes. In impedance and VI modes, K varied with time as a function of the cocontractions. In these modes, as cocontraction increased, so did the stiffness of the device to mimic innate stiffness control. The block diagram of the control architecture is provided in Fig. 7.4.

Finally, when vibrotactile feedback was used, position error was multiplied by an experimentally-determined gain to control the voltage on a small (7×24 mm) vibration motor (Precision Microdrives Ltd.), placed on the back of the hand. Higher position error correlated to higher force, which was in turn proportional to the amplitude and frequency of vibrations, thus providing force-feedback information to the user. In the case of VI mode, the feedback was scaled to changes in the stiffness to provide standardized feedback throughout the testing (Fig. 7.5).

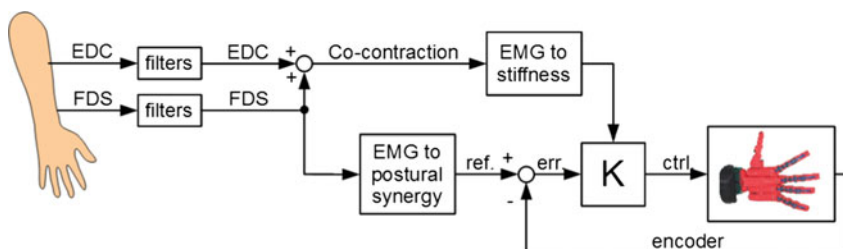


Fig. 7.4 Block diagram of the control pattern used to drive the Pisa/IIT SoftHand with myoelectric signals

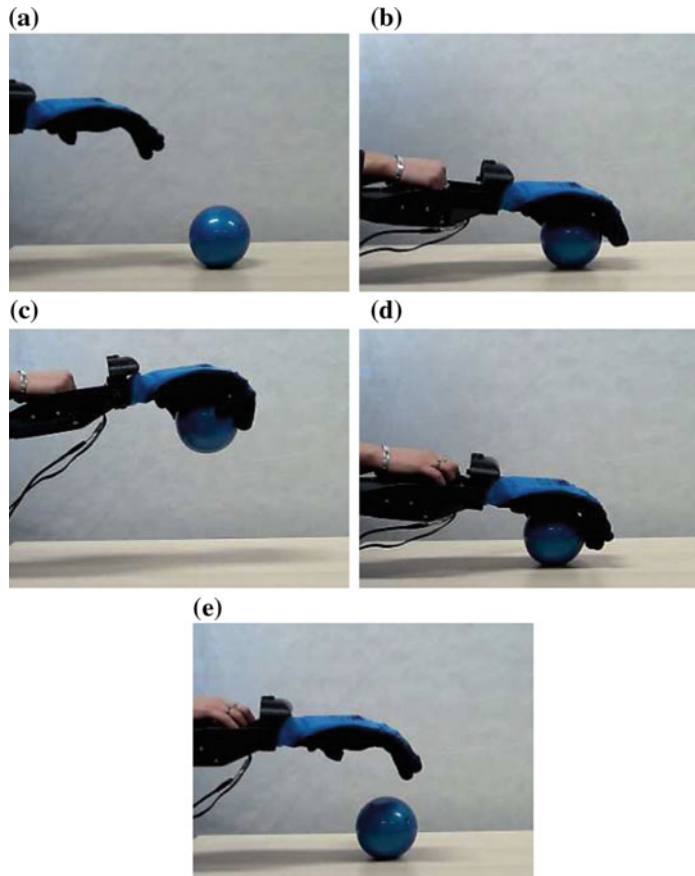


Fig. 7.5 Photographic sequence of a typical grasp. Five phases are noticeable: in order, **a** reach, **b** grasp, **c** lift, **d** release, and **e** withdraw

7.1.6 Questionnaire

Questionnaires were employed throughout the testing process to better evaluate the user-SoftHand control interface. Following operation of each mode, users were asked to rate the amount of physical and mental effort required to control the hand on a 5-point Likert scale. After concluding the grasping experiment, subjects were again asked to rate the overall amount of physical and mental effort as well as to agree or disagree with the following statements, again on a 5-point Likert scale: (1) The hand was easier to use in mode 2 (impedance). (2) The hand was easier to use with feedback. (3) The hand was easier to use with both features (VI mode).

7.1.7 Data Analysis

The number of successful grasps in each mode was tabulated and averaged across subjects. Survey data was also tabulated and is presented raw. To analyze FDS EMG data, the filtered signal used to control the SoftHand was further processed in MATLAB. A minimum threshold was established experimentally for active EMG. The EMG amplitude above this threshold was averaged and the total time spent above threshold calculated. Because muscular effort in this study is essentially isometric, mechanical work of the muscle cannot be calculated. Instead, we calculated the energy cost of the physical effort used to control the hand as the integral of the EMG amplitude over time, only considering above-threshold samples.

7.2 Results

All subjects were able to generate sufficient EMG signal to drive the SoftHand and study procedures were well tolerated. Subjects performed the series of grasps after a brief familiarization period with the device. No difference in grasp ability was found between the four modes; out of 16 attempted grasps, subjects averaged 14.75, 15.25, 15.25, and 15 successful grasps in standard, impedance, vibrotactile, and VI modes, respectively. An example of a grasp sequence can be found in Fig. 8.14. The corresponding raw and processed EMG data as well as the position and impedance signals sent to the motor can be found in Figs. 7.6 and 7.7, respectively. A video of the experiments is available at [25].

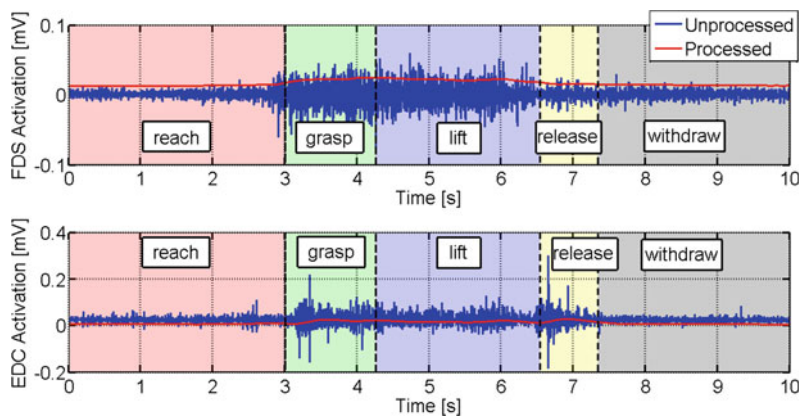


Fig. 7.6 Activation of FDS (top) and EDC (bottom) during a typical grasping sequence. Different colors indicate the five phases of the grasp extracted from video recordings

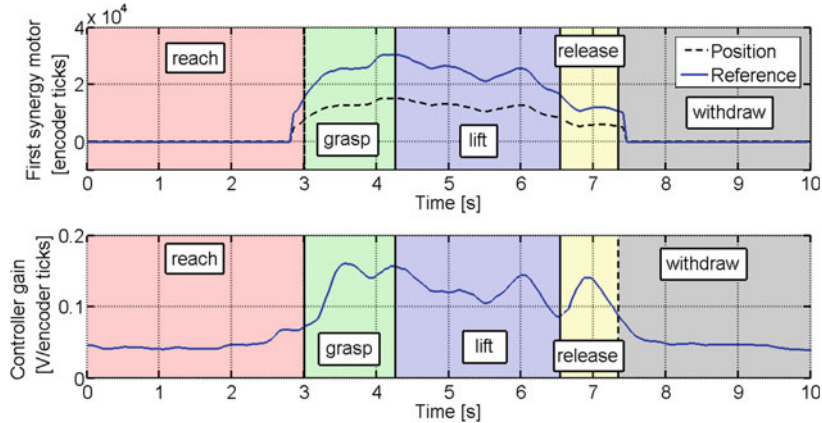
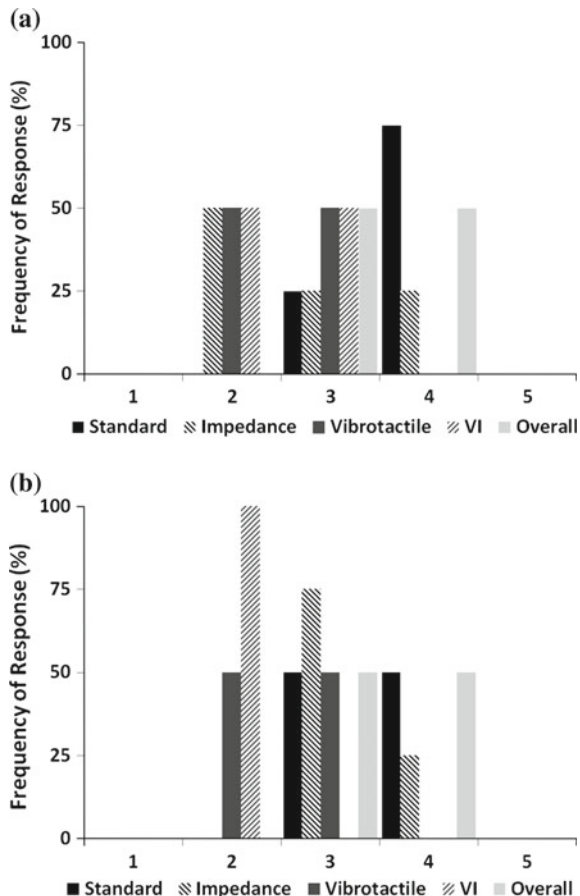


Fig. 7.7 Actual and reference position sent to the motor (*top*) and the stiffness level used (*bottom*), determined by cocontraction. Different colors indicate the five phases of the grasp extracted from video recordings

The results of the questionnaire on perceived physical and mental effort required to use the device revealed differences between the control modes. Figure 7.8 shows the results on the physical (a) and mental (b) effort questionnaire. Estimates of required mental effort in each mode roughly mirror perceived physical effort. Both impedance and vibrotactile modes required less physical and mental effort than standard mode and the VI mode showed the lowest mental effort of the four modes and lower physical effort than standard or impedance modes. This comparison between modes is reflected in the final questionnaire: when asked if the impedance mode was easier to use, 2 subjects were neutral and 2 agreed. Regarding whether control was easier with feedback, one participant disagreed, one agreed, and two strongly agreed. Finally, 3 participants agreed and one strongly agreed when asked if control was easier with both features (impedance control and vibratory feedback).

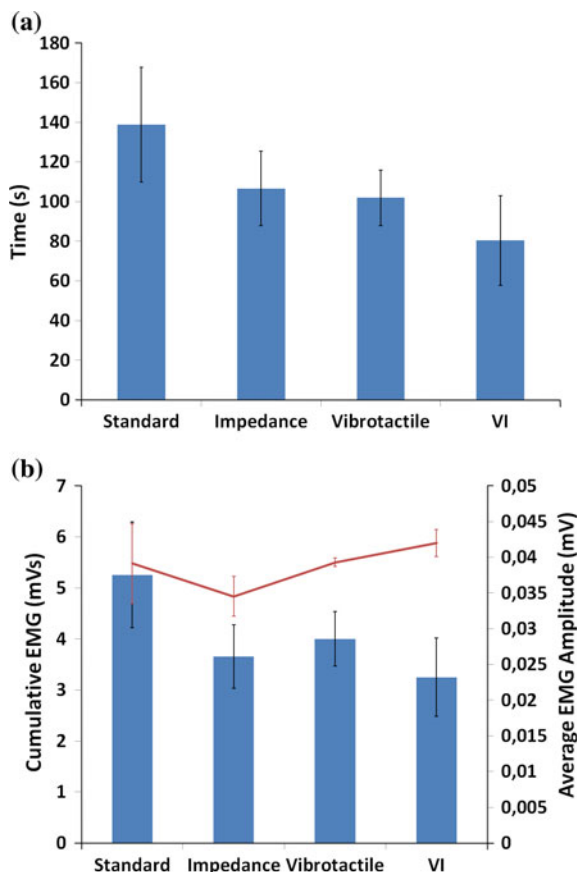
Figure 7.9 presents a summary of the FDS EMG data. The total time spent above threshold is presented in Fig. 7.9a: subjects spent the longest time in standard mode, less time in impedance and vibrotactile modes, and the least time in VI mode (mean time above threshold in s: 138.8 ± 57.9 , 106.7 ± 37.4 , 102.0 ± 27.9 , and 80.4 ± 45.1 , for standard, impedance, vibrotactile, and VI modes, respectively). We calculated both the average EMG amplitude above threshold as well as a cumulative EMG measure (Fig. 7.9b, line and bars on graph, respectively). There was little difference between the modes in average EMG; the impedance mode showed slightly lower EMG levels than the other three modes (average EMG amplitude in mV,

Fig. 7.8 Questionnaire results for physical (*top*) and mental (*bottom*) effort. Darker bars indicate lower perceived amount of effort.
a Physical effort. **b** Mental effort



0.0391 ± 0.0111 , 0.0345 ± 0.056 , 0.0393 ± 0.012 , and 0.04200 ± 0.038 , for standard, impedance, vibrotactile, and VI modes, respectively). As an estimate of total effort, cumulative EMG amplitude was also calculated. Similar to the time spent above threshold in each mode, the highest energy cost was seen in the standard mode, while lowest was in VI mode.

Fig. 7.9 Time spent above threshold averaged across subjects (*top*). Average FDS EMG amplitude (*bottom, bars*) and cumulative EMG (*bottom, line*). **a** Duration of EMG activity. **b** EMG activity



7.3 Conclusions

Overall, the results of this study suggest the SoftHand could be used successfully as a myoelectric prosthesis. With a short familiarization period (less than five minutes), subjects were able to successfully grasp and release roughly 15 out of 16 trials in all modes. Subjects reported lower physical and mental effort while using impedance and vibrotactile feedback modes compared to standard mode and least effort in the combined VI mode. Anecdotally, one subject advocated for the combined VI mode stating that control took less concentration with feedback and less physical effort with impedance control.

These qualitative results agree with the quantitative EMG data: subjects activated the flexors for less time in impedance and vibrotactile modes compared to standard mode and the least time in VI mode. A learning effect is possibly a confounding factor in this analysis; however, a familiarization period was included for each mode to remove the steepest part of the learning curve, and the high grasp ability across

all modes suggests there was minimal learning to be gained from the task. Interestingly, the time for both single-feature control modes (impedance and vibrotactile) was similar and higher than the combined mode, suggesting increased benefit from using both strategies together. Subjects had slightly higher energy cost in vibrotactile mode compared to impedance and VI modes. The vibrotactile motor used in this study had low resolution, thus it is possible subjects exaggerated their contractions to benefit from the feedback. The results suggest added benefit from the impedance controller and vibrotactile feedback; however, since functionality was still high with the standard controller, this may be a feasible alternative in users with limited myoelectric control or diminished cognitive function. This study shows the feasibility of transferring complexity from the user and control architecture of a myoelectric prosthesis to the hardware to decrease cost and physical and cognitive load without sacrificing performance. Future work will include testing with amputees as well as improving the sensitivity of the current control system.

Chapter 8

Exploring Teleimpedance and Tactile Feedback for Intuitive Control of the Pisa/IIT SoftHand

To further exploit the efficiency and robustness of a synergy-driven robotic hand, we present a novel myoelectric impedance controller. This chapter extends the impedance control scheme and hand synergy reference models, previously presented in Chap. 7, and presents a novel teleimpedance controller for the Pisa/IIT SoftHand. In addition, different haptic interfaces are developed to provide the user with some information about the grasping forces and texture.

Haptics in Prosthesis: State of Art—The hand is an especially complex part of the body containing a variety of sensing capabilities that can differentiate between light or firm touch, sense an object slipping from grasp, and determine the texture of an object, among others. Haptic information provided by mechanoreceptors of the fingertips is crucial to accomplish every day activities such as grip control and detection of object properties [158–160]. In amputees, this kind of information is absent; such an absence of haptic feedback was demonstrated to affect the usage of prosthetic hands as well as the sense of ownership of these devices [161–163]. Thus another major avenue of prosthetics research explores providing feedback to the user about the prosthesis’ interaction with the manipulated object or environment. For example, the cable tension felt in body-powered prostheses provides limited but functional feedback relating grip force to the user. With myoelectrics, this feedback is lost and users must rely on visual feedback. While, to the authors’ knowledge, no commercial devices provide the user with feedback, the research community is actively pursuing various methods of providing any haptic feedback to prosthesis users.

Feedback methods can be roughly broken down into two categories: invasive and non-invasive [164]. An example of the former is targeted reinnervation surgery, where severed nerves are rerouted from the amputated limb to residual muscles and skin [165, 166]. The latter typically consists of delivering sensory feedback to intact sensory systems normally not involved in the task, e.g., on the forearm. Common haptic feedback modalities include vibrotactile feedback [164, 167], skin stretch

feedback [168] and force feedback [163, 169]. Such mechanical feedback was able to increase the acceptance and the ability to control the prosthetic hands, e.g. [170–173]. In [174] a multi-function haptic device that conveys multi-cue information such as pressure, vibration and shear force to transhumeral amputees was presented. Although promising, such a device is complex and could be cumbersome. In [175] a new miniature haptic device, a tacter, which delivers touch, pressure, shear, and temperature sensation, was proved to enhance grip force control in transradial (TR) amputees. Furthermore, according to authors in [175], in order to obtain intuitive haptic feedback, it is important to satisfy two conditions: somatotopic matching (usually achievable via TR surgery) and modality matching, i.e. to feel what effectively happens. For example, when we press an object we should feel pressure.

In this chapter, we present a multi-cue procedure to convey haptic stimuli to the forearm and upper limb of subjects wearing the Pisa/IIT SoftHand. The stimuli are a classic force/pressure stimulus, related to the grip force and a vibrotactile one. To test the effectiveness of such approach, we designed two types of experiments: one focuses on low-frequency (force-information), the other on high-frequency information. In the first experiment, the task was to grasp objects with different elastic properties. The task is common in many experiments to test force feedback provided to users of prosthetic hands, see e.g. [163, 173], since an effective grasp is a fundamental action in daily life. The haptic interface is a cuff whose stretching state is controlled in order to convey the force resulting from the interaction of the artificial hand with the external world. The novelty we introduced does not retain in the haptic device/strategy itself but in the technique we used to provide users with some knowledge of task interaction forces. To achieve this goal, we developed a grasp interaction force observer that relies on the pre-identified disturbance model of the hand. These interaction forces are then fed back to the user via the mechanical cuff, providing the user a sense of grasp forces in an intuitive manner. In the second experiment, we used the mechanotactile force feedback cuff on the upper arm and the series of vibrotactile surface feedback motors on the forearm of the subjects to the high-frequency accelerations that occur during real-world contacts. Such an experiment was motivated by the importance of the perception of surface properties such as texture in daily life [176]. For this reason, we developed a vibrotactile interface relying on surface irregularities and acceleration signals from the accelerometers mounted on the artificial hand. Users wear a forearm cuff of vibrotactile motors that relay the accelerometer signal to inform them of surface roughness. The vibrotactile feedback we propose is inspired by the works [177–179], and it is directly related to the texture of the surfaces explored by the robotic hand. In this sense, it is different from the vibrotactile feedback presented in literature, where vibration is used to convey force cues (such e.g. in [164]) and hence related to convey low-frequency data, and more devoted to accomplish modality matching.

8.1 Human-SoftHand Interface

Synergies are often thought of as kinematically coordinated movements of the hand joints [156]. Others give evidence to the existence of such pattern in dynamic coordinates [180], i.e., in the space of muscular activations [181, 182]. These observations promote the idea of exploring the minimum number of muscles necessary to decode and extract the information related to hand stiffness and posture references. To that end, we choose the major antagonist pair acting on the fingers: The extensor digitorum communis (EDC) and flexor digitorum superficialis (FDS).

It is well known that muscle force increases with muscular activity [183]. While individual muscular forces affect and modify joint torques, their synchronized increase in antagonistic configuration actively adjusts the impedance of the corresponding joint [47]. Now by taking into account the forward dynamics of the grasp along the first synergy, we can write

$$\begin{aligned}\tau &= a_\tau \delta, \\ a_\tau \delta &= I \ddot{q}_s + c \dot{q}_s + K_s (q_s - q_0) + \tau_E,\end{aligned}\quad (8.1)$$

where τ , a_τ and τ_E denote the torque synergy, its gain and external torques, respectively; q_s and q_0 are the position of the hand and the object along the first synergy; δ is a function of the difference activation of the antagonistic muscles (*FDS – EDC*), and I , c and K_s are the inertia, damping and stiffness of the hand along the first synergy, respectively. *FDS* and *EDC* are the processed EMG signals of the corresponding muscles. Now, by neglecting the effect of inertia and external torques in the above equation and rearranging it, we can write

$$\dot{q}_s = \frac{-K_s}{c} (q_s - q_0) + \frac{a_\tau}{c} \delta. \quad (8.2)$$

This dynamics can be estimated in discrete time as follows

$$q_{s_{k+1}} = \left(1 - \frac{K_s T}{c}\right) q_{s_k} + \frac{T a_\tau}{c} \delta + \frac{K_s T}{c} q_0 \quad (8.3)$$

where T and k are the time step and iteration number. To establish δ and K_s mappings based on experimental data, we used two functions of a modified hyperbolic tangent shape. The flexibility and capability of this function in generation of various output profiles have been discussed in [184]. We write

$$\delta = \frac{a_q [1 - e^{-b_q (\text{FDS-EDC})}]}{[1 + e^{-b_q (\text{FDS-EDC})}]}, \quad (8.4)$$

where a_q and b_q are the constant gains, to be identified experimentally. Similarly for the stiffness

$$K_s = \frac{a_k[1 - e^{-b_k(FDS+EDC)}]}{[1 + e^{-b_k(FDS+EDC)}]}, \quad (8.5)$$

where a_k and b_k are similar as above and K_s , denoting the stiffness synergy reference, which is allocated in the stiffness interval of the robotic hand.

To identify the parameters of the above functions, subjects were asked to open and close the hand, trying to mimic the first synergy. As a reference, the SoftHand was slowly opened and closed. Meanwhile, FDS and EDC muscular activities were recorded. Subjects performed 20 grasping trials. Next, subjects were asked to perform the grasp at 5 different FDS and EDC co-contraction levels. Visual feedback of the summated FDS and EDC levels was provided during the trial to assist the subjects in maintaining steady co-contraction levels. Four trials were recorded for each level, resulting in 40 trials total, 20 slow grasps and 20 grasps at various co-contraction levels.

Parameter identification of δ and stiffness model (K_s), and the corresponding motor position reference and SoftHand stiffness level, respectively, was performed on even numbered trials while using FDS and EDC inputs. The odd numbered trials were used for the evaluation of the mappings. This led to the normalized root-mean-squared error (NRMSE) values of 17.6 and 13.4 % for the postural and stiffness test trials, respectively, averaged across subjects. In the future, parameter identification of the models in amputees is likely feasible through standard training techniques such as mental imagery, teacher imitation, or bilateral action via mirror box [185].

8.2 Interaction Torque Observer

As mentioned previously, a single DC motor is incorporated in the design of the Soft-Hand to pull the tendon and drive the finger joints according to the first hand synergy. The equation of motor dynamics¹ is then defined by:

$$J_n \ddot{q} = K_m I_{ref} - \tau_{dist}, \quad (8.6)$$

with \ddot{q} , K_m , and I_{ref} denoting the motor angular acceleration, torque constant, and motor current, respectively. $J_n = J_m + \frac{J_h}{N^2}$ represents the total inertia (motor inertia plus hand inertia reflected to the motor side).

In our setup, due to the low velocity profiles of the hand closure and the relatively high gear ratio, the reflected inertia of the hand, $\frac{J_h}{N^2}$, is neglected. The disturbance torque, τ_{dist} , combines all the internal and external disturbance torques and is assumed to be formed by four components: the elastic torque generated by the hand tendons

¹In this chapter, if not stated explicitly, all the variables and equations are described on the motor side (including interaction torque). Therefore, a gearbox ratio of $N = 84$ must be taken into account for the presentation of the variables after the gearbox.

during closure (τ_{te}), the gravitational effect (τ_{grav}), the frictional torque due to friction in the hand joints and pulleys (τ_f), and the interaction torque (τ_{int}). We can write:

$$\begin{aligned}\tau_{dist} &= \tau_{model} + \tau_{int} \\ &= \tau_{te} + \tau_f + \tau_{grav} + \tau_{int}.\end{aligned}\quad (8.7)$$

In the above equation, due to the lightweight design of the hand, the effect of gravitational torque is neglected. The hand closure elastic torque component is modeled as a function of the motor shaft rotation angle. In addition, an antisymmetric piecewise-linear function of the motor speed and tendon tension is exploited for the modeling of the viscous and Coulomb friction of the hand [186], as follows,

$$\tau_f(\dot{q}) = \begin{cases} D_1\dot{q} + n_{s_1}K_{te}(q - q_o)\dot{q} > 0 \\ D_2\dot{q} - n_{s_2}K_{te}(q - q_o)\dot{q} < 0, \end{cases}\quad (8.8)$$

with D_i , n_{s_i} , K_{te} , and q_o representing the viscous damping and Coulomb friction coefficients, the reflected hand tendon stiffness, and motor angular position at rest (hand open), respectively. Incorporating the above assumptions in the disturbance model of the hand will result in:

$$\tau_{model} = \begin{cases} (1 + n_{s_1})K_{te}(q - q_o) + D_1\dot{q} > 0 \\ (1 - n_{s_2})K_{te}(q - q_o) + D_2\dot{q} < 0, \end{cases}\quad (8.9)$$

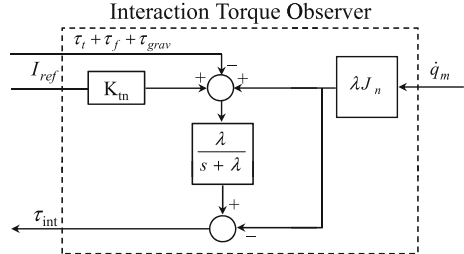
Therefore, the hand closure and opening models will be identified separately, as described below.

Supposing that the hand has not come in contact with the object to be grasped (i.e. $\tau_{int} = 0$ in Eq. 8.7), the hand model torque (τ_{model}) can be computed from the motor current and its motion response. Such calculation would require motor current and acceleration sensing with the latter being sensitive to noise if computed from position differentiation. To achieve reliable hand model torque estimation while taking into account the minimum hardware requirements, a robust torque observation technique is used here (Fig. 8.1). In particular, the hand model torque is estimated based on the angular velocity as follows:

$$\begin{aligned}\hat{\tau}_{model} &= K_{tn}I_{ref} - J_n\ddot{q} \\ \hat{\tau}_{model}(s) &\simeq \frac{\lambda}{s + \lambda}(K_{tn}I_{ref} - J_ns\dot{q}) \\ &\simeq \frac{\lambda}{s + \lambda}(K_{tn}I_{ref} + \lambda J_n\dot{q}) - \lambda J_n\dot{q}.\end{aligned}\quad (8.10)$$

Here, s is the Laplace operator and λ represents the filter cutoff frequency which affects the disturbance rejection capability [187]. The major design criterion is to choose λ low enough to result in a robust system, while considering the introduced filtering delay. To estimate the reflected interaction torque caused by the contact

Fig. 8.1 Interaction torque observer block diagram



of the hand with the environment, we take Eqs. (8.6) and (8.10) into account and subtract the identified hand model torque (Eq. (8.9)), from the external torque effect as follows:

$$\hat{\tau}_{int} = \frac{\lambda}{s + \lambda} (K_{tn} I_{ref} + \lambda J_n \dot{q} - \hat{\tau}_{model}) - \lambda J_n \dot{q}. \quad (8.11)$$

As noted above, in our setup, we assume that the Coulomb and viscous friction components can be described as antisymmetric, first-order linear functions of the motor velocity. To that end, and with the purpose of the parameter identification of the hand model (Eq. 8.9), the hand controller was driven with fixed and low velocity (quasi-static) reference trajectories. Such motion reference profiles were designed to result in complete hand closure, starting from fully extended fingers. This process was repeated in the reverse direction as well, to account for the antisymmetric and velocity dependent properties of the friction model during opening and closure.

Consequently, the resultant current, position, and velocity profiles were used to estimate the components of the Eq. (8.9), by means of conventional least squares identification algorithm. The identification process led to two feed-forward, velocity dependent estimates of the hand disturbance model, $\hat{\tau}_{model}$. To evaluate our friction model, the hand stiffness parameter (outer position loop gain) was set to low values and a desired trajectory was tracked with and without the presence of identified friction model. The desired trajectories were designed to result in several complete hand closures (with different speed), starting from fully extended fingers. In each experiment, the mean absolute error (MAE) value for the motor position was calculated. In all cases, incorporation of friction model resulted in more accurate tracking of the desired trajectory (e.g. 35 % reduction of MAE when the hand stiffness was set to 5 N m/rad), that gives evidence to the accuracy of the identified hand disturbance model.

Experimental validation of the observed interaction torques requires force/torque sensing while fingers are interacting with the object. However, since the motor dynamic parameters in Eq. (8.6) are known and the motor position and velocity are accurately measured through high resolution encoders, accuracy of the identified hand disturbance model (as discussed above) results in fairly reliable estimation of the interaction torques between the hand and the object [187–189]. The realized interaction forces between the robot and the environment can also be used to explore and identify the object properties, such as shape and compliance [20].

8.3 Tactile Interfaces

The interaction that happens between the external environment and the user, mediated by a robotic or prosthetic hand, represents a typical tele-operation scenario, where the human user is the master and the artificial hand, exploring/grasping/manipulating external objects is the slave. Under these conditions, in order to enable realistic perception, it is fundamental to provide the user with the haptic sensations arising from this interaction. More specifically, tool mediated activities comprise both low-frequency forces and high-frequency accelerations or vibrotactile stimuli. While it is straightforward to understand the need and the role of force-feedback, e.g. to properly accomplish grasp operations and achieve stability, vibrotactile cues also convey essential haptic information, the absence of which might cause a haptic system to feel less natural [190]. For example high-frequency accelerations are responsible for human perception of haptic surface properties such as texture and roughness [177, 178, 190], elicited by the stimulation of Pacinian corpuscles. Furthermore, information on tangential surface exploration (dragging) and discontinuities can also be important for humans to implement lower-level neural control laws according to “a non slip strategy” in independent control of fingertip forces [191].

8.3.1 Mechano-Tactile Feedback

Mechanotactile displays have seen a large amount of progress, rendering relevant feedback stimuli to the human. Such tactile feedback is suggested to be beneficial for intuitive control of a prosthetic limb for transradial amputees and healthy users [192]. In our setup a custom made, adjustable pressure cuff was worn on the upper arm to provide the user with the task interaction forces while grasping (see Fig. 8.2 and Eq. 8.11). The cuff incorporates a belt, driven by a small DC motor to adjust the

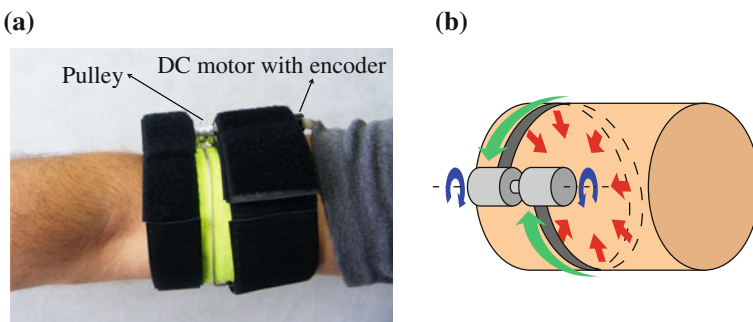
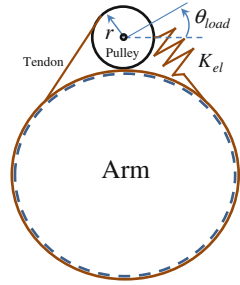


Fig. 8.2 Upper arm cuff, actuated by a DC motor picture (*left*) and schematics (*right*). The motor generated torque (*blue*), generates a pulling force (*green*) on the black tendon, which in turn causes, by constriction, a distribution of internal pressure (*red*) around the arm

Fig. 8.3 Loading scheme of the upper arm cuff



amount of applied mechanical pressure. The motor was driven by an active impedance controller, providing the possibility of establishing safe and reliable control of the applied pressure. The gains of the impedance controller were set experimentally and kept fixed among all experiments. The loading scheme of the upper arm cuff is demonstrated in Fig. 8.3.

As reference commands, the estimated interaction torques by the observer unit (Sect. 8.2) were converted, scaled and tracked by the cuff's controller. To do so, the required amount of displacement for the cuff's motor (θ_{load}) was calculated based on the following equation

$$\delta x_{load} \simeq \frac{a_{cuff} \tau_{int}}{K_{el}}, \quad (8.12)$$

where a_{cuff} is an experimentally chosen coefficient that scales the observed interaction torques to a desired force to be applied with the cuff, and K_{el} is the outer position gain of the cuff's controller (stiffness gain, chosen experimentally). x_{load} is the tendon displacement² and can be calculated from r and θ_{load} in Fig. 8.3.

8.3.2 Vibro-Tactile Feedback

Among surface properties, texture is one of the most important in everyday haptic perception [176], relying on surface irregularities and acceleration signals. In order to enhance the immersiveness of the haptic experience during tool-mediated and tele-operation tasks, it is, thus, crucial to replicate this high-frequency information arising from the contact of real objects and recorded on the tool (slave) side on the human (master) side [193]. To achieve this goal, we developed an electronic acquisition and control circuit (see Fig. 8.4), following the scheme proposed in [177].

²Here we assume that the cuff's tendon stiffness is very high and the damping effect is negligible due to the slow variations of the observed interaction torques.



Fig. 8.4 Block diagram of the acceleration feedback system

8.3.2.1 Acceleration Sensing and Processing

Acceleration data were recorded using an Analog Devices ADXL327 MEMS-based accelerometer, which is a small, low power, 3-axis accelerometer with signal conditioned voltage outputs and a minimum full-scale range of $\pm 2\text{ g}$. The sensors were mounted on the dorsal part of the distal phalanges of the five robotic fingers. This location was chosen since it does not interfere with the motion of the fingers during the opening/closing phases. In our setup, we replicated on the master (human) side only the x-axis acceleration sensed by the robotic fingers, by means of vibrational feedback (cf. Fig. 8.4). The main motivations for this choice are: first, to maintain the simplicity of the acquisition/control circuit, in agreement with the synergy-driven design philosophy. Second, although we know that the complete acceleration signal depends on the sensing along all three axes, for our purposes the tangential x-oriented acceleration contains the most useful information for dragging tasks and slip-prevention applications. Third, trying to appropriately map multi-dimensional inputs to single axis actuators such as the ones we used introduces some technological problems. For a complete description of these problems as well as for a comparison and discussion of different solutions see e.g. [178, 193]. Using a scheme replicating only one axis acceleration from the slave to the master side represents a good trade-off between control simplicity and immersiveness of the haptic experience; it is also important to notice that this information can be reproduced using a single axis actuator, despite its axis orientation, since the human hand can not discriminate vibration directions from one another [176].

As in [177], the accelerometer bandwidth is configured using an on-board first-order low-pass filter set at 1000 Hz, followed by a DC block capacitor. Afterward, the signal is amplified with an adjustable gain A (ranging from 0 to 4) and band-pass filtered. The band is from 46 to 307 Hz; in this manner, low frequencies, which can not be reproduced by the vibrational motor are removed. This frequency range is coherent with the one reported in [177], and it was chosen also to take into account the behavior of Pacinian corpuscles in human skin, which are sensitive to vibratory stimuli from 20 to 1000 Hz, with a peak sensitivity between 250 and 550 Hz [194].

Finally the signal is applied to the motor, after current amplification (scaling factor up to 7), using a push-pull configuration. In our setup, a small ($24 \times 7\text{ mm}$), low-cost vibration motor (Precision Microdrives³) was utilized. Four³ of these motors were

³To allow adequate spacing of the motors in the vibrotactile cuff, only digits 1–4, thumb to ring finger, were used to provide texture feedback.

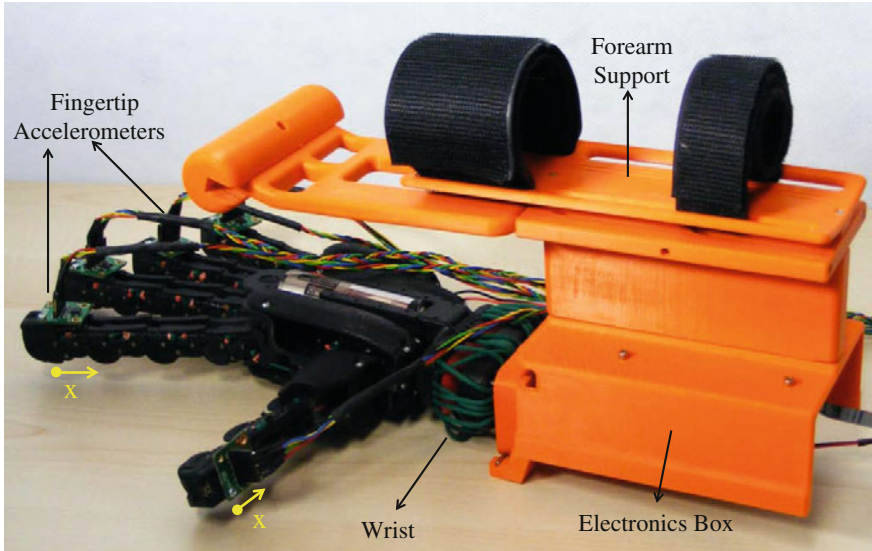


Fig. 8.5 SoftHand equipped with the able-bodied adapter (forearm support) and fingertip accelerometers

sewn with 15 mm distance on an adjustable size cuff, and mounted on the forearm of the subjects. They were mounted mainly on the dorsal part of the forearm, on the hairy skin. We chose this solution for sake of space since on the inferior part of the forearm there were the wires leading the signals from and to the robotic hand. Such a solution was adopted, as it was demonstrated in [195] that vibrotactile amplitude detection threshold is higher for hairy skin than for glabrous skin.

Such a distance is coherent with the results on the distance resolution for two-point discrimination of vibrotactile stimuli found in [196]. Figure 8.5 demonstrates additional components of the SoftHand for the haptic experimental setup, while processing stages of each accelerometer data are shown in Fig. 8.4. The additional support/interface parts seen in Fig. 8.5 were developed to permit the attachment of the hand to non-amputee users for the purpose of experimental validation of the system.

8.3.3 Texture Rendering and Psychophysical Considerations

The stimuli provided by the vibrotactile system are basically related to the texture, i.e. roughness, of the surface explored by the robotic hand. In order to better exploit such artificial feedback it is essential to properly relate it with (a) human perception capabilities and (b) physical roughness, i.e. the roughness of the surface that is effectively touched by the prosthetic hand. Considering the point (a), many aspects

Table 8.1 Mean vibrotactile detection thresholds (μm), discriminable increments (Δf) and Weber Fractions ($\Delta f/f$) for frequency discrimination, on the forearm at the standard frequencies of 20, 50, 100, and 200 Hz [198]

| Frequency (Hz) | μm | Δf | $\Delta f/f$ |
|----------------|------------------|----------------|-----------------|
| 20 | 149 ± 9.0 | 7.6 ± 1.1 | 0.36 ± 0.07 |
| 50 | 114.9 ± 8.7 | 18.0 ± 5.1 | 0.38 ± 0.1 |
| 100 | 114.1 ± 10.2 | 27.2 ± 8.5 | 0.27 ± 0.09 |
| 200 | 49.2 ± 3.7 | 33.9 ± 7.3 | 0.17 ± 0.04 |

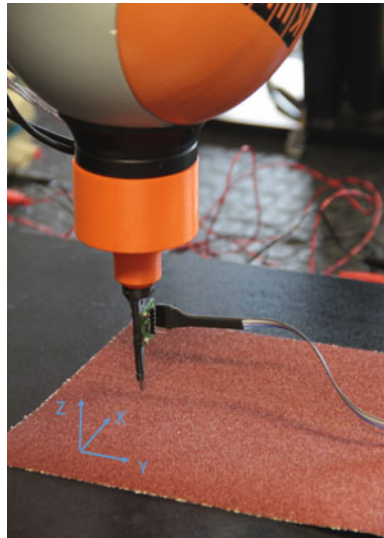
Values are means \pm SE (Standard Error)

of vibrotactile and texture perception have already been extensively studied in literature. For example, in [195] authors demonstrated that the vibrotactile amplitude detection threshold is higher for hairy skin than for glabrous skin and it depends on the initial amplitude reference stimulus as well as on frequency [197]. For our purposes, we have exploited the results from [198], which have been reported for sake of clarity in Table 8.1. It is also important to notice that vibration is strictly connected to roughness (texture) perception; indeed, according to [199], vibration and hence the relative motion between skin and surface is the *sine qua non* for texture perception. In [200], the perception of roughness by active and passive touch was analyzed, revealing no difference between the two haptic modalities, while the relation between physical roughness and the perceived roughness was investigated in [201]. The authors showed that such relation is exponential with an exponent of 1.76. This means that on average, subjects use a logarithmic mapping from physical roughness onto perceived roughness. The results on vibration and texture perception as well as the findings on two-point discrimination reported in the previous subsection have been used to craft the proposed haptic system.

Considering point (b), the amplitude modulation of the vibromotor is directly related to the voltage provided by the control circuit and hence to the texture of the surface. To better clarify this point, we have performed some experiments using a KUKA/DLR Lightweight Robot arm with an ADXL327 MEMS-based accelerometer end-effector, see Fig. 8.6.

This accelerometer provided inputs to the control circuit that drives the motor. The Kuka arm was moved along the y-axis (distance 13 cm, see reference axis in Fig. 8.6) with a linear trajectory and controlled in force in order to exert a maximum normal force along the z-axis of 5 N. The motion velocity was of 5 cm/s and the joint stiffness was set to 2000 N/mm along the y and x-axis and to 1 N/mm along the z-axis. Both force and velocity values were heuristically chosen to match typical parameters of the explorative actions performed by humans with the Pisa/IIT SoftHand. The Kuka was moved along two different surfaces: one smooth surface and one covered with sandpaper no. 40. While the end effector moved over each surface, the accelerometer recorded the signal along the motion axis (y-axis) and feed the circuit with it. Meanwhile, the voltage output from the power stage of the circuit was measured and recorded with an oscilloscope. The Root Mean Square (RMS) of the voltage output

Fig. 8.6 The end-effector on the KUKA/DLR arm with the accelerometer. Reference coordinates are also indicated



for the sandpaper no. 40 was 0.8840 V, while for the smooth surface it was 0.3859 V. Interpolating from the specs of the motor, such values lead to motor vibration of 0.4119 g at 120 Hz and no vibration for the smooth case. The maximum operating voltage for the motor is 1.8 V.

8.4 Control Architecture

As an alternative method to the bilateral master-slave teleoperation, teleimpedance control has been previously presented to overcome the stability issues raised in classical force-reflecting teleoperation scenarios, as well as enabling more natural task completion [2, 3]. In our proposed algorithm, task-oriented equilibrium position and stiffness profiles are estimated on the master side and realized by the teleoperated slave robot, in realtime.

Here, to incorporate the user's intent in the control of the soft and robust grasp, a novel teleimpedance controller is developed. The overall block diagram of the proposed controller is shown in Fig. 8.7. In this control scheme, the inner hand motor control loop is a high bandwidth current regulator while the outer loop implements an impedance controller which incorporates a time varying gain and is updated by the user's hand stiffness synergy profile in realtime, based on the stiffness synergy model developed in Sect. 8.1. The bounds of the stiffness gain ($[5 \text{--} 50] \text{ N m/rad}$) were experimentally chosen to guarantee good tracking performance, stability, and high grasp compliance. Simultaneously, acquired muscular activities were used to determine reference position profiles as described earlier in Sect. 8.1.

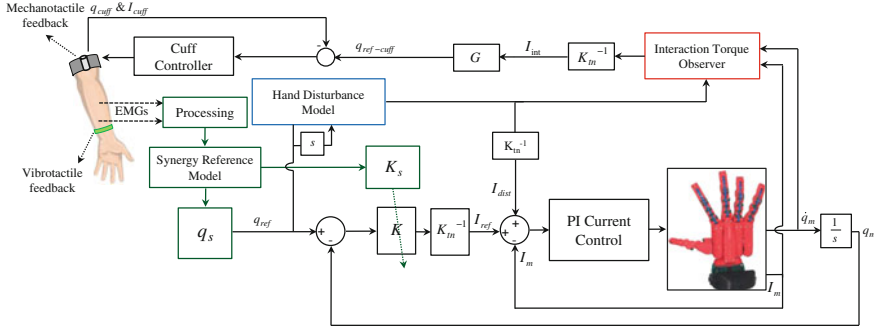


Fig. 8.7 Block diagram of the synergy-driven hand teleimpedance controller

The hand disturbance model block estimates the hand model torque, based on previously developed and identified feed-forward models (Eq. 8.9). The estimated torque is then converted to the current and fed to the inner current controller as I_{dist} . Simultaneously, the estimated hand model torque is used by the interaction torque observer (Fig. 8.1), to estimate the interaction torques due to contact with the grasped object. Subsequently, the resulting interaction torque is converted, scaled, and applied to the cuff's controller in order to provide the user with some indication of the grasp state and force (Sect. 8.3.1). Furthermore, users wear a forearm cuff of vibrotactile motors that relay fingertip accelerometer signals to inform them of surface roughness and object slippage.

8.5 Experimental Setup

Analog electromyography signals were measured and amplified with a Delsys-Bagnoli 16 (Delsys Inc.) apparatus. Acquired signals were band-pass filtered within the 20–450 Hz frequency range. Resulting signals were sampled at 2 kHz (PCI-6220, National Instruments) and fully rectified for further processing. A digital, non-causal FIR linear phase low-pass filter was used for the detection of the envelope of the signal, which approximately corresponds to muscle activity. EMG normalization was performed automatically. Each time the system was activated, subjects were given 5 s to perform a large, brief co-contraction. This input was then used to normalize the EMG signals online. In addition, two online moving-average filters were implemented to detect the magnitude of drift in the lower bounds of each EMG channel, resulting from noise or change in limb configuration. The averaging was performed on a narrow and predefined amplitude interval of the normalized signals. At each time step, corresponding values were subtracted from the processed EMG measurements. Finally, resultant signals were fed into the model described in Sect. 8.1.

The hand unit and power driver for the motors (SoftHand and force feedback cuff) are custom control boards based on the Texas Instruments Luminary DSP chip

LM3S8962. The DSP control loop is executed at 1 kHz while the communication with the host PC is achieved through a real time Ethernet link. Motor current measurement is performed by a hall effect based current sensor (ACS714, Allegro Microsystems Inc.) and appropriate signal conditioning integrated in the motor power driver module.

The data acquisition and synchronization interfaces between the motor controller boards, the interaction torque observer, the hand model torque, the EMG acquisition board, the hand synergy reference model, and the upper-arm cuff were developed in C++. The acquisition, processing and control ran at 1 kHz sampling frequency. Two sets of experiments were carried out. Subjects wore the SoftHand using a custom made forearm support (see Fig. 8.5).

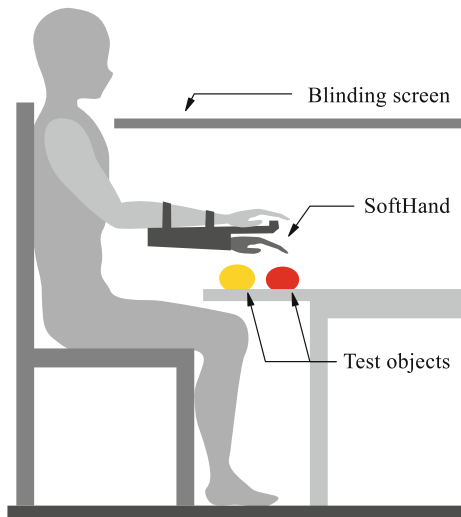
8.5.1 *Grasping Experiments*

The first experimental setup was designed to evaluate the effectiveness of feedback interaction forces and user-modified compliance in controlling the natural, robust grasp of the SoftHand. For this reason, objects with different elastic properties were grasped under the following hand controller parameters: (i) fixed and relatively high stiffness gain (Stiff), (ii) fixed and relatively low stiffness gain (Compliant), and (iii) user modified hand compliance (Teleimpedance), all with or without the effect of interaction force feedback. Postural synergy commands were derived from the model, described in Sect. 8.1, and were consistent among all experiments. Subjects were seated in front of a table and reached to grasp an object. Successful grasp was achieved when the SoftHand held the object securely off the surface of the table. Each grasp was attempted 3 times. To minimize any learning effects, subjects were provided with adequate training before the experiments and the order of the trials was randomized. Five right-handed subjects (one female, four males, mean age = 28.6) participated in this setup.

8.5.2 *Haptic Experiments*

For the second experimental setup, five right-handed subjects (two females, three males, mean age = 27) wore the SoftHand and the series of vibrotactile surface feedback motors on the forearm and the mechanotactile force feedback cuff on the upper arm (see Fig. 8.8). The setup for interacting with the test objects was modeled after the Haptic Black Box (HBB [202]) design. The objects were constrained within an experimental tray with low sides. A screen was placed parallel to this surface to occlude the objects from view without limiting the subject's visual feedback from the surrounding environment (to avoid balance issues, etc.). Subjects were also provided with music via headphones to minimize the effect of auditory feedback which may impart texture information. Subjects were presented three pairs of objects before the experiment and then asked to retrieve the objects without visual or audio feedback.

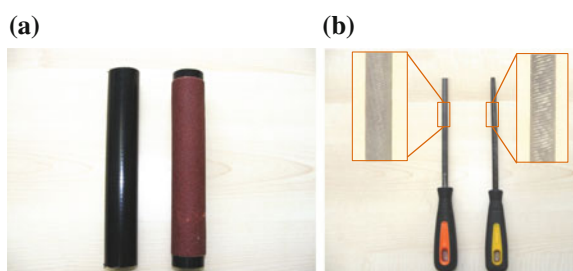
Fig. 8.8 Experimental setup for haptic experiments



Each pair was formed by two objects of similar size, shape, and weight but with different surface properties. Object pairs were chosen to represent various typical shapes encountered and require different grasps used in activities of daily living. The first pair (Obvious) consisted of two similar plastic bars ($3 \times 18\text{ cm}$), one with a smooth surface and the other covered with a fine sand paper. An average-size apple and orange were used in the second (Mid) pair. And finally, the third pair (Subtle) was formed by two round, metal files (25 cm long, with 1 cm file diameter, and 3 cm handle diameter) with either parallel or cross-cut teeth (see Fig. 8.9).

Each object pair was tested four times for each of three modes (36 trials for each subject): with mechanotactile feedback only (Mech), with Mech and partial (index and thumb) vibrotactile surface feedback (Half), and with Mech and full surface feedback (Full). For each object pair in each mode, subjects were asked to explore the space to find the desired object (two times for each object, in each object pair), and then grasp and lift it off the table. To minimize learning effects, subjects were allowed a familiarization period with each mode and the order of modes and object retrieval was randomized. Each trial was rated as successful or unsuccessful in two

Fig. 8.9 Plastic bars (a) and the filing tools (b) used in haptic experiments



categories: choice, based on the selection of the correct object, and grasp, based on subjects ability to lift the object within three attempts.

In order to test for statistical significance of the results, the effects of the main factors (feedback modality and object pair) as well as the effects of their interaction must be analyzed. Since our data are binomial, and non-normally distributed, a classic two-way repeated measures ANOVA approach is not applicable; at the same time a Fisher-test for proportions can not be used since it does not take into account the within subject versus between subject variability and the interaction effect between main factors. For these reasons, results were processed using Generalized Linear Mixed Models (GLMM), which are proven to be useful for the analysis of clustered/binomial data [203–206]. GLMMs are a generalization of the Generalized Linear Models (GLMs) (see e.g. [207]) and they incorporate fixed and random effects, for example, the fixed effects of feedback modality and object pair and the random effect of a heterogenous sample. In this manner a single model is estimated across all subjects. Let Y be the dichotomous response variable (1 for a successful trial or 0 otherwise), whose values can be regarded as observations from the binomial distribution, with $i : 1 \dots N$ subjects and $j = 1 \dots n_i$ repeated observations nested within each subject. In this case a classic mixed-effect logistic regression model can be used, whose formulation within the general GLMM framework can be expressed as

$$P(Y_{i,j} = 1 | \nu_i, x_{ij}, z_{ij}) = g^{-1}(\eta_{ij}) = \Psi(\eta_{ij}) \quad (8.13)$$

where η_{ij} , the linear predictor, is given as: $\eta_{ij} = x_{i,j}^T \beta + z_{ij}^T \nu_i$. $x_{i,j}$ is the vector of regressors, β contains the fixed effect coefficients,⁴ $z_{i,j}$ is the vector of variables having random effects and ν_i the vector of random effects. g is the link function, which relates the response variables to the linear predictors. In this case such a function is the *logit* function,

$$g(\mu_{ij}) = \text{logit}(\mu_{ij}) = \log \left[\frac{\mu_{ij}}{1 - \mu_{ij}} \right] = \eta_{ij} \quad (8.14)$$

where $\mu_{ij} = E(Y_{ij} | \nu_i, x_{ij})$ is the conditional expectation of the response variable, which equals $P(Y_{ij} = 1 | \nu_i, x_{ij})$, i.e. the conditional probability of a response given the random effects. $\Psi(\eta_{ij})$ is the inverse link function, in this the logistic cumulative distribution function (*cdf*). For a more detailed description of GLMMs see e.g. [206, 208, 209], while for a review on the approaches for the processing of the random effects on dichotomous data see [210].

⁴Usually the intercept of the fit model is indicated by β_0 .

8.6 Results

8.6.1 Interaction Torque Observer

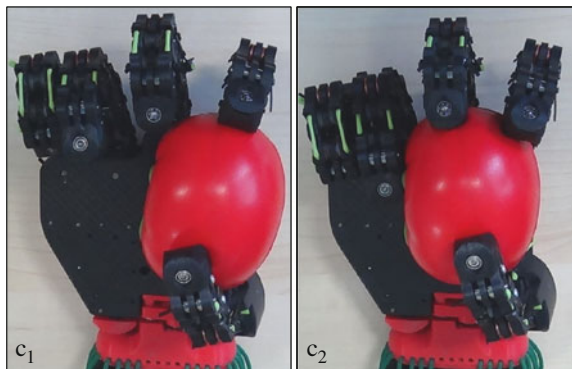
In order to validate the accuracy of the identified hand model, the hand controller was provided with a sine wave position trajectory. The trajectory led to the execution of four SoftHand half-closure and full-opening movements. A soft, deformable ball was grasped during the second and third closures and removed on the first and the last. By pre-determined placement of the soft obstacle along the hand closure, the hand conformed around the obstacle with two (Fig. 8.10c₁) or three fingers (Fig. 8.10c₂) contacting the object, causing small deformations on the ball's surface. The motor current (I_{ext}) was measured and used for the detection of contact and estimation of the interaction torque during the grasping of the ball.

Figure 8.11 illustrates the results of this experiment. The top three plots demonstrate the position tracking, motor current, and motor voltage profiles, from the top down. Observed interaction torques once the soft obstacle is squeezed by two (c₁) or three (c₂) fingers are provided in the bottom plot. During the first and last closures, the fingers did not contact the object, resulting in low interaction torques. In addition, although a soft and deformable obstacle was grasped by only two or three fingers, interaction torque fluctuations were efficiently monitored.

8.6.2 Grasping Experiments

As noted above, five subjects participated in grasping experiments. Subjects were able to grasp objects with different elastic properties with all controllers (see Sect. 8.5 for details of the setup), but had a higher failure rate with the Compliant controller than the Stiff or Teleimpedance controllers. However, the Stiff controller caused undesired deformations in the surface of soft objects. These deformations were not observed in

Fig. 8.10 The SoftHand molds around the obstacle by two (c₁) and three (c₂) fingers, during grasping



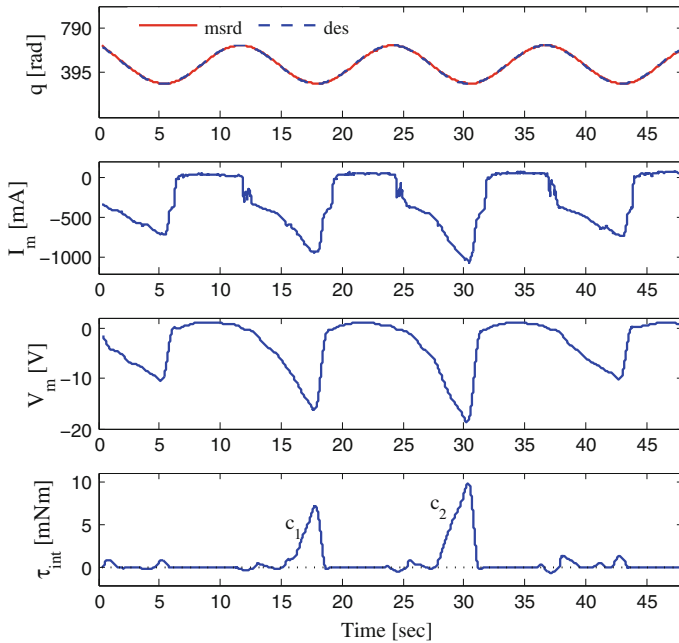


Fig. 8.11 Results of a grasping experiment with fixed stiffness gain. A soft, deformable ball was used as an object to grasp during the second and third closures and removed on the first and the last. The top three plots demonstrate the position tracking, motor current and motor voltage profiles, from the top down. Observed interaction torques once the soft obstacle was squeezed by two (c_1) or three (c_2) fingers are provided in the bottom plot

the experiments in which the hand controller was running under Teleimpedance and Compliant modes. In the latter, subjects were able to shape the SoftHand around all objects, but were unable to reliably lift heavy and low-friction objects (e.g. mug and ball) due to low levels of grasp force resulting in object slippage on lift. Nevertheless, it is worth noting that, since the motor is provided with estimated hand disturbance current (I_{dist} , see Fig. 8.7), fairly good position tracking is achieved even when the SoftHand is operated under the Compliant controller.

Typical results of an experiment, in which the subject grasped a rigid object (mug) are illustrated in Figs. 8.12 and 8.13. Here, the SoftHand was executed under Stiff (Fig. 8.12a), Compliant (Fig. 8.12b) and Teleimpedance (Fig. 8.13) controllers. The top and middle plots contain the desired and measured postural synergy references (upper portion of each) and the observed interaction torques between the hand and the grasped object (lower portion of each) for Stiff and Compliant controllers, respectively. Muscular activities of the subject with the SoftHand under Teleimpedance control are illustrated in the third plot, Fig. 8.13. The stiffness synergy reference, K_s , as a result of subject co-contractions is normalized to the chosen maximum stiffness gain (50 N m/rad) and depicted in the bottommost portion of Fig. 8.13.

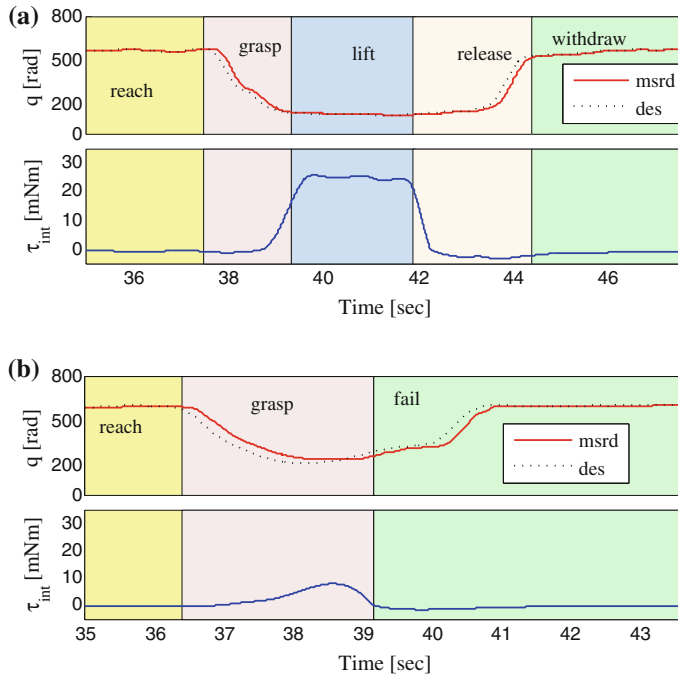


Fig. 8.12 Experimental results of the SoftHand grasping a hard object (mug), with the controller under **a** high, fixed stiffness gain ($K = 40 \text{ Nm/rad}$), **b** low, fixed stiffness gain ($K = 10 \text{ Nm/rad}$ for this subject)

As shown in the plots, high interaction forces are realized once the grasp is executed with the Stiff controller under high, fixed gain. Such behavior is not desirable when grasping fragile or soft objects and can cause damage or deformation, either to the object or the prosthesis itself. In addition, abrupt changes in interaction forces are seen due to the rigidity of the hand. On the other hand, the Compliant controller with reduced stiffness gain produced lower interaction forces but was unable to provide the grasp forces required to complete the task.

Unlike the Compliant and Stiff cases, user-modified compliance of the hand used in Teleimpedance control, together with the postural synergy profiles, provides the possibility of adjusting task-related grasp forces (Fig. 8.13). With this controller, lower co-contractions resulted in high compliance, allowing gentle grasping of fragile or deformable objects (see Fig. 8.15), while higher stiffness values were generated with higher co-contractions to grasp heavier or more rigid objects. This feature enables smooth modulations of the grasp forces, in contrast with the Stiff controller, while still allowing task completion. Figure 8.16a shows the average interaction forces across subjects and objects grasped with each controller. The SoftHand teleimpedance controller was also tested with activities of daily living

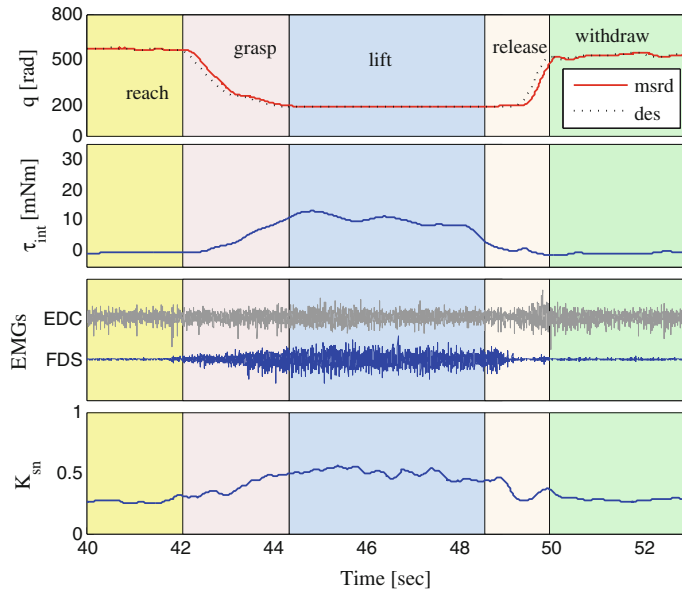


Fig. 8.13 Experimental results of the SoftHand grasping a hard object (mug), with the controller under teleimpedance ($a_{q_{norm}} = 1$, $b_q = 5.03$, $a_k = 1.87$, and $b_k = 0.579$, for this subject)

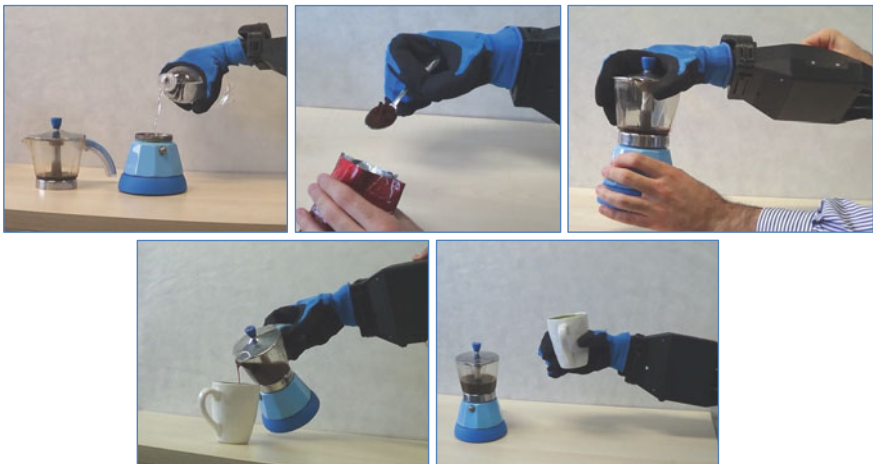


Fig. 8.14 SoftHand making an espresso

(e.g. opening and closing a jar lid, etc.). In Fig. 8.14, a subject uses the SoftHand to demonstrate the steps to make an espresso.

As noted before, observed interaction forces were fed back to the users by a haptic interface to provide information about grasping forces. The effect of such

Fig. 8.15 Grasping delicate objects



haptic feedback on muscular activity levels was tested in conjunction with the above controller tests. Figure 8.16b shows the effect of feedback on cocontraction (FDS + EDC) EMG levels during Teleimpedance; lower cocontraction levels with feedback suggest a reduction in physiological load. A video of the experiments is available at [26].

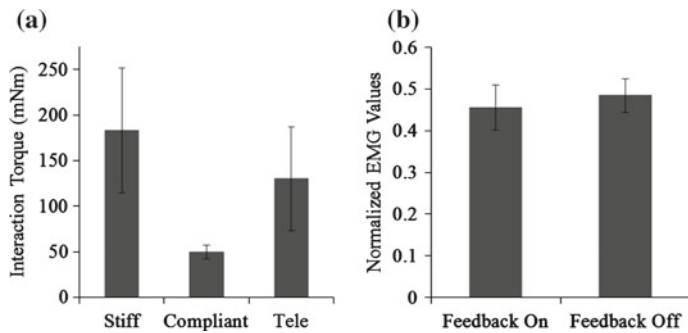


Fig. 8.16 **a** Average interaction forces for five subjects grasping different objects with SoftHand controlled under Stiff, Compliant and Teleimpedance controllers. **b** Average processed EMG signals for five subjects, grasping different objects. The averaging was performed on all trials either with or without the effect of interaction force feedback in Teleimpedance experiments

8.6.3 Haptic Experiments

As described in the Experimental Setup section above, we used a GLMM to analyze the Haptic Experiment results. The explanatory variables we used as regressor (in η_{ij}) are the two main factors we want to investigate: feedback modality (Fd)—with the levels *Full*, *Half* and *Mech*—and the object pairs subjects were asked to grasp/explore (Ob)—with the levels *Obvious*, *Mid*, *Subtle*. GLMMs models were fit to grasp and haptic data: (1) in the first model ($Fd * Ob$) both the main effects and their interaction were taken into account; (2) in the second model ($Fd + Ob$), only main effects without interaction were considered. Based on maximum likelihood (ML), we estimated parameters (fixed effect coefficients, hereinafter *Coefficients*) for both models, using the Gauss-Hermite quadrature or Laplace approximation in R⁵ package *lme4* [211]. The function *glmer* provides adjustments to fixed effects of the model for each subject. No significant difference ($p > 0.4$) was found between the fit of the two models using the Likelihood Ratio test (LR) [206]. Furthermore model ($Fd + Ob$) exhibits the minimum value for the Akaike Information Criterion (AIC [212]), in both sets of data. Note that, AIC value furnishes a criterion for model selection: the preferred model is the one with the minimum AIC value. These observations lead us to use model($Fd + Ob$), which is simpler than $Fd * Ob$ and to disregard any interaction between the two factors. In the following, we report results of data fitting, where fitting coefficients (β) for the fixed effects are listed along with their significance assessed by Wald statistics. Note that the coefficients obtained by means *glmer* provide contrasts between the indicated level and the omitted reference level. For both types of data, we considered two reference levels for the main factors: *Full* for the feedback modality and *Mid* for the object pair (cfr. Tables 8.2 and 8.4, for haptic and grasp data, respectively) and *Half* for the feedback modality and *Obvious* for the object pair (cfr. Tables 8.3 and 8.5, for haptic and grasp data, respectively). For the haptic data, results indicate a significant positive effect of factor level *Full* compared with *Mech*, suggesting a significant effect of the full vibrotactile feedback compared with the purely mechanical one. This same positive effect was observed for *Half* w.r.t *Mech*, and *Half* w.r.t *Full*, although these were not significant. For Object Pair, significant positive effect of *Obvious* w.r.t *Subtle* and *Subtle* w.r.t *Mid*, and highly significant positive effect of *Obvious* w.r.t *Mid* were also observed. Such differences in significance levels might indicate a difficulty in the discrimination for the middle object pair, which might be solved by increasing the training period for subjects during the experiments, while they manipulate different object pairs.

Analogous results were obtained with grasp data, where a positive highly significant effect of factor level *Full* compared with *Mech* was observed, suggesting a significant effect of the full vibrotactile feedback compared with the purely mechanical one for grasp actions. Same positive effect was observed for *Half* w.r.t *Mech*, and *Full* w.r.t *Half*, although non-significant. For the objects, positive significant effects of *Mid* w.r.t *Subtle* and highly significant positive effect of *Obvious* w.r.t *Mid*

⁵The R Project for Statistical Computing—see www.r-project.org.

Table 8.2 Results of the fit of *Fd + Ob* model using *glmer* function

| Coefficients | Estimate | Std. error | z value | Pr (> z) | |
|--------------|----------|------------|---------|-----------|-----|
| (Intercept) | 4.0454 | 0.8345 | 4.848 | 1.25e-06 | *** |
| Half | -0.6394 | 0.5757 | -1.111 | 0.266755 | |
| Mech | -1.1153 | 0.5544 | -2.012 | 0.044266 | * |
| Mid | -2.6524 | 0.7767 | -3.415 | 0.000638 | *** |
| Subtle | -1.6544 | 0.8091 | -2.045 | 0.040873 | * |

The fit was applied to data of haptic discrimination experiment. Reference levels are *Full* and *Obvious*. In the first column the *Coefficients* are reported, then their estimate and standard (Std) error. The z values refer to the standard normal distribution Z used to get the p-values reported in the last column (Wald statistics). Signif. codes: 0 ***, 0.001 **, 0.01 *, 0.05, 0.1, 1

Table 8.3 Results of the fit of *Fd + Ob* model using *glmer* function

| Coefficients | Estimate | Std. error | z value | Pr (> z) | |
|--------------|----------|------------|---------|-----------|-----|
| (Intercept) | 0.7536 | 0.4080 | 1.847 | 0.064774 | . |
| Full | 0.6394 | 0.5757 | 1.111 | 0.266758 | |
| Mech | -0.4759 | 0.4917 | -0.968 | 0.333123 | |
| Obvious | 2.6524 | 0.7767 | 3.415 | 0.000638 | *** |
| Subtle | 0.9980 | 0.4639 | 2.151 | 0.031448 | * |

The fit was applied to data of haptic discrimination experiment. Reference levels are *Half* and *Mid*. In the first column the *Coefficients* are reported, then their estimate and standard (Std) error. The z values refer to the standard normal distribution Z used to get the p-values reported in the last column (Wald statistics). Signif. codes: 0 ***, 0.001 **, 0.01 *, 0.05, 0.1, 1

Table 8.4 Results of the fit of *Fd + Ob* model using *glmer* function

| Coefficients | Estimate | Std. error | z value | Pr (> z) | |
|--------------|----------|------------|---------|-----------|-----|
| (Intercept) | 2.6804 | 1.2114 | 4.633 | 3.61e-06 | *** |
| Half | -0.7647 | 0.6335 | -1.207 | 0.227379 | |
| Mech | -2.1214 | 0.6021 | -3.523 | 0.000427 | *** |
| Mid | -2.9315 | 1.1052 | -2.653 | 0.007990 | ** |
| Subtle | -3.8765 | 1.0983 | -3.530 | 0.000416 | *** |

The fit was applied to data of grasp experiment. Reference levels are *Full* and *Obvious*. In the first column the *Coefficients* are reported, then their estimate and standard (Std) error. The z values refer to the standard normal distribution Z used to get the p-values reported in the last column (Wald statistics). Signif. codes: 0 ***, 0.001 **, 0.01 *, 0.05, 0.1, 1

and *Obvious* w.r.t *Subtle* were also observed. These results suggest full vibrotactile feedback modality enhances both haptic discrimination and grasp actions and that object pairing also plays a significant role in both of these.

Table 8.5 Results of the fit of $Fd + Ob$ model using *glmer* function

| Coefficients | Estimate | Std. error | z value | Pr (> z) | |
|--------------|----------|------------|---------|-----------|-----|
| (Intercept) | 1.9158 | 0.5808 | 3.299 | 0.000972 | *** |
| Full | 0.7647 | 0.6335 | 1.207 | 0.227366 | |
| Mech | -1.3567 | 0.5163 | -2.628 | 0.008598 | ** |
| Obvious | 2.9316 | 1.1052 | 2.653 | 0.007989 | ** |
| Subtle | -0.9450 | 0.4678 | -2.020 | 0.043360 | * |

The fit was applied to data of grasp experiment. Reference levels are *Half* and *Mid*. In the first column the *Coefficients* are reported, then their estimate and standard (Std) error. The z values refer to the standard normal distribution Z used to get the p-values reported in the last column (Wald statistics). Signif. codes: 0 *** , 0.001 ** , 0.01 * , 0.05 , 0.1 , 1

8.7 Discussion

In this chapter, a novel synergy-based teleimpedance controller was developed to gather the user's postural and stiffness synergy references from two EMG channels. Two nonlinear functions were utilized in order to establish the mapping between the EMGs and the postural and stiffness synergies. This was followed by a parameter identification process. Resulting synergy commands were then tracked by the developed SoftHand controller in realtime.

In addition, two haptic interfaces (Mechano- and vibro-tactile) were developed to facilitate natural control of the prosthetic limb. The mechanotactile interface was employed to provide the user with information on grasp forces, to enable intuitive modulations of task-required forces. While the vibrotactile interface was developed to provide the user with information about object slippage and perception of surface properties such as texture.

The efficiency of the novel synergy-driven teleimpedance controller, while employing haptic interfaces, was evaluated through two sets of experiments. The first set was designed to assess the capabilities of the teleimpedance controller with force feedback in natural grasping. Incorporation of the above features resulted in robust and reliable grasps, regardless of the elastic properties of the grasped object. This was achieved since the subjects were able to modify the task forces via modified grasp compliance and force feedback.

The second set of experiments concerned the use of two haptic interfaces with the proposed teleimpedance controller for the detection and grasping of various objects with different surface properties. From the experimental results, we can conclude that the full vibrotactile feedback modality seems to enhance both haptic discrimination and grasp actions and that there is also some evidence of significant effect of the role of object types. However, the full vibrotactile haptic feedback appears to play a more dominant role in grasp tasks than in haptic discrimination tasks. Although these results are preliminary and should be validated with a larger number of subjects and trials, they illustrate the feasibility of effective and simple haptic interfaces to control artificial robotic hands in common actions.

The mechanotactile-only results suggest meaningful texture information transfers through the device and forearm support to inform the user. However, additional feedback may provide added benefit, as seen with the full- and half-haptic results, especially in amputees where socket liners provide additional damping. The additional haptic feedback also provided benefit in blind grasping, a feature potentially useful to amputees given the current reliance on visual feedback to execute successful grasps. With respect to grasp success by object shape, it is worth noting the ease with which users grasped the cylinder and the high failure rate and variability for the sphere. Anecdotally, the SoftHand was able to mold around the cylinder from a myriad of starting positions. In comparison, subjects would misalign the SoftHand with the sphere, resulting in object slippage before lift off or orient the SoftHand palm at the top of the sphere, resulting in the fingers failing to reach the sphere. This phenomenon is likely also attributable to the large size of the spheres tested; smaller and/or more compliant spheres would lend themselves to a wider variety of grasping strategies and likely have higher grasp success rates. Grasping of the sphere was best with full-haptic feedback, likely because users were better able to understand the position of the SoftHand relative to sphere.

In the future, further investigation of optimal stimulation sites and spacing for various feedback modalities will be examined and this investigation will be extended to amputees. While these results need to be validated with amputees, they provide some evidence that a low-cost, robust hand employing hardware-based synergies might be a good alternative to traditional myoelectric prostheses. Furthermore, they illustrate the benefits of incorporating tactile interfaces for more intuitive control of the SoftHand.

Part IV

**Teleimpedance Control of a Compliant
Knee Exoskeleton**

Chapter 9

Teleimpedance Based Assistive Control for a Compliant Knee Exoskeleton

Assistive exoskeletons have undergone continuous technological development over the last few years. Depending on the application, such devices can augment the muscular force of healthy individuals [213], provide motion assistance to the elderly or to those with limited physical capability [214] and be used for rehabilitational purposes for patients with impaired mobility function [215, 216].

The main aspects in developing effective and high performance exoskeletons are the employed actuation technology and the pertinent control methods. This is due to the fact that exoskeletons interact physically with humans. Regarding the actuation, a step forward has been taken by introducing series elastic actuators (SEA) which can significantly decrease the output mechanical impedance of the system and intrinsically adapt to interaction and absorb impacts [217–219]. Thus, the physical human-robot interaction (pHRI) can be essentially improved. Additionally, the inserted elasticity can be utilized as a torque sensor which permits for precise force control.

Several assistive control approaches have also been proposed [220, 221], in which the manner of inferring the user's intent and the associated interpretation play a vital role. For instance, by sensing the ground forces of the foot and the joint angles [213] the required joint torques can be derived using the inverse dynamics model. In [222] a finite-state machine was developed for commanding the powered orthosis, in which only the joint angles were used in order to deduce the intended motion of the user. Another alternative is the utilization of electromyographic signals (EMGs) which are directly measured from human muscles [223, 224]. As the exoskeleton adds mechanical impedance to the legs, an inertia compensation control was proposed in [225] in order to remedy this drawback. Moreover, a very common approach that has been applied mainly in rehabilitation settings is the incorporation of predefined trajectories with either an impedance controller [216] or a variable gain controller [222] which generate corrective assistive torques. However, when employing such solutions the patients are not able to move their limbs at will.

Furthermore, as the impedance profiles of the human joints vary during motion, the employment of variable impedance systems has been deemed essential [21, 226, 227]. For instance, in [228] the impedance of the orthotic joint is modulated during the gait cycle. The concept of impedance adjustment around human joints has also been proposed in [229], where the target stiffness, damping and inertia parameters are identified with the Recursive Least Square (RLS) method. Most methods for regulating exoskeleton joint stiffness rely on either modeling, or off-line learning and optimization methods. In this work we propose instead to select and control the impedance of the exoskeleton joint based on the real-time measurement of the impedance of the corresponding human joints.

To this end, in this chapter, we present a novel control scheme for a knee exoskeleton that can provide motion assistance and also augment the stiffness of the human knee joint utilizing the user muscular activity as an input. Consequently, the user is able to intrinsically and naturally control the exoskeleton according to his/her intent. The proposed knee exoskeleton is a passive compliant device for inherently soft interaction based on the series elastic actuation (SEA) principle. Regarding the control scheme, the scope is to incorporate the variability of human joints impedance into the exoskeleton motion regulation using the concept of teleimpedance control [2, 3] (see Sect. 9.4). Particularly, we are considering that the stiffness of the exoskeleton joint should be regulated in time according to the flexibility of the corresponding human joint. In other words, the exoskeleton should provide stiffness augmentation for tracking the reference trajectory when the user stiffens his/her muscles, while presenting low levels of compliance when the operator reduces his/her muscle activation. Therefore, the transmission of the forces becomes smoother and the motion assistance more effective while the transparency and comfort of the user is significantly increased.

To achieve the above features, a musculoskeletal model of the knee joint, which takes into account the non-linear relationship between muscle activation and joint torques, has been developed. This model derives the estimated user torque and the stiffness trend index. The estimated torque is used to determine the user's intended motion and the stiffness trend index (*STI*) to realize the stiffness of the user's knee joint which is fed as the stiffness reference to the teleimpedance controller.

9.1 Musculoskeletal Model of the Knee Joint

In order to account for musculoskeletal bio-feedbacks such as muscular forces-moments, two general approaches have been proposed. Inverse dynamic methods, investigate this problem by means of measurements of the joint positions and applied external forces. However, several drawbacks are attributed to such techniques [183]. For instance, the muscles acting on each joint are grouped and divided to agonist and antagonist blocks and consequently, the external flexion and extension moments are balanced. Therefore, these methods are not reliable enough for individual estimation of muscular forces since *a priori* assumptions are made on the role of individual

muscles during the optimization of a predefined cost function [230]. The problem grows when it comes to the modeling of complex tasks which combine highly non-linear activation-contraction dynamics and geometry variations. As a result, alternative solutions which are associated with forward dynamic approaches are proposed. In these methods, neural commands are extracted and fed to the detailed musculoskeletal model of the limbs. In most of the proposed models (e.g. see [231]), which are developed based on Hill's original work [232], the overall musculoskeletal system is structured by muscle activation dynamics, muscle contraction dynamics and body-segmental dynamics sub sections. By taking into account the precision of the model-based techniques in the estimation of the knee joint stiffness trend and torque by means of antagonistic muscle torques, we exploit and re-identify a detailed musculoskeletal model of the knee joint as follows.

9.1.1 Activation Dynamics

Electromyography (EMG) signals inherit patterns of activations of involved muscles. In order to extract muscular activations, the raw EMG signals must be processed. First, these signals are high-pass filtered to remove offsets and movement artifacts. This stage is followed by full rectification techniques. Consequently, the resulting signals are low-pass filtered and normalized in order to provide traces of the neural activation of the muscles. Concerning the motor unit level, it has been observed that muscle force variations with respect to neural commands demonstrate an exponential trend [233]. As a result, activation of the muscles is defined by:

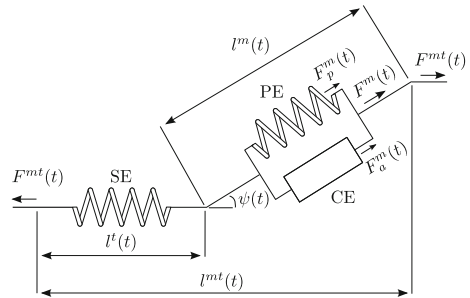
$$a_i(t) = \frac{e^{Au_i(t)} - 1}{e^A - 1} \quad (9.1)$$

where $a_i(t)$ is the activation of the muscle number i , $u(t)$ corresponds to processed EMGs and $-3 < A < 0$ is a nonlinear shape factor.

9.1.2 Contraction Dynamics

Large scale modeling of the muscular force as result of activation dynamics is widely performed based on Hill's muscle model [232] and its extension proposed by Zajac [231]. In such models, the muscle-tendon unit is modeled as a muscle fiber in series with a viscoelastic tendon (see Fig. 9.1). Muscle fiber itself is modeled by a contractile element in parallel with an elastic component. The general equation associating the

Fig. 9.1 Representation of the muscle-tendon unit based on Hill's model



generated force by the contractile element with the muscle-tendon force $F_i^{mt}(t)$ reads as follows:

$$F_i^{mt}(t) = F_i^{max} [f_i(l) f_i(v) a_i(t) + f_{p_i}(l)] \cos(\psi_i(t)) \quad (9.2)$$

where $F_i^{mt}(t) = F_i^t(t)$, with F_i^t , $f_i(l)$, $f_i(v)$ corresponding to the tendon force, normalized force-length and normalized force-velocity curves of the contractile element of muscle number i , and f_{p_i} refers to the passive elastic normalized force-length relation (see details in [231, 233]). The pennation angle, which is defined as the angle between the tendon and the muscle fibers, is denoted by $\psi_i(t)$ and can be given by the following equation:

$$\psi_i(t) = \sin^{-1} \left(\frac{l_{o_i}^m \sin(\psi_{o_i})}{l_i^m(t)} \right) \quad (9.3)$$

where $l_i^m(t)$ is the muscle fiber length and ψ_{o_i} the pennation angle at the optimal muscle length $l_{o_i}^m$.

It has been observed that the optimal muscle fiber length varies in response to activation fluctuations [233]. In order to account for such changes, we exploit the following equation:

$$l_{o_i}^m(t) = l_{o_i}^{m*} (\gamma(1 - a_i(t)) + 1) \quad (9.4)$$

where $l_{o_i}^{m*}$ represents the optimal fiber length at maximum activation and γ is the percentage change in optimal fiber length, chosen 15 % [233].

Dense body of literature reports on the linear relationship between the tendon slack length l_s^t , tendon force and the tendon length l^t . Such mapping is shown to be valid for $l^t > l_s^t$ [183, 233]. Here, same assumptions have been taken into account in order to model the tendon length. In addition, we can write:

$$l_i^t(t) = l_i^{mt}(t) - l_i^m(t) \cos(\psi_i(t)) \quad (9.5)$$

with l^{mt} denoting the muscle-tendon length.

9.1.3 Musculoskeletal Geometry

The lengths of the muscle-tendon complexes acting on the knee joint are shown to be functions of the knee joint angle [234]. In these works, the muscle length values were fitted to a second order polynomial by means of least squares optimization technique. Consequently, $\bar{l}_i^{mt}(t)$ which accounts for the percentage of segment length (the origin to insertion length relative to its length in full extension of the knee) is defined and identified as follows:

$$\bar{l}_i^{mt}(t) = C_{0i} + C_{1i}\theta_{knee}(t) + C_{2i}\theta_{knee}^2(t) \quad (9.6)$$

where θ_{knee} represents the knee joint angle in degrees and C_{0i} , C_{1i} and C_{2i} are constants (see [234] for details). By adopting (9.5) and (9.6) the muscle fiber length will be identified and used for the estimation of the activation and contraction dynamic models.

The muscle moment arms $r_i(t)$ of the muscle-tendon unit can be described based on the displacements method proposed in [235] which is defined by:

$$r_i(t) = \frac{\partial l_i^{mt}(t)}{\partial \theta_{knee}}. \quad (9.7)$$

Consequently, the moment arms are determined as follows:

$$r_i(t) = [C_{1i} + 2C_{2i}\theta_{knee}(t)] \frac{180}{\pi}. \quad (9.8)$$

Once we have estimated the forces (9.2) and the moment arms (9.8) of all chosen muscles acting on the joint, we are able to convert the muscle forces to joint torques τ by means of the following equation:

$$\tau(t) = \left| \sum_{i=1}^n \tau_i(t) \right|_{agonist} - \left| \sum_{j=1}^k \tau_j(t) \right|_{antagonist} \quad (9.9)$$

where $\tau_i(t) = F_i(t)r_i(t)$, $\tau_j(t) = F_j(t)r_j(t)$ with n and k being the number of agonist and antagonist muscles acting on the joint, respectively.

It has been shown that a simultaneous increase in antagonistic muscle torques acting on the joint, does not affect the joint torque (as seen in (9.9)) although does increase joint stiffness [236]. Therefore, we can define the stiffness trend index (STI) as:

$$STI(t) = \left| \sum_{agonist} \tau_i(t) \right| + \left| \sum_{antagonist} \tau_j(t) \right| \quad (9.10)$$

and the stiffness of the knee joint as:

$$K(t) = \alpha \times STI(t) + \beta \quad (9.11)$$

where α (rad^{-1}) and β (N m/rad) are to be identified constants.

9.2 Model Identification-Calibration

Several caveats apply to the forward dynamic methods, described in Sect. 9.1. To begin with, concerning the EMG signals, one must take into account reliable post-processing techniques in order to maximize robustness of the estimation of muscular activations. For instance, day-to-day and subject to subject variations, temperature and humidity fluctuations, electrode misplacement, crosstalk between signals and movement artifacts will give rise to inaccuracy and drift of the estimated signals. Furthermore, the model parameters (9.2)–(9.6) vary among subjects.

For minimizing the modeling uncertainty, the parameters of the model must be re-identified based on each user's experimental data. For this reason, we have set up identification-calibration experiments to re-identify the parameters as described below.

9.2.1 Model Identification Experiments

One healthy subject (male, 27 years old) participated in identification-calibration experiments. Three antagonistic muscle groups (six muscles) which are denoted as being the dominant surface muscles acting on the knee joint were chosen in order to form the musculoskeletal model of the knee joint. Six electrodes (Bagnoli-16, Delsys Inc.) were attached to the extensor [rectus femoris (RF), vastus medialis (VM) and vastus lateralis (VL)] and flexor [biceps femoris (BF), semimembranous (SM) and semitendinosus (ST)] muscles. The raw EMG signals were processed (at 1 kHz) and the muscular activities were estimated during the identification experiments as well as during the teleimpedance control experiments that are to be described in Sect. 9.4.

The initial values of the model parameters (peak force, optimal fiber length, optimal slack length, pennation angle, nonlinear shape factor and other constants) were extracted from the literature [183–230, 232–235]. In order to chose the number of parameters to be re-identified, one must consider the reasonable tradeoff between modeling uncertainty and identification complexity. Hence, seven constant parameters of each muscle referring to the activation and contraction dynamics and muscle-tendon geometry were chosen to be adjusted relying on identification experiments. The chosen parameters were F^{max} , ψ_o , l_o^m , A , C_0 , C_1 and C_2 .

During the identification experiments, the subject was wearing the knee exoskeleton while having the EMG electrodes attached. In order to take into account the mus-

cle activation of both the knee flexor and the extensor in the model identification, we performed two tasks that involved each of the antagonistic group of muscles separately. During the first task the subject assumed a stand posture (equilibrium position of exoskeleton set to 0°) and was instructed to repeatedly flex and extend his right knee with the minimum possible contraction (flexor contribution) while during the second task the subject was seated (equilibrium position of exoskeleton set to 90°) and was asked to repeatedly extend and flex his knee with minimum contraction as well (extensor contribution). An impedance controller was implemented on the exoskeleton joint and both tasks were executed for stiffness level varying from 0 to 200 N m/rad in intervals of 40 N m/rad. Thus, the torque applied by the human during the movement is given by the following equation:

$$\hat{\tau}_h = \tau_e + \tau_g = \tau_s + (m_{sh} + m_{lseg})gl_{com} \sin(\theta_{knee}) \quad (9.12)$$

where τ_e is the torque applied by the exoskeleton and equals to the measured elastic torque τ_s , τ_g the gravitational torque, m_{sh} the mass of shank, m_{lseg} the mass of the lower segment of the exoskeleton and l_{com} the center of mass of the combined lower link and shank. Two trials were recorded for each stiffness step. Even trials were chosen for the identification while the odd ones were kept for evaluative analysis of the identification procedure. Movements were carried out at low knee angular velocity and acceleration. For this reason, the inertial moment effects were negligible in our setup.

The six-channel processed EMGs data together with the torques $\hat{\tau}_h$ and τ_e were used in order to identify the musculoskeletal model parameters, described in Sect. 9.1. Due to the nonlinear dependency between the knee joint torque and the corresponding muscular activities, the nonlinear least square algorithm is utilized for the identification of the model parameters while being constrained to $\pm 10\%$ above/below of their nominal values.

9.2.2 Model Validation

Typical results of the validation of the identified model by means of extension and flexion test trials are demonstrated in Fig. 9.2a, b, respectively. The trial in Fig. 9.2a performed with the exoskeleton stiffness being at 40 N m/rad while the trial in Fig. 9.2b being at 60 N m/rad. As is shown in the upper plots, the model provides reasonable tracking of the knee joint torque ($\tau_e + \tau_g$). In addition, the position of the knee joint θ_{knee} is depicted in the upper plots. The corresponding fully rectified EMG signals are presented in the lower plots of the figures. The normalised root mean square error (NRMSE) across all test trials (extension and flexion), resulted in an average value of 12.4 %.

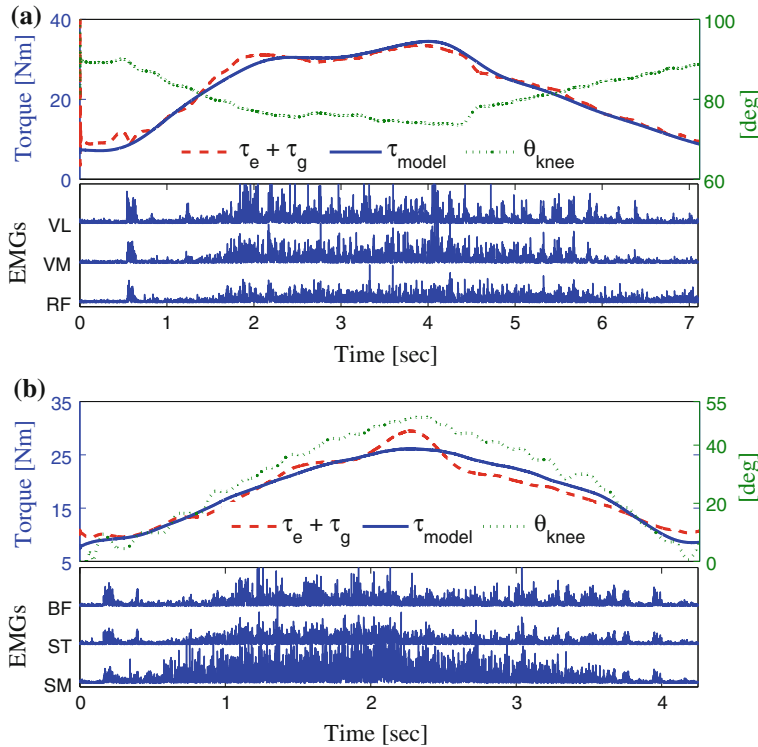
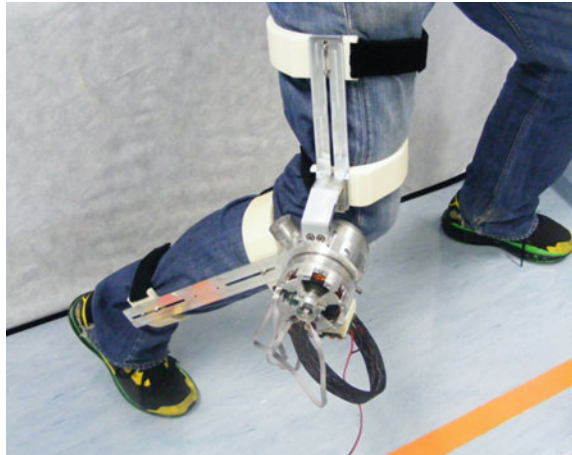


Fig. 9.2 Comparison of the estimated torque of the knee joint and the one derived from the musculoskeletal model in extension (a) and flexion (b) identification trials. Red (dashed) and blue (solid) lines in the upper plots demonstrate the actual and estimated knee torque profiles. Corresponding knee angle trajectories during extension (a) and flexion (b) are plotted in green (dotted). Lower plots demonstrate fully rectified EMG activities of the three dominant extensor (a) and flexor (b) muscles

9.3 Knee Exoskeleton Hardware

As illustrated in Fig. 9.3, the proposed knee exoskeleton consists of two link segments (upper and lower) which are fixed to the thigh and the shank, respectively and the rotational actuation system (CompAct-RS) which drives the joint. The exoskeleton is mounted on the user leg with the axis of rotation of the exoskeleton joint aligned with the axis of the user knee joint. Ensuring perfect alignment in practice during operation may not though be possible. Small misalignments are accommodated by the elasticity in the interface of the upper and lower links with the thigh and the shank, respectively. This is realized by means of rigid braces and Velcro straps with the latter incorporating certain level of compliance. Hence, in this manuscript the axis of the subject knee joint θ_{knee} is considered to be aligned to the axis of the exoskeleton joint q . The location of the braces can be adjusted along the structure to accommodate different

Fig. 9.3 The intrinsically compliant knee exoskeleton device



leg sizes. Particular attention was paid to fast and easy donning and doffing (estimated less than one minute). Moreover, the range of motion of the knee exoskeleton in the sagittal plane is between 0° and 120° where 0° corresponds to full extension of the knee. Mechanical locks ensure that the actuator operates within this motion range and render the exoskeleton safe to use.

9.3.1 Mechatronic System

The knee exoskeleton is powered by a series elastic actuator with offline reconfigurable stiffness. The CompAct-RS [237, 238] operation is based on the lever arm mechanism with a variable pivot axis (see Fig. 9.4). CompAct-RS comprises two main subassemblies. The elastic module that embodies the lever arm mechanism with the reconfigurable pivot point and the motor module. The elasticity is provided by two compression springs which have been installed pre-compressed to half of their maximum deflection. Note that the location of the pivot point can be adjusted manually by tuning two set screws (see Fig. 9.5a). For this work, the pivot point was set to a position that corresponded to a stiffness value at $K_S = 200 \text{ N m/rad}$ that was suitable for the execution of the experiments which are described in Sects. 9.2 and 9.6.

The elastic module employs one 16 bit optical encoder (Avago Technologies) which monitors the angular deflection of the output link and a potentiometer which measures the location of the pivot point. The presence of the passive elastic element allows us to avoid the use of an additional torque sensor (which is delicate and expensive), as the elastic torque τ_s is given by the following equation:

$$\tau_s = -K_S(\theta_s)\theta_s. \quad (9.13)$$

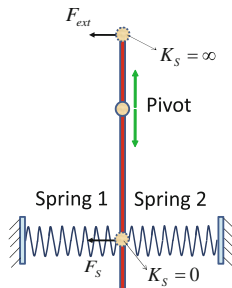


Fig. 9.4 Functional principle of CompAct-RS; Stiffness can be adjusted theoretically from zero to infinite by varying the position of the pivot

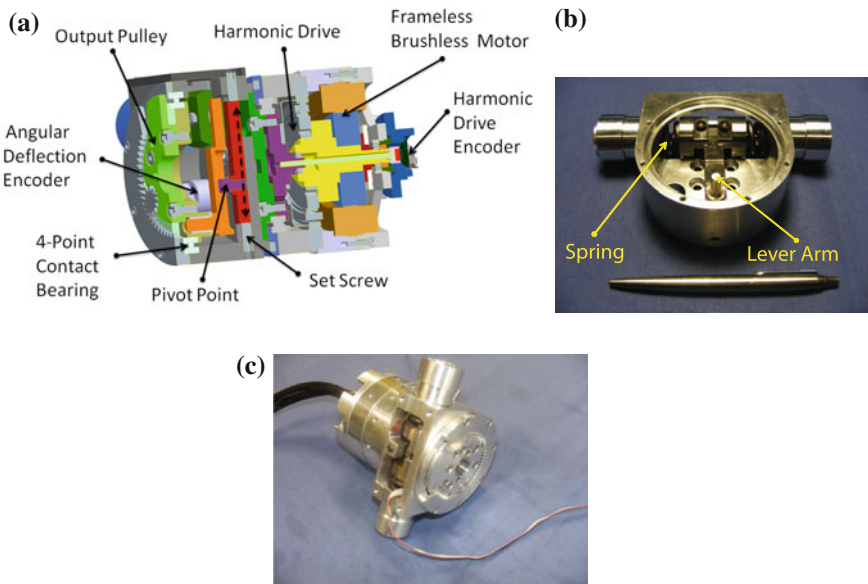


Fig. 9.5 **a** Section of the CAD assembly of CompAct-RS and its components. **b** View of the elastic module. **c** Overall view of CompAct-RS

The second subassembly includes a frameless brushless DC motor (Kollmorgen), a harmonic drive CSD 25 with gear ratio 100:1, one optical incremental encoder (MicroE Systems with 12 bit of resolution) for measuring the position of the motor and one 12 bit magnetic absolute encoder (Austria Microsystems) which monitors the position of the motor after the harmonic drive. In Table 9.1 are shown the mechanical specifications of the CompAct-RS.

Table 9.1 Specifications of CompAct-RS

| Description | Symbol | Value | Unit |
|---------------------------|------------|-----------|--------|
| Elastic torque (Max) | τ_s | 80 | Nm |
| Torque of motor (Max) | τ_M | 1.53 | Nm |
| Elastic deflection (Max) | θ_s | 11 | deg |
| Elastic energy (Max) | U_s | 5.5 | J |
| Allowable stiffness range | K_S | 200 ~ 800 | Nm/rad |
| Diameter | D_A | 90 | mm |
| Overall length | L_A | 135 | mm |
| Total weight | W_A | 2.1 | kg |

9.4 Teleimpedance Based Assistive Control

Impedance controlled systems generate forces in reaction to imposed motions. As these systems have been deemed capable of interacting with unknown environments, they have found wide application in lower limb exoskeletons and orthoses. For instance, ANdROS [239] utilizes an impedance controller by applying corrective torques to the wearer's knee based on the deviation from a reference trajectory. On the other hand, adaptive control has been also used to command a powered orthosis in order to introduce adaptation to the parameters of the human-orthosis dynamic system [228, 240]. Note that in the proposed control scheme there is no need to identify the parameters of the human-exoskeleton physical system.

Teleimpedance as an alternative method to unilateral position based control or bilateral force reflecting control was previously proposed during teleoperated tasks which require significant dynamics variation or being performed in uncertain remote environments. The algorithm provides the robot with task-related stiffness profile in addition to position-orientation trajectories [2, 3]. In order to realize the concept of teleimpedance control, an impedance controller was designed and implemented in the exoskeleton's actuator. It is composed by an outermost position loop and an inner torque loop while the exoskeleton joint torque is obtained by measuring the deflection of the intrinsic elasticity (see also Sect. 9.3). The impedance reference followed by the impedance controller is:

$$Z_c = K_c + B_c s \quad (9.14)$$

where K_c , B_c represent the stiffness and the damping parameters of the impedance reference, respectively.

A fundamental aspect when designing assistive control strategies is the detection of the user's intent and the associated interpretation. Here, the user's intention of motion is derived from the estimated user torque $\hat{\tau}_h$. The musculoskeletal model described in Sect. 9.1 uses as inputs the rectified EMGs and the knee angle q and outputs the estimated user torque $\hat{\tau}_h$ and the stiffness trend index STI (see Fig. 9.6).

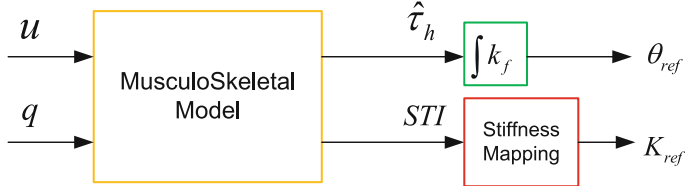


Fig. 9.6 Schematic of the derivation of the position and the stiffness reference

These two outputs are then used for the derivation of the position and stiffness reference of the knee exoskeleton joint. Particularly, to generate assistive torques towards the direction of motion we select to update the equilibrium position of the knee exoskeleton joint in accordance to the user's intended motion, the equilibrium of which is obtained from the estimated user torque $\hat{\tau}_h$ using the following formula:

$$\theta_{ref} = \begin{cases} \int k_f (\hat{\tau}_h - a) dt & \hat{\tau}_h > a \\ 0 & -a < \hat{\tau}_h < a \\ \int k_f (\hat{\tau}_h + a) dt & \hat{\tau}_h < -a \end{cases} \quad (9.15)$$

where k_f and a are the sensitivity constant and the noise dead band constant, respectively.

To obtain the stiffness reference of the knee exoskeleton the stiffness trend index (STI) from (9.10) is mapped to a desired stiffness range that is defined according to the task requirements. Thus, the identification of α and β in Eq. (9.11) is task-oriented. In this manuscript, the desired stiffness range is determined experimentally based on a satisfactory assistance performance related to the motion task (see Sect. 9.6). As illustrated in Fig. 9.7, the position and stiffness reference described above feed the

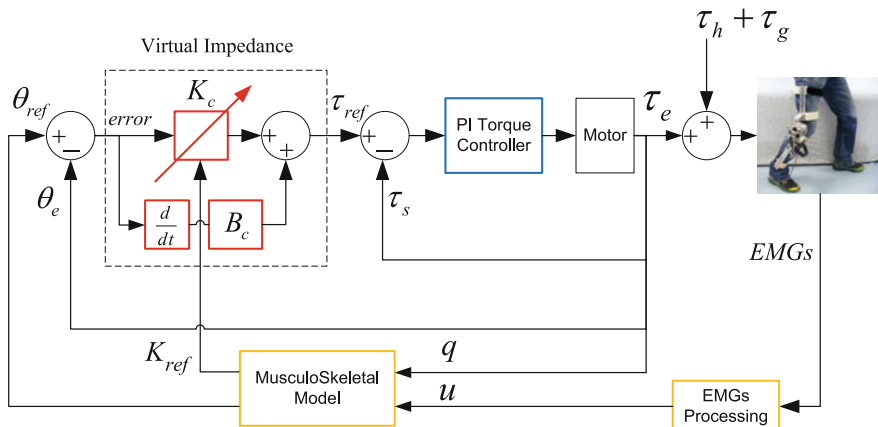


Fig. 9.7 Block diagram of the implemented teleimpedance controller that provides stiffness augmentation based on human stiffness trend

equilibrium position and the active stiffness of the teleimpedance controller, respectively. By deriving the equilibrium position of the controller from (9.15), assistive forces augment the user desired actions/motions via the virtual impedance Z_c . Additionally, the exoskeleton device is able to provide stiffness augmentation to the user on the basis of his/her stiffness trace with the purpose of achieving effective assistance when is needed or to present low level of compliance when the muscle activation of the user is low for increasing transparency and comfort.

9.5 The Human-Exoskeleton System Dynamics for the Standing-Up Motion

9.5.1 System Modeling and Simulation

A simplified human body model of 1-DOF in the sagittal plane coupled with the knee exoskeleton is considered in order to derive the dynamics of the overall human-exoskeleton system during the standing-up motion (see Fig. 9.8). The external torques acting on the system are formed by the exoskeleton's actuator torque τ_e , the human muscle torque τ_h and the gravitational torque τ_g as shown in Fig. 9.9. During the sitting to standing transition the system motion can be described by the following equation in matrix form:

$$\begin{bmatrix} I_h & 0 \\ 0 & I_e \end{bmatrix} \begin{bmatrix} \ddot{q} \\ \ddot{\theta}_e \end{bmatrix} + \begin{bmatrix} B_h & 0 \\ 0 & B_e \end{bmatrix} \begin{bmatrix} \dot{q} \\ \dot{\theta}_e \end{bmatrix} + \begin{bmatrix} K_S & -K_S \\ -K_S & K_S \end{bmatrix} \begin{bmatrix} q \\ \theta_e \end{bmatrix} = \begin{bmatrix} \tau_h - m_h g l \sin q \\ \tau_e \end{bmatrix} \quad (9.16)$$

where $\theta_e = \frac{\theta_m}{N}$, $\dot{\theta}_e = \frac{\dot{\theta}_m}{N}$ are the position and velocity of the exoskeleton motor, respectively reflected at the link side after the gear reduction ($N = 100 : 1$). In addition, $I_e = N^2 J_m$ denotes the reflected motor inertia after the reduction drive while $B_e = N^2 B_m$ is the damping of the exoskeleton motor reflected also after the reduction drive. Moreover, q and \dot{q} refer to the position and velocity of the knee joint, while I_h denotes the combined inertia of the human body (masses of the torso, pelvis and thigh are combined into a single body of inertia I_h and mass m_h). Finally, l refers to the distance from the knee joint center to the center of the combined human body mass.

To validate the operational concept of the teleimpedance based assistive control simulation studies were conducted on the 1-DOF system shown in Fig. 9.9. The estimated torque $\hat{\tau}_h$ and the stiffness reference K_{ref} , that were recorded during the experiment described in Sect. 9.6, were used as inputs of the simulation model. Additionally, the combined mass of the human body was set as $M_h = 30\text{ kg}$. The viscous damping of the knee joint varies significantly with muscle contraction and knee flexion angle and is reported to be within the range 1–5 Nms/rad [241, 242]. Based on

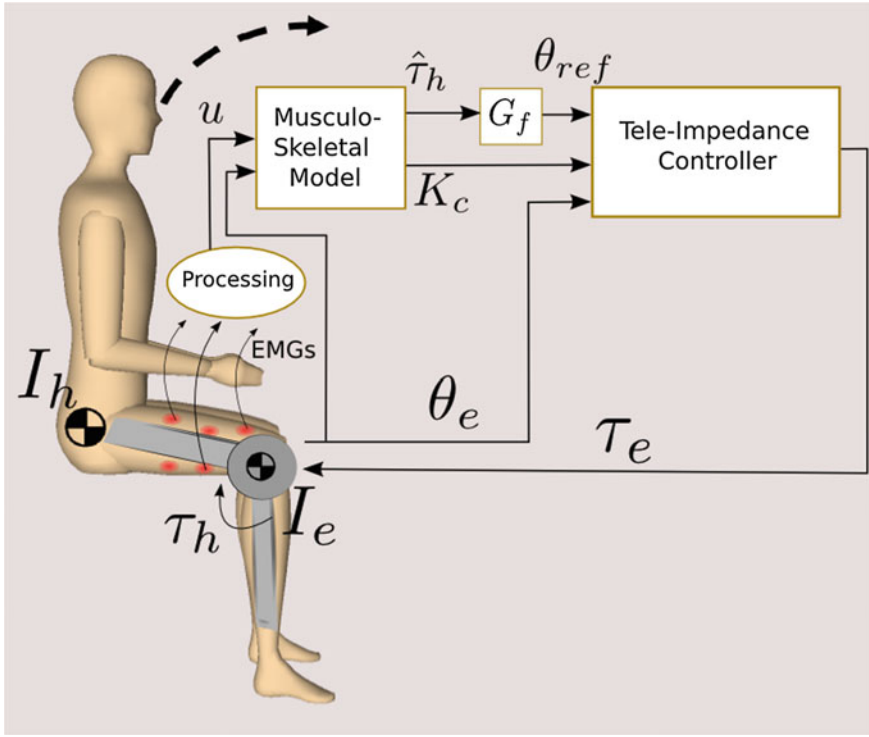
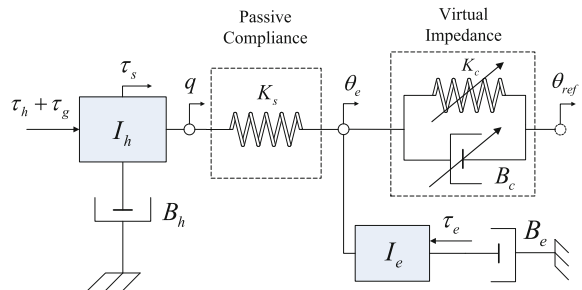


Fig. 9.8 Representation of the simplified physical system of the human-knee exoskeleton and the concept of the teleimpedance control

Fig. 9.9 Conceptual schematic that illustrates the interaction mechanics between exoskeleton and human including the teleimpedance controller



these findings the damping of the human knee joint was selected at $B_h = 4 \text{ N ms/rad}$. Moreover, the motor inertia and damping both reflected after the reduction drive were $I_e = 0.36 \text{ kg m}^2$ and $B_e = 0.607 \text{ N ms/rad}$, while the active damping were set to vary proportionally to the active stiffness as $B_c = 0.01K_c$. The sensitivity constant was tuned at $k_f = 0.034$ for deriving a sufficiently fast position reference for the standing-up motion.

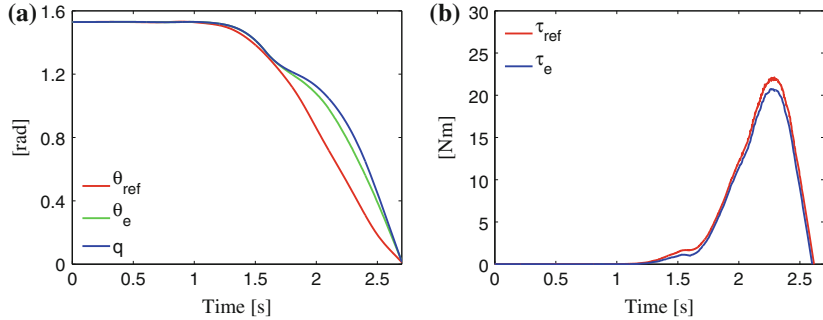


Fig. 9.10 Simulation results corresponding to the standing-up motion

In Fig. 9.10 are depicted the trend of the knee angle q towards the position reference θ_{ref} and the deflection $\theta_s = \theta_e - q$ of the elastic element which allows the transmission of the assistive torque from the actuator's motor to the knee joint. Additionally, the exoskeleton torque tracking of the torque reference τ_{ref} is shown in Fig. 9.10b.

9.5.2 Stability and Performance Analysis

In this subsection the stability of the controller is studied and proved. The coupled pair (human leg + exoskeleton device) discussed in Sect. 9.5.1 can be described in the frequency domain by the following equations:

$$(G_h + G_s)X_h = \tau_h + \tau_g + G_s X_e \quad (9.17)$$

$$(G_e + G_s)X_e = N\tau_m + G_s X_h \quad (9.18)$$

where $X_h = \mathcal{L}[q(t)]$ and $X_e = \mathcal{L}[\theta_e(t)]$ with \mathcal{L} symbolizing the Laplace operator. The combined human body is modeled as a second order linear impedance: $G_h = I_h s^2 + B_h s$. Additionally, $G_s = K_S$ represents the elasticity between the motor and the output link and $G_e = I_e s^2 + B_e s$ resembles the mass and damping properties of the motor.

Considering that the motor can track the reference torque ideally, it can be written:

$$\tau_m = G_c(X_{eq} - X_e) \quad (9.19)$$

where $G_c = K_c + B_c s$ is the virtual impedance of the controller and $X_{eq} = \mathcal{L}[\theta_{ref}(t)]$. As mentioned in Sect. 9.4, the reference position is derived from the estimated user torque as:

$$X_{eq} = G_f \tau_h \quad (9.20)$$

where $G_f = k_f/s$.

By inserting (9.20) into (9.19), substituting τ_m in (9.18) and then substituting τ_h in (9.17), while rearranging with respect to X_h gives:

$$X_h = \frac{NG_f G_c + NG_c + G_{es}}{G_f G_{es} G_{hs} + NG_f G_c G_{hs} - G_f G_s^2} X_e + \frac{NG_c + G_{es}}{G_{es} G_{hs} + NG_c G_{hs} - G_s^2} \tau_g \quad (9.21)$$

where $G_{hs} = G_h + G_s$ and $G_{es} = G_e + G_s$ are used only for simplifying the equation.

The characteristic equation of the transfer function $\frac{X_h}{X_e}$ is the following:

$$\begin{aligned} & G_f G_{es} G_{hs} + NG_f G_c G_{hs} - G_f G_s^2 \\ &= I_h I_e k_f s^4 + (B_h I_e + B_e I_h + B_c I_h N) k_f s^3 \\ &+ (B_h B_e + I_h K_s + B_c B_h N + I_h K_c N + I_e K_s) k_f s^2 \\ &+ (B_h K_s + B_e K_s + B_h K_c N + B_c K_s N) k_f s + K_c K_s k_f N. \end{aligned} \quad (9.22)$$

Equation (9.22) satisfies the Routh-Hurwitz criterion if and only if $K_c > 0$ and $(B_h I_e + B_e I_h + B_c I_h N) > 0$. In the case that $G_c = 0$, (e.g. no motion assistance provided by the exoskeleton) the transfer function in (9.21) is reduced to a third-order transfer function and the characteristic equation reads:

$$I_h I_e k_f s^3 + (B_h I_e + B_e I_h) k_f s^2 + (B_h B_e + I_h K_s + I_e K_s) k_f s + (B_e + B_h) K_s k_f \quad (9.23)$$

which is Hurwitz if and only if:

$$B_e B_h + I_e K_s + I_h K_s > \frac{I_h I_e K_s (B_h + B_e)}{B_h I_e + B_e I_h} \quad (9.24)$$

or simplified,

$$B_e B_h (B_h I_e + B_e I_h) + K_s (B_h I_e^2 + B_e I_h^2) > 0 \quad (9.25)$$

which is also satisfied. Notice that the value of the sensitivity constant k_f does not affect the stability of the system.

Since the main feature of the proposed teleimpedance control scheme is the real-time variation of the active stiffness, we investigate the frequency response of the system within a range of K_c close to the one which was applied during the experiments. Figure 9.11 demonstrates the Bode plots of the $\frac{X_h}{X_e}$ dynamics for different values of K_c while the intrinsic stiffness was set at $K_S = 200 \text{ N m/rad}$. As shown, considerable changes of the resonant peak occur within the range $0 < K_c < 40 \text{ N m/rad}$.

By safely neglecting the furthest away pole pair with respect to the imaginary axis, we can approximate the system using a second-order equation. Hence, we can intuitively evaluate the performance of the teleimpedance controller in terms of system response. The natural frequency ω_n and the damping ratio ζ of the second-

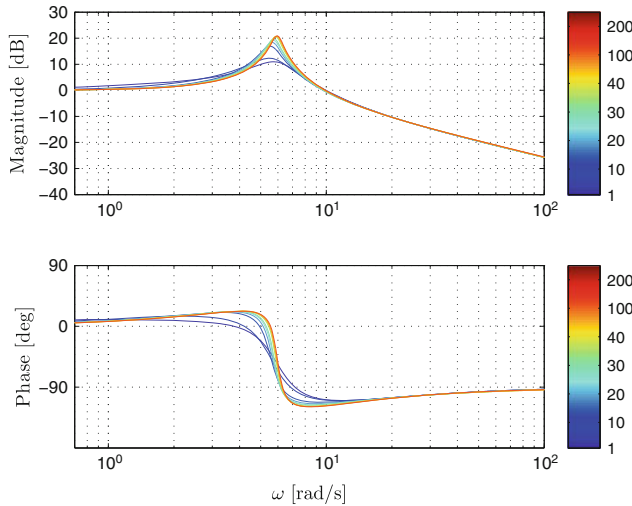
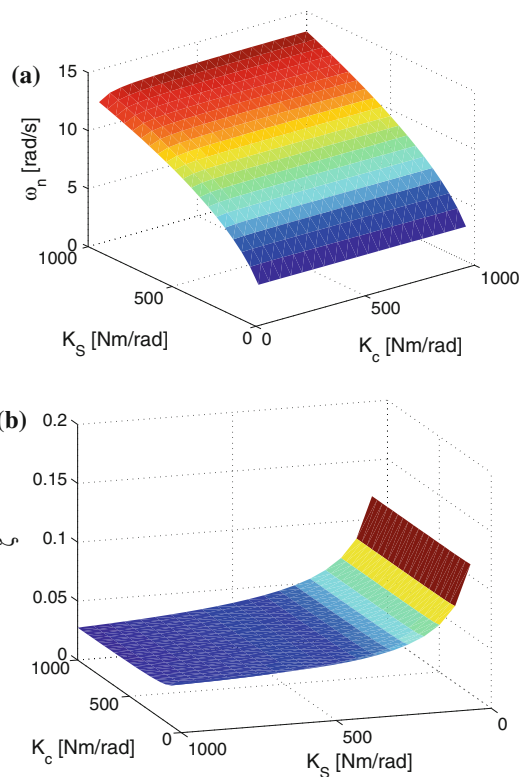


Fig. 9.11 Bode plots of the transfer function $\frac{X_h}{X_e}$ for different values of the active stiffness K_c (N m/rad)

Fig. 9.12 Natural frequency
(a) and damping ratio (b) for different values of K_c and K_S



order closed loop system were calculated for different values of K_c and K_S and are depicted in Fig. 9.12. As shown, both the natural frequency ω_n and the damping ratio ζ do not present a significant variation by altering the K_c . This is due to the fact that the value of the active stiffness K_c does not considerably affect the dominant pole pair of the transfer function $\frac{X_h}{X_e}$.

9.6 Experimental Results

In order to validate the aforementioned control strategy, the sit-to-stand movement was considered. The same subject who participated in the calibration experiments described in Sect. 9.2 was instructed to stand up from a sitting posture while wearing the exoskeleton on his right leg (see Fig. 9.13). During the execution of the experiment the subject was asked to support most of his body weight with the right leg. The minimum and maximum values of the STI were obtained from the minimum and maximum co-contraction of the thigh muscles of the subject. These were then mapped to the desired stiffness range that was set from 0 to 200 N m/rad. This range was validated through trials in order for the exoskeleton to provide sufficient levels of assistive torques (e.g. around 20 N m).

Figure 9.14 illustrates the experimental data during the standing-up motion. The variation of the active stiffness follows the trace of the subject's joint stiffness. The active stiffness demonstrates a smooth rise in the very beginning of the motion. At a certain point the subject increases his knee joint stiffness to overcome the effect of the increased gravitational torque and to be able to accomplish the motion. There-

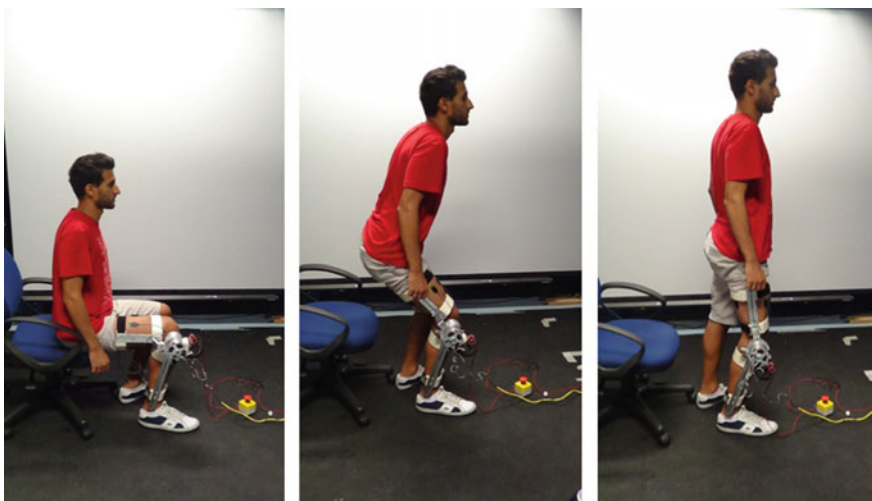


Fig. 9.13 Standing-up motion task for experimental evaluation

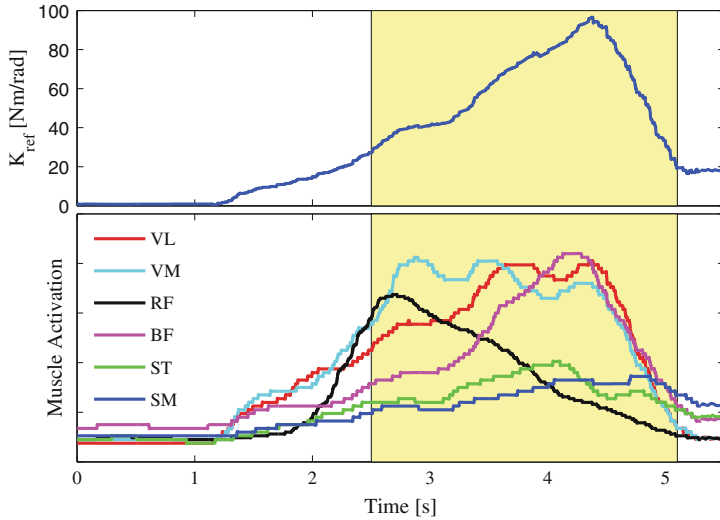


Fig. 9.14 Active stiffness of the teleimpedance controller during standing up based on the trace of the user's joint stiffness and the processed EMGs of the six muscles

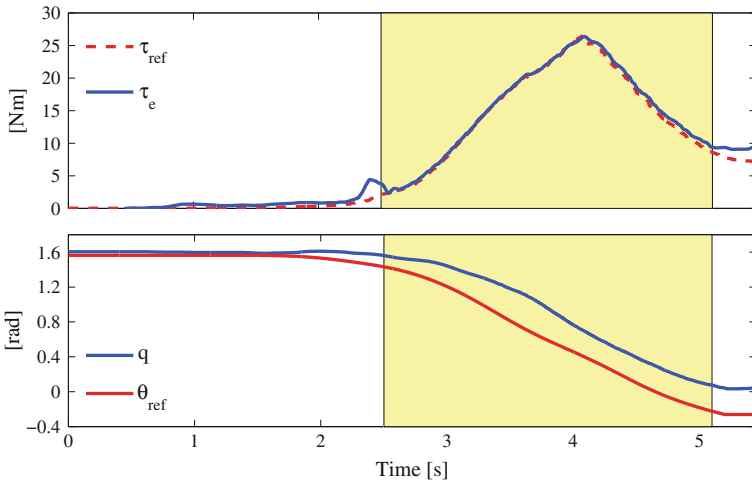


Fig. 9.15 The torque and position reference and the torque and position of the knee exoskeleton device

fore, the stiffness reference increases and the exoskeleton can provide the required amount of assistive torque (see Fig. 9.15). In the final phase of the task the subject loses his knee joint (gravitation load reduces in this final stage) in order to decrease the assistive torque provided by the exoskeleton while exploiting the straight knee singular position. In a sense, the subject is intrinsically and naturally controlling the equilibrium position of the virtual network to remain close to the standing pos-

ture. Additionally, in Fig. 9.15 the trend of the knee angle q towards the equilibrium position θ_{ref} and the attracting torque τ_e which is generated by the exoskeleton are depicted, respectively. As shown, the exoskeleton motor can track very effectively the reference torque τ_{ref} . The intrinsic stiffness of the exoskeleton was selected at $K_S = 200 \text{ N m/rad}$. In addition, the noise dead band constant in (9.15) was set at $a = 1 \text{ N m}$ while the torque integration constant k_f was experimentally tuned at $k_f = 0.04$ ensuring that the reference position update from (9.15) was adequately fast for the standing task execution.

9.7 Conclusion

This work proposed a teleimpedance based assistive control strategy for a compliant knee exoskeleton. The presented knee exoskeleton utilizes the CompAct-RS, a series elastic actuator, to achieve an improved compliant physical interaction with the operator. A musculoskeletal model, which takes into account the nonlinearity between the muscle activation and the joint torque, was developed in order to obtain the user's intent and his/her stiffness trend through electromyography. These reference signals were fed to a teleimpedance controller which can regulate its active stiffness based on the joint stiffness induced by the user's muscles. In addition, a simulation study of the overall human-exoskeleton system and the stability analysis of the teleimpedance based assistive controller were conducted. Experimental evaluation of the proposed control strategy was carried out and resulted that the user was able to intrinsically and naturally control the knee exoskeleton device and in addition to receive an effective motion assistance.

Regarding the improvements, the model calibration method needs to be enhanced for achieving faster and more convenient use of the exoskeleton. Future work will also include the experimentation with different motion tasks such as walking and climbing stairs and the implementation of the proposed control strategy in a full lower limb exoskeleton.

Chapter 10

Human-Inspired Balancing Assistance: Application to a Knee Exoskeleton

During every day life, unexpected external disturbances are a common event. Especially for elderly people and individuals with mobility disorders maintaining balance is a challenging task. Several biomechanical and physiological studies have been conducted to investigate strategies of human balancing during quiet standing and also during disturbances [243–245]. However, many questions concerning the mechanisms of the human's biomechanical system strategy still remain unanswered.

Researchers suggested that when small and slow disturbances in the anteroposterior direction occur humans try to reposition the center of mass (CoM) by swaying as an inverted pendulum primarily about the ankle with some hip or knee motion [246]. This muscle activation pattern has been named ankle strategy. However, it has been shown that the postural responses to larger and faster disturbances are acting at the hip joint (hip strategy) [243]. Moreover, in [247] has been proposed a mixed hip-ankle strategy to account for disturbances of any speed where the objective of optimization is a minimal neural effort.

A dense body of literature [248, 249] revealed that the intrinsic mechanical stiffness of the ankle is insufficient for stabilizing, where intrinsic ankle stiffness implies the instantaneous mechanical stiffness provided by the combination of active muscle, tendon, connective tissue and foot. In other words, stabilization cannot be achieved by the stiffness of the ankle muscles without the contribution of anticipatory active control. In particular, anticipatory (or feedforward) control and stiffness stabilization constitute synergistic mechanisms with a sharing of balancing actions.

Thus, a weak musculature or a decreased capability of the neuro-motor control results to a insufficient stabilization of balance. To date few lower limb exoskeletons have been proposed to address this issue [250–252]. However, as lower limb exoskeletons have found wide application as assistive or rehabilitation devices, providing balance stabilization to the user has become to a greater extent a prerequisite.

Furthermore, it is well known that the impedance of the human joints alters during several motion tasks such as walking, stair climbing and balancing [228]. Hence, exoskeletons, orthoses and prostheses that will present biological torque-angle behavior can have beneficial effects and not only provide effective motion assistance but also help to restore natural behavior of the subject's joints in a

rehabilitation setting. This study constitutes a first step towards the development of exoskeletons that will be able to reproduce the impedance regulation skills of humans and be naturally and volitionally controlled by the user's intended motions. Starting point is the better understanding of the biomechanical behavior of human during dynamic tasks. Hence, we perform a human balancing experiment and by using a model-based method to derive joint stiffness we carry out correlation analysis of the experimental data. Motivated by the findings of this study we propose a human-inspired control method for lower limb exoskeletons to assist balancing based on the intensity of the external disturbance.

10.1 Model-Based Joint Stiffness Estimation

10.1.1 EMG-Driven Musculoskeletal Model Description

The purpose of the presented musculoskeletal model is to map the electromyographic measurements to the active joint stiffness, where active stiffness implies the joint stiffness that depends on the muscle activation.

To achieve that, we extend the Hill-type musculoskeletal model we have developed in [10]. This model is composed by the activation dynamics, contraction dynamics and musculoskeletal geometry sections and is able to predict robustly the muscle forces and the antagonist joint torques. Hence, given the fact that we can estimate the muscle forces, we model the musculotendinous stiffness k^{mt} by considering the muscle stiffness k^m to be in series with the tendon stiffness k^t [253]. Thus, the musculotendinous stiffness can be given by:

$$k^{mt} = \frac{k^m k^t}{k^m + k^t}. \quad (10.1)$$

In [254] tendon stiffness was assumed to be a function of the tendon length l^t and the average cross-sectional area (CSA) of the external tendon A^t as follows:

$$k^t = E \frac{A^t}{l^t} \quad (10.2)$$

where E is the elastic modulus of the tendon. The muscle fiber stiffness was assumed to be inversely proportional to the muscle length l^m and direct proportional to the muscle force F^m :

$$k^m = c \frac{F^m}{l^m} \quad (10.3)$$

where c is a constant.

The joint stiffness is associated with the musculotendinous stiffness by the following equation:

$$\begin{aligned}
 K_{joint} &= \frac{\partial \tau_{joint}}{\partial \theta} = \frac{\partial r^T F^{mt}}{\partial \theta} \\
 &= r^T \frac{\partial F^{mt}}{\partial l^{mt}} \frac{\partial l^{mt}}{\partial \theta} + \frac{\partial r^T}{\partial \theta} F^{mt} \\
 &= r^T K^{mt} r + \frac{\partial r^T}{\partial \theta} F^{mt}
 \end{aligned} \tag{10.4}$$

where $K^{mt} = diag(k^{mt})$, l^{mt} , r and F^{mt} are the vectors of the muscle-tendon length, the moment arms and the musculotendinous forces, respectively.

10.1.2 Adjusting the Musculoskeletal Model Parameters

To establish the mapping between the muscular activities and the resulting joint stiffness, the model parameters were first adopted from the literature [183, 254, 255]. With the purpose of minimizing the effect of subject-to-subject variations of the mentioned parameters, we re-identified the stiffness model (Eq. 10.4) by means of direct estimations of the joint stiffness in isometric conditions. In particular, this can be done using a nonlinear least square algorithm that minimizes the squared difference of the predicted joint stiffness and the experimental identified stiffness. The result of this minimization is a set of values of the model parameters (maximum isometric force F_{max} , activation dynamics parameter A , optimal pennation angle ψ_o , optimal muscle length l_o^m , A^t , c) that were selected to be re-identified while being constrained to $\pm 15\%$ above/below of their nominal values.

In this work, our goal is to estimate the knee joint stiffness and thus adjust the parameters of the model for the case of knee the joint. To that end, following standard methods [253], we applied stochastic position perturbations (SD of 0.5°) to the subject's knee joint using the KUKA robotic arm. For this purpose, a special plastic brace was designed to be worn by the subject around his shank while being in a sitting posture. The external side of the brace mounted on a 6 axis ATI force/torque sensor and attached to the endpoint of the robot. The measured forces as a result of imposed position perturbations (Gaussian white noise) were then converted to joint torque and used for the knee joint stiffness estimation. The knee joint angular displacement was monitored with an optical tracking system (Natural Point, Inc.).

Experiments were performed in eight different conditions while two trials for each condition were recorded. Half of the trials were used for adjusting the model parameters and the other half for the model validation. Each trial had duration of 35 s with the first 5 s being discarded. The first six conditions were conducted without co-contraction (CC) for three levels of activation in the extension and flexion directions. Particularly, the target torque levels were ± 10 , ± 20 and ± 40 % of the maximum

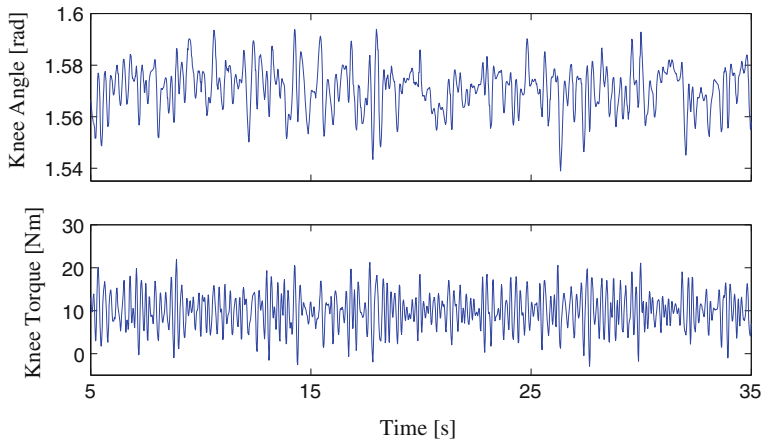


Fig. 10.1 Applied stochastic perturbations and resulting torque response while the subject was applying constant flexion torque of 10 %MVC

voluntary contraction (MVC). The next two conditions included CC of 10 %MVC and 20 %MVC with the net torque being zero. In addition, two extra trials were recorded with 0 %MVC and no CC in order to estimate the passive stiffness of the knee joint. As the proposed model predicts only the active stiffness the passive stiffness was subtracted from all measurements.

Figure 10.1 illustrates the position perturbation and the corresponding torque response of a typical experiment in which the subject was applying constant torque (10 %MVC). Visual feedback was provided to facilitate the subject keeping the applied torque very close to the target torque. Direct electromyographic measurements were obtained from the six dominant antagonist muscles acting about the knee: rectus femoris (RF), vastus medialis (VM) and vastus lateralis (VL), biceps femoris (BF), semimembranous (SM) and semitendinosus (ST).

A non-parametric algorithm was adopted to identify the empirical transfer function of the knee joint impedance in frequency domain (MATLAB, The MathWorks Inc.). The smoothed spectral estimates of input and outputs (using windowing techniques) were fed to this algorithm in order to identify the above transfer function. Consequently, we adopted a parametric, second order, linear model of each impedance transfer function of the type:

$$G(s) = Is^2 + Bs + K, s = 2\pi f \quad (10.5)$$

where I , B and K denote the inertia, viscosity and stiffness matrices, respectively. The parameters of the second order linear model were identified based on least squares algorithm in frequency range from 0 to 10 Hz. Figure 10.2 demonstrates

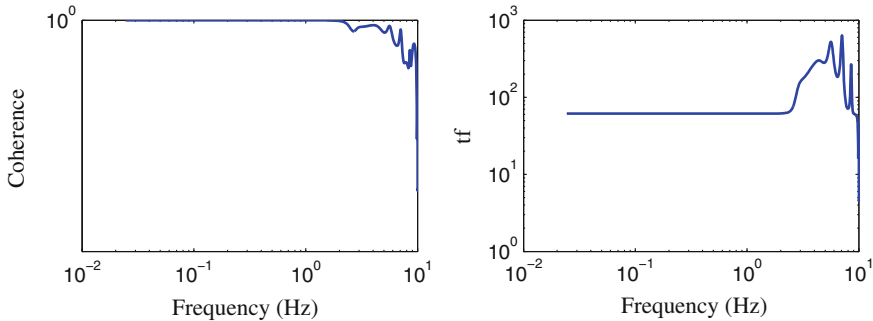
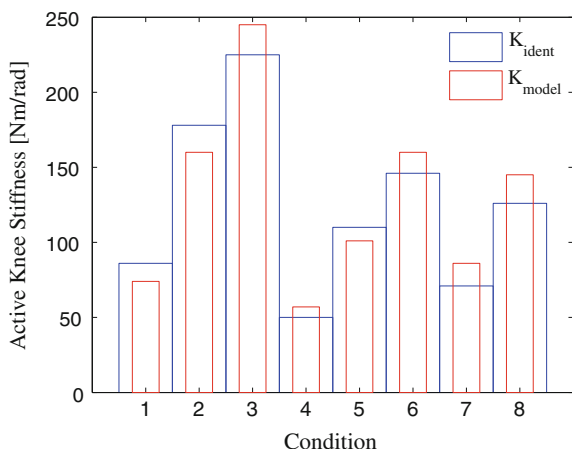


Fig. 10.2 Coherence and non-parametric transfer function of the impedance obtained from stochastic perturbations

Fig. 10.3 Active stiffness of the knee joint identified during perturbations for eight different conditions and the corresponding model-based stiffness estimates



the resulting coherence and identified non-parametric transfer function of the trial shown in Fig. 10.1. Furthermore, Fig. 10.3 depicts the identification results of the active stiffness for the half trials in comparison with the averaged values of the corresponding model estimates. As it is shown, the model can reasonably predict the identified stiffness, resulting a normalized root mean square error of 16.7%. Table 10.1 indicates the target activation of each condition. Additionally, as it was expected the stiffness in the extension direction is greater in comparison with the one in the flexion direction. Note that, the presented model was calibrated based on isometric conditions fact that renders its prediction during dynamic conditions to be limited. However, it is adequate to investigate stiffness function of humans during balancing maneuvers and implement biological-inspired impedance controls to exoskeletons.

Table 10.1 Conditions during the perturbation experiment

| Condition | Target torque level |
|-----------|---------------------------|
| 1 | +10 %MVC |
| 2 | +20 %MVC |
| 3 | +40 %MVC |
| 4 | -10 %MVC |
| 5 | -20 %MVC |
| 6 | -40 %MVC |
| 7 | 0 %MVC with CC of 10 %MVC |
| 8 | 0 %MVC with CC of 20 %MVC |

10.2 Human Balancing Experiment

10.2.1 Description of the Experimental Setup

Several different methods based on external disturbances have been applied by researchers that aim at the quantification of the human response as well as the understanding of the system strategies [243]. In our balancing experiments two healthy subjects (males) participated. In total 39 markers were placed to each subject to fit the full body model. The Vicon motion capture system with 6 cameras (250 Hz) and the Plug-in Gait were used to reconstruct the kinematics (i.e. knee and ankle joint trajectories) and compute the trajectory of the center of mass. Using a Kistler force platform we derived the center of pressure (CoP) trajectory in the anteroposterior and the mediolateral axes. In addition, nine electrodes (Bagnoli-16, Delsys Inc.) were attached to the right subject's leg to obtain direct electromyography (EMG) measurements. In particular, the chosen muscles were: rectus femoris (RF), vastus medialis (VM) and vastus lateralis (VL) (knee extensor muscles), biceps femoris (BF), semimembranous (SM) and semitendinosus (ST) (knee flexor muscles), gastrocnemius (GA) and soleus (SL) (plantarflexor) and anterior tibial (TA) (dorsiflexor). All three systems (Vicon, Bagnoli and Kistler force plate) were synchronized under the Vicon Nexus Software. Particular attention was paid to the calibration of Vicon system regarding the force plate integration to avoid misalignments between the markers trajectories and the ground reaction forces (GRF).

Each subject stood on the force platform with the center of his ankles approximately 20 cm apart and was asked to flex his knees around 10°. External disturbances were applied perpendicularly to the subject's chest by using a rod. At the end point of the rod a 6-axis force sensor was mounted to monitor the level of the disturbance forces. A series of continual disturbances were applied with each individual pushing action occurring every time the subject returned to the initial posture. The subject was instructed to maintain balance without performing any step. Seven trials for each subject with interval of 50 s each were recorded.

10.2.2 Data Analysis

The experimental data that was subjected to analysis contains the EMG signals of the nine muscles, the knee and ankle angular positions, and the center of mass (CoM) and center of pressure (CoP) excursions. The raw EMG signals were high-pass filtered to remove offsets and movements artifacts. This stage was followed by full rectification techniques. Then, the resulting signals were low-pass filtered and normalized to provide the traces of the neural activation of the muscles. These muscle activations were fed to the musculoskeletal model described in Sect. 10.1 to derive the joint stiffness estimates. In addition, all the kinematic data, CoM and CoP trajectories in the anteroposterior axis were subjected to low-pass filtering, while possible slow drift component of the signals were removed. The first 5 s of all trials were discarded.

Cross-correlation analysis was conducted using the processed data. The cross-correlation functions between the two selected signals were computed with a maximal shift of 2 s and for two separate epochs of each trial. The sample step of 40 ms was selected to increase the value of the correlation coefficient needed for significance and therefore avoid false positives. In particular, cross-correlations functions were evaluated between the anteroposterior motions of the CoP x_{CoP} and : (1) the anteroposterior motions of the CoM x_{CoM} , (2) the EMG activity of rectus femoris (RF), (3) the EMG activity of gastrocnemius (GA), (4) the ankle angle θ_{ankle} , (5) the knee angle θ_{knee} and (6) the stiffness of the knee K_{joint} that was estimated using the musculoskeletal model described in Sect. 10.1. These two specific muscles were selected based on the measured electromyographic signals that indicated that they are the most dominant muscles for this motion task.

Figure 10.4 illustrates the correlation coefficient r that is a maximum or a minimum of the cross-correlation function averaged for all trials separately for each subject. The cross-correlation function between the anteroposterior motion of CoP and the ankle

Fig. 10.4 The averaged correlation coefficient (r) that is the maximum of the computed cross-correlation functions

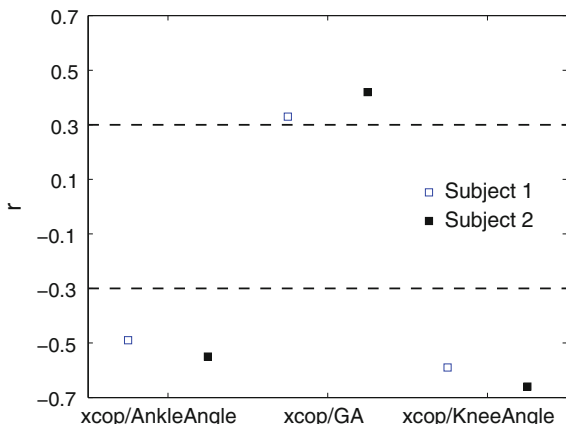
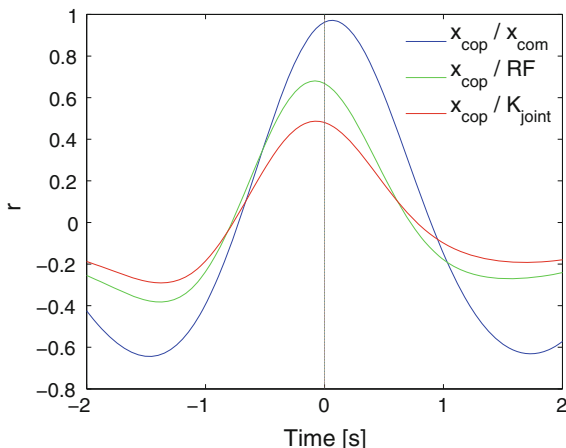


Fig. 10.5 Averaged cross-correlation functions of all trials for the interval from 6th to 28th second with maximum lag of 2 s

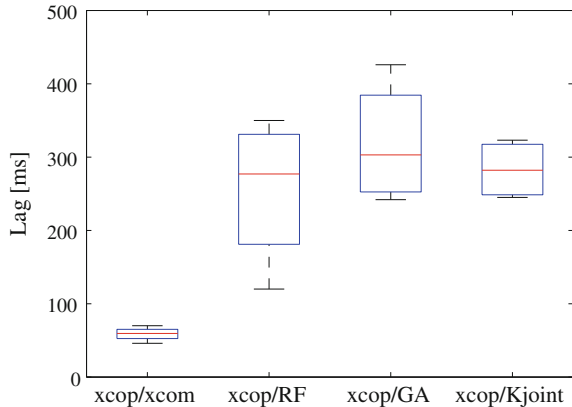


angle in the sagittal plane had a moderately high negative maximum which indicates that as the CoP moves backwards the ankle extends. In addition, a moderate positive correlation was found between x_{CoP} and the EMG activity of the gastrocnemius (GA) while the cross-correlation function between the knee angular position and x_{CoP} presented a moderately high minimum. The latter indicates that as the CoP moves backwards the subject extends his knee to prevent falling.

The averaged cross-correlation functions for the first epoch of all the trials of both subjects are depicted in Fig. 10.5. As is shown the peak of the cross-correlation function between the CoM and CoP trajectories in the anteroposterior direction is very close to one. This indicates a highly linear relationship between the two signals, fact which have been also reported in other studies [256]. A high positive correlation was found between x_{CoP} and the EMG activity of rectus femoris, which is considered as a dominant extensor muscle at the knee joint. In addition, the correlation between x_{CoP} and the model-based estimated stiffness of the knee joint presented a significant ($P < 0.001$) moderate positive maximum which confirms our assumption that the subject stiffens his muscles about knee to impede the acceleration of the center of mass caused by the external disturbance.

Phase lags of the maximum or minimum of the cross-correlation functions are illustrated in Fig. 10.6. The delay of the CoM does not exceed 70 ms. Remarkable is the fact that the EMG activity of RF and GA and the knee stiffness lead ahead the anteroposterior motions of the CoP. However, to interpret this finding a better understanding of the operation of the neural-motor control is required.

Fig. 10.6 Lags of the maximum or minimum of the corresponding cross-correlation functions



10.3 Balancing Assistance Control

An ideal assistive device should generate supporting forces upon the user's request or disturbance, and present high levels of transparency during no assistance condition. This implies that it should mimic the physiological behavior of human limb during the time. In some extent we address this challenge by introducing a hybrid approach that combines teleimpedance with a CoP-guided control and permits for volitional balancing assistance. The concept of teleimpedance control has been previously introduced as a practical approach for transferring human impedance regulation skills and equilibrium position profiles to robots, in real-time [2]. To produce teleimpedance control an impedance controller is required to be implemented in the exoskeleton's actuator [10]. In our case, it is composed of an outermost position loop and an inner torque loop. The impedance reference signal tracked by the impedance controller is:

$$Z_c = K_c + B_c s \quad (10.6)$$

where K_c , B_c represent the stiffness and the damping parameters of the active impedance, respectively.

The analysis in Sect. 10.2.2 revealed that there is a significant ($P < 0.001$) positive correlation between the knee joint stiffness and the x_{CoP} . In this work, we adopted a simplified relationship between these two variables and hence the desired stiffness for the impedance controller was selected to vary as follows:

$$K_{ref} = \begin{cases} b(|x_{CoP}| - a) & x_{CoP} > a \\ K_{model} & -a \leq x_{CoP} \leq a \\ b(|x_{CoP}| + a) & x_{CoP} < -a \end{cases} \quad (10.7)$$

where a , b are the dead band parameter and linear constant, respectively.

The reason of introducing a dead band zone is dual: to avoid the fact that firstly the noise from the force platform and secondly the fluctuations due to slight movements on the force platform affect the regulation of the exoskeleton stiffness. In this manner, we are able to acquire the resultant variation of the center of pressure caused only by the external disturbances. As shown in (10.7) within this dead band interval the active stiffness is chosen to be equal with the stiffness of the user's knee as is estimated in real-time by the EMG-driven musculoskeletal model. Therefore, at no disturbance condition the control is able to present a faster adaptation (for the next disturbance) as according to anticipatory control studies it has been observed that muscle activation can occur also before the initiation of the movement [245]. In other words, the exoskeleton is able to mimic the natural stiffness function of the human knee. The center of pressure excursions x_{CoP} were subjected to real-time low pass filtering. Moreover, it was necessary to remove the offset of x_{CoP} that depended on the initial position of the subject on the force platform.

10.4 Knee Exoskeleton Application

To preliminary test the proposed biologically-inspired control method an inherently compliant knee exoskeleton was used. The exoskeleton (see Fig. 10.7) consists of two link segments (upper and lower) which are fixed to the thigh and the shank, respectively and the rotational actuation system (CompAct-RS) [10] which drives the joint. The exoskeleton is attached on the user's leg with the axis of rotation of

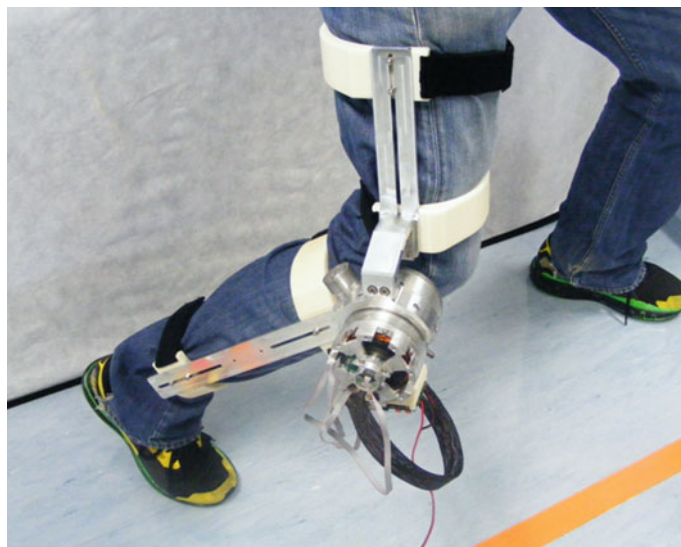


Fig. 10.7 The knee exoskeleton, used in experiments

the joint aligned with the axis of the user knee joint. It interfaces with the wearer by means of four rigid braces and is fastened with four Velcro straps at thigh and shank. Moreover, the range of motion of the knee exoskeleton in the sagittal plane is between 0° and 120° where 0° corresponds to full extension of the knee.

Similar balancing experiment with the one described in Sect. 10.2.1 was carried out while the subject was wearing the exoskeleton and having attached six EMG electrodes on his right leg (see Sect. 10.1.2 for selection of muscles). The external perturbations were applied also in this case by means of a rod, while each trial had duration of 35 s (see Fig. 10.8).

Figure 10.9 illustrates the variation of the center of pressure in the anteroposterior direction during external disturbances and the knee angle as measured from the exoskeleton. The intervals that θ_{knee} are almost constant correspond to the short rest pauses. The active stiffness and the exoskeleton torque are depicted in Fig. 10.10. The high level of the applied torque to the user indicates the effectiveness of the proposed



Fig. 10.8 Human balancing experiment. The subject is wearing the knee exoskeleton while electrodes are attached to six muscles about the knee to derive the stiffness estimates

Fig. 10.9 Center of pressure trajectory in the anteroposterior axis and knee angle changes during balancing under external disturbances

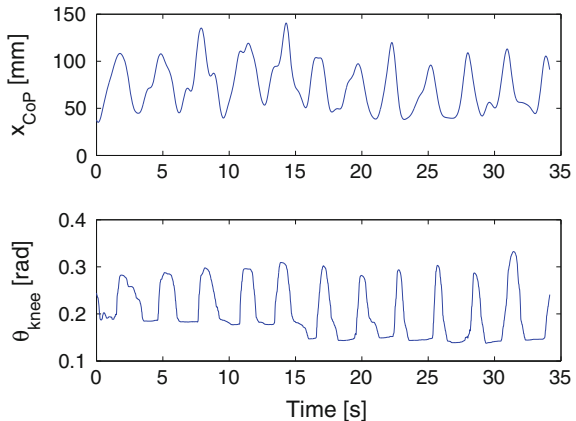
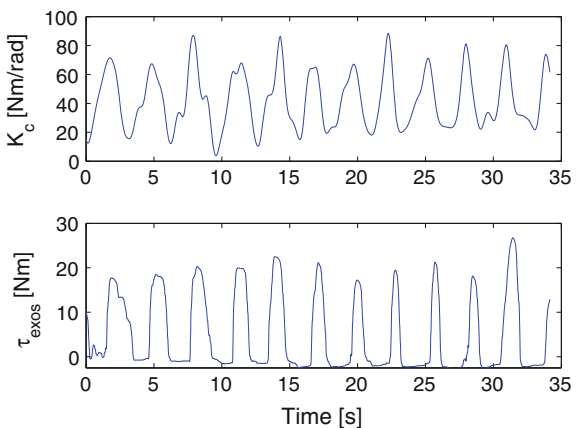


Fig. 10.10 The CoP-guided active stiffness of the impedance controller and the torque applied by the exoskeleton during the experiment of the balancing assistance



control technique. As long as the x_{CoP} lies within the dead band, the exoskeleton regulates its stiffness based on the real-time estimations of the subject's knee stiffness and therefore it does not impede his motion. As the x_{CoP} increases (which implies that the subject is getting closer to a fall) the exoskeleton supports the subject's leg by stiffening the joint. In this manner, the exoskeleton is transparent at no disturbance condition (where the subject's joint present high compliance) while it can provide to the subject the desired level of assistive torque that is based on the intensity of the disturbance.

In this work, the regulation of the active stiffness was performed around the equilibrium position which for each trial was set as the initial angular position of the knee. The parameters a and b were tuned through trial and error ($a = 0.008$, $b = 760$) while the active damping was set to vary as $B_c = 0.01K_c$. Note that, the substitution of the force platform with a ground reaction forces (GRF) sensing system integrated into the exoskeleton foot will allow us to apply the proposed or similar control technique also for different motion tasks such as walking, stair climbing, etc.

10.5 Conclusions

We have concluded a first stage in the development of exoskeletons that are able to produce human-like mechanics and therefore improve their adaptability, force transmission as well as detection of the user's intention. The challenging task of real-time stiffness estimation was addressed using a EMG-driven musculoskeletal model that was experimentally calibrated in isometric conditions. Human balancing experiments were carried out to analyze correlations of the anteroposterior motions of the center of pressure with the model-based stiffness of the knee, the electromyographic activity of muscles that are considered most dominant in maintaining balance, and others. One of our findings was that the knee stiffness profiles were significant ($P < 0.001$) positive correlated with the center of pressure excursions in the anteroposterior direction. Inspired from these results, a CoP-guided control method combined with the concept of teleimpedance was introduced that aims to allow a lower limb exoskeleton provide effective balancing assistance to the user in a natural and volitional manner. The proposed control technique was preliminary evaluated utilizing a knee exoskeleton. As our control technique constitutes a general approach, future work will focus on its implementation in a full lower limb exoskeleton for both legs and the examination of possible hurdles. In addition, future efforts will investigate correlations between the CoP coordinates and the lower limb joint stiffness during walking and stair climbing.

Chapter 11

Conclusions

In this book the concept of teleimpedance control was introduced, as a method to effectively transfer the task-oriented stiffness profile from the human master to the robotic slave device. As an alternative to position-based or closed-loop bilateral force-reflecting teleoperation, the proposed approach enriches the command sent to the slave robot by combining the position reference with a stiffness (or full impedance) reference estimated from the human operator. The stiffness command to the robot was derived in real time from the measurement of EMGs from corresponding muscles of the operator.

Results of the implementation of the teleimpedance control using a Cartesian impedance controller demonstrated that the tasks are done better and more efficiently compared to classical position or fixed-stiffness control methodologies. Experimental results also suggested that humans tend to use limb geometry to change the directionality of the realized stiffness ellipsoid, prior to the use of co-activation of the involved muscles. This is due to the major contribution of the limb geometry to the efficient modifications of the ellipsoid directionality, and its cost efficient nature. These observations promoted the idea of realizing a common mode and configuration dependent stiffness control in our robotic setup. Implementation of such human like impedance controller resulted in good interaction performance and generation of natural motions in robots, similar to the ones observed in humans.

Teleimpedance concept was also used as a basis for the development of a novel synergy-driven impedance controller, and gathered the user's postural and stiffness synergy references from two EMG channels. In addition, two haptic interfaces (Mechano- and vibro-tactile) were developed to facilitate natural control of the prosthetic limb. The mechanotactile interface was employed to provide the user with information on grasp forces, to enable intuitive modulations of task-required forces. While the vibrotactile interface was developed to provide the user with information about object slippage and perception of surface properties such as texture.

The efficiency of the novel synergy-driven teleimpedance controller, while employing haptic interfaces, was evaluated through two sets of experiments. The first set was designed to assess the capabilities of the teleimpedance controller with

force feedback in natural grasping. Incorporation of the above features resulted in robust and reliable grasps, regardless of the elastic properties of the grasped object. This was achieved since the subjects were able to modify the task forces via modified grasp compliance and force feedback.

To evaluate the efficiency of the teleimpedance control regarding lower extremities, an assistive control strategy for a compliant knee exoskeleton was proposed. A detailed musculoskeletal model was developed in order to obtain the user's intent and stiffness trend using EMG measurements. These reference signals were fed to a teleimpedance controller and consequently the knee joint angle and its stiffness were actively controlled. Efficiency of the proposed teleimpedance controller was evaluated in assistive and balancing tasks.

Overall results suggest that incorporation of human motor control principles in the motion control architectures for humanoid robots or assistive and prosthesis devices will permit these systems not only to produce a desired interaction performance, but also to generate natural motion profiles resembling those executed by humans during manipulation and locomotion.

Bibliography

Author's

1. A. Ajoudani, N. Tsagarakis, A. Bicchi, Tele-Impedance: preliminary results on measuring and replicating human arm impedance in tele operated robots, in *IEEE International Conference on Robotics and Biomimetics—ROBIO* (2011), pp. 216–223
2. A. Ajoudani, N.G. Tsagarakis, A. Bicchi, Tele-Impedance: teleoperation with impedance regulation using a body-machine interface. *Int. J. Robot. Res.* **31**(13), 1642–1655 (2012)
3. A. Ajoudani, N. Tsagarakis, A. Bicchi, Tele-impedance: towards transferring human impedance regulation skills to robots, in *International Conference of Robotics and Automation—ICRA*, Saint Paul, 14–18 May 2012 (Best Manipulation Paper Award Finalist)
4. A. Ajoudani, M. Gabiccini, N.G. Tsagarakis, A. Albu-Schäffer, A. Bicchi, TeleImpedance: exploring the role of common-mode and configuration-dependant stiffness, in *IEEE-RAS International Conference on Humanoid Robots* (2012)
5. A. Ajoudani, M. Gabiccini, N.G. Tsagarakis, A. Bicchi, Human-like impedance and minimum effort control for natural and efficient manipulation, in *IEEE International Conference on Robotics and Automation—ICRA* (2013)
6. A. Ajoudani, N. Tsagarakis, J. Lee, M. Gabiccini, A. Bicchi, Natural redundancy resolution in dual arm manipulation through configuration dependent stiffness (cds) control, in *International Conference of Robotics and Automation—ICRA* (2014)
7. S. Godfrey, A. Ajoudani, M. Catalano, G. Grioli, A. Bicchi, A synergy-driven approach to a myoelectric hand, in *IEEE International Conference on Rehabilitation Robotics—ICORR* (2013), pp. 1–6
8. A. Ajoudani, S. Godfrey, M. Bianchi, M. Catalano, G. Grioli, N. Tsagarakis, A. Bicchi, Exploring teleimpedance and tactile feedback for intuitive control of the Pisa/IIT softhand. *IEEE Trans. Haptics* **7**, 203–215 (2014)
9. A. Ajoudani, S. Godfrey, M. Catalano, G. Grioli, N. Tsagarakis, A. Bicchi, Teleimpedance control of a synergy-driven anthropomorphic hand, in *IEEE International Conference on Intelligent Robots and Systems—IROS* (2013)
10. N. Karavas, A. Ajoudani, N.G. Tsagarakis, J. Saglia, A. Bicchi, D.G. Caldwell, Tele-impedance based stiffness and motion augmentation for a knee exoskeleton device, in *IEEE International Conference on Robotics and Automation—ICRA* (2013)
11. N. Karavas, A. Ajoudani, N. Tsagarakis, J. Saglia, A. Bicchi, D.G. Caldwell, Tele-impedance based assistive control for a compliant knee exoskeleton: stiffness augmentation and motion assistance, *Robotics and Autonomous Systems* (2014)

12. N. Karavas, A. Ajoudani, N. Tsagarakis, D. Caldwell, Human-inspired balancing assistance: application to a knee exoskeleton, in *IEEE International Conference on Robotics and Biomimetics—ROBIO* (2013) (Best Student Paper Award)
13. A. Ajoudani, N.G. Tsagarakis, A. Bicchi, Tele-impedance based teleoperation: peg-in-hole experimental results, in *IEEE International Conference on Robotics and Biomimetics—ROBIO* (2011), pp. 2239–2240
14. A. Ajoudani, N. Tsagarakis, A. Bicchi, Transferring human impedance regulation skills to robots, in *SIDRA (Automatica.it)* (2014) (Best Presentation Award Finalist)
15. A. Ajoudani, J. Lee, A. Rocchi, M. Ferrati, E.M. Hoffman, A. Settimi, D.G. Caldwell, A. Bicchi, N.G. Tsagarakis, A manipulation framework for compliant humanoid coman: application to a valve turning task, in *IEEE-RAS International Conference on Humanoid Robots* (2014)
16. J. Lee, A. Ajoudani, E.M. Hoffman, A. Rocchi, A. Settimi, M. Ferrati, A. Bicchi, N.G. Tsagarakis, D.G. Caldwell, Upper-body impedance control with variable stiffness for a door opening task, in *IEEE-RAS International Conference on Humanoid Robots* (2014)
17. A. Ajoudani, J. Lee, A. Rocchi, M. Ferrati, E.M. Hoffman, A. Settimi, D.G. Caldwell, N.G. Tsagarakis, A. Bicchi, Dual arm impedance control with a compliant humanoid: application to a valve turning task, in *IEEE International Conference on Intelligent Robots and Systems (IROS)—Workshop on Compliant Manipulation: Challenges in Learning and Control* (2014)
18. C. Castellini, P. Artemiadis, M. Wninger, A. Ajoudani, M. Alimusaj, A. Bicchi, B. Caputo, W. Craelius, S. Dosen, K. Englehart, D. Farina, A. Gijsberts, S.B. Godfrey, L. Hargrove1, M. Ison, T. Kuiken, M. Markovic, P.M. Pilarski, R. Rupp, E. Scheme, Peripheral machine interfaces: going beyond traditional surface electromyography, in *Frontiers in Neurorobotics* (2014) (submitted)
19. P. Pilarski, C. Castellini, W. Craelius, D. Farina, M. Markovic, S. Dosen, P. Artemiadis, A. Bicchi, S.B. Godfrey, A. Ajoudani, Present and future of non-invasive pns-machine interfaces, in *Workshop on IEEE International Conference on Rehabilitation Robotics—ICORR* (2013)
20. C. Rosales, A. Ajoudani, M. Gabiccini, A. Bicchi, Object representation enhancement through intrinsic tactile continuous exploration, in *IEEE International Conference on Intelligent Robots and Systems—IROS* (2014)
21. M. Mosadeghzad, N. Karavas, A. Ajoudani, E. Spyrapos, N. Tsagarakis, D. Caldwell, Optimal human-inspired ankle stiffness regulation for humanoid balancing control, in *IEEE-RAS International Conference on Humanoid Robots* (2014)

Author's Videos

22. Tele-Impedance: preliminary results on measuring and replicating human arm impedance in tele operated robots, Video (2011), <http://www.youtube.com/watch?v=KPO6I07Tr-Q>
23. Tele-impedance: towards transferring human impedance regulation skills to robots, Video (2012), <http://www.youtube.com/watch?v=Fn2dObnFpw>
24. A human-like impedance and minimum effort control for efficient and natural manipulation, Video (2013), <http://www.youtube.com/watch?v=6cqu7XqIeZs>
25. A synergy-driven approach to a myoelectric hand, Video (2013), <http://www.youtube.com/watch?v=cTkimp6yD5g>
26. Teleimpedance control of a synergy driven anthropomorphic hand, Video (2013), http://www.youtube.com/watch?v=XKYApA_dEyI

Press

27. An interview by TG5 channel about SoftHand/Teleimpedance. Video (2014), https://www.youtube.com/watch?v=E51O9-AL_Hg&feature=youtu.be
28. SoftHand/Teleimpedance in BBC Science magazine, Italy (2014), pp. 55–56
29. An article in Le Scienze (The Science) magazine about the SoftHand/Teleimpedance (2014), http://www.lescienze.it/lanci/2013/10/24/news/centro_e_piaggio_al_festival_della_scienza_la_mano_robotica_che_pu_prendere_le_fragole-1860676/
30. An article in Torino Scienza magazine about the SoftHand/Teleimpedance. http://www.torinoscienza.it/articoli/e_delicata_e_precisa_la_mano_robotica_tutta_italiana_26347

Projects

31. THE (2010–2014) The hand embodied. European Community’s Seventh Framework Programme (FP7/2007-2013) under Grant Agreements n. ICT-248587—2010, <http://www.thehandembodied.eu>
32. SoftHands (2012–2015) A theory of soft synergies for a new generation of artificial hands. European Research Council Advanced Grant n. 291166—2012, <http://softhands.eu/project.html>
33. SAPHARI (2011–2015) Safe and autonomous physical human-aware robot interaction. European Community’s Seventh Framework Programme (FP7/2007-2013) under Grant Agreements n. ICT- 287513—2011, <http://www.saphari.eu>
34. WEARHAPS (2013–2017) Wearable haptics for humans and robots. European Community’s Seventh Framework Programme (FP7-ICT-2011-9-2.1) under Grant Agreements n. 601165, <http://www.wearhap.eu/>
35. WALKMAN (2013–2017) Whole-body adaptive locomotion and manipulation. European Community’s 7th Framework Programme: FP7-ICT 611832. Cognitive Systems and Robotics: FP7-ICT-2013-10, <http://www.walk-man.eu/>

Miscellaneous

36. B. Hannaford, A design framework for teleoperators with kinesthetic feedback. *IEEE Trans. Robot. Autom.* **5**(4), 426–434 (1989)
37. T. Imaida, Y. Yokokohji, M. Oda, T. Yoshikawa et al., Ground-space bilateral teleoperation of ETS-VII robot arm by direct bilateral coupling under 7-s time delay condition. *IEEE Trans. Robot. Autom.* **20**(3), 499–511 (2004)
38. G. Niemeyer, J. Slotine, Telemanipulation with time delays. *Int. J. Robot. Res.* **23**(9), 873–890 (2004)
39. W.S. Kim, B. Hannaford, A. Fejczy, Force-reflection and shared compliant control in operating telemanipulators with time delay. *IEEE Trans. Robot. Autom.* **8**(2), 176–185 (1992)
40. L.J. Love, W.J. Book, Force reflecting teleoperation with adaptive impedance control. *IEEE Trans. Syst. Man Cybern. Part B: Cybern.* **34**(1), 159–165 (2004)
41. R.V. Dubey, T.F. Chan, S.E. Everett, Variable damping impedance control of a bilateral tele-robotic system. *IEEE Control Syst.* **17**(1), 37–45 (1997)
42. A. Feldman, Functional tuning of the nervous system with control of movement or maintenance of a steady posture. ii. Controllable parameters of the muscle. *Biophysics* **11**(3), 565–578 (1966)

43. T. Milner, C. Cloutier, A. Leger, D. Franklin, Inability to activate muscle maximally during cocontraction and the effect on joint stiffness. *Exp. Brain Res.* **107**, 293–305 (1995)
44. T. Milner, Contribution of geometry and joint stiffness to mechanical stability of the human arm. *Exp. Brain Res.* **143**, 515–519 (2002)
45. R. Trumbower, M. Krutky, B. Yang, E. Perreault, Use of self-selected postures to regulate multijoint stiffness during unconstrained tasks. *PLoS One* **4**(5), e5411 (2009)
46. F.A. Mussa-Ivaldi, N. Hogan, E. Bizzi, Neural, mechanical, geometric factors subserving arm posture in humans. *J. Neurosci.* **5**(10), 2732–2743 (1985)
47. R. Osu, H. Gomi, Multijoint muscle regulation mechanisms examined by measured human arm stiffness and EMG signals. *J. Neurophysiol.* **81**(4), 1458–1468 (1999)
48. R. Osu, H. Gomi, Multijoint muscle regulation mechanism examined by measured human arm stiffness and EMG signals. *J. Neurophysiol.* **81**, 1458–1468 (1999)
49. H. Gomi, R. Osu, Task-dependent viscoelasticity of human multi joint arm and its spatial characteristics for interaction with environments. *J. Neurosci.* **18**, 65–78 (1998)
50. E. Perreault, R. Kirsch, P. Crago, Multijoint dynamics and postural stability of the human arm. *Exp. Brain Res.* **157**, 507–517 (2004)
51. E. Burdet, R. Osu, D. Franklin, T.E. Milner, M. Kawato, The central nervous system stabilizes unstable dynamics by learning optimal impedance. *Nature* **414**(6862), 446–449 (2001)
52. N. Hogan, The mechanics of multi-joint posture and movement control. *Biol. Cybern.* **52**(5), 315–331 (1985)
53. F. Mussa-Ivaldi, N. Hogan, E. Bizzi, Neural, mechanical, geometric factors subserving arm posture in humans. *J. Neurosci.* **5**(10), 2732–2743 (1985)
54. J. Dolan, M. Friedman, M. Nagurka, Dynamic and loaded impedance components in the maintenance of human arm posture. *IEEE Trans. Syst. Man Cybern.* **23**, 698–709 (1993)
55. T. Tsuji, Y. Takeda, Y. Tanaka, Analysis of mechanical impedance in human arm movements using a virtual tennis system. *Biol. Cybern.* **91**(5), 295–305 (2004)
56. T. Tsuji, P. Morasso, K. Goto, K. Ito, Human hand impedance characteristics during maintained posture. *Biol. Cybern.* **72**, 475–485 (1995)
57. D. Shin, J. Kim, Y. Koike, A myokinetic arm model for estimating joint torque and stiffness from EMG signals during maintained posture. *J. Physiol.* **101**, 387–401 (2009)
58. L. Selen, P. Beek, J.V. Dieen, Can co-activation reduce kinematic variability? A simulation study. *Biol. Cybern.* **93**, 373–381 (2005)
59. D. Franklin, R. Osu, E. Burdet, M. Kawato, T. Milner, Adaptation to stable and unstable dynamics achieved by combined impedance control and inverse dynamics model. *J. Neurophysiol.* **90**(5), 3270–3282 (2003)
60. S. Pfeifer, H. Vallery, M. Hardegger, R. Riener, E.J. Perreault, Model-based estimation of knee stiffness. *IEEE Trans. Biomed. Eng.* **59**(9), 2604–2612 (2012)
61. R. Osu, D. Franklin, H. Kato, H. Gomi, K. Domen, T. Yoshioka, M. Kawato, Short- and long-term changes in joint co-contraction associated with motor learning as revealed from surface EMG. *J. Neurophysiol.* **88**, 991–1004 (2002)
62. K. Akazawa, T. Milner, R. Stein, Modulation of reflex EMG and stiffness in response to stretch of human finger muscle. *J. Neurophysiol.* **49**, 16–27 (1983)
63. H. Gomi, M. Kawato, Human arm stiffness and equilibrium-point trajectory during multi-joint movement. *Biol. Cybern.* **76**(3), 163–171 (1997)
64. P. Gribble, D. Ostry, Compensation for loads during arm movements using equilibrium-point control. *Exp. Brain Res.* **4**(135), 474–482 (2000)
65. P. Gribble, L. Mullin, N. Cothros, A. Mattar, Role of cocontraction in arm movement accuracy. *J. Neurophysiol.* **89**, 2396–2405 (2003)
66. E. Perreault, R. Kirsch, P. Crago, Voluntary control of static endpoint stiffness during force regulation tasks. *J. Neurophysiol.* **87**, 2808–2816 (2002)
67. G.A. Pratt, M.M. Williamson, Series elastic actuators, in *Proceedings. 1995 IEEE/RSJ International Conference on Intelligent Robots and Systems 95. Human Robot Interaction and Cooperative Robots*, vol. 1 (IEEE, 1995), pp. 399–406

68. R. Bischoff, J. Kurth, G. Schreiber, R. Koeppe, A. Albu-Schäffer, A. Beyer, O. Eiberger, S. Haddadin, A. Stemmer, G. Grunwald, et al., The KUKA DLR lightweight robot arm-a new reference platform for robotics research and manufacturing, in *41st International Symposium on Robotics (ROBOTIK)* (VDE, 2010), pp. 1–8
69. A. Bicchi, G. Tonietti, M. Bavaro, M. Piccigallo, *Variable stiffness actuators for fast and safe motion control*, in *Robotics Research* (Springer, Berlin, 2005), pp. 527–536
70. S.A. Migliore, E.A. Brown, S.P. DeWeerth, Biologically inspired joint stiffness control, in *Proceedings of the 2005 IEEE International Conference on Robotics and Automation, 2005. ICRA 2005* (IEEE, 2005), pp. 4508–4513
71. M. Laffranchi, N. Tsagarakis, F. Cannella, D. Caldwell, Antagonistic and series elastic actuators: a comparative analysis on the energy consumption, in *IEEE/RSJ International Conference on Intelligent Robots and Systems* (IEEE, 2009), pp. 5678–5684
72. A. Jafari, N. Tsagarakis, B. Vanderborght, D. Caldwell, A new variable stiffness actuator (CompAct-VSA): design and modelling, in *IEEE/RSJ International Conference on Intelligent Robots and Systems (IROS)* (2011), pp. 378–384
73. M. Mancini, G. Grioli, M.G. Catalano, M. Garabini, F. Bonomo, A. Bicchi, Passive impedance control of a qbird multi-dof vsa manipulator, in *International Conference of Robotics and Automation-ICRA 2012*, Saint Paul 14–18, May 2012
74. M. Grebenstein, A. Albu-Schaffer, T. Bahls, M. Chalon, O. Eiberger, W. Friedl, R. Gruber, S. Haddadin, U. Hagn, R. Haslinger, et al., The dlr hand arm system, in *IEEE International Conference on Robotics and Automation (ICRA)* (IEEE, 2011), pp. 3175–3182
75. N. Hogan, Impedance control: an approach to manipulation: parts 1, 2, 3. *J. Dyn. Syst. Meas. Control* **107**, 1–24 (1985)
76. C. Ott, *Cartesian Impedance Control of Redundant and Flexible-joint Robots*, in *Springer Tracts in Advanced Robotics*, vol. 49 (Springer Publishing Company, Berlin, 2008)
77. O. Khatib, A unified approach for motion and force control of robot manipulators: the operational space formulation. *IEEE J. Robot. Autom.* **3**(1), 43–53 (1987)
78. L.M. Miller, J. Rosen, Comparison of multi-sensor admittance control in joint space and task space for a seven degree of freedom upper limb exoskeleton, in *2010 3rd IEEE RAS and EMBS International Conference on Biomedical Robotics and Biomechatronics (BioRob)* (IEEE, 2010), pp. 70–75
79. S.-F. Chen, I. Kao, Conservative congruence transformation for joint and Cartesian stiffness matrices of robotic hands and fingers. *Int. J. Robot. Res.* **19**(9), 835–847 (2000)
80. M. Mosadeghzad, G.A. Medrano-Cerdá, J.A. Saglia, N.G. Tsagarakis, D.G. Caldwell, Comparison of various active impedance control approaches, modeling, implementation, passivity, stability and trade-offs, in *2012 IEEE/ASME International Conference on Advanced Intelligent Mechatronics (AIM)* (IEEE, 2012), pp. 342–348
81. A. Albu-Schaffer, G. Hirzinger, Cartesian impedance control techniques for torque controlled light-weight robots, in *Proceedings. ICRA'02. IEEE International Conference on Robotics and Automation*, vol. 1 (IEEE, 2002), pp. 657–663
82. A. Albu-Schäffer, C. Ott, G. Hirzinger, A unified passivity-based control framework for position, torque and impedance control of flexible joint robots. *Int. J. Robot. Res.* **26**(1), 23–39 (2007)
83. F. Petit, A. Albu-Schaffer, Cartesian impedance control for a variable stiffness robot arm, in *IEEE/RSJ International Conference on Intelligent Robots and Systems (IROS)* (IEEE, 2011), pp. 4180–4186
84. P. Culmer, A. Jackson, M. Levesley, J. Savage, R. Richardson, J. Cozens, B. Bhakta, An admittance control scheme for a robotic upper-limb stroke rehabilitation system, in *Proceedings of the 2005 IEEE Engineering in Medicine and Biology 27th Annual Conference* (2005)
85. M. Garabini, A. Passaglia, F. Belo, P. Salaris, A. Bicchi, Optimality principles in variable stiffness control: the VSA hammer, in *2011 IEEE/RSJ International Conference on Intelligent Robots and Systems (IROS)* (IEEE, 2011), pp. 3770–3775
86. M. Howard, D.J. Braun, S. Vijayakumar, Transferring human impedance behavior to heterogeneous variable impedance actuators. *IEEE Trans. Robot.* **29**(4), 847–862 (2013)

87. P.K. Artemiadis, P.T. Katsiaris, M.V. Liarokapis, K.J. Kyriakopoulos, Human arm impedance: characterization and modeling in 3d space, in *2010 IEEE/RSJ International Conference on Intelligent Robots and Systems (IROS)* (IEEE, 2010), pp. 3103–3108
88. L. Peternel, T. Petrič, E. Oztop, J. Babič, Teaching robots to cooperate with humans in dynamic manipulation tasks based on multi-modal human-in-the-loop approach. *Auton. Robot.* **36**(1–2), 123–136 (2014)
89. D.E. Whitney, Resolved motion rate control of manipulators and human prostheses. *IEEE Trans. Man-Mach. Syst.* **10**(2), 47–53 (1969)
90. H. Seraji, Task options for redundancy resolution using configuration control, in *Proceedings of the 30th IEEE Conference on Decision and Control* (IEEE, 1991), pp. 2793–2798
91. Y. Nakamura, *Advanced Robotics: Redundancy and Optimization* (Addison-Wesley Longman Publishing Co., Inc, Boston, 1990)
92. S. Chiaverini, Singularity-robust task-priority redundancy resolution for real-time kinematic control of robot manipulators. *IEEE Trans. Robot. Autom.* **13**(3), 398–410 (1997)
93. J. Baillieul, Kinematic programming alternatives for redundant manipulators, in *Proceedings. 1985 IEEE International Conference on Robotics and Automation*, vol. 2 (IEEE, 1985), pp. 722–728
94. B. Cao, G.I. Dodds, G.W. Irwin, Redundancy resolution and obstacle avoidance for cooperative industrial robots. *J. Robot. Syst.* **16**(7), 405–417 (1999)
95. K. Suh, J.M. Hollerbach, Local versus global torque optimization of redundant manipulators, in *Proceedings. 1987 IEEE International Conference on Robotics and Automation*, vol. 4 (IEEE, 1987), pp. 619–624
96. H. Seraji, R. Colbaugh, Improved configuration control for redundant robots. *J. Robot. Syst.* **7**(6), 897–928 (1990)
97. A.A. Maciejewski, C.A. Klein, Obstacle avoidance for kinematically redundant manipulators in dynamically varying environments. *Int. J. Robot. Res.* **4**(3), 109–117 (1985)
98. W. Owen, E. Croft, B. Benhabib, Acceleration and torque redistribution for a dual-manipulator system. *IEEE Trans. Robot.* **21**(6), 1226–1230 (2005)
99. A. Albu-Schäffer, M. Fischer, G. Schreiber, F. Schoepppe, G. Hirzinger, Soft robotics: what Cartesian stiffness can obtain with passively compliant, uncoupled joints? in *IEEE/RSJ International Conference on Intelligent Robots and Systems*, vol. 4 (IEEE, 2004), pp. 3295–3301
100. W. Owen, E. Croft, B. Benhabib, Stiffness optimization for two-armed robotic sculpting. *Ind. Robot: Int. J.* **35**(1), 46–57 (2008)
101. R. Goertz, R. Blomgren, J. Grimson, G. Forster, W. Thompson, W. Kline, The ANL model 3 master-slave electric manipulator—its design and use in a cave. *Trans. Am. Nucl. Soc.* **4**(2), 219–220 (1961)
102. B. Hannaford, R. Anderson, Experimental and simulation studies of hard contact in force reflecting teleoperation, in *International Conference on Robotics and Automation* (1988), pp. 584–589
103. T. Imaida, Y. Yokokohji, M.O.T. Doi, T. Yoshikawa, Ground space bilateral teleoperation of ETS-VII robot arm by direct bilateral coupling under 7-s time delay condition. *IEEE Trans. Robot. Autom.* **20**(3), 499–511 (2004)
104. G. Leung, B. Francis, J. Apkarian, Bilateral controller for teleoperators with time delay via mu-synthesis. *IEEE Trans. Robot. Autom.* **11**, 105–116 (1995)
105. A. Eusebi, C. Melchiorri, Force reflecting telemanipulators with timedelay: stability analysis and control design. *IEEE Trans. Robot. Autom.* **14**(4), 635–640 (1998)
106. T. Sheridan, Space teleoperation through time delay: review and prognosis. *IEEE Trans. Robot. Autom.* **9**(5), 592–606 (1993)
107. A. Albu-Schäffer, S. Haddadin, C. Ott, A. Stemmer, T. Wimbock, G. Hirzinger, The DLR lightweight robot lightweight design and soft robotics control concepts for robots in human environments. *Ind. Robot J.* **34**, 376–385 (2007)
108. A. Bicchi, G. Tonietti, Fast and soft arm tactics: dealing with the safety-performance trade off in robot arms design and control. *IEEE Robot. Autom. Mag.* **11**(2), 22–33 (2004)

109. G. Tonietti, R. Schiavi, A. Bicchi, Design and control of a variable stiffness actuator for safe and fast physical human/robot interaction, in *IEEE International Conference on Robotics and Automation* (2005), pp. 526–531
110. M. Kawato, Internal models for motor control and trajectory planning. *Current Opin. Neurobiol.* **9**, 718–727 (1999)
111. B. Adorno, A. Bo, P. Fraisse, P. Poignet, Towards a cooperative framework for interactive manipulation involving a human and a humanoid, in *IEEE International Conference on Robotics and Automation* (2011), pp. 3777–3783
112. A. Billard, D. Grollman, *Encyclopedia of the Sciences of Learning* (Springer, Berlin, 2011) (ch. Imitation Learning (of robots))
113. F. Mussa-Ivaldi, L. Miller, Brain-machine interfaces: computational demands and clinical needs meet basic neuroscience. *Trends Neurosci.* **26**(6), 329–334 (2003)
114. J. Millan, F. Renkens, J. Mourino, W. Gerstner, Non-invasive brain-actuated control of a mobile robot by human EEG. *IEEE Trans. Biomed. Eng.* **51**(6), 1026–1033 (2004)
115. T. Gulrez, A. Tognetti, A. Fishbach, S. Acosta, C. Scharver, D. De Rossi, F. Mussa-Ivaldi, Controlling wheelchairs by body motions: a learning framework for the adaptive remapping of space, in *International Conference on Cognitive Systems* (2008)
116. C. Castellini, P. Van Der Smagt, Surface EMG in advanced hand prosthetics. *Biol. Cybern.* **100**(1), 35–47 (2009)
117. M. Howard, D. Braun, S. Vijayakumar, Constraint based equilibrium and stiffness control of variable stiffness actuators, in *IEEE Conference on Robotics and Automation (ICRA)* (2011)
118. O. Fukuda, T. Tsuji, M. Kaneko, A. Otsuka, A human-assisting manipulator teleoperated by EMG signals and arm motions. *IEEE Trans. Robot. Autom.* **19**(2), 210–222 (2003)
119. P. Artimeiadis, K. Kyriakopoulos, An EMG-based robot control scheme robust to time-varying EMG signal features. *IEEE Trans. Inf. Technol. Biomed.* **14**(3), 582–588 (2010)
120. J. Vogel, C. Castellini, P. Der Smagt, EMG-based teleoperation and manipulation with the DLR LWR-III: design and modelling, in *IEEE/RSJ International Conference on Intelligent Robots and Systems (IROS)* (2011), pp. 672–678
121. M. Turvey, Action and perception at the level of synergies. *Hum. Mov. Sci.* **26**(4), 657–697 (2007)
122. P. Weiss, *The Self-Differentiation of the Basic Patterns of Coordination* (The Williams & Wilkins Company, Baltimore, 1941)
123. S. De Serres, T. Milner, Wrist muscle activation patterns and stiffness associated with stable and unstable mechanical loads. *Exp. Brain Res.* **86**, 451–458 (1991)
124. G. Schreiber, A. Stemmer, R. Bischoff, The fast research interface for the KUKA lightweight robot, in *IEEE Conference on Robotics and Automation (ICRA)* (2010)
125. K. Mann, F. Werner, A. Palmer, Frequency spectrum analysis of wrist motion for activities of daily living. *J. Orthop. Res.* **7**, 304–306 (1989)
126. K. Tee, E. Burdet, C. Chew, T. Milner, A model of force and impedance in human arm movements. *Biol. Cybern.* **90**, 368–375 (2004)
127. J. Wakeling, A. Liphardt, B. Nigg, Muscle activity reduces soft-tissue resonance at heel-strike during walking. *J. Biomech.* **36**, 1761–1769 (2003)
128. G. Genta, *Vibration of Structures and Machines* (Springer, New York, 1995)
129. H. McCallion, G. Johnson, D. Pham, A compliant device for inserting a peg in a hole. *Ind. Robot: Int. J.* **6**(2), 81–87 (1979)
130. D. Whitney, J. Rourke, Mechanical behavior and design equations for elastomer shear pad remote center compliances. *J. Dyn. Syst. Meas. Control* **108**(3), 223–232 (1986)
131. F. Lacquaniti, M. Carrozzo, N. Borghese, Time-varying mechanical behavior of multijointed arm in man. *J. Neurophysiol.* **69**, 1443–1463 (1993)
132. O. Khatib, E. Demircan, V. De Sario, L. Sentis, T. Besier, S. Delp, Robotics-based synthesis of human motion. *J. Physiol.-Paris* **103**(3), 211–219 (2009)
133. Y. Uno, M. Kawato, R. Suzuki, Formation and control of optimal trajectory in human multijoint arm movement. *Biol. Cybern.* **61**(2), 89–101 (1989)

134. G. Golub, V. Pereyra, The differentiation of pseudo-inverses and nonlinear least squares problems whose variables separate. *SIAM J. Numeri. Anal.* **10**, 413–432 (1973)
135. D. Matsui, T. Minato, K.F. MacDorman, H. Ishiguro, Generating natural motion in an android by mapping human motion, in *2005 IEEE/RSJ International Conference on Intelligent Robots and Systems, 2005. (IROS 2005)* (IEEE, 2005), pp. 3301–3308
136. A.M. Zanchettin, P. Rocco, L. Bascetta, I. Symeonidis, S. Peldschus, Kinematic analysis and synthesis of the human arm motion during a manipulation task, in *2011 IEEE International Conference on Robotics and Automation (ICRA)* (IEEE, 2011), pp. 2692–2697
137. T. Wimböck, C. Ott, A. Albu-Schäffer, G. Hirzinger, Comparison of object-level grasp controllers for dynamic dexterous manipulation. *Int. J. Robot. Res.* **31**(1), 3–23 (2012)
138. S. Schneider, R. Cannon Jr, Object impedance control for cooperative manipulation: theory and experimental results. *IEEE Trans. Robot. Autom.* **8**(3), 383–394 (1992)
139. R. Bonitz, T. Hsia, Internal force-based impedance control for cooperating manipulators. *IEEE Trans. Robot. Autom.* **12**(1), 78–89 (1996)
140. F. Caccavale, P. Chiacchio, A. Marino, L. Villani, Six-dof impedance control of dual-arm cooperative manipulators. *IEEE/ASME Trans. Mechatron.* **13**(5), 576–586 (2008)
141. A. Dietrich, T. Wimbock, A. Albu-Schaffer, Dynamic whole-body mobile manipulation with a torque controlled humanoid robot via impedance control laws, in *Proceedings of 2011 IEEE/RSJ International Conference on Intelligent Robots and Systems (IROS)* (2011), pp. 3199–3206
142. Y. Guiard, Asymmetric division of labor in human skilled bimanual action: the kinematic chain as a model. *J. Motor Behav.* **19**, 486–517 (1987)
143. K. Hinckley, R. Pausch, D. Proffitt, J. Patten, N. Kassell, Cooperative bimanual action, in *Proceedings of the ACM SIGCHI Conference on Human Factors in Computing Systems* (ACM, 1997), pp. 27–34
144. Y. Guiard, The kinematic chain as a model for human asymmetrical bimanual cooperation. *Adv. Psychol.* **55**, 205–228 (1988)
145. A. Mohri, M. Yamamoto, G. Hirano, Cooperative path planning for two manipulators, in *Proceedings. 1996 IEEE International Conference on Robotics and Automation*, vol. 3 (IEEE, 1996), pp. 2853–2858
146. J.-D. Choi, S. Kang, M. Kim, C. Lee, J.-B. Song, Two-arm cooperative assembly using force-guided control with adaptive accommodation, in *Proceedings. 1999 IEEE/RSJ International Conference on Intelligent Robots and Systems, 1999. IROS '99*, vol. 2 (1999), pp. 1253–1258
147. J. Lee, P. Chang, R. Jamisola, Relative impedance control for dual-arm robots performing asymmetric bimanual tasks. *IEEE Trans. Ind. Electron.* **61**, 3786–3796 (2013)
148. N. Staff, *Amputation Statistics by Cause, Limb Loss in the United States* (National Limb Loss Information Center, Knoxville, 2008)
149. World Health Organization, *United States Department of Defense, and MossRehab Amputee Rehabilitation Program* (World Health Organization, The rehabilitation of people with amputations, 2004)
150. N. Jiang, K. Englehart, P. Parker, Extracting simultaneous and proportional neural control information for multiple-dof prostheses from the surface electromyographic signal. *IEEE Trans. Biomed. Eng.* **56**(4), 1070–1080 (2009)
151. D. Naidu, C. Chen, A. Perez, M. Schoen, Control strategies for smart prosthetic hand technology: an overview, in *Engineering in Medicine and Biology Society, EMBS 2008. 30th Annual International Conference of the IEEE* (IEEE, 2008), pp. 4314–4317
152. M. Catalano, G. Grioli, A. Serio, E. Farnioli, C. Piazza, A. Bicchi, Adaptive synergies for a humanoid robot hand, in *IEEE-RAS International Conference on Humanoid Robots* (2012)
153. M. Gabiccini, A. Bicchi, D. Prattichizzo, M. Malvezzi, On the role of hand synergies in the optimal choice of grasping forces. *Auton. Robot.* **31**(2), 235–252 (2011)
154. A. Bicchi, M. Gabiccini, M. Santello, Modelling natural and artificial hands with synergies. *Philos. Trans. R. Soc. B: Biol. Sci.* **366**(1581), 3153–3161 (2011)
155. L. Birglen, C. Gosselin, T. Laliberté, *Underactuated Robotic Hands*, vol. 40 (Springer, Berlin, 2008)

156. M. Santello, M. Flanders, J. Soechting, Postural hand synergies for tool use. *J. Neurosci.* **18**(23), 10105–10115 (1998)
157. A. Perotto, E. Delagi, *Anatomical Guide for the Electromyographer: The Limbs and Trunk* (Charles C Thomas Pub Limited, Springfield, 2005)
158. P. Jenmalm, R. Johansson, Visual and somatosensory information about object shape control manipulative fingertip forces. *J. Neurosci.* **17**(11), 4486–4499 (1997)
159. G. Cadoret, A. Smith, Friction, not texture, dictates grip forces used during object manipulation. *J. Neurophysiol.* **75**, 1963–1969 (1996)
160. J. Flanagan, A. Wing, The stability of precision grip forces during cyclic arm movements with a hand-held load. *Exp. Brain Res.* **105**(3), 455–464 (1995)
161. G. Lundborg, B. Rosen, Sensory substitution in prosthetics. *Hand Clin.* **17**, 481–488 (2001)
162. P. Kyberd, C. Wartenberg, L. Sandsjönsson, D. Gow, J. Frid, C. Almstrom, L. Sperling, Survey of upper-extremity prosthesis users in Sweden and the United Kingdom. *J. Prosthet. Orthop.* **19**, 55–62 (2007)
163. J. Brown, R. Gillespie, The effect of force/motion coupling on motor and cognitive performance, in *IEEE World Haptics Conference (WHC)* (2011), pp. 197–202
164. C. Cipriani, M. D’Alonzo, M. Carrozza, A miniature vibrotactile sensory substitution device for multi-fingered hand prosthetics. *IEEE TBME* (2011)
165. T. Kuiken, G. Dumanian, R. Lipschutz, L. Miller, K. Stubblefield, Targeted reinnervation for enhanced prosthetic arm function in a woman with a proximal amputation: a case study. *Lancet* **369**(1), 371–380 (2007)
166. T. Kuiken, L. Miller, R. Lipschutz, B. Lock, K. Stubblefield, P. Marasco, P. Zhou, G. Dumanian, The use of targeted muscle reinnervation for improved myoelectric prosthesis control in a bilateral shoulder disarticulation amputee. *Prosthet. Orthot. Int.* **28**(3), 245–253 (2004)
167. A. Chatterjee, V. Aggarwal, A. Ramos, S. Acharya, N. Thakor, A brain-computer interface with vibrotactile feedback for haptic information. *J. Neuroeng. Rehabil.* **4**, 40 (2007)
168. J. Wheeler, K. Bark, J. Savall, M. Cutkosky, Investigation of rotational skin stretch for proprioceptive feedback with application to myoelectric systems. *IEEE Trans. Neural Syst. Rehabil. Eng.* **18**(1), 58–66 (2011)
169. R. Gillespie, J. Contreras-Vidal, P. Shewokis, M.O. Malley, J. Brown, H. Agashe, R. Gentili, A. Davis, Toward improved sensorimotor integration and learning using upperlimb prosthetic devices, in *Annual International Conference of the IEEE Engineering in Medicine and Biology Society (EMBC)* (2010), pp. 5077–5080
170. S. Meek, S. Jacobsen, P. Goulding, Extended physiologic tactio: design and evaluation of a proportional force feedback. *J. Rehabil. Res. Dev.* **26**(3), 53–62 (1989)
171. G. Lundborg, B. Rosen, K. Lindstrom, S. Lindberg, Artificial sensibility based on the use of piezoresistive sensors. *J. Hand Surg.* **23**(5), 620–626 (1998)
172. C. Pylatiuk, A. Kargov, S. Schulz, Design and evaluation of a low-cost force feedback system for myoelectric prosthetic hands. *JPO J. Prosthet. Orthot.* **18**(2), 57 (2006)
173. J. Brown, A. Paek, M. Syed, M. O’Malley, P. Shewokis, J. Contreras-Vidalk, A. Davis, R. Gillespie, Understanding the role of haptic feedback in a teleoperated/prosthetic grasp and lift task, in *IEEE World Haptics Conference (WHC)* (2013), pp. 271–276
174. K. Kim, J. Colgate, J. Santos-Munne, A. Makhlin, M. Peshkin, On the design of miniature haptic devices for upper extremity prosthetics. *IEEE Trans. Mechatron.* **15**(1), 27–39 (2010)
175. K. Kim, J. Colgate, Haptic feedback enhances grip force control of sEMG-controlled prosthetic hands in targeted reinnervation amputees. *IEEE Trans. Neural Syst. Rehabil. Eng.* **20**(6), 798–805 (2012)
176. N. Landin, J. Romano, W. McMahan, K. Kuchenbecker, Dimensional reduction of high-frequency accelerations for haptic rendering, in *Haptics: Generating and Perceiving Tangible Sensations*. Lecture Notes in Computer Science, vol. 6192 (Springer, Berlin, 2010), pp. 79–86
177. K. Kuchenbecker, J. Gewirtz, W. McMahan, D. Standish, P. Martin, J. Bohren, P. Mendoza, D. Lee, Verrotouch: High-frequency acceleration feedback for telerobotic surgery. *Haptics: Gener. Perceiving Tang. Sensat.* **6191**, 189–196 (2010)

178. J. Romano, K. Kuchenbecker, Creating realistic virtual textures from contact acceleration data. *IEEE Trans. Haptics* **5**(2), 109–119 (2012)
179. H. Culbertson, J. Romano, P. Castillo, M. Mintz, K. Kuchenbecker, Refined methods for creating realistic haptic virtual textures from tool-mediated contact acceleration data, in *Haptics Symposium (HAPTICS)* (IEEE, 2012), pp. 385–391
180. V.M. Zatsiorsky, M.L. Latash, Multifinger prehension: an overview. *J. Motor Behav.* **40**(5), 446–476 (2008)
181. W. Lee, Neuromotor synergies as a basis for coordinated intentional action. *J. Motor Behav.* **16**(2), 135–170 (1984)
182. M. Flanders, J.F. Soechting, Arm muscle activation for static forces in three-dimensional space. *J. Neurophysiol.* **64**(6), 1818–1837 (1990)
183. T. Buchanan, D. Lloyd, K. Manal, T. Besier, Neuromusculoskeletal modeling: estimation of muscle forces and joint moments and movements from measurements of neural command. *J. Appl. Biomech.* **20**(4), 367 (2004)
184. C.-T. Chen, W.-D. Chang, A feedforward neural network with function shape autotuning. *Neural Netw.* **9**(4), 627–641 (1996)
185. C. Castellini, E. Gruppioni, A. Davalli, G. Sandini, Fine detection of grasp force and posture by amputees via surface electromyography. *J. Physiol.-Elsevier* **103**(3), 255 (2009)
186. C.C. De Wit, P. Lischinsky, Adaptive friction compensation with partially known dynamic friction model. *Int. J. Adapt. Control Signal Process.* **11**(1), 65–80 (1997)
187. T. Murakami, F. Yu, K. Ohnishi, Torque sensorless control in multidegree-of-freedom manipulator. *IEEE Trans. Ind. Electron.* **40**(2), 259–265 (1993)
188. S. Katsura, K. Ohnishi, Human cooperative wheelchair for haptic interaction based on dual compliance control. *IEEE Trans. Ind. Electron.* **51**(1), 221–228 (2004)
189. H. Seki, M. Iso, Y. Hori, How to design force sensorless power assist robot considering environmental characteristics-position control based or force control based, in *Industrial Electronics Society, IEEE, 28th Annual Conference of the IECON 02*, vol. 3. (IEEE, 2002), pp. 2255–2260
190. W. McMahan, J. Romano, A. Abdul Rahuman, K. Kuchenbecker, High frequency acceleration feedback significantly increases the realism of haptically rendered textured surfaces, in *2010 IEEE Haptics Symposium* (2010), pp. 141–148
191. B.B. Edin, G. Westling, R.S. Johansson, Independent control of human finger-tip forces at individual digits during precision lifting. *J. Physiol.* **450**(1), 547–564 (1992)
192. C. Antfolk, M. D'Alonzo, M. Controzzi, G. Lundborg, B. Rosen, F. Sebelius, C. Cipriani, Artificial redirection of sensation from prosthetic fingers to the phantom hand map on transradial amputees: vibrotactile versus mechanotactile sensory feedback. *IEEE Trans. Neural Syst. Rehabil. Eng.* (2012)
193. K.J. Kuchenbecker, J. Fiene, G. Niemeyer, Improving contact realism through event-based haptic feedback. *IEEE Trans. Vis. Comput. Graph.* **12**(2), 219–230 (2006)
194. J. Bell, S. Bolanski, M.H. Holmes, The structure and function of Pacinian corpuscles: a review. *Prog. Neurobiol.* **42**(1), 79–128 (1994)
195. M. Merzenich, T. Harrington, The sense of flutter-vibration evoked by stimulation of the hairy skin of primates: comparison of human sensory capacity with responses of mechanoreptive afferents innervating the hairy skin of monkeys. *Exp. Brain Res.* **9**, 236–260 (1969)
196. M. D'Alonzo, C. Cipriani, M. Carrozza, Vibrotactile sensory substitution in multi-fingered hand prostheses: evaluation studies, in *IEEE International Conference on Rehabilitation Robotics (ICORR)* (2011), pp. 1–6
197. E. Francisco, V. Tannan, Z. Zhang, J. Holden, M. Tommerdahl, Vibrotactile amplitude discrimination capability parallels magnitude changes in somatosensory cortex and follows weber's law. *Exp. Brain Res.* **191**, 49–56 (2008)
198. D. Mahns, N. Perkins, V. Sahai, L. Robinson, M. Rowe, Vibrotactile frequency discrimination in human hairy skin. *J. Neurophysiol.* **95**, 1442–1450 (2006)
199. D. Katz, Der abbau taswell. *Z. Psychol.* **11**, 1–270 (1925)
200. S. Lederman, The perception of surface roughness by active and passive touch. *Bull. Psychon. Soc.* **18**(5), 253–255 (1981)

201. W. Bergmann Tiest, A. Kappers, Analysis of haptic perception of materials by multidimensional scaling and physical measurements of roughness and compressibility. *Acta Psychol. (Amst.)*, **121**(1), 1–20 (2006)
202. E.P. Scilingo, N. Sgambelluri, D. De Rossi, A. Bicchi, Towards a haptic black box for free-hand softness and shape exploration, in *Proceedings. ICRA'03. IEEE International Conference on Robotics and Automation*, vol. 2 (IEEE, 2003), pp. 2412–2417
203. D. Cox, The regression analysis for binary sequences. *J. R. Stat. Soc. B* **20**, 214–242 (1958)
204. N. Breslow, D. Clayton, Approximate inference in general linear mixed models. *J. Am. Stat. Assoc.* **88**, 9–25 (1993)
205. B.M. Bolker, M.E. Brooks, C.J. Clark, S.W. Geange, J.R. Poulsen, M.H.H. Stevens, Generalized linear mixed models: a practical guide for ecology and evolution. *Trends Ecol. Evol.* **24**(3), 127–135 (2009)
206. A. Moscatelli, M. Mezzetti, F. Lacquaniti, Modeling psychophysical data at the population-level: the generalized linear mixed model. *J. Vis.* **12**(11), 1–17 (2012)
207. B. Treutwein, Adaptive psychophysical procedures. *Vis. Res.* **35**(17), 2503–2522 (1995)
208. A. Agresti, J. Booth, J. Hobart, B. Caffo, Modeling clustered ordered categorical data. *Sociol. Methodol.* **30**, 345–371 (2000)
209. D. Hedeker, Generalized linear mixed models, in *Encyclopedia of Statistics in Behavioral Science* (Wiley, New York, 2005)
210. J. Pandergast, S. Gange, M. Newton, M. Lindstrom, M. Palta, M. Fisher, A survey of methods for analyzing clustered binary response data. *Int. Stat. Rev.* **64**, 89–118 (1996)
211. D. Bates, M. Maechler, B. Bolker, lme4: Linear mixed-effects models using s4 classes. R package version 0.999375-39 (2011)
212. H. Akaike, Information theory and an extension of maximum likelihood principle, in *Proceedings of the 2nd International Symposium on Information Theory* (1973), pp. 267–281
213. A. Zoss, H. Kazerooni, A. Chu, Biomechanical design of the Berkeley lower extremity exoskeleton (bleex). *IEEE/ASME Trans. Mechatron.* **11**(2), 128–138 (2006)
214. K. Kong, D. Jeon, Design and control of an exoskeleton for the elderly and patients. *IEEE/ASME Trans. Mechatron.* **11**(4), 428–432 (2006)
215. J. Veneman, R. Kruidhof, E. Hekman, R. Ekkelenkamp, E. Van Asseldonk, H. van der Kooij, Design and evaluation of the lopes exoskeleton robot for interactive gait rehabilitation. *IEEE Trans. Neural Syst. Rehabil. Eng.* **15**(3), 379–386 (2007)
216. R. Riener, L. Lunenburger, S. Jezernik, M. Anderschitz, G. Colombo, V. Dietz, Patient-cooperative strategies for robot-aided treadmill training: first experimental results. *IEEE Trans. Neural Syst. Rehabil. Eng.* **13**(3), 380–394 (2005)
217. K. Kong, J. Bae, M. Tomizuka, Control of rotary series elastic actuator for ideal force-mode actuation in human-robot interaction applications. *IEEE/ASME Trans. Mechatron.* **14**(1), 105–118 (2009)
218. J. Pratt, B. Krupp, C. Morse, S. Collins, The roboknee: an exoskeleton for enhancing strength and endurance during walking, in *Proceedings. ICRA '04. 2004 IEEE International Conference on Robotics and Automation*, vol. 3 (2004), pp. 2430–2435
219. K. Kong, J. Bae, Tomizuka, A compact rotary series elastic actuator for human assistive systems. *IEEE/ASME Trans. Mechatron.* **17**(2), 288–297 (2012)
220. J.A. Saglia, N.G. Tsagarakis, J.S. Dai, D.G. Caldwell, Control strategies for patient-assisted training using the ankle rehabilitation robot (arbot). *IEEE/ASME Trans. Mechatron.* **99**, 1–10 (2012)
221. N. Tsagarakis, D. Caldwell, A preliminary study on the use of haptic feedback to assist users with impaired arm coordination during mouse interactions. *Appl. Bionics Biomech.* **8**(1), 13–20 (2011)
222. R. Farris, H. Quintero, M. Goldfarb, Preliminary evaluation of a powered lower limb orthosis to aid walking in paraplegic individuals. *IEEE Trans. Neural Syst. Rehabil. Eng.* **19**(6), 652–659 (2011)
223. A. Tsukahara, R. Kawanishi, Y. Hasegawa, Y. Sankai, Sit-to-stand and stand-to-sit transfer support for complete paraplegic patients with robot suit HAL. *Adv. Robot.* **24**(11), 1615–1638 (2010)

224. C. Fleischer, G. Hommel, A human-exoskeleton interface utilizing electromyography. *IEEE Trans. Robot.* **24**(4), 872–882 (2008)
225. G. Aguirre-Ollinger, J. Colgate, M. Peshkin, A. Goswami, Inertia compensation control of a one-degree-of-freedom exoskeleton for lower-limb assistance: initial experiments. *IEEE Trans. Neural Syst. Rehabil. Eng.* **20**(1), 68–77 (2012)
226. E. Martinez-Villalpando, H. Herr, Agonist-antagonist active knee prosthesis: a preliminary study in level-ground walking. *J. Rehabil. Res. Dev.* **46**(3), 361–373 (2009)
227. T.C. Bulea, R. Kobetic, C.S. To, M.L. Audu, J.R. Schnellenberger, R.J. Triolo, A variable impedance knee mechanism for controlled stance flexion during pathological gait. *IEEE/ASME Trans. Mechatron.* **17**(5), 822–832 (2012)
228. J. Blaya, H. Herr, Adaptive control of a variable-impedance ankle-foot orthosis to assist drop-foot gait. *IEEE Trans. Neural Syst. Rehabil. Eng.* **12**(1), 24–31 (2004)
229. S. Lee, Y. Sankai, Power assist control for walking aid with HAL-3 based on EMG and impedance adjustment around knee joint. *IEEE/RSJ Int. Conf. Intell. Robot. Syst.* **2**, 1499–1504 (2002)
230. T.S. Buchanan, D.A. Shreeve, An evaluation of optimization techniques for the prediction of muscle activation patterns during isometric tasks. *J. Biomech. Eng.* **118**(4), 565–574 (1996)
231. F. Zajac et al., Muscle and tendon: properties, models, scaling, and application to biomechanics and motor control. *Crit. Rev. Biomed. Eng.* **17**(4), 359 (1989)
232. A. Hill, The heat of shortening and the dynamic constants of muscle. *Proc. R. Soc. Lond. Ser. B Biol. Sci.* **126**(843), 136–195 (1938)
233. D.G. Lloyd, T.F. Besier, An EMG-driven musculoskeletal model to estimate muscle forces and knee joint moments in vivo. *J. Biomech.* **36**(6), 765–776 (2003)
234. J. Visser, J. Hoogkamer, M. Bobbert, P. Huijing, Length and moment arm of human leg muscles as a function of knee and hip-joint angles. *Eur. J. Appl. Physiol. Occup. Physiol.* **61**(5), 453–460 (1990)
235. K. An, K. Takahashi, T. Harrigan, E. Chao, Determination of muscle orientations and moment arms. *J. Biomech. Eng.* **106**, 280 (1984)
236. R. Osu, D. Franklin, H. Kato, H. Gomi, K. Domen, T. Yoshioka, M. Kawato, Short-and long-term changes in joint co-contraction associated with motor learning as revealed from surface emg. *J. Neurophysiol.* **88**(2), 991–1004 (2002)
237. N.C. Karavas, N.G. Tsagarakis, J. Saglia, D.G. Caldwell, A novel actuator with reconfigurable stiffness for a knee exoskeleton: design and modeling, in *Advances in Reconfigurable Mechanisms and Robots I*, ed. by J.S. Dai, M. Zoppi, X. Kong (Springer, London, 2012), pp. 411–421
238. N. Karavas, N. Tsagarakis, D. Caldwell, Design, modeling and control of a series elastic actuator for an assistive knee exoskeleton, in *2012 4th IEEE RAS EMBS International Conference on Biomedical Robotics and Biomechatronics (BioRob)* (2012), pp. 1813–1819
239. O. Unluhisarcikli, M. Pietrusinski, B. Weinberg, P. Bonato, C. Mavroidis, Design and control of a robotic lower extremity exoskeleton for gait rehabilitation, in *2011 IEEE/RSJ International Conference on Intelligent Robots and Systems (IROS)* (2011), pp. 4893–4898
240. H. Rifai, S. Mohammed, B. Daachi, Y. Amirat, Adaptive control of a human-driven knee joint orthosis, in *2012 IEEE International Conference on Robotics and Automation (ICRA)* (2012), pp. 2486–2491
241. L.-Q. Zhang, G. Nuber, J. Butler, M. Bowen, W.Z. Rymer, In vivo human knee joint dynamic properties as functions of muscle contraction and joint position. *J. Biomech.* **31**(1), 71–76 (1997)
242. J. Abbas, H. Chizeck, Neural network control of functional neuromuscular stimulation systems: computer simulation studies. *IEEE Trans. Biomed. Eng.* **42**(11), 1117–1127 (1995)
243. D. Winter, Human balance and posture control during standing and walking. *Gait Posture* **3**(4), 193–214 (1995)
244. I.D. Loram, M. Lakie, Human balancing of an inverted pendulum: position control by small, ballistic-like, throw and catch movements. *J. Physiol.* **540**(3), 1111–1124 (2002)

245. P. Crenna, C. Frigo, A motor programme for the initiation of forward-oriented movements in humans. *J. Physiol.* **437**(1), 635–653 (1991)
246. P. Gatev, S. Thomas, T. Kepple, M. Hallett, Feedforward ankle strategy of balance during quiet stance in adults. *J. Physiol.* **514**(3), 915–928 (1999)
247. A. Kuo, An optimal control model for analyzing human postural balance. *IEEE Trans. Biomed. Eng.* **42**(1), 87–101 (1995)
248. I.D. Loram, M. Lakie, Direct measurement of human ankle stiffness during quiet standing: the intrinsic mechanical stiffness is insufficient for stability. *J. Physiol.* **545**(3), 1041–1053 (2002)
249. P.G. Morasso, V. Sanguineti, Ankle muscle stiffness alone cannot stabilize balance during quiet standing. *J. Neurophysiol.* **88**(4), 2157–2162 (2002)
250. S. Agrawal, S. Banala, A. Fattah, V. Sangwan, V. Krishnamoorthy, J. Scholz, H. Wei-Li, Assessment of motion of a swing leg and gait rehabilitation with a gravity balancing exoskeleton. *IEEE Trans. Neural Syst. Rehabil. Eng.* **15**(3), 410–420 (2007)
251. S. Krut, M. Benoit, E. Dombre, F. Pierrot, Moonwalker a lower limb exoskeleton able to sustain bodyweight using a passive force balancer, in *IEEE International Conference on Robotics and Automation (ICRA)* (2010), pp. 2215–2220
252. S. Banala, S. Agrawal, A. Fattah, V. Krishnamoorthy, H. Wei-Li, J. Scholz, K. Rudolph, Gravity-balancing leg orthosis and its performance evaluation. *IEEE Trans. Robot.* **22**(6), 1228–1239 (2006)
253. S. Pfeifer, H. Vallery, M. Hardegger, R. Riener, E.J. Perreault, Model-based estimation of knee stiffness. *IEEE Trans. Biomed. Eng.* **59**(9), 2604–2612 (2012)
254. L. Cui, E.J. Perreault, H. Maas, T.G. Sandercock, Modeling short-range stiffness of feline lower hindlimb muscles. *J. Biomech.* **41**(9), 1945–1952 (2008)
255. E. Arnold, S. Ward, R. Lieber, S. Delp, A model of the lower limb for analysis of human movement. *Ann. Biomed. Eng.* **38**, 269–279 (2010)
256. O. Caron, T. Gelat, P. Rougier, J. Blanchi, A comparative analysis of the center of gravity and center of pressure trajectory path lengths in standing posture: an estimation of active stiffness. *J. Appl. Biomech.* **16**(3), 234–247 (2000)